Lecture Notes in Civil Engineering

Kasinathan Muthukkumaran
Ravi Sankar Jakka
C. R. Parthasarathy
B. Soundara *Editors*

Soil Behavior and Characterization of Geomaterials

Proceedings of Indian Geotechnical Conference 2021 Volume 1

Springer

Lecture Notes in Civil Engineering

Volume 296

Lecture Notes in Civil Engineering (LNCE) publishes the latest developments in Civil Engineering—quickly, informally and in top quality. Though original research reported in proceedings and post-proceedings represents the core of LNCE, edited volumes of exceptionally high quality and interest may also be considered for publication. Volumes published in LNCE embrace all aspects and subfields of, as well as new challenges in, Civil Engineering. Topics in the series include:

- Construction and Structural Mechanics
- Building Materials
- Concrete, Steel and Timber Structures
- Geotechnical Engineering
- Earthquake Engineering
- Coastal Engineering
- Ocean and Offshore Engineering; Ships and Floating Structures
- Hydraulics, Hydrology and Water Resources Engineering
- Environmental Engineering and Sustainability
- Structural Health and Monitoring
- Surveying and Geographical Information Systems
- Indoor Environments
- Transportation and Traffic
- Risk Analysis
- Safety and Security

To submit a proposal or request further information, please contact the appropriate Springer Editor:

– Pierpaolo Riva at pierpaolo.riva@springer.com (Europe and Americas);
– Swati Meherishi at swati.meherishi@springer.com (Asia—except China, Australia, and New Zealand);
– Wayne Hu at wayne.hu@springer.com (China).

All books in the series now indexed by Scopus and EI Compendex database!

Kasinathan Muthukkumaran · Ravi Sankar Jakka ·
C. R. Parthasarathy · B. Soundara
Editors

Soil Behavior and Characterization of Geomaterials

Proceedings of Indian Geotechnical Conference 2021 Volume 1

Springer

Editors
Kasinathan Muthukkumaran
Department of Civil Engineering
National Institute of Technology
Tiruchirappalli, Tamil Nadu, India

Ravi Sankar Jakka
Department of Earthquake Engineering
Indian Institute of Technology Roorkee
Roorkee, Uttarakhand, India

C. R. Parthasarathy
Sarathy Geotech and Engineering Services
Pvt. Ltd.
Bengaluru, Karnataka, India

B. Soundara
Department of Civil Engineering
Saveetha University
Chennai, Tamil Nadu, India

ISSN 2366-2557 ISSN 2366-2565 (electronic)
Lecture Notes in Civil Engineering
ISBN 978-981-19-6512-8 ISBN 978-981-19-6513-5 (eBook)
https://doi.org/10.1007/978-981-19-6513-5

This Springer imprint is published by the registered company Springer Nature Singapore Pte Ltd.
The registered company address is: 152 Beach Road, #21-01/04 Gateway East, Singapore 189721, Singapore

Preface

The Indian Geotechnical Society, Trichy (IGS-Trichy) Chapter, and National Institute of Technology (NIT) Tiruchirappalli, India, organized the Indian Geotechnical Conference (IGC-2021) at Trichy during 16–18 December 2021. The main theme of the conference was **"GEO-INDIA"—GEO**TECHNICS FOR **IN**FRASTRUCTURE **D**EVELOPMENT AND **I**NNOVATIVE **A**PPLICATIONS.

The sub-themes of the conference included:

1. Soil Behaviour and Characterization of Geomaterials
2. Geotechnical, Geological and Geophysical Investigation
3. Foundation Engineering
4. Ground Improvement Techniques
5. Geo-environmental Engineering
6. Soil Dynamics and Earthquake Geotechnical Engineering
7. Earth Retaining Structures, Dams and Embankments
8. Slope Stability and Landslides
9. Transportation Geotechnics
10. Geosynthetics Application
11. Computational, Analytical and Numerical Modelling
12. Rock Engineering, Tunnelling, Deep Excavations and Underground Constructions
13. Forensic Geotechnical Engineering and Case Studies
14. Others: Behaviour of Unsaturated Soils, Offshore & Marine Geotechnics, Remote Sensing & GIS, Instrumentation & Monitoring, Retrofitting of Geotechnical Structures, Reliability in Geotechnical Engineering, Geotechnical Education, Codes & Standards, & any other relevant topic.

The proceedings of this conference consists of selected papers presented at the conference. The proceedings is divided into six volumes. A special issue on IGC-2021 keynote and theme lecture presentations were published by Indian Geotechnical Journal.

We sincerely thank all the authors who have contributed their papers to the conference proceedings. We also thank all the theme editors and reviewers who have been instrumental in giving their valuable inputs for improving the quality of the final papers. We greatly appreciate and thank all the student volunteers for their unwavering support that was instrumental in preparation of this proceedings. Finally, thanks to Springer team for their support and full cooperation for publishing six volumes of this IGC-2021 proceedings.

Trichy, India

Kasinathan Muthukkumaran
Chairman IGC-2021

Contents

About the Editors

Dr. Kasinathan Muthukkumaran is currently Professor in Civil Engineering at National Institute of Technology, Tiruchirappalli, India. He obtained Ph.D. in Soil-Structure Interaction and Marine Geotechnical Engineering from Indian Institute Technology Madras. He has published more than 150 papers in international and national journals and conferences. He has completed 5 R&D (including ISRO—**Chandrayaan-2 Mission project**) and 70 major consultancy projects in Geotechnical Engineering and published two patent including "**Moon Soil**" (A Method for Manufacture of Highland Lunar Soil Simulant). He has guided 10 Ph.D. scholars and 6 more are in progress, 5 MS (by research) and more than 40 M.Tech. students in Geotechnical and allied research areas. He is the **Founder Chairman** of Indian Geotechnical Society (IGS-Trichy) Trichy Chapter. He is a member of Technical Committee (TC-301 on "**Preservation of Historic Sites**") of International Society for Soil Mechanics and Geotechnical Engineering. Prof. Muthukkumaran area of research is in geotechnical engineering, which includes pile foundation, soil-structure interaction, marine geotechnics and foundations, field instrumentation, geotechnical physical modeling, ground improvement and forensic geotechnical engineering. He has received DST Young Scientist Award, IGS-Smt. Indra Joshi Biennial Award and Keynote Paper Award—GEOMATE Conference 2015 at Osaka, Japan. He is an Associate Editor of *Australian Journal of Civil Engineering* and serving editorial board member of several journals. Prof. Muthukkumaran has significant administrative contribution as Estate Officer, Associate Dean (Planning and Development), Member of Buildings and Works Committee and Member of **Board of Governors (BoG)** of National Institute of Technology, Tiruchirappalli and Member of Buildings and Works Committee, IIM Trichy. He has received **NIT Trichy Achiever Awards** for research publications, research projects, maximum citation and consultancy projects.

Dr. Ravi Sankar Jakka is working as Associate Professor in the Department of Earthquake Engineering, Indian Institute of Technology (IIT) Roorkee. He is also currently serving as Secretary, Soil Dynamics Forum, Indian Society of Earthquake Technology (ISET). He graduated in Civil Engineering from Andhra University Engineering College in the year 2001. He has obtained Master's and Doctorate degrees

from IIT Delhi in the years 2003 and 2007, respectively. His areas of interest are dynamic site characterization, soil liquefaction, seismic slope stability of dams, landslides, and foundations and seismic hazard assessment. He has published over 100 articles in reputed international journals and conferences. He has supervised over 35 Master's Dissertations and 6 Ph.D. theses, while he is currently guiding 10 Ph.D. theses. He has received prestigious DAAD and National Doctoral fellowships. He has obtained University Gold Medal from Andhra University. He also received 'Young Geotechnical Engineer Best Paper Award' from Indian Geotechnical Society. He was instrumental in the development of Earthquake Early Warning System for Northern India, a prestigious national project.

Dr. C. R. Parthasarathy holds B.E. and M.E. degrees in Civil/Geotechnical Engineering from Bangalore University and Ph.D. (Geotechnical) from Indian Institute of Science, (IISc) Bangalore, India, in 2002. He started his career as geotechnical engineer in 1993. He was involved in numerous large-scale site investigation/engineering studies at various levels for multi-storied complexes, industrial buildings, embankments, bridges, water-retaining structures, subways, pavements, offshore platforms, pipelines, mobile drilling units, etc. Dr. Parthasarathy has undertaken pile drivability studies, jack-up rig foundation investigations, and design including jack-up rig moves. He was involved in the pile installation, monitoring of several offshore platforms, and has served QA/QC Engineer for several Geotechnical Investigations on dedicated survey vessels. His sphere of activities has extended beyond from India to South East Asia and Middle East, Africa, and USA. Dr. Parthasarathy is Founder Director of Sarathy Geotech and Engineering Services Pvt. Ltd. The company with its registered office at Bangalore, India, was established in 2008 to provide both offshore and on land integrated geotechnical engineering services in India and abroad. As Technical Partner of Pile Dynamics, USA, he is instrumental in promoting quality testing of deep foundations in India and Authorized Trainer for high strain dynamic pile testing. He is Life Fellow of Indian Geotechnical Society and Member of several other professional bodies like DFI, ISRM, Indian concrete Institute, Institution of Engineers, etc. He is currently Elected National Executive Member of Indian Geotechnical Society (IGS) for 3 consecutive terms and Chairman, Indian Geotechnical Society-Bengaluru Chapter.

Dr. B. Soundara is Professor in the Department of Civil Engineering at Saveetha University Chennai, and has a Ph.D. in Geotechnical Engineering from Indian Institute of Technology (IIT) Madras. Her research interest includes study on the behavior of problematic soils, various ground improvement methods, and physical modeling of geostructures. She has received grants from various government funding agencies like AICTE, DST NIMAT, SERB, and TNSCST and Recipient of the Early Career Research Award from Science and Engineering Research Board (DST) in 2016. She has published around 25 peer-reviewed journal papers, 40 conference papers, 3 chapters, and published 2 patents. She is an active reviewer in six leading journals, organized and attended more than 25 skill development programs, and also delivered about 30 guest lectures. She has guided 3 Ph.D. scholars and currently

guiding 6 members. She is a professional member of American Society of Civil Engineers, International Society for Soil Mechanics and Geotechnical Engineering, Indian Geotechnical Society, and Indian Society for Technical Education.

Chapter 1
Characteristic Properties of Natural Aggregate Incorporated Fibre Reinforced Compressed Earth Blocks

Deb Dulal Tripura, Jagadish Lohar, and Kasinikota Pardhasaradhi

Introduction

Earth construction is renewing interest by virtue of eco-friendliness and sustainable development as an integral part of green thinking [1]; however, the variability of soil, lack of consensus among nationalized standards, and people negative perception towards earth hinders its dissemination. Furthermore, in developed countries, the cost of earth construction is reported higher compared to conventional techniques. Compressed earth block (CEB) technology is evolved from adobe block to improve the mechanical strength and durability of earth block in order to compete with conventional building materials such as fired brick and concrete for modern construction [2]. Stabilization using binders such as cement, lime, bitumen further enhanced the block strength and insensivity to water to a greater extent [3, 4]. Generally, the stabilizer dosages vary from 4 to 12% by weight. Soil is the most influential factor governing the block characteristics. Various international standards stated the different soil fractions best suited for compressed earth block (CEB)/compressed stabilized earth block (CSEB) construction [5, 6]. Soils lacking these desired fractions are suggested to dilute with natural sand/gravel/clay for production of CSEBs. Reinforcing the soil with natural and synthetic fibres was started in ancient times to reduce the drying shrinkage and improve the mechanical resistance and durability of earth blocks [7]. The use of natural fibres over synthetic fibres is more beneficial as they are locally available. Fibres have greater tensile strength compared to surrounding soil/soil–cement matrix leading to greater cohesion and strength [8]. Straw is the most explored natural fibre to reinforce earth blocks [9]. Other natural fibres such as jute, coir, date palm and sisal; synthetic fibres such as polypropylene, wool are mostly investigated in CSEBs [8, 10–13]. However, not all fibres are advantageous, previous studies reported different strength behaviour depending

D. D. Tripura · J. Lohar · K. Pardhasaradhi (✉)
Department of Civil Engineering, National Institute of Technology, Agartala 799046, India
e-mail: pardhu.saradhi87@gmail.com

K. Muthukkumaran (eds.), *Soil Behavior and Characterization of Geomaterials*,
Lecture Notes in Civil Engineering 296, https://doi.org/10.1007/978-981-19-6513-5_1

on fibre type such as positive, negative, and positively up to a maximum dosage and then negative [11, 13]. Furthermore, the natural fibres degrade quickly, and the dimensional changes happen due to moisture and temperature variation influences the matrix–fibre interface characteristics [10]. Treating fibres is also encouraged to improve its durability as well as to improve the adhesion between matrix–fibre [10, 13]. Nevertheless, the common feature of fibres under loading is the failure more gradual resembles ductile rather than brittle. Combination of binder and fibre maximizes the benefits.

Coconut trees are widely cultivated in tropical and subtropical regions with warm climate. Coir or coconut fibre is obtained from coconut husk. India is one of the largest producers of coir fibre in the world besides Philippines and Indonesia. While processing, coir fibre generates huge amount of waste as agricultural by-product which could be used for reinforcing the soil. Further, coir fibre degrades slowly compared to other fibres, hence long lasting life, allowing researchers to integrate in construction field [14]. Ghavami [10] studied the feasibility of using sisal and coconut fibres as additive to soil matrix for production of adobe blocks. The percentage and length of fibres were maintained as 4% by weight and 50 mm. Results revealed that inclusion of 4% sisal/coconut fibres considerably improved the ductility but partly strength. Emulsified bitumen treatment improved the durability of fibre however did not enhanced the adhesion between soil matrix and fibre. Later in 2005, Khedari et al. [12] developed a novel soil–cement block with low thermal conductivity using coir fibre. Blocks were prepared by blending soil, cement, and sand in different proportions by volume ratio and with varying coir contents. Compressive strength, bulk density, and thermal conductivity decreased consistently with increase in coir fibre content. Danso et al. [15] investigated the effect of influence of fibre aspect ratio on mechanical properties of unstabilized compressed earth blocks. Three agricultural waste fibres, namely coconut, bagasse, and oil palm were used to produce blocks with aspect ratio varying from 25–125 and tested for compression and tensile strength. Test results concluded that the aspect ratio is a significant parameter which needs to be specified. The optimum aspect ratio implying maximum strength varies depending on fibre type. For coconut fibre, the strength steadily improved as the aspect ratio reaches to 125 corresponding to a length of 50 mm, while for bagasse fibre and oil palm fibre, the strength improved up to ratio of 100 corresponding to a length of 80 mm and 38 mm followed by reduction was noticed. Danso et al. [7] presented the physical, mechanical, and durability properties of unstabilized compressed earth blocks prepared using two different soils and reinforced with coconut, bagasse, and oil palm fibres. The dosages of fibres chosen are 0, 0.25, 0.5, 0.75, and 1% with cutting length of 50 mm. Results indicated the soil type was most influential parameter in compressive strength with high clay content soil outperformed, while fibre type played key role in tensile strength. Although the optimum content of fibre varies between 0.25–0.5% by weight, 0.5% is recommended in common for practical applications to improve the strength and durability of CEBs. Inclusion of fibres reduced the density; linear shrinkage and increased the water absorption, while the wearing and erosion tests suggested that the fibre addition considerably improved the durability of CEBs. Thanushan et al. [16] investigated the strength and durability properties of coconut fibre reinforced soil–cement blocks and concluded that

the ductility, residual strength, energy absorption, and durability of blocks against water and chemical attacks improved by fibre reinforcement. Recently, Sai et al. [17] investigated the engineering properties of coir fibre reinforced rammed earth blocks. They concluded that 1 and 3% coir satisfied the strength and durability criteria specified by standards. The optimum percentage and length of coir are reported as 1% and 25 mm. From the literature, it was evident that previous studies concentrated on determining the optimum content and length of coir fibre in natural state of soil; however, various national and international codes allowed to modify the soil texture, if it lacks the particular fraction in desired amount. Moreover, change in soil texture modifies the characteristics from original state which implies the engineering properties of CSEBs/CEBs. Consequently, the author identified that a detailed study is needed to understand the properties of CSEBs.

This research study aims to improve the strength and durability of unstabilized and stabilized compressed earth blocks (CSEBs) using natural aggregates (NA), cement, and coir fibre. Mechanical properties such as dry–wet compressive strength, flexural strength, and physical properties as dry density, water absorption were determined, and the optimum mix combination is proposed for production of CSEBs.

Materials and Methods

Soil used in this study was collected from NIT Agartala campus at a depth of 0.5–1.5 m below the ground surface which was sieved through 4.75 mm sieve before characterization. The index properties of soil such as granulometry, liquid and plastic limits, specific gravity, optimum moisture content (OMC), and maximum dry density (MDD) were determined according to Indian standard procedures [18–20]. The particle size distribution curve of soil shown in Fig. 1.1 is well within the limits recommended by IS 1725 [5]. The natural aggregate (NA) used was stone chips of size between 2–8 mm for better control of overall granulometry. Ordinary Portland cement 43 grade was used as a binder for manufacturing stabilized blocks, due to its abundance availability and superior properties over other binders. Coir fibre used was collected from local suppliers. The fibres obtained are 100–300 mm long which then cut into lengths between 40–50 mm. Fibre dosages were selected as 0.25, 0.5, and 0.75% by weight proportions. Summary of material properties is listed in Table 1.1.

Mix Design and Sample Preparation

The experimental study was carried out in two stages. Firstly, the effect of percentage of natural aggregate 0, 10, 20, 30, and 40% as partial replacement to soil by weight on physical and mechanical properties of unstabilized and stabilized earth blocks with cement contents 0, 4, 7, and 10% was investigated. Total 20 mixtures were prepared

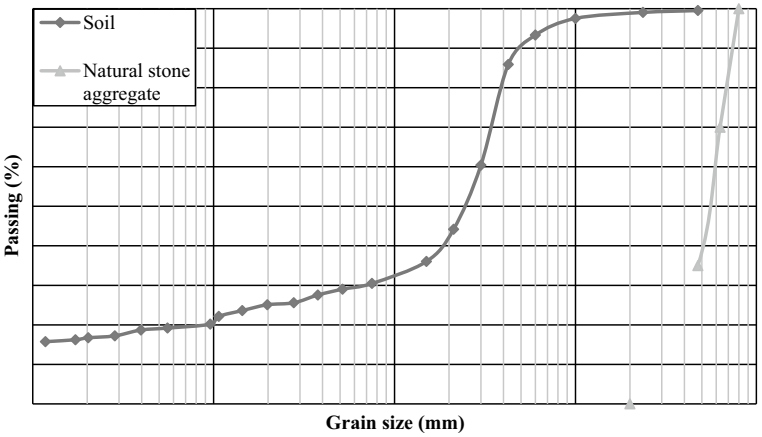

Fig. 1.1 Grain size distribution curve of soil and natural stone aggregate

Table 1.1 Physical properties of raw materials used

Property	Parameter	Details
Grain size distribution	Sand	63.97%
	Silt	19.31%
	Clay	16.72%
Atterberg limits	Liquid limit (LL)	34.10%
	Plastic limit (PL)	23.80%
	Plasticity index (PI)	10.30%
Optimum moisture content (OMC)		17.27%
Maximum dry density (MDD)		1803 kg/m^3
Cement	Initial setting time	80 min
	Final setting time	190 min
Coir fibre		
	Mean diameter (mm)	0.45
	Density (kg/m^3)	1285
	Tensile strength (MPa)	94.02

without any fibre reinforcement. After determining the optimum NA content, the effect of coir fibre reinforcement 0.25, 0.5, and 0.75% by weight of soil as well the effect of cement content 0, 4, 7, and 10% by weight of soil on dry compressive strength, flexural strength, and dry density of blocks with/without NA was evaluated in second stage using 24 mixtures. Overall, 44 mixtures were prepared. Prior to preparation of samples, the water content required for each mix variation is determined through Standard Proctor test. Blocks were manufactured by static compaction using manual press, which can operate with compaction ratio vary from 1.65–1.85.

In current study, the compaction ratio is fixed at 1.65. The size of CSEBs was 290 × 140 × 100 mm. Unstabilized blocks without any additive (C0) were produced by statically compressing the raw wet soil mixture. While the cement stabilized blocks without aggregate and fibre (Cx) were produced by uniform mixing of soil and cement before adding water and then compaction. For natural aggregate incorporated unstabilized (C0Sy) and stabilized earth blocks (CxSy), where required quantities of raw materials such as soil, NA and cement were mixed thoroughly prior to addition of water followed by compaction. Similar mixing procedure was followed for fibre reinforced unstabilized (C0Fz) and stabilized without NA (CxFz) and NA incorporated unstabilized (C0SyFz) and stabilized (CxSyFz) earth blocks where the raw materials soil, NA, cement, and fibre were initially mixed to attain a homogeneous mixture then water was added followed by compaction. Hereafter, the designations given are used for specifying mix where C indicates cement, S indicates natural aggregate, and F indicates coir fibre while x, y, and z refer to corresponding contents/percentages. Blocks compressed in press were immediately ejected and covered with a polyethene cover for 24 h and then cured for 28 days in laboratory under wet gunny bags. After successful completion of curing period, the blocks were dried for seven days before testing.

Test Methods

The dry–wet compressive (Fig. 1.2a) was determined in accordance with IS 4332 part V [21] and flexural strength (Fig. 1.3b) according to SA 195 [6]. The tests were conducted using a universal testing machine (UTM) with peak load capacity of 400 kN at the loading rate of 2.5 kN/min. The water absorption and dry density were determined according to SA 195 [6] and IS 4332 part V [21].

(a) (b)

Fig. 1.2 Blocks after compression test: **a** unreinforced and **b** reinforced

Fig. 1.3 Blocks under flexure loading: **a** before test and **b** after test

Results and Discussion

Unreinforced Blocks

Dry Density

The dry density of compressed earth blocks (CEBs) largely depends on the weighted density of its constituents. Figure 1.4 shows the effect of natural aggregate (NA) and cement content on oven dry densities of unstabilized and cement stabilized compressed earth blocks (CSEBs). All values reported are average of minimum five samples. It can be seen that the dry density of CEBs is directly proportional to the NA and cement contents, which is due to higher density of NA compared to soil particles. The dry densities of unstabilized blocks were within 1545–1764 kg/m^{3}and CSEBs were between 1668–2018 kg/m^3 as the NA content varies from 0–40%, respectively. The dry density of CSEBs without NA increases by almost 15.97% as the cement content reaches to 10%. This was explained by filling effect of cement particles in soil matrix as well as formation of hydrated products. In addition, the increase in block density was accelerated by inclusion of NA. The maximum increase in dry density was obtained for C10S40 as 30.58% compared to C0 and 14.37% as compared to C0S40, respectively. The former increment is attributed to combined effect of higher density of NA compared to soil particles and cement hydration while the later could be attributed to cement hydrated products alone. Overall, the dry densities obtained are in consistence with earlier studies [3, 4, 22].

Water Absorption

Water absorption is a key parameter to evaluate the quality of CSEB where durability is of major concern. The water absorption is measured only for CSEBs because

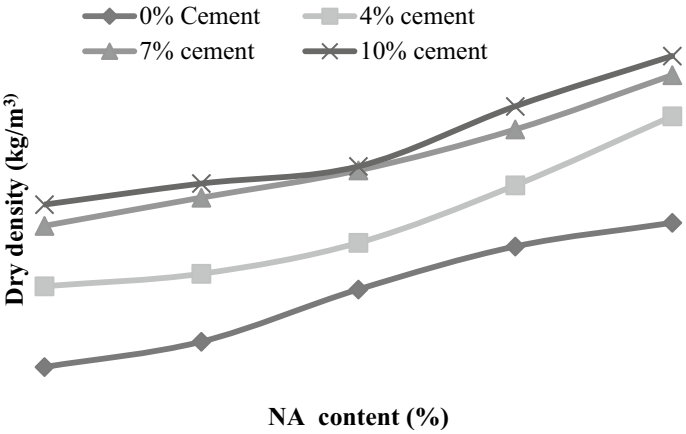

Fig. 1.4 Variation of block dry density with NA content for different cement contents

unstabilized blocks disintegrate immediately after immersion due to loss of cohesion [23]. The effect of natural aggregate content on water absorption of CSEBs is shown in Fig. 1.5. As shown, for particular cement content the addition of NA reduces the water absorption of CSEBs and with increasing cement content this value is further reduced. For instance, the water absorption of CSEBs made with 4% cement decreases from 20.45 to 14.71% as the NA content varies from 0 to 40%. As expected, decrease in clay content with replacement of NA could be the reason for reduction in water absorption of NA incorporated blocks. According to Riza et al. [24], water absorption is a function of clay and cement content. As the cement content rises from 4 to 10%, the water absorption of blocks without NA reduces by almost 36%, while for blocks with 10–40% NA reduces by approximately ±29%. This could be attributed to change in the microstructure of CSEB due to interaction of cement with alumina-silicates in soil leads to formation of hydrated products which fill the voids and thereby reduction in water absorption [25]. The water absorption values lies in range of 10.41%–20.45%. Except C4S0, the water absorption of all blocks is lesser than the maximum of 18% recommended by IS 1725-2013[5].

Compressive Strength

For all blocks produced, the dry and wet compressive strength results were analysed at 28 days of curing. Figure 1.6 shows the effect of NA and cement content on compressive strength of blocks and each value represent the mean of five samples. From Fig. 1.6, it is clear that the strength increases with addition of NA until an optimum value is reached, then slightly declines with further replacement levels. The same trend is noticed in both dry and wet conditions regardless of cement content. The reason for initial increase is due to better particle size distribution and good grading at low replacement levels, while reduction in strength beyond 30% is because of

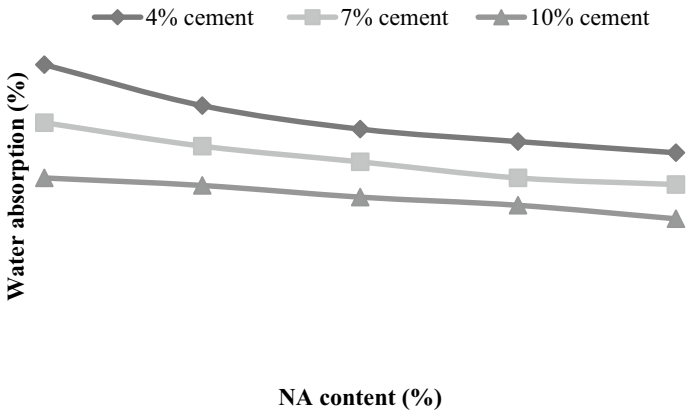

Fig. 1.5 Variation of water absorption of CSEBs with NA content

increase in gravel proportion. Thus, the optimum NA content is determined as 30% by weight of dry soil. The dry strengths of C0S10, C0S20, C0S30, and C0S40 were improved by 9.77, 19.55, 29.32, and 26.31% compared to C0. While in wet state, the blocks disintegrate immediately after immersion due to lack of cohesion. Inclusion of cement content further improves the strength of blocks with/without aggregates in both dry and wet states. For instance, at 4% cement content, the increase in dry compressive strength lies in range of 76.69–125.59% as compared to unstabilized blocks for NA content ranges from 0–40%. Similarly, as the cement content reaches to 10%, the dry compressive strength increases by about 361.65–454.07% for NA content ranges from 0–40%. Islam et al. [26] observed an increase of 37–310% for CSEBs with 0–9% cement. In addition, when compared to blocks with 4% cement, the increase in compressive strength of 7 and 10% cement stabilized blocks varies in range of 81.70–181.51% for dry state and 71.56–338.46% for wet state with NA content varied from 0–40%, respectively. This increase is attributed to filling up the voids in the matrix with cement hydrated products, which leads to enhancement of rigidity of its structure by forming a large number of rigid bonds connecting sand particles [22, 27]. The maximum dry compressive strength at optimum (30%) NA content ranges between 1.66 and 9.53 MPa as cement content varies from 0–10%. The corresponding wet strength values are in range of 1.47–3.86 MPa. Overall, the mix with 30% NA and stabilized with 10% cement (C10S30) exhibited the maximum strength, and wet to dry strength ratio of all blocks was found as 0.22–0.41. This was in consistent with findings of previous studies, where the ratio was varied in between 0.21–0.60 [22, 26, 28].

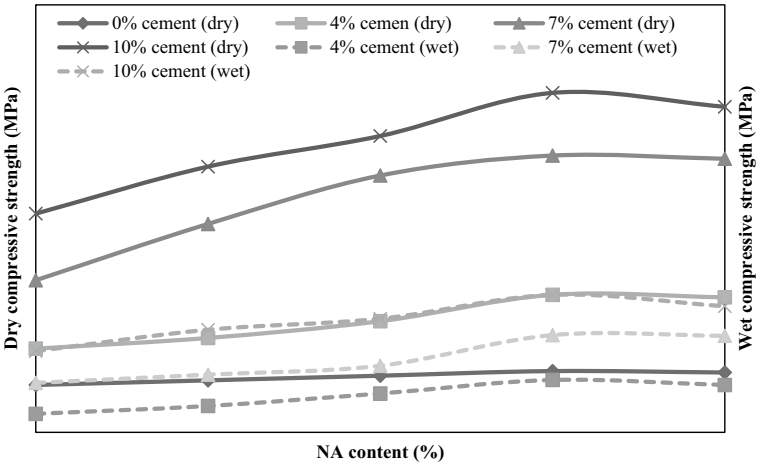

Fig. 1.6 Variation of dry and wet compressive strength of blocks with NA content for different cement contents

Flexural Strength

The effect of NA and cement content on wet flexural strength of blocks is shown in Fig. 1.7. Each reading represents the mean of five samples. Flexural strength of cement stabilized blocks increases with increase in NA content and reaches a peak at 30% NA content. Thereafter, the strength reduces slightly at 40% NA content. It is evident that flexural strength results exhibited similar patterns to compressive strength response. According to results, the flexural strengths of C4S10, C4S20, C4S30, and C4S40 were improved by 91.67%, 133.33%, 258.33%, and 225% compared to C4, respectively. Similarly, for C7S10, C7S10, C7S20, C7S30, and C7S40 were improved by 45.95%, 75.68% 121.62% and 116.22% as compared to C7; for C10S10, C10S10, C10S20, C10S30, and C10S40 were improved by 16.18%, 39.70%, 64.71% and 60.29% as compared to C10, respectively. The reason explained for compressive strength applies here also. Besides, with increase in cement content, the flexural strength steadily increases for all NA contents. For example, as the cement content increased from 4 to 7%, the flexural strength increases by about 1.91–3.08 times; from 7 to 10% cement, the strength increases by about 1.36–1.84 times for the NA content 0–40%. The maximum wet flexural strength is found for a combination of 30% NA content and 10% cement content, 1.12 MPa. Overall, the flexural strength values lie in the range of 0.12–1.12 MPa. These results are in good agreement with other works [3, 4]. Walker [3] obtained the flexural strength ranges between 0.11 MPa and 0.81 MPa for 5–10% cement contents. Reddy and Gupta [4] reported flexural strengths in range of 0.48–1.22 MPa for 6–12% cement contents. Considering the test results, C10S30 is recommended for further study.

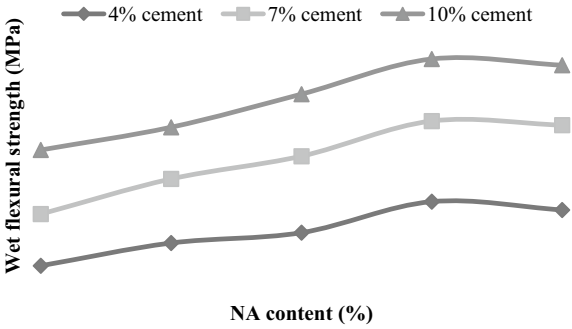

Fig. 1.7 Variation of wet flexural strength of CSEBs with NA content

Coir Fibre Reinforced Blocks

After identifying the optimum NA content in production of CEBs/CSEBs, the effect of coir fibre on mechanical properties of blocks with/without optimum NA is investigated further to specify the optimum mix combination.

Dry Density

Figures 1.8 and 1.9 illustrate the effect of coir fibre on dry density of unstabilized and stabilized earth blocks with/without NA. It can be observed from Fig. 1.8 that dry density of blocks without NA decreases with increase in fibres content. The replacement of dense material such as soil with coir fibre (light material) and development of air voids in matrix due to addition of fibre were the possible reasons for reduction in density [12]. These results are in consensus with previous studies [7, 12]. Besides, increase in cement content increases the dry density; however, the values decreased with increase in fibre content. The dry density of unstabilized blocks ranges from 1445–1545 kg/m^3 and CSEBs in the range of 1668–1792 kg/m^3. As the cement content increases from 0 to 10%, the percentage increase in density was approximately within ±17% as fibre content rises from 0 to 0.75%. The lowest density was recorded for blocks with 0.75% fibre content and 0% cement (C0F75) which is about 6.48% lower than C0, while the highest density corresponds to 0% fibre content and 10% cement content (C10F0), the value is 15.96% higher than C0. Similar to blocks without NA, the dry density of blocks with 30% NA is negatively influenced by fibre content as shown in Fig. 1.9. These values ranged between 1531 and 1941 kg/m^3. The highest decrease in density was reported for C0S30F75 as 11.44% compared to C0S30F0. This reduction in density is attributed to light coir fibres as compared to soil. Overall, the densities of most samples are within the typical range of 1500–2000 kg/m^3 as reported by Riza et al. [24].

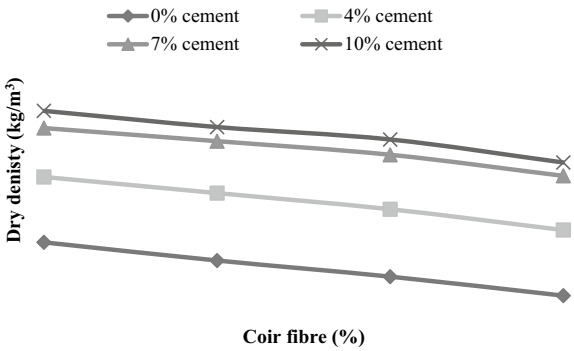

Fig. 1.8 Variation of dry density of blocks with coir fibre content for different cement contents

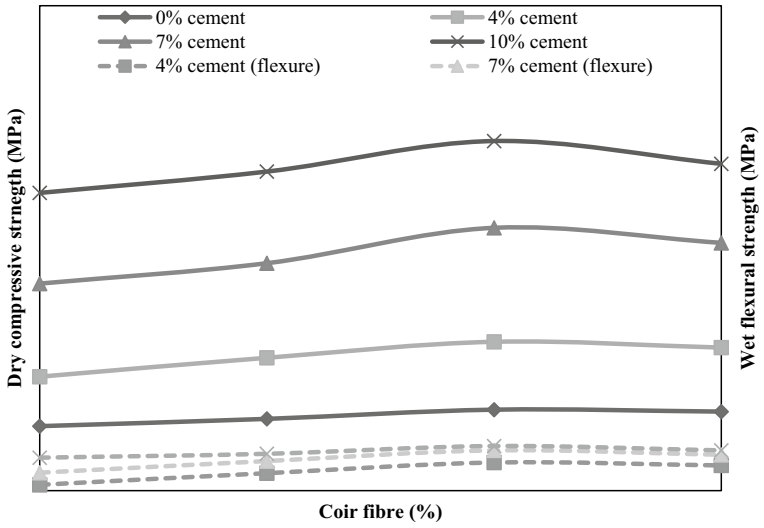

Fig. 1.9 Variation of dry compressive strength and wet flexural strength of blocks with coir fibre content for different cement contents

Compressive Strength

The effect of coir fibre content (0.25, 0.5, and 0.75%) on average dry compressive strength of unstabilized and cement stabilized (4, 7, and 10% cement) earth blocks is shown in Fig. 1.10. It can be seen from Fig. 1.10 that both coir fibre and cement improves the compressive strength of earth blocks. Irrespective of cement content, increase in coir content up to 0.5% increases the strength followed by a gradual decrease with further replacements. The reason for initial increase is because of friction between fibre and soil particles, which holds the matrix firmly against spreading of cracks by forming bridges across them; whereas reduction in adhesion

with soil due to increase fibre content is responsible for later decrease in strength [7]. Thus, the optimum content of coir fibre was found as 0.5%, which is in line with previous studies. Danso et al. [7] anticipated the optimum content of coir fibre may lie in between 0.25–0.5% and finally recommended 0.5% for practitioners. The compressive strength of C0, C0F25, C0F50, and C0F75 was 1.33 MPa, 1.48 MPa, 1.67 MPa, and 1.63 MPa, respectively. Inclusion of 0.5% fibre increases the compressive strength of C0F50 by almost 25.56% as compared to C0. Danso et al. [7] witnessed a 41 and 57% increase for two soils at 0.5% fibre content. Addition of 4–10% cement content improves the strength by about 76.69–361.65% compared to unstabilized blocks as the fibre contents vary from 0–0.75%. This increase could be attributed to increase in cement hydrated products with addition of cement content along with better adhesion of fibres with soil matrix. However, similar to unstabilized blocks, the compressive strength of stabilized blocks declines at fibre content greater than 0.5%, which can be explained by domination of fibres in soil–cement matrix over cement hydration. Moreover, as the cement content increases, the effect of coir fibre on increase in compressive strength decreases. For instance, when compared to strength of unreinforced blocks, the increase in compressive strength of blocks with 0.5% coir fibre was 30.64 for 4% cement; 27.53 for 7% cement; and 17.43 for 10% cement. The maximum dry compressive strength at optimum fibre content (0.5%) increases from 1.67–7.21 MPa for cement content in range of 0–10%. Overall, the strength values range between 1.33 and 7.21 MPa which is in accordance with [7, 12, 29].

Figure 1.11 shows the effect of fibre content (0.25, 0.5, and 0.75%) and cement (4, 7, and 10%) content on dry compressive strength of compressed earth blocks incorporated with 30% NA. It was evident that inclusion of 30% NA to soil–fibre–cement matrix further improves the compressive strength. However, similar to blocks without 30% NA, the strength of reinforced blocks with 30% NA start decreasing beyond 0.5% fibre content. The strength of C0S30F25, C0S30F50, and C0S30F75 was improved by 4.07, 12.79, and 11.05% compared to C0S30F0. Besides, when compared to blocks without 30% NA, the strength increases by 1.16–1.29 times,

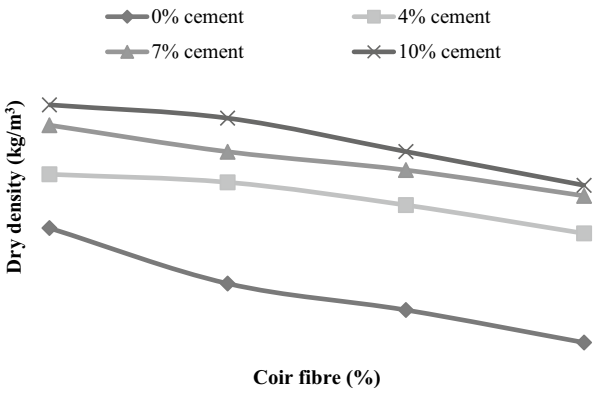

Fig. 1.10 Variation of dry density of 30% NA incorporated blocks with coir fibre content for different cement contents

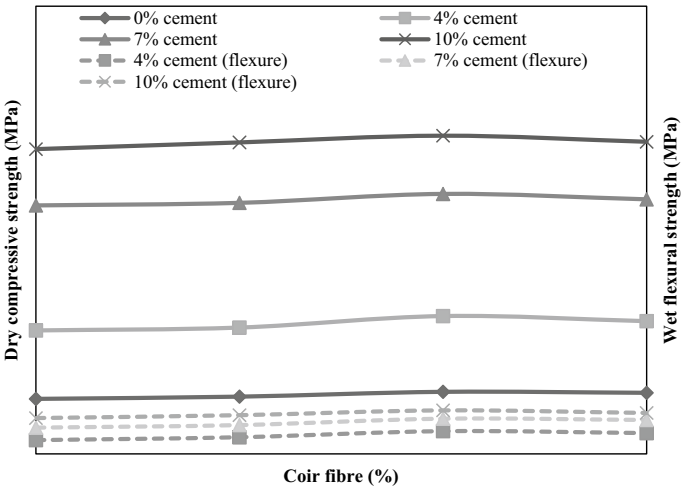

Fig. 1.11 Variation of dry compressive strength and wet flexural strength of 30% NA incorporated blocks with coir fibre content for different cement contents

respectively. This improvement is primarily due to better particle size distribution and good interlocking of NA incorporated blocks. With addition of 4–10% cement content, the strength of 30% incorporated reinforced blocks increased by about 117.28–454.07% compared to unstabilized blocks for fibre content varies from 0–0.75%, which could be attributed to filling effect of cement particle in pores as well as reaction between cement and alumina-silicates in soil, which further directly related to cement content. Moreover, as the cement content increases, the effect of coir fibre on increase in compressive strength of blocks with 30% NA decreases. For instance, when compared to strength of unreinforced blocks, the increase in compressive strength of blocks with 0.5% coir fibre was 11.66 for 4% cement; 4.63 for 7% cement; and 4.41 for 10% cement. On the other hand, when compared to stabilized blocks without 30% NA, the strength of 30% NA incorporated reinforced blocks increases by 1.40–1.64 times for 4% cement; 1.5–1.82 times for 7% cement, and 1.38–1.55 times for 10% cement. These findings clearly demonstrate that NA has major influence compared to fibre on compressive strength of stabilized blocks. Of all, the maximum strength was obtained as 9.95 MPa for a combination of 30% NA, 0.5% fibre with 10% cement.

Flexural Strength

The effect of coir fibre content (0.25, 0.5, and 0.75%) on average wet flexural strength of CSEBs with 4, 7 and 10% cement content is shown in Fig. 1.10. As can be seen from Fig. 1.10, both coir fibre and cement improves the compressive strength of earth blocks. For all cement contents, the wet flexural strength increases with increase of

fibre content from 0 to 0.5%, subsequently increase in fibre content beyond 0.5% there is reduction in strength. This is similar to compressive strength. Thus, the optimum content of coir fibre was found as 0.5%, which agrees with Danso et al. [7]. Unreinforced blocks failed suddenly by split into two parts, showing brittle nature, whereas reinforced blocks failed in gradual manner with formation of multiples cracks and considerable deformation, like a ductile material. Although the reinforced blocks split into two parts, they were held together by the fibres which demonstrate the bridging effect of fibres under flexure [7]. For 4% cement content, the flexural strength of C4F25, C4F50, and C4F75 was improved by 3–4.8 times compared to C4F0. With further increase in cement content, the effect of coir fibre on increase in flexural strength decreases. When compared to unreinforced samples, the strength of reinforced samples improved by 1.65–2.24 times for 7% cement and 1.12–1.35 times for 10% cement, as the fibre content varies from 0.25%–0.75%, respectively. The maximum wet flexural strength at optimum fibre content (0.5%) increases from 0.58 to 0.92 MPa for cement content in range of 4–10%. Overall, the strength values range between 0.12 and 0.92 MPa which are in accordance with [3, 4].

Figure 1.11 shows the effect of fibre content (0.25, 0.5, and 0.75%) and cement (4, 7 and 10%) content on wet flexural strength of CSEBs incorporated with 30% NA. The results indicate that inclusion of 30% NA contributes to further improvement in wet flexural strength of soil–fibre–cement matrix. However, similar to blocks without 30% NA, the strength of reinforced blocks start decreasing beyond 0.5% fibre content. The strength of C4S30F0, C4S30F25, C4S30F50, and C4S30F75 was improved by 0.43, 0.52, 0.71, and 0.68 MPa. With further increase in cement content, the flexural strength of 30% NA incorporated reinforced blocks increases consistently for the fibre content vary from 0.25–0.75%. This could be attributed to filling effect of cement particle in pores as well as reaction between cement and alumina-silicates in soil, which further directly related to cement content. However, as the cement content increases, the effect of coir fibre on increase in flexural strength of blocks with 30% NA decreases. For instance, when compared to strength of unreinforced blocks, the increase in compressive strength of blocks with 0.5% coir fibre were 65.16 for 4% cement; 34.16 for 7% cement; and 21.43 for 10% cement. On the other hand, when compared to stabilized blocks without 30% NA, the strength of 30% NA incorporated reinforced blocks increases by 1.33–3.58 times for 4% cement, 1.33–2.22 times for 7% cement and 1.48–1.65 times for 10% cement, which is undoubtedly due to better particle size distribution and good interlocking of NA incorporated blocks. Overall, the maximum strength was obtained as 1.36 MPa for a combination of 30% NA, 0.5% fibre with 10% cement.

Conclusions

The present study aimed at evaluating the influence of cement content, natural aggregate (NA) content, and coir fibre on properties of compressed earth blocks. The investigation was performed in two stages. The effect of NA and cement content on dry

density, water absorption, dry–wet compressive strength, and wet flexural strength was discussed in first stage. After specifying the optimum NA content to replace soil, the effect of coir fibre on dry density, dry compressive strength, and wet flexural strength of compressed earth blocks with/without optimum NA was analysed with varying cement contents. Based on test results obtained in this study, the following conclusions were drawn:

1. The inclusion of NA as a partial replacement of soil induced an increase in dry density of unstabilized and stabilized earth blocks due to higher density of NA compared to soil particles. For 40% NA replacement, the dry density of unstabilized blocks increases by 14.18 and 30.58% for CSEBs.
2. The water absorption values of CSEBs decrease with increase in amount of NA content. The lowest value was measured in CSEB with 40% aggregate for 10% cement.
3. The compressive strengths of unstabilized and stabilized blocks are improved with addition of NA due to better particle size distribution. The optimum NA content was found as 30%, at which the increase in dry compressive strength lies in the range of 124.42–454.1% compared to C0S30 for 4–10% cement content. The dry–wet compressive strength ranges between 0.22–0.41.
4. The maximum wet flexural strength of CSEBs was obtained at 30% NA content, similar to compressive strength, which increases from 0.43–1.12 MPa as the cement content increases from 4 to 10%. The optimum mix proportion is obtained for 30% NA with 10% cement.
5. The inclusion of coir fibre alone as a partial replacement of soil caused a decrease in dry density of unstabilized and stabilized earth blocks due to lower density of fibre compared to soil particles. For 0.75% fibre replacement, the dry density reduced by 6.48% for unstabilized blocks and 5.97% for CSEBs. Moreover, addition of fibre to 30% NA blocks reduces the dry density of unstabilized blocks by 11.44% and 7.16% for CSEBs.
6. The compressive strengths of unstabilized and stabilized blocks are improved with addition of coir fibre. The optimum fibre content was found as 0.5%, at which the increase in dry compressive strength lies in the range of 76.69–331.74% compared to C0F50 for 4–10% cement content. Moreover, addition of 30% NA to reinforced mixtures further improved the strength. The optimum mix proportion is found for a combination of 30% NA and 0.5% fibre, regardless of cement content. The strength of 30% NA reinforced CSEBs increases by 1.16–1.5 times compared to corresponding blocks without NA, for cement content 0–10%.
7. Similar to compressive strength, the maximum wet flexural strength of CSEBs was obtained at 0.5% fibre, increases from 0.58 MPa to 0.92 MPa as the cement content increases from 4 to 10%. Addition of 30% NA to reinforced mixtures further improved the wet flexural strength. Irrespective of cement content, the optimum mix proportion is obtained for a combination of 30% NA and 0.5% fibre. When compared to reinforced blocks without 30% NA, the strength of similar blocks with 30% NA increases by 1.22–1.48 times as the cement content vary form 4–10%. Overall, the mix consisted of 30% NA, 0.5% fibre and 10% cement achieved the maximum strength.

References

1. Jannat N, Hussien A, Abdullah B, Cotgrave A (2020) Application of agro and non-agro waste materials for unfired earth blocks construction: a review. Constr Build Mater 254:119346. https://doi.org/10.1016/j.conbuildmat.2020.119346
2. Heathcote K, Jankulovski E (1993) Relationship between moisture content and strength of soil-crete blocks: results of experimental investigation into relationship between moisture content and compressive strength of cement-stabilized soilcrete blocks. Build Res Inf 21:103–108. https://doi.org/10.1080/09613219308727269
3. Walker PJ (1995) Strength, durability and shrinkage characteristics of cement stabilised soil blocks. Cem Concr Compos 17:301–310. https://doi.org/10.1016/0958-9465(95)00019-9
4. Reddy BVV, Gupta A (2005) Characteristics of soil-cement blocks using highly sandy soils. Mater Constr 38:651. https://doi.org/10.1617/14265
5. Indian Standard (2013) Stabilized soil blocks used in general building construction-Specification, IS 1725, New Delhi, India
6. Standard Australia (2002) The Australian earth building handbook
7. Danso H, Martinson DB, Ali M, Williams JB (2015) Physical, mechanical and durability properties of soil building blocks reinforced with natural fibres. Constr Build Mater. https://doi.org/10.1016/j.conbuildmat.2015.10.069
8. Millogo Y, Morel JC, Aubert JE, Ghavami K (2014) Experimental analysis of pressed adobe blocks reinforced with *Hibiscus cannabinus* fibers. Constr Build Mater. https://doi.org/10.1016/j.conbuildmat.2013.10.094
9. Quagliarini E, Lenci S (2010) The influence of natural stabilizers and natural fibres on the mechanical properties of ancient Roman adobe bricks. J Cult Herit 11:309–314. https://doi.org/10.1016/j.culher.2009.11.012
10. Ghavami K (2005) Bamboo as reinforcement in structural concrete elements. Cem Concr Compos 27:637–649. https://doi.org/10.1016/j.cemconcomp.2004.06.002
11. Bouhicha M, Aouissi F, Kenai S (2005) Performance of composite soil reinforced with barley straw. Cem Concr Compos. https://doi.org/10.1016/j.cemconcomp.2004.09.013
12. Khedari J, Watsanasathaporn P, Hirunlabh J (2005) Development of fibre-based soil-cement block with low thermal conductivity. Cem Concr Compos. https://doi.org/10.1016/j.cemconcomp.2004.02.042
13. Taallah B, Guettala A, Guettala S, Kriker A (2014) Mechanical properties and hygroscopicity behavior of compressed earth block filled by date palm fibers. Constr Build Mater. https://doi.org/10.1016/j.conbuildmat.2014.02.058
14. Hejazi SM, Sheikhzadeh M, Abtahi SM, Zadhoush A (2012) A simple review of soil reinforcement by using natural and synthetic fibers. Constr Build Mater 30:100–116. https://doi.org/10.1016/j.conbuildmat.2011.11.045
15. Danso H, Martinson DB, Ali M, Williams J (2015) Effect of fibre aspect ratio on mechanical properties of soil building blocks. Constr Build Mater 83:314–319. https://doi.org/10.1016/j.conbuildmat.2015.03.039
16. Thanushan K, Yogananth Y, Sangeeth P (2019) Strength and durability characteristics of coconut fibre reinforced earth cement blocks. J Nat Fibers 1–16. https://doi.org/10.1080/15440478.2019.1652220
17. Sai S, Raavi D, Tripura DD (2020) Predicting and evaluating the engineering properties of unstabilized and cement stabilized fibre reinforced rammed earth blocks. Constr Build Mater 262:120845. https://doi.org/10.1016/j.conbuildmat.2020.120845
18. Indian Standard (1980) Methods of test for soils: determination of water content-dry density relation using light compaction, IS 2720 (Part 7), New Delhi, India
19. Indian Standard (1985) Methods of test for soils: grain size analysis, IS 2720 (Part 4), New Delhi, India
20. Indian Standard (1985) Methods of test for soils: determination of liquid limit and plastic limit, IS 2720 (Part 5), New Delhi, India

21. Indian Standard (1974) Methods of test for stabilized soils. Determination of unconfined compressive strength of stabilized soils, IS 4332 (Part 5), New Delhi, India, 11:76. https://doi.org/10.1016/0148-9062(74)92925-8
22. Tripura DD, Singh KD (2014) Characteristic properties of cement-stabilized rammed earth blocks. J Mater Civ Eng 27:1–8. https://doi.org/10.1061/(ASCE)MT.1943-5533.0001170
23. Bogas JA, Silva M, Glória Gomes M (2019) Unstabilized and stabilized compressed earth blocks with partial incorporation of recycled aggregates. Int J Arch Herit 13:569–584. https://doi.org/10.1080/15583058.2018.1442891
24. Riza FV, Rahman IA, Mujahid A, Zaidi A (2010) A brief review of compressed stabilized earth brick (CSEB), CSSR 2010—2010 Int Conf Sci Soc Res 999–1004. https://doi.org/10.1109/CSSR.2010.5773936
25. Nagaraj HB, Rajesh A, Sravan MV (2016) Influence of soil gradation, proportion and combination of admixtures on the properties and durability of CSEBs. Constr Build Mater 110:135–144. https://doi.org/10.1016/j.conbuildmat.2016.02.023
26. Islam MS, Tausif-E-Elahi, Shahriar AR, Nahar K, Hossain TR (2020) Strength and durability characteristics of cement-sand stabilized earth blocks. J Mater Civ Eng 32:04020087. https://doi.org/10.1061/(asce)mt.1943-5533.0003176
27. Bahar R, Benazzoug M, Kenai S (2004) Performance of compacted cement-stabilised soil. Cem Concr Compos 26:811–820. https://doi.org/10.1016/j.cemconcomp.2004.01.003
28. Reddy BVV, Latha MS (2014) Influence of soil grading on the characteristics of cement stabilised soil compacts. Mater Constr 47:1633–1645. https://doi.org/10.1617/s11527-013-0142-1
29. Raj S, Mohammad S, Das R, Saha S (2017) Coconut fibre reinforced cement stabilized rammed earth blocks. World J Eng 14. https://doi.org/10.1108/WJE-10-2016-0101

Chapter 2
Soil Contamination Level in Cauvery Delta Region Through Machine Learning and GIS Techniques

A. Valarmathi, S. Nalini, and M. Kalidhas

Introduction

Agriculture is the backbone of the Indian economy. The water resources available are to provide the various kinds of agricultural activities in its delta region. The river Cauvery plays a major role in farming and provides major crop productivity within Tamil Nadu. The river water gets polluted by various means. The polluted water in turn affects the soil to get contaminated. The contamination may be in the form of soil nutrient deficiency or the deposition of unwanted chemicals in the soil. The district wastewater thrown into the river has the potential to contaminate the soil, and in addition to that, industrial wastes such as tanning waste discharge are being mixed with the river water. This could have an impact on the significant loss of water quality and aquatic biodiversity, in which the waste water discharge has deteriorated to the point where it is no longer drinkable for local people and cattle. Hence, there raise the water shortage problem in that area. Furthermore, it was also revealed that the quality and quality of crops in the Cauvery River had also declined significantly. The most concerning assertion is that heavy metals enter human bodies through the food chain, putting the health of the local population particularly children in jeopardy. In addition, harvests on the Cauvery River were found to be significantly worse in quantity and quality. Most seriously, heavy metals have been reported to invade the human body through the food chain, which seriously threatens the health of locals,

A. Valarmathi
Department of Computer Applications, University College of Engineering, BIT Campus, Anna University, Trichy 620024, India

S. Nalini (✉)
Department of Computer Science and Engineering, University College of Engineering, BIT Campus, Anna University, Trichy 620024, India
e-mail: nalinis@aubit.edu.in

M. Kalidhas
University College of Engineering, BIT Campus Anna University, Trichy 620024, India

K. Muthukkumaran (eds.), *Soil Behavior and Characterization of Geomaterials*,
Lecture Notes in Civil Engineering 296, https://doi.org/10.1007/978-981-19-6513-5_2

especially children in the community. The contaminated soils affect the productivity of the crop's growth in these regions. The Cauvery delta zone (CDZ) covers the eastern part of Tamil Nadu where the Bay of Bengal surrounds the eastern half of Tamil Nadu, with Trichy district on the west. In the southwest, Pudukkottai district is covered. Perambalur and Ariyalur districts on the northwest and Cuddalore district on the north, in which the Tiruchirappalli and Thanjavur regions are identified as experiment areas in the Cauvery delta region.

The physical and chemical properties of soil contamination were used to infer the pollution characteristics. Both manual interpolation and model generation are time-consuming and labour-intensive processes. In such cases, the GIS approach is effectively used. Due to its rapid growth and widespread application in various fields, it has been proposed to use GIS for soil contamination analysis [1]. The goal of this experiment is to create continuous surfaces using various spatial interpolation methods, by determining the optimal interpolation method, and to characterize the study area using a contamination map.

A geographical information system (GIS) captures, stores, manipulates, analyses, manages, and presents spatial or geographic data. The spatial data hold the location tag as the primary tuple in the database. A significant problem will arise while dealing with large databases over the long period of observation. During the last decade, the soil parameters have interpolated through the spatial variation map in GIS. The river Cauvery plays a major role in farming and provides major crop productivity within Tamil Nadu. The heavy metals, solid wastage, industrial waste, etc., pollute the environmental river water, which adversely affects the water sources. The polluted water in turn affects the soil to be contaminated. The contaminated soils pose a severe threat to crop health and affect the productivity of the crops grown in Cauvery delta regions. When the contamination levels of the particular region soil are determined, then as a precaution measure of rapid and comprehensive solutions are taken to improve the soil health such that it can be suitable for crop productivity. These predictions of the soil contamination levels are modelled and made readily available in the GIS datasets for the Cauvery delta region.

Literature Survey

Rapid industrialization in developing countries like India is producing large amount of waste and increasing the shortage of land for the safe disposal of hazardous waste. Waste is classified under the solid or liquid pattern. Waste liquid leachates produced by solid waste percolate into the soil, causing problems such as groundwater pollution, vegetation deterioration, and ‘ in the soil property. The source of soil is due to foundation failure, land subsidence, landslides, and groundwater pollution, among other things [2]. Many tannery industries operate near the Cauvery delta zone in Trichy. The liquid and solid wastes produced by these industries not only contaminate groundwater but also affect soil behaviour [3], resulting in decreased

crop productivity. To assess the overall level of contamination, it is necessary to understand the contamination characteristics of the soil in and around the area.

There is a cation exchange capacity in the soil that influences the absorption and retention of heavy metals including nickel, lead, cadmium, and others [4]. This suits the various classification techniques for real-world spatial datasets. Features such as the relationship of neighbourhood data input training data and the original map geometry affect the accuracy of the generated map.

As a result, the report states measurements that compare the accuracy of the investigated methods on various datasets. The spatial database system compared the region of the estimated map with the original map [5]. The spatial distribution for the agricultural fields is evaluated through the geographical information system (GIS) and nearly 106 samples are tested and results are determined. The Kriging mechanism was utilized to determine the spatial patterns of risk elements and the anticipated risk element concentrations exceeding their referenced index is calculated using disjunctive kriging [6].

The multicriteria technique is used in spatial modelling, to provide an integrated analysis, a universal scale of values for varied and dissimilar inputs is required. The most typical application of the weighted overlay function is site appropriateness analysis, which identifies the most suitable places for a given occurrence. The weighted function, on the other hand, may produce inconsistent results for very dissimilar input, and the most favourable criteria result in larger raster values when identifying the best places. The use of the fuzzy overlay function in multicriteria spatial modelling is discussed [1, 7]. It is based on the fuzzy logic theory notion of defining membership using a Gaussian function on each raster input value as an alternative to providing each rank in the overlay function [8]. A multiple linear regression modelling mechanisms combined with the spatial analysis were used to detect and to recognize the driving factors of soil Hg contamination in each subclass of agricultural land. As a result, the estimated spatial distribution maps of estimated soil Hg concentrations in the vegetable field and paddy field are plotted. The evaluation results show that the greater mean of soil Hg concentrations exists in the vegetable field and paddy field over the orchard field. The evaluation results state that the greater mean of soil Hg concentrations is higher in the vegetable fields and paddy fields over the orchard field. According to the Environmental Quality Standard of agricultural soils, both metrics are below the maximum permissible concentration. Soil Hg concentrations in vegetable fields are directly related to the chimneys with the shortest distances between the chimney and soil samples. Soil Hg concentration variance [9] was the driving element in agriculture fields that produce rice crops, where both soil sampling slopes and distances from soil samples to the nearest roads were measured. Several experimental analyses have been applied to determine the contamination level in soil and groundwater analysis through the machine learning models [10, 11]. The decision map is created using spatial multi criteria decision analysis (MCDA), and the layers are constructed using the overlay technique. Similar to overlay analysis, spatial MCDA techniques are well known. The author [9] focuses on the use of a

Table 2.1 Study area Tiruchirappalli and Thanjavur

State	Tamil Nadu (Tiruchirappalli and Thanjavur district)			
Geographical coordinates decimal degrees (WGS84)	Tiruchirappalli district		Thanjavur district	
	Latitude: 10.8155000° N Longitude: 78.6965100° E		Latitude: 10°47′06″ N Longitude: 79°08′20″ E	
Study area (8 taluks)	Thuraiyur, Lalgudi, Musri, Tiruchirappalli, Thottiyam, Manachanallur, Thiruverumpur, Srirangam, and Thiruvaiyaru			
Climate	Subtropical climate			
Soil type	Loamy, clayey and sandy alluvial			
Rain fall	Annual rain fall 850 mm			
Temp	Min	17 °C	Max	41 °C
Population	In accordance with 2011 census, Tiruchirappalli district had a population of 2,722,290. Thanjavur district had a population of 2,405,890			
Total area	2892 km^2			

GIS-based spatial MCDA to optimize site selection for the development of an agro-tourism infrastructure, using the fuzzy MCDA mechanism within a geographical information system structure.

Study Area

In the Cauvery delta region, Tiruchirappalli and Thanjavur districts were identified for the experimental analysis. The Cauvery river basins are highly polluted by the public, Tannery effluents, etc. The contamination affects the soil behaviour which reduces agriculture productivity. The selected region varied by patterns of cultivated lands, barrel land, and the existing land uses within the coverage of Tiruchirappalli and Thanjavur districts. The further details of the study area of the above two districts were represented in Table 2.1.

The digitizes map of the study area site illustrates the sampling points and 500 m buffer zone which are shown in Fig. 2.1.

Material and Methods—Data Capturing

The Palin test SKW 500 Complete Soil Kit is a water-resistant and durable kit that is used to test soil samples in the field. The SKW 500 soil kit quickly detects the most important soil health indices, such as macronutrients and micronutrient levels, for effective soil and agronomy management. The key techniques used are provided by the soil test10 Bluetooth photometer, multiparameter pocket sensor and the Palin

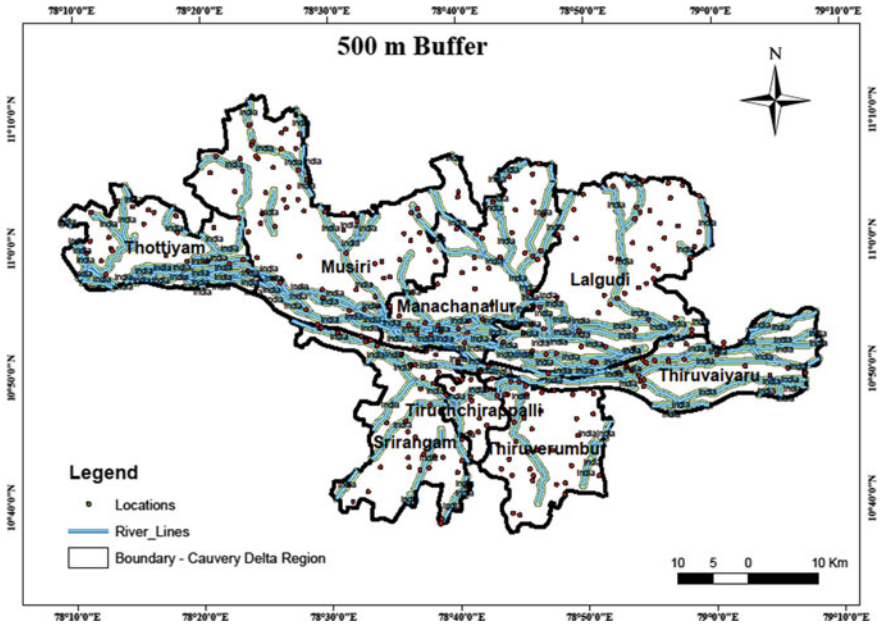

Fig. 2.1 500 m buffer zone of study area

test tablet count method. Multiparameter pocket sensor was used to determine the amount of hydrogen ion concentration and electrical conductivity in the samples. A photometer was used to determine the macronutrients of soil characteristics such as nitrogen and phosphorus. The presence of micronutrients such as Fe, Zn, Mn, and Cu in the samples was determined using an atomic absorption photometer. The soil samples were hand gathered from the required sites using polythene bags and labelled properly for top soil, deeper layers, and multiple layers sampling. The collected sand samples were taken at a depth of approximately topsoil 6–12 in. (0.15–0.3 m). The multilayer's depth ranges from 0 to 6, 6 to 12 in. Global positioning system (GPS) recorded the geographical location of sampling points. Nearly, 30 locations spatial data are framed. The soil samples were air-dried, crushed, and sieved using a 2 mm sieve size before being analysed.

Formation of Spatial Database

Table 2.2 depicts a spatial database with the presence of hydrogen ions, electrical conductivity, micro, and macronutrients in the Tiruchirappalli district. The location place along with their corresponding latitude and longitude is digitized. The quality of the digitizing procedure determines the accuracy of the GIS database. The digitization

errors such as dangles, consisting overshoot, undershoot and missing labels and polygons are rectified, and through data coding, the points are related.

Table 2.2 Soil sample collected locations

Location	Latitude	Longitude
Sriramasamudram	10.9663	78.2081
Thinnanur	11.0408	78.6072
Sirukalappur	11.0377	78.9057
Thuvakudi	10.7517	78.8208
Lalgudi	10.8657	78.8265
Kajamalai	10.7755	78.6926
Kamaraj Nagar	10.8049	78.7274
Sholanganallur	10.8135	78.6589
Ananjanur	10.8771	78.5517
Thottiyam	10.9806	78.3381
Kannakudi	10.9792	78.9709
Thiruvellarai	11.0372	78.6172
Vitalapuram	10.8799	78.9709
Avaravelli	10.9899	78.7758
Musiri	10.953	78.4349
Pettavaithalai	10.8985	78.4828
Amoor	10.9207	78.5623
Silayathi	10.8874	78.6439
Thiruvanaikoil	11.0372	78.6172
MelaChinthamani	10.8351	78.6947
Thandalaiputhur	10.9899	78.5217
Urakkarai	11.1301	78.3995
Surampatti	11.0421	78.4131
Bharathipuram	11.0448	78.2716
Chithanatham	10.6911	78.5218
Navarlukottapattu	10.7521	78.609
Maruthinagar	10.7097	78.7202
Elandapatti	10.6886	78.7918
Kulumani	10.8437	78.6037
Mandaiyur	10.6886	78.7918
Koodacheri	11.2458	78.0024
Nallapalayam	11.2217	79.205
Orathanadu	10.6139	79.2704
Manaparai	10.5264	78.1019

Mapping in GIS

The physical and chemical characteristics measured in Tiruchirappalli and Thanjavur districts are assessed using GIS. The physiochemical features of soil parameters can differ from one location to another. It is determined by both surface features. The presence of landfills, open dumps, fertilizer use, industrial waste disposal, and other factors alters the quality of the soil. The field parameters of physical and chemical properties were selected after digitizing the base map to develop the special mode. The spatial distribution maps of major soil parameters like NPK, pH, EC, Zn, Mn, Cu, and Fe are generated using spatial interpolation techniques in Arc GIS software. In the realm of soil research, the IDW is one of the most widely used and deterministic interpolation techniques. The spatial variation map for pH, electrical conductivity, macronutrient, and micronutrient is shown in Figs. 2.2, 2.3, 2.4, 2.5, 2.6, 2.7, 2.8, and 2.9. The nearby locations are estimated through the IDW technique. For the interpolating points, the weights are assigned by calculating the inverse of its distance. As a result, close points are given more weights (and so have more impact) than distant points and vice versa. The parameters employed in IDW interpolation methods for constructing soil prediction maps were established based on the idea that nearby locations have more correlations and similarities than distant data. Table 2.3 represents the parameter location with the region that coves with maximum and minimum range. The contamination level has been then assigned to a different category such as manual, defined interval, quantile, and standard deviation.

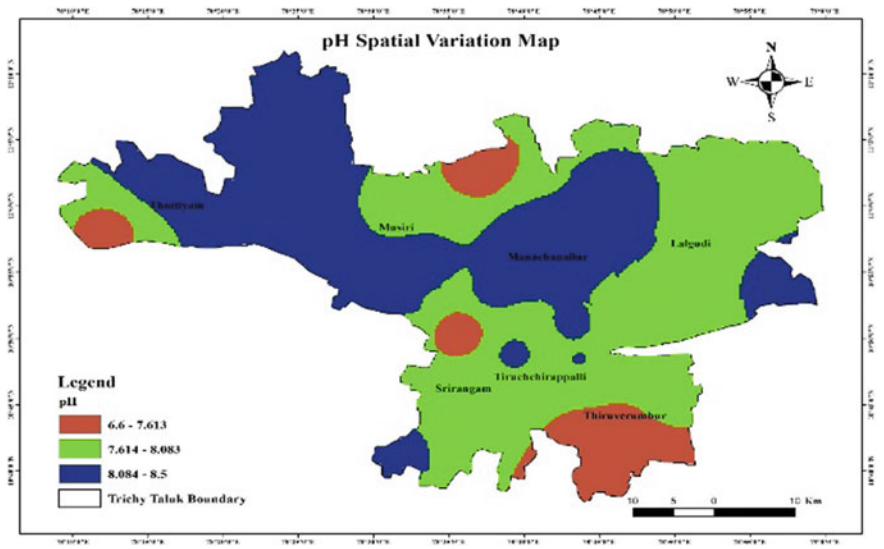

Fig. 2.2 Spatial variation map for pH

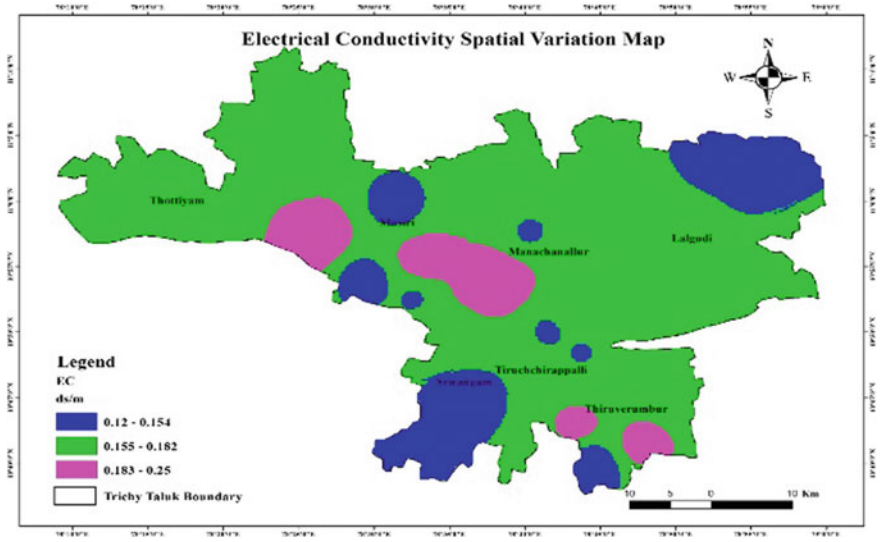

Fig. 2.3 Spatial variation map for EC

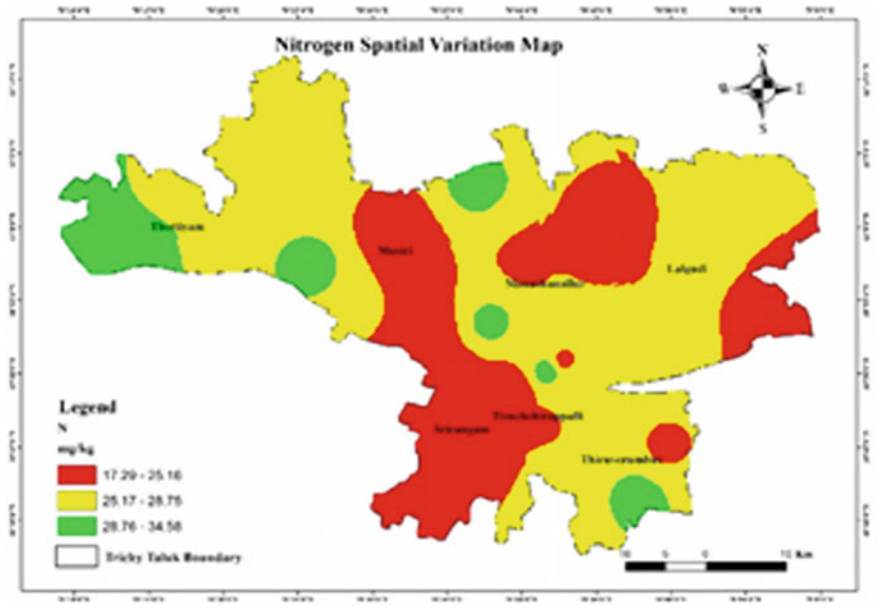

Fig. 2.4 Spatial variation map for nitrogen

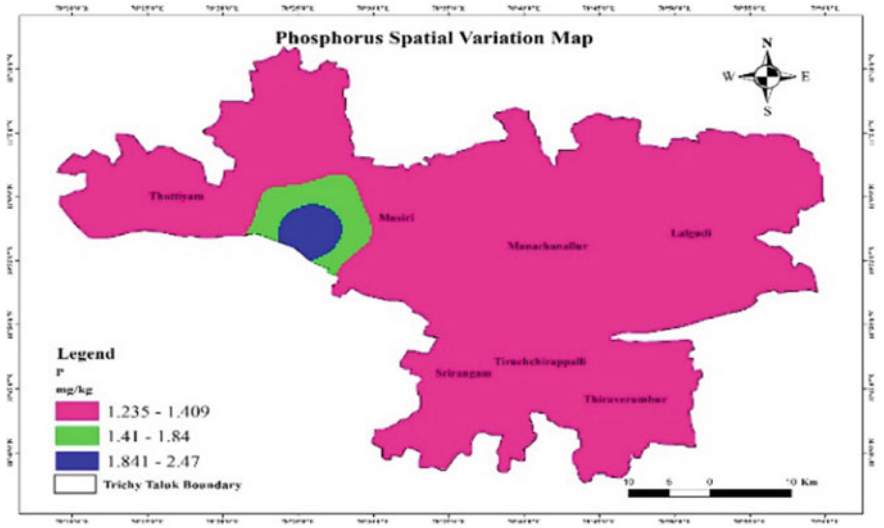

Fig. 2.5 Spatial variation map for PO4

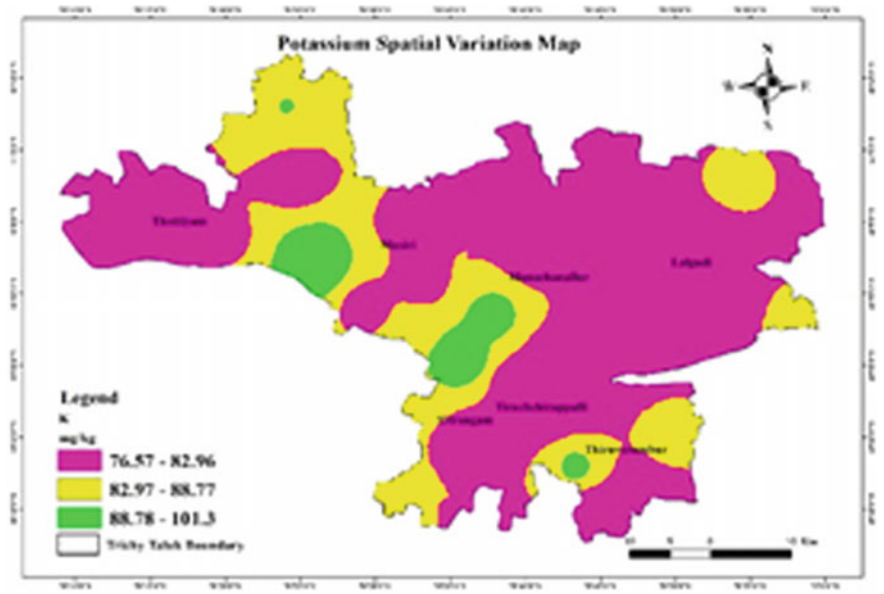

Fig. 2.6 Spatial variation map for K

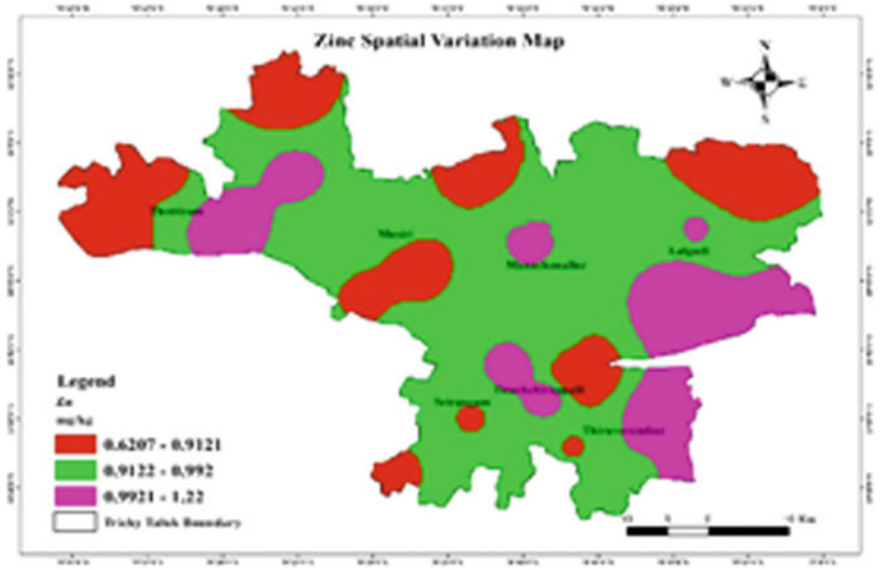

Fig. 2.7 Spatial variation map for Zn

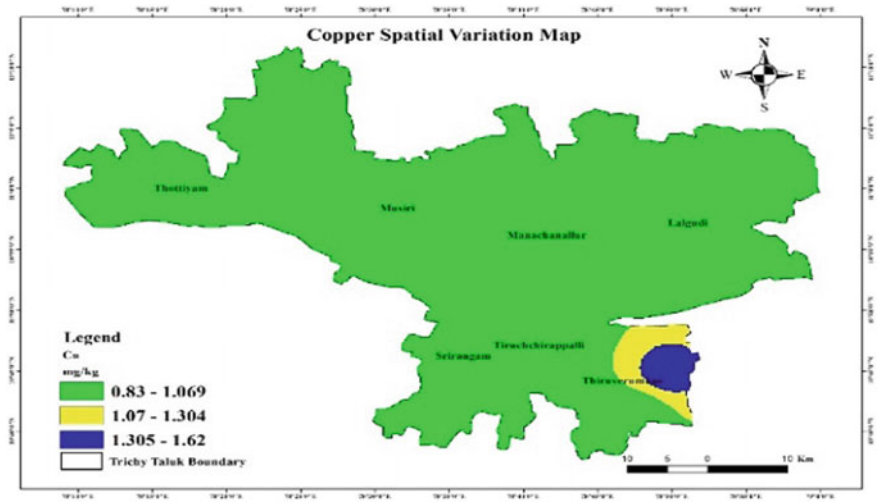

Fig. 2.8 Spatial variation map for Cu

Fuzzy Overlay Mechanism

In multicriterion overlay analysis, the fuzzy overlay tool provides for the investigation of the potential of a phenomenon belonging to more than one set, where the tool

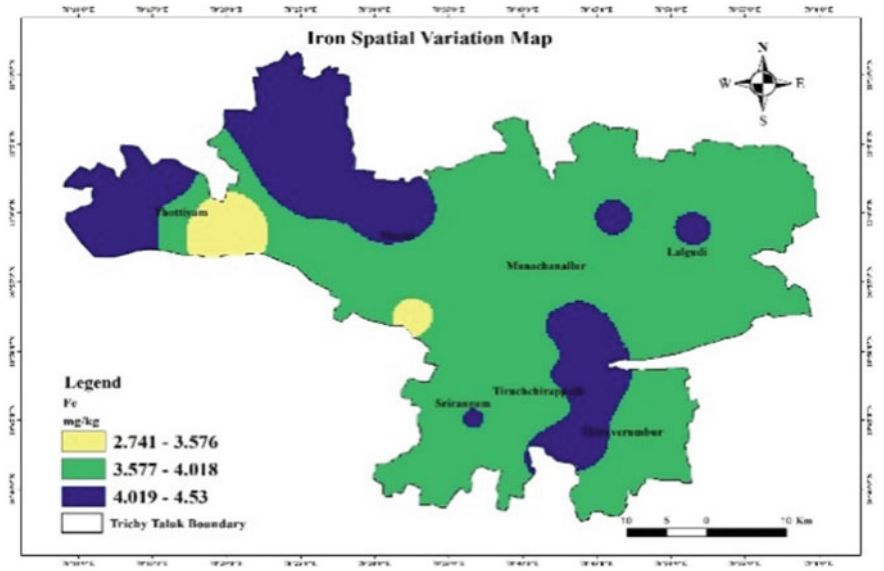

Fig. 2.9 Spatial variation map for Fe

Table 2.3 Parameters ranges

Parameters	Max (identified region)	Min (identified region)
Electrical conductivity	Musiri, Amoor, Elanthapatti	Pattavaithalai, Thadalaiputhur, Chiththanatham, and Mandaiyur
pH	Thottiyam, Manachanallur, Melachinthamani, Musiri, Tiruchirappalli	Kulumani, Mandaiyur, Sriramasamudram
Nitrogen	Musiri, Sholanganallur, Sriramasamudram	Aravalli, Thadalaiputhur, Chiththanatham, and Amoor
Phosphorus	Musiri	Aravalli, Thadalaiputhur, Chiththanatham, Lalgudiandamoor
Potassium	Musiri, Kulumani, and Maruthi Nagar	Aravalli, Thadalaiputhur, Lalgudi and Kajamalai
zinc	Thottiyam, Lalgudi, Elanthapatti, and Thuvakudi	Urakarai, Pettavaithalai, and Kajamalai
Manganese	Bharathipuram, Musiri, Amoor, Elanthapatti, and Chithanatham	Sriramasamudram, Thinnanur, and Sirukalappur
Copper	Thuvakudi	Amoor, Musiri, Aravalli, and Lalgudi
Iron	Sriramasadram, Thandalaiputhur, Aravalli, Kajamalai, and MelaChinthamani	Thottiyam, Ananjanur

Table 2.4 Fuzzy overlay map values

Classes	Location	Indicator colour in map
Slightly low	Musiri, Thuvagudi, and Surampatti	Green (0.09–0.28)
Low	Lalgudi and Vittalapuram	Blue (0.28–0.42)
Medium	Sirukalappur and Mandaiyur	Rose (0.42–0.53)
High	Urakkarai and Vitalapuram	Light green (0.53–0.66)
Slightly high	Avaravalli and Thiruvanaikovil	Amber (0.66–0.82)
Extreme high	Thandalaiputhur and Kannagudi	Red (0.82–1)

examines the numerous links between the memberships of multiple sets. There are a variety of approaches available, ranging from logical operations (fuzzy and, fuzzy or) to fuzzy arithmetic (fuzzy product, fuzzy sum) and fuzzy gamma. Each strategy gives a different feature of each cell's membership for the many input criteria.

A set that holds raster input of nine different measured parameters is interpreted through the fuzzy overlay method. The interactions between all the parameters with different criteria are analysed. In MCDA overlay analysis, the fuzzy membership function is used to merge all raster data from various sets. It also executes a fuzzy MCDA process using the idea of fuzzy sets to analyse the relationships between the memberships of the numerous sets. Fuzzification is performed on the layers criteria by the membership functions.

- Combines the layers that have become fuzzified (fuzzy operators).
- Fuzzy overlay analysis (FOA) algorithm is implemented.
- Sorts the many options into categories (fuzzy classification).

The analysis classification is categorized under six different classes. Table 2.4 denotes the locations that are classified under a different category for Fig. 2.10.

Conclusion

To assess the soil contamination level in the Cauvery delta zone comprising of Tiruchirappalli and Thanjavur districts, the selected location covers the cultivated and barren land as an experimental analysis. Soil samples of various depths were collected, and spatial database was created based on the collected data. Spatial interpolation uses points with known values to estimate the values at other points. The spatial interpolation technique converts the point data to surface data. Samples collected from 33 sites including soil samples of different depth were analysed. Using chemical analysis data, we developed spatial models by interpolation techniques. Through a suitable spatial interpolation technique, the contamination level in the soil was derived. The pH, EC, sulphate, chlorides, chromium, TDS, and organic matter were used for assessing the level of soil contamination using interpolation techniques as IDW. The IDW method has been observed to be the most suitable method for all

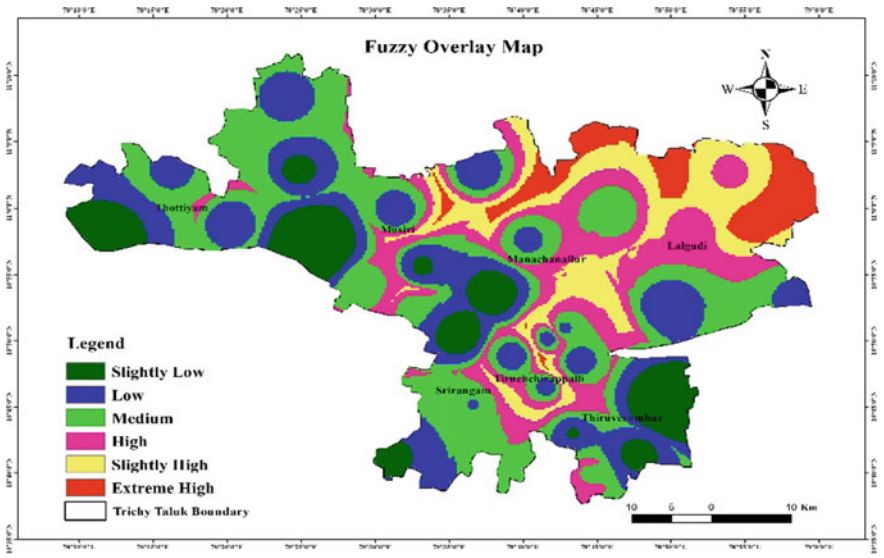

Fig. 2.10 Fuzzy overlay map

the chemical parameters, which was found by the cross-validation technique. The contamination map generated in the present experiment analysis represents the level and extent of soil within the experiment area. The soil contamination level has been effectively classified at various labelling levels in and around river basin as slightly low, low, medium, high, slightly high, and extremely high, and it was noted that soil near river basin area is highly contaminated.

Acknowledgements This work was supported by NRDMS, DST Ref No: NRDMS/01/184/2016(G), and we would also like to extend our sincere thanks to the NRDMS organization.

References

1. Hai TS, Thuy NT (2012) Image classification using support vector machine and artificial neural network. Int J Inf Technol Comput Sci (IJITCS) 4(5)
2. Sobhacyrus, Roy .M Thoms (1996) Effluent of tannery waste on the behavior of soils. In: Indian geotechnical conference, vol 2, pp 544–546
3. Dungan JL (1998) Spatial prediction of vegetation quantities using ground and image data. Int J Remote Sens 19(2):267–285
4. IBM industry insights: 2.5 quintillion bytes of data created every day. How does CPG and retail manage it? https://www.ibm.com/blogs/insights-onbusiness/consumer-products/2-5-quintillion-bytes-of-data-created-every-dayhow-does-cpg-retail-manage-it/. Accessed 30 Oct 2017

5. Hani E, Pazira M, Manshouri S, BabaieKafaky MG (2010) Spatial distribution and mapping of risk elements pollution in agricultural soils of southern Tehran, Iran. Plant Soil Environ 56:288–296
6. Baidya P, Chutia D, Sudhakar S, Goswami C, Goswami J, Saikhom V, Singh PS, Sarma KK (2014) Effectiveness of fuzzy overlay function for multi-criteria spatial modeling—a case study on preparation of land resources map for Mawsynram Block of East Khasi Hills District of Meghalaya, India. J Geogr Inf Syst 6:605–612
7. Ghareb AS, Bakar AA, Hamdan AR (2016) Hybrid feature selection based on enhanced genetic algorithm for text categorization. Expert Syst Appl 49:31–47
8. Jiang X, Zou B, Feng H, Tang J, Tu Y, Zhao X (2018) Spatial distribution mapping of Hg contamination in subclass agricultural soils using GIS enhanced multiple linear regression. J Geochem Explor 17:30351–30355 0375 6742
9. Aliki C, Hatzichristos T (2019) A GIS-based spatial multi-criteria decision analysis: crisp and fuzzy methods. AGILE 2019, Limassol. https://www.editorialmanager.com/jgsi/default.aspx
10. Gangappa M, Kiran Mai C, Sammula P (2018) Techniques for machine learning based spatial data analysis: research directions
11. Hu C, Wright AL, Lian G (2019) Estimating the spatial distribution of soil properties using environmental variables at a catchment scale in the loess hilly area, China. Int J Environ Res Public Health 16:491–496

Chapter 3
Chemical and Mineralogical Evaluation of Soils for Their Suitability in Geotechnical Application

Sameer Vyas, Beena Anand, and R. P. Pathak

Introduction

Soil is a weathered material of parental rocks, and after combined with other inorganic and organic substances, its composition varies from site to site. Therefore, physical and chemical properties of soils depend on various factors including mineralogy, climatic conditions, types of vegetation, and moisture contents. The soils are the basic support material on which the foundation of any civil engineering structure is laid down. Therefore, for the sustainability and stability of structure, the detailed investigations related to physical and chemical parameters need to evaluate for suitability of soils in engineering applications. The history of failures of slope and structures has been witnessed the improper investigations and understanding of the materials behaviour.

The civil engineering applications of soils for foundation and as fill materials required detailed investigations as per standard codes and practices. Besides physical and engineering tests, the chemical analysis is also important to conduct for assessing its suitability as a construction material. Soils are the mixture of inorganic, organic, and mineral components, and there variable compositions are the deciding factors of its geotechnical properties.

Chemical Properties of Soils Significant for Civil Engineering

Apart from engineering properties, the chemical properties of soil also have a significant role to play in civil engineering works. A number of tests are conducted on soils to determine the soluble salt contents (TSS), pH value, water soluble chloride,

S. Vyas (✉) · B. Anand · R. P. Pathak
Central Soil and Materials Research Station, New Delhi 110016, India
e-mail: Samyog78@yahoo.com

K. Muthukkumaran (eds.), *Soil Behavior and Characterization of Geomaterials*,
Lecture Notes in Civil Engineering 296, https://doi.org/10.1007/978-981-19-6513-5_3

water soluble sulphate, calcium carbonate, organic matter, cation exchange capacity and dispersive characteristics.

pH value: The pH of a soil extract solution is the measure of hydrogen ion concentration which is measured on 0 to 14 logarithmic scale. The pH value shows acidic and alkaline characteristics of soils. The pH of soil water solution plays an important role in problems involving grouting in weak rocks, soil stabilization process using lime and resinous materials, and corrosion of steel in concrete. Soil pH can affect cation exchange capacity.

Acidic and alkaline nature of soils depends on various factors such as surrounding geology, climatic conditions, degree of precipitation, and anthropogenic inputs.

Testing procedure as per IS 2720 Part. 26, 1987.

Total Soluble Salts

The presence of soluble salts in a soil is one of the important aspects requiring examination since water soluble solids greatly influence the engineering properties of soil. Primary minerals are ultimate origin of soluble salts in soils. It is generally reported in terms of conductivity. Soils with excessive salts are said to be saline soil. Its conductivity exceeds 4 millimhos/cm. A saline soil is said to be saline alkali soil if its sodium content is more than half of the total soluble cation content. The following classification of soil depending upon the conductivity of soil water (1:10) extract is reported in IS:2720 Part 27.

Testing procedure as per **IS-**2720 (PART 21)-1977, (Reaffirmed 1995).

Electrical Conductivity: The measurement of electrical conductivity of soil water extract can also indicated about the presence of approximate amount of soluble salts in soil. It is measured in μmhos/cm or μS/cm at 25 °C. Relationship between conductivity and soluble salts contents is presented in Table 3.1.

The determination of total soluble salts is used for adopting suitable remedial measures at the time of construction.

Calcium Carbonate Content

The high amount of calcium carbonate is present in soil indicated its calcareous nature and cementing property. Its amount depends upon surrounding geology and mineralogy. Calcium carbonate contents are a strength giving parameter; however,

Table 3.1 Relationship between conductivity and soluble salts contents

Electrical conductivity in mmhos/cm	Presence of soluble salts
Less than 1	Normal
Between 1 and 2	Fairly good
Between 2 and 3	High
Between 3 and 4	Very high

its presence in high amount can affect physical structure of soils which need to be evaluate before any application.

Testing procedure as per IS 2720 pt. 23, 1976, (Reaffirmed 2006).

Sulphate

Excessive sulphate in soil may be deleterious for concrete placed in the ground on account of inducing expansive characteristics. Sulphate ions react with calcium hydroxide of cement in the pores of concrete to produce gypsum, i.e. calcium sulphate which on crystallization gives $CaSO_4$, $2H_2O$ accompanied by 17.7% increases its volume. In the second category, sulphate ions attack the tricalcium aluminate to form tricalcium sulphoalluminate accompanied by expansion in volume. The expansion which accompanies crystallization induces internal stresses in the concrete, which results in mechanical disintegration.

IS:456-1976 given the classification of soil and ground water according to sulphate content.

Testing procedure as per IS:2720 (Part XXVII)-1977 (Reaffirmed 2006).

Chloride

The presence of soluble chloride salts in soils is of great concern particularly when concrete or reinforced structures buried in such soils. The dissolution of chloride ions in soils pore water can initiated corrosion of buried reinforcement.

Organic Matter

Organic matter is considered deleterious for soil engineering values, since it contributes a spongy unstable structure and is chemically reactive. Organic soils are problematic soils. The high amount of organic matter responsible for poor strength, high compressibility, high void ratio, large deformations, reduced bearing capacity, high swelling-shrinkage potential and increased compressibility. Organic matter influences soil structure and all associated properties. Chemically, soil organic matter affects the cation exchange capacity and the capacity for buffering changes in soil pH.

Testing procedure as per IS:2720 pt.22,1972, (Reaffirmed 2010).

Dispersive Characteristics of Soil

Dispersive soils are problematic soils for civil engineering application particularly when such soils are used for earthen embankment and canal lining. The fine-grained soils with the presence of high amount of soluble sodium salts in their pore water exhibit property of colloidal dispersion. Clay particles of such soils deflocculates under the current of water and forming tunnels and deep gullies causing damage to earth dams, canals, and other hydraulic structures.

Materials and Methods

Soil samples received from two different earthen dam project sites were selected for detail chemical analysis. The details of sample size and method of testing are presented in Table 3.2.

The experimental analytical setup are presented in Figs. 3.1 and 3.2.

Table 3.2 Details of parameters, sample size, and testing methods

Sl. No.	Name of test	Procedure	Quantity required for test	Sample size
1	pH	pH metre direct reading type	30 g of the soil in 75 ml distil water	Sample passed on 425-μ IS Sieve
2	Total soluble salts, TSS	Portable conductivity meter	1:10 soil water extract	Sample pass on 2 mm Sieve
3	Water soluble sulphate	Precipitation method	1:10 soil water extract	Sample passed on 425-micron IS Sieve
4	Water soluble chloride	Volumetric estimation	1:10 soil water extract	Sample passed on 425-μ IS Sieve
5	Calcium carbonate	Acid–base Volumetric titration	5 g	Sample pass on 2 mm Sieve
6	Organic matter	Volumetric redox titration	100 g air drying	Sample pass on 2 mm Sieve
7	Dispersive character	Chemical analysis of pore water extract for determination of Na, K, Ca, and Mg	Flame photometric method	Sample passed on 425-μ IS Sieve

Fig. 3.1 Determination pH of soil water extract

Fig. 3.2 Determination of sodium and potassium in pore water extract with flame photometer and determination of chloride with automatic titrater

X-ray Diffraction Analysis (XRD)

The mineralogical examination of soils can be done with the help of X-ray diffraction technique (XRD). The expensive and dispersive nature of problematic soils can be further characterized with the help of XRD by identifying the types of dominant clay minerals present in soils (Fig. 3.3).

All parameters were analysed as per standard BIS codes IS:2720 and procedures mentioned in ASTM. Standards.

Fig. 3.3 X-ray diffractometer

Results and Discussion

The test results of core chemical parameters are presented in Tables 3.3 and 3.4 for soil samples from project-1.

Results of Table 3.3 show that all soil samples are acidic in nature, while other parameters are within normal acceptable range. The test results presented in Table 3.4 shows that sample no. 2, 3, and 4 are dispersive in nature; however, sample no. 1 is intermediate in nature. The interpretation of dispersive nature is based on Fig. 3.4.

% Na range	Categorization	Recommendation
(i) 60–100	Dispersive	A
(ii) Up to 40	Non-dispersive	B
(iii) 40–60	Intermediate	C

The results of soil samples from project-2 are presented in Tables 3.5 and 3.6.

Results of Table 3.5 show that both samples are alkaline in nature, while other parameters are within normal acceptable range. The pore water which results in Table 3.6 shows that both the soil samples are intermediate in nature as per interpretation given in Fig. 3.4.

Table 3.3 Results of chemical test of soil samples (project-1)

Sl. No.	Parameters	Sample-1	Sample-2	Sample-3	Sample-4
1	**pH** value as per IS:2720 Pt. 26 1987	5.63	5.69	5.60	5.79
2	**$CaCo_3$ %** by wt. as per IS:2720 Pt. 23. 1976	Nil	Nil	Nil	Nil
3	**Total soluble salts** in terms of conductivity millimhos/cm as per IS:2720 Pt. 21. 1977	0.011	0.015	0.034	0.062
4	Water soluble s**ulphate** % by wt. as per IS:2720 Pt. 27. 1977	0.025	0.038	0.055	0.117
5	Water soluble c**hloride** % by wt. as per standard text book	0.01	0.01	0.03	0.04
6	**Organic matter** (%) by wt.	0.40	0.35	0.48	0.20

Table 3.4 Results of chemical analysis of pore water extract (dispersivity test) (project-1)

Sample No.	Mili equivalent./l				Total cations	Sodium (%)	Remarks grade
	Na	K	Ca	Mg			
1	2.19	0.47	0.8	0.4	3.86	56.73	C
2	3.20	0.69	0.6	0.2	4.69	68.23	A
3	4.12	1.01	1.0	0.6	6.73	61.21	A
4	3.44	0.80	0.6	0.2	5.04	68.25	A

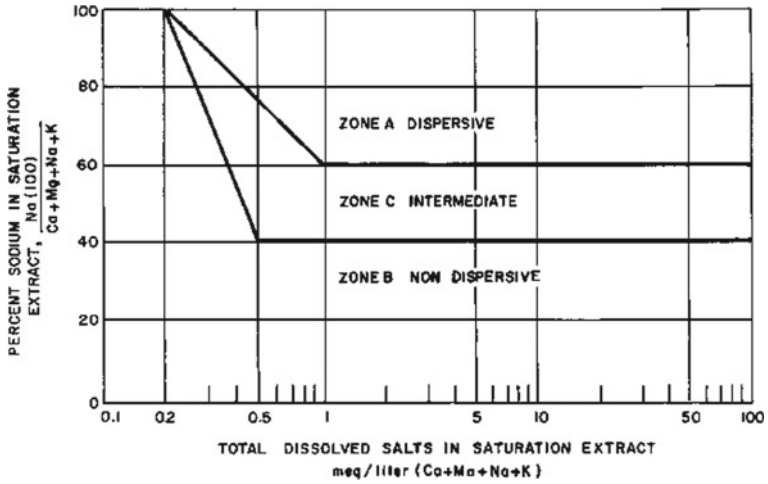

Fig. 3.4 Plot of TDS versus per cent sodium

Table 3.5 Results of chemical test of soil samples (project-2)

Sl. No.	Parameters	Sample-5	Sample-6
1	**pH** value as per IS:2720 Pt. 26 1987	8.47	8.61
2	**$CaCO_3$ %** by wt. as per IS:2720 Pt. 23. 1976	2.0	8.0
3	**Total soluble salts** in terms of conductivity millimhos/cm as per IS:2720 Pt. 21. 1977	0.034	0.067
4	Water soluble s**ulphate** % by wt. as per IS:2720 Pt. 27. 1977	0.009	0.018
5	Water soluble c**hloride** % by wt. as per standard procedure	0.01	0.05
6	**Organic matter** (%) by wt.	0.55	0.35

Table 3.6 Results of chemical analysis of pore water extract [dispersivity test (project-2)]

Sample No.	Mili equivalent./l				Total cations	Sodium (%)	Remarks grade
	Na	K	Ca	Mg			
Sample-5	4.17	2.66	0.6	0.4	7.83	53.25	**C**
Sample-6	3.61	2.69	1.0	0.2	7.50	48.13	**C**

The dispersive nature of soil sample from project-1 was also evaluated by XRD analysis. The XRD patterns presented in Fig. 3.5 confirm the presence of minerals causing soil dispersion.

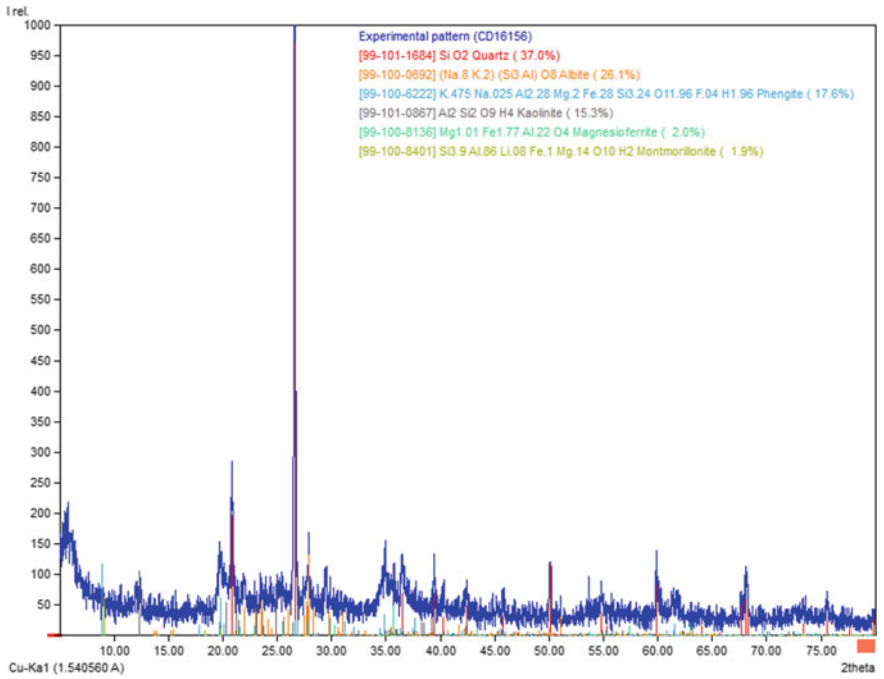

Fig. 3.5 XRD pattern of dispersive soil

Conclusion

- The chemical analysis results of soil samples from project-1 show acidic nature. The pH value below 6.0 is not good for soils to be used for foundation or stabilization purpose. The concrete structures buried in such soils may suffer problems related to leaching and corrosion of reinforcement.
- The presence of other parameters is within permissible limit.
- Three soil samples from project-1 show dispersive character while one sample falls in intermediate range. The confirmation of dispersive nature should also be needed to evaluate with other civil engineering tests before use as fill material or for embankment purpose.
- Chemical analysis results of two soil samples from project-2 show alkaline nature. The suitable pH range for soil to be used as foundation purpose should be in the range of 6.5–8.5. Soil pH beyond this range affects civil engineering properties.
- Other parameters such as total soluble salts, sulphate, and chloride are within normal range in soil samples. The presence of significant amount of calcium carbonate contents in one of sample from project-2 supports the cementing property of soils.
- With the low organic matter contents, soils from both projects are suitable for civil engineering applications.

- The XRD pattern helps in characterizing and identifying dispersive behaviour of soils based on mineralogical assessment.

Chapter 4
Prediction of Suitable Percentage of Waste Materials for Improving Geotechnical Properties of Black Cotton Soil Using AI Approaches

Jitendra Khatti and Kamaldeep Singh Grover

Introduction

The surface and subsurface of the earth are formed by soil and rocks. The soils and rocks are classified based on their color, mineralogical composition, and mechanical properties. Cohesive and cohesionless soils are the types of soil. The cohesive soils are problematic soil because it swells when it comes to contact with water and shrinks when water disperse. The phenomenon of swell and shrink develops the unequal settlement beneath the structure or buildings. The stabilization technique is used to improve the mechanical properties of cohesive soils [1]. The mechanical, cement, lime, bituminous, and chemical stabilizations are the types of stabilization. These are the traditional stabilization method, but the disposal of waste materials is another drastic problem in the present time. Many researchers, Ji-ru et al. [2]; Edil et al. [3]; Hakari et al. [4]; Mehta et al. [5]; Karthik et al. [6]; Rajak et al. [7]; Pallavi et al. [8], etc. stabilized soil by fly ash. It was reported that fly ash can improve soil's mechanical properties, and the stabilization process is a time-consuming, tedious, and cumbersome task. Human resources are also required to execute the stabilization process.

Numerous researchers and scientists developed different methods and methodologies to compute the mechanical properties of soil. Vahdani et al. [9] developed a response surface method (RSM) to predict the mechanical properties of frozen soil. The authors carried out the published research work using three cases studies [9]. Forty percent of the available data was used to develop the models, and the rest of the data was used to validate the models. The authors concluded that the RSM has the potential to predict the experimental data and find significant factors. The

J. Khatti (✉) · K. S. Grover
Department of Civil Engineering, RTU, Kota, Rajasthan 324010, India
e-mail: jitendrakhatti197@gmail.com

K. S. Grover
e-mail: ksgrover@rtu.ac.in

K. Muthukkumaran (eds.), *Soil Behavior and Characterization of Geomaterials*,
Lecture Notes in Civil Engineering 296, https://doi.org/10.1007/978-981-19-6513-5_4

authors also stated that the dataset plays a vital role in the accuracy of the model. A large dataset is required to achieve a better performance model. Premarathne and Sawangsuriya [10] proposed a multiple linear regression model for predicting the UCS of cement stabilized pavement materials. The authors proposed three regression equations—

$$\text{UCS} = 8.518 + 0.069 * \text{CBR} + 3.834 * c - 0.323 * f \tag{4.1}$$

$$\text{UCS} = -58.332 + 33.169 * \text{MDD} + 3.791 * c - 0.379 * f \tag{4.2}$$

$$\text{UCS} = -52.005 + 28.882 * \text{MDD} + 0.048 * \text{CBR} + 3.787 * c - 0.319 * f \tag{4.3}$$

Using Eqs. (4.1), (4.2), and (4.3), the ranking index of the MLRA model was 0.19, 0.18, and 0.18 observed in predicting UCS of stabilized soil and compared with published equations of Sunitsakul et al. by Premarathne and Sawangsuriya [10]. It was found that the equation proposed by Premarathne and Sawangsuriya [10] did not help to predict the UCS of non-plastic soils [10]. Onyelowe and Bui Van [11] evolved multiple regression models to predict the strength parameters of stabilized lateritic soil using ash. The authors concluded that the regression models can be applied to field soil stabilization. Ahmed et al. [12] developed the best-fit model to predict the mechanical properties, such as MDD, OMC, PI, UCS, LL, and FS of fly ash-stabilized clayey soil. The authors concluded that the results obtained from F-test and t-test showed that the used parameters contribute to developing the model and achieving better prediction. Rashidi et al. [13] used UCS, resilient modulus (RM), and indirect tensile strength (IDT) of cementitious materials to develop the relationship between UCS, IDT, and RM. The authors concluded that the proposed model can be used to design the pavement. Sas et al. [14] used statistical approaches to estimate the mechanical properties of lime stabilized soil. The authors concluded that the proposed equations can predict the mechanical properties of stabilized soil. The authors also stated that the resilient modulus calculation shows that the cyclic loading of stabilized soil can be improved by lime content. Shi et al. [15] proposed the polynomial, RBF, and sigmoid kernel-based SVM model to predict the strength of cement stabilized soil. The performance of polynomial, RBF, and sigmoid kernel-based models was 0.9532, 0.9913, and 0.9427, respectively. The authors concluded that the proposed SVM model can predict the compressive strength of cement stabilized soil with higher accuracy. The performance of SVM models was compared with the ANN model, and it was concluded that the SVM model outperformed the ANN model. The authors also concluded that the SVM model performs better for small datasets. It was stated that the performance of the SVM model is also based on the selection of the kernel.

Aim of present research work

The literature survey shows that artificial intelligence has the potential to predict the mechanical properties of stabilized soil. The following aims of the present research work are mapped from the literature study—

- Predict the suitable percentage of FA for the desired mechanical properties of fly ash stabilized soil.
- Determine the best methodology and approach and architecture and optimum performance AI model for predicting the suitability of percentage of FA for improving the geotechnical properties of black cotton soil.
- Minimize the number of laboratory experiments and human resources.

Methodology

The multilinear regression, support vector regression, Gaussian process regression, random forest, decision tree, and artificial neural network AI approaches have been used to develop the AI models. The proposed models have been used to predict the suitability of waste material (FA) to improve the geotechnical properties of BC soil. The AI models have been developed in MATLAB R2020a using different hyperparameters. The support vector regression, Gaussian process regression, random forest, and decision tree are associated with machine approaches. The artificial neural network is associated with deep learning approaches. The hyperparameters of AI models are given in Table 4.1.

The AI models have been developed by elements (liquid limit, optimum moisture content, plastic limit, plasticity index, and maximum dry density) for predicting the percentage of fly ash. The architecture of developed AI models is given in Table 4.2.

The multilinear regression, support vector regression, Gaussian process regression, random forest, decision tree, and artificial neural network models are designated by MLR_FA, SVR_FA, GPR_FA, RF_FA, DT_FA, and ANN_XHY_FA, respectively. In an artificial neural network model, the X is the one to five hidden layers, and Y is the ten neurons. An equation has been proposed while developing the MLR model to predict the percentage of fly ash. The proposed equation is—

$$\mathrm{FA}' = 76.769 - 1.008 * \mathrm{LL} + 0.7912 * \mathrm{PI} + 0.4196 * \mathrm{OMC} - 23.47 * \mathrm{MDD} \tag{4.4}$$

Data Analysis

Eighty-two datasets of fly ash (FA) stabilized soil have been collected from published research articles. The datasets have been collected from the published article of

Table 4.1 Hyperparameters of AI models

Hyperparameters of machine learning models				
Hyperparameters	SVR	GPR	RF	DT
Basic and Kernel function	Auto	Auto	–	–
Kernel scale	Auto	Auto	–	–
Signal std deviation	–	Auto	–	–
Sigma/epsilon	Auto	Auto	–	–
Standardize	Enable	Enable	–	–
Optimize numerical parameters	–	Enable	–	–
Box constraint	Auto	–	–	–
Ensemble method	–	–	Auto	–
Min. leaf size	–	–	Auto	Auto
Number of learners	–	–	Auto	–
Learning rate	–	–	0.1	–
No. of predictors to sample	–	–	All	–
Max. surrogates per nodes	–	–	–	10
Optimizer options for machine learning models				
Optimizer	Bayesian optimization			
Acquisition function	Expected improvement per second plus			
Iterations	30			
Max. training time in seconds	300			
Number of grid divisions	10			
Hyperparameters of deep learning (ANN) models				
Hidden layers	One, two, three, four, five			
Neurons	Ten neurons on each layer			
Backpropagation algorithm(s)	Levenberg–Marquardt			
Normalizing function(s)	Min–max for input and log for output parameters			
Activation function(s)	Sigmoid at hidden layers, linear at the output layer			
Train: validation ratio	70: 30			
Epochs	1000 (default)			
Network type	Feed-forward backpropagation			
Network class	Multilayer perceptron class (MLP)			
Mu	0.001			
Max fail	6			
Min gradient	10e−7			

Table 4.2 Architecture of AI models

Approaches	Type	Model architecture
Multilinear regression	Linear	MLR_FA
Support vector regression	Nonlinear	SVR_FA
Gaussian process regression	Nonlinear	GPR_FA
Random forest	Nonlinear	RF_FA
Decision tree	Nonlinear	DT_FA
Artificial neural network	Nonlinear	ANN_XHY_FA

Karthik et al. [6]; Edil et al. [3]; Ji-ru et al. 2002 [2]; Trivedi et al. [16]; Rajak et al. [7]; Kodicherla et al. [17]; Pallavi et al. [8]; Bin-Shafique et al. [18]; Shaoo et al. [19]; Mehta et al. [5]; Murmu et al. [20]; Kulkarni et al. [21]; Hakari et al. [4]; Vukicevic et al. [22], Sahu et al. [23]; Ratna Prasad and Drga Kumar [24]; Senol et al. [25]; Mohanty [26] and Maheshwari et al. [27]. The geotechnical properties such as index properties (liquid and plastic limit, plasticity index) and compaction parameters (OMC and MDD) have been collected from the referred research articles. The statistics of geotechnical properties of datasets are given in Table 4.3.

The relationship between geotechnical properties and the percentage of FA has been mapped using the correlation coefficient method. The Pearson matrix of the correlation is given in Table 4.4.

Table 4.3 Statistics of geotechnical properties of datasets

	% FA	LL	PL	PI	OMC	MDD
Min	0.00	23.00	10.50	5.00	8.20	1.35
Max	60.00	75.00	40.50	46.00	32.00	2.35
Mean	16.11	45.94	22.69	23.26	20.50	1.72
Mode	0.00	39.00	24.00	25.00	19.00	1.65
Median	10.00	45.20	22.70	24.00	20.00	1.68
St. dev	17.76	13.57	6.78	10.97	6.22	0.24
Con. level	3.90	2.98	1.49	2.41	1.37	0.05

Table 4.4 Pearson matrix of the geotechnical properties

	% FA	LL	PL	PI	OMC	MDD
% Waste	1.0000					
LL	0.1229	1.0000				
PL	0.2881	0.5973	1.0000			
PI	0.0259	0.8686	0.1213	1.0000		
OMC	0.2852	0.4938	0.0268	0.5945	1.0000	
MDD	0.1732	0.5383	0.4233	0.4046	0.7153	1.0000

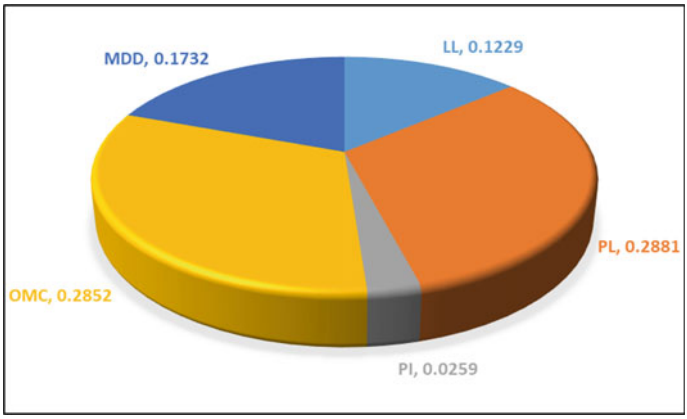

Fig. 4.1 Correlation of geotechnical properties with the percentage of fly ash

The plastic limit and optimum moisture content show a good correlation with the percentage of fly ash. The correlation of liquid limit, maximum dry density, and plasticity index with the percentage of fly ash is relatively weak [28]. The correlation of LL, PL, PI, OMC, and MDD with the percentage of fly ash is shown in Fig. 4.1.

Training and Testing Datasets

Eighty-two datasets have been collected from various published research articles. These datasets consist of geotechnical properties, such as liquid limit, plastic limit, plasticity index, optimum moisture content, and maximum dry density. These geotechnical properties were determined for virgin soil and soil stabilized at different percentages of fly ash. These datasets have been divided into 58 training and 24 testing datasets. The multilinear regression, support vector regression, Gaussian process regression, random forest, and decision tree AI models have been trained by 58 datasets and tested by 24 datasets. Fifty-eight datasets have also been subdivided into 41 training and 17 validation datasets to train and validate the proposed artificial neural network models. Twenty-four datasets have tested the proposed ANN models.

Results and Discussion

The multilinear regression analysis model has been developed using the Data Analysis Tool of Microsoft Excel 2019. The Gaussian process regression, support vector regression, random forest, decision tree, and artificial neural network models have been developed using the MATLAB R2020a. RMSE, R, and MAE have determined the performance of the proposed AI models. The performance of models has been discussed.

Table 4.5 Performance of MLR model

Model	Training performance			Testing performance		
	RMSE	R	MAE	RMSE	R	MAE
MLR_FA	16.3358	0.4512	13.1069	14.2931	0.4447	12.3740

Multilinear Regression (MLR) Analysis

Fifty-eight datasets of soil have trained the proposed multilinear regression (MLR) model. Twenty-four datasets have tested the proposed MLR model, and during the training and testing of the MLR model, the performance of the MLR has been recorded. The training and testing performances of the MLR model are given in Table 4.5.

Support Vector Regression (SVR)

The support vector regression is based on the kernel functions, and these kernel functions are Gaussian, polynomial, quadratic, and cubic. Default hyperparameters of the SVR model have determined the best architecture SVR model. The training performance of the SVR model is shown in Fig. 4.2, and the training and testing performances of the SVR model are given in Table 4.6.

The proposed SVR model has achieved maximum performance at nine iterations with a Gaussian kernel. The performance of the SVR_FA model is 0.3593.

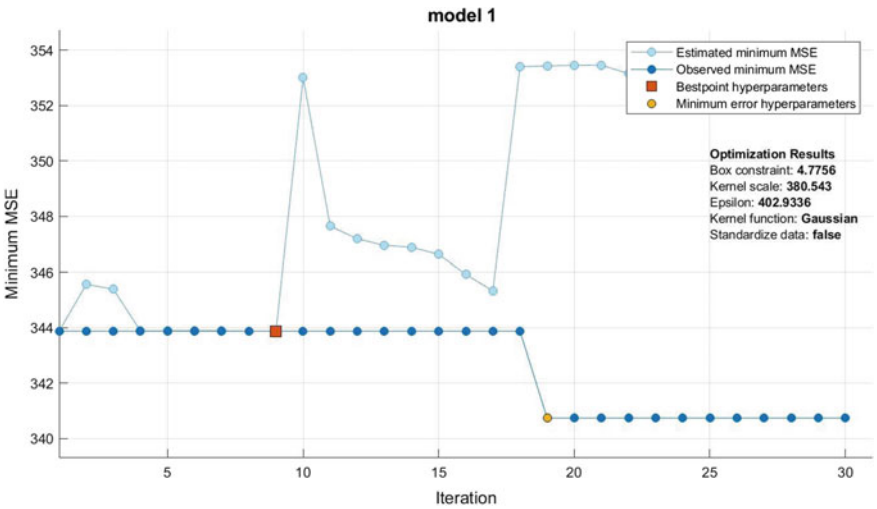

Fig. 4.2 Training performance of the SVR model

Table 4.6 Performance of SVR model

Model	Training performance			Testing performance		
	RMSE	R	MAE	RMSE	R	MAE
SVR_FA	18.7970	0.3606	15.3030	14.6055	0.3593	12.5330

Gaussian Process Regression (GPR)

The Gaussian process regression is also based on the kernel functions, and these kernel functions are RBF, Matern, Rational quadratic, Exp-sin-square, and dot-product. Default hyperparameters of the GPR model have determined the best architecture GPR model. The training performance of the GPR model is shown in Fig. 4.3, and the training and testing performances of the GPR model are given in Table 4.7.

The proposed GPR model has achieved maximum performance at nineteen iterations with a non-isotropic exponential kernel. The performance of the GPR_FA model is 0.8789.

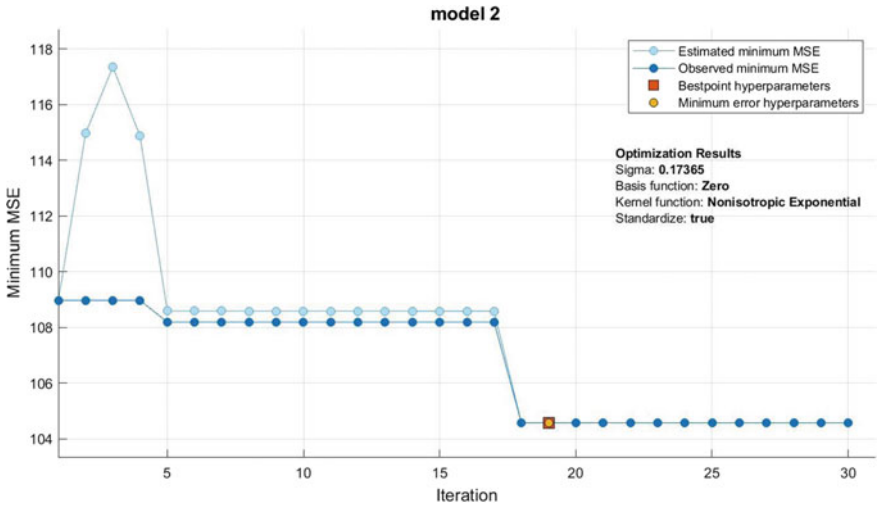

Fig. 4.3 Training performance of the GPR model

Table 4.7 Performance of GPR model

Model	Training performance			Testing performance		
	RMSE	R	MAE	RMSE	R	MAE
GPR_FA	10.2260	0.8367	7.1819	7.6273	0.8789	5.3294

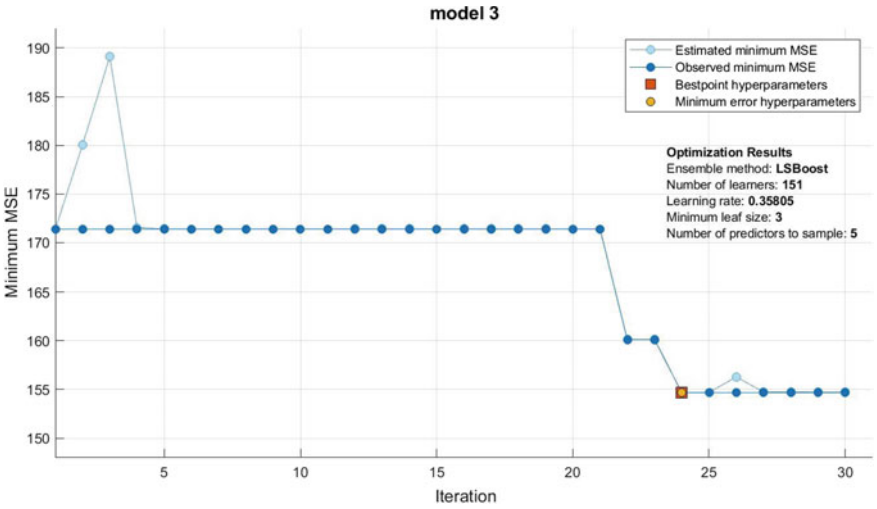

Fig. 4.4 Training performance of the RF model

Table 4.8 Performance of RF model

Model	Training performance			Testing performance		
	RMSE	R	MAE	RMSE	R	MAE
RF_FA	12.4370	0.7483	9.3322	10.8658	0.7296	7.8687

Random Forest (RF)

The random forest is based on supervised learning, and it is used for solving classification and regression problems [29]. Many decision trees form a random forest, and the algorithm is used to combine these decision trees and produce an ensemble learning rule for prediction. Default hyperparameters of the RF model have determined the best architecture RF model. The training performance of the RF model is shown in Fig. 4.4, and the training and testing performances of the RF model are given in Table 4.8.

The proposed RF_FA model has achieved maximum performance at twenty-four iterations with a three minimum leaf size. The performance of the RF_FA model is 0.7296.

Decision Tree (DT)

The decision tree is also used to solve the classification and regression problems. The decision tree is a supervised learning-based approach. Default hyperparameters of

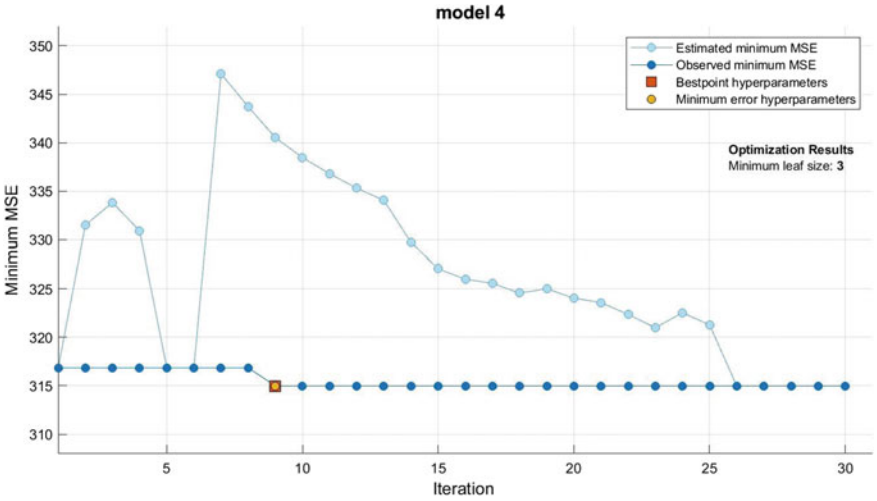

Fig. 4.5 Training performance of the DT_FA model

Table 4.9 Performance of DT_FA model

Model	Training performance			Testing performance		
	RMSE	R	MAE	RMSE	R	MAE
DT_FA	17.7480	0.3317	13.9090	12.7877	0.6341	8.7621

the DT approach have determined the best architecture DT_FA model. The training performance of the DT_FA model is shown in Fig. 4.5.

The training and testing performances of the DT_FA model are given in Table 4.9.

The proposed DT_FA model has achieved maximum performance at nine iterations with a three minimum leaf size. The performance of the DT_FA model is 0.6341.

Artificial Neural Network

The artificial neural network is a network of layers. One to five hidden layers have been selected to develop to predict the suitable percentage of fly ash. The training and testing performances of developed ANN models are given in Table 4.10.

The ANN_2H10_FA model has been identified as the best architecture artificial neural network based on model performance. The training performance of the ANN_2H10_FA model is shown in Fig. 4.6.

Table 4.10 Performance of ANN_FA model

Model	Training performance			Testing performance		
	RMSE	R	MAE	RMSE	R	MAE
ANN_1H10_FA	1.5616	0.4874	0.1276	15.8849	0.5025	11.0056
ANN_2H10_FA	0.2444	0.9899	0.0221	12.3209	0.7770	7.5445
ANN_3H10_FA	0.8895	0.8036	0.0139	12.6717	0.6320	8.9928
ANN_4H10_FA	1.1370	0.6765	0.0425	13.4568	0.5389	9.9483
ANN_5H10_FA	1.4021	0.4836	0.0728	14.7106	0.3856	10.7175

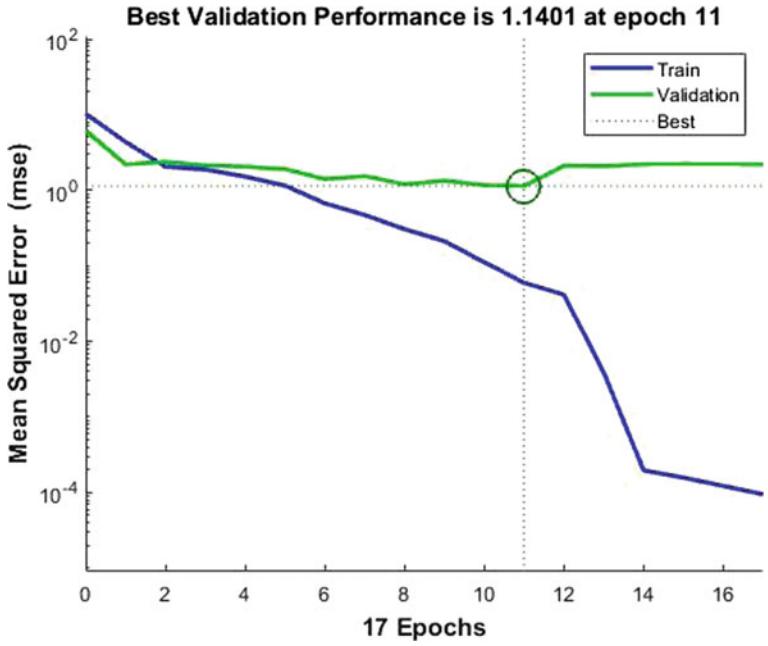

Fig. 4.6 Training performance of the ANN_2H10_FA model

The proposed ANN_2H10_FA model has achieved maximum performance at eleven epochs with minimum RMSE. The performance of the ANN_2H10_FA model is 0.7770.

Optimum Performance AI Model

The performance of the proposed AI models has been compared to identify the optimum performance AI model. The comparison of RMSE and MAE performance

of the proposed AI models is shown in Fig. 4.7, and the comparison of R performance is also shown in Fig. 4.8.

From Figs. 4.7 and 4.8, it has been observed that the GPR_FA models outperformed the other AI models. The RMSE, R, and MAE performances of the GPR_FA model are 7.6273, 0.8789, and 5.3294, comparatively less to other models. The suitable percentage of fly ash for improving the geotechnical properties of BC soil has been predicted using the GPR_FA model. From the comparison of results, the GPR_FA model can predict the percentage of fly ash. The comparison of laboratory test results and predicted results is shown in Fig. 4.9.

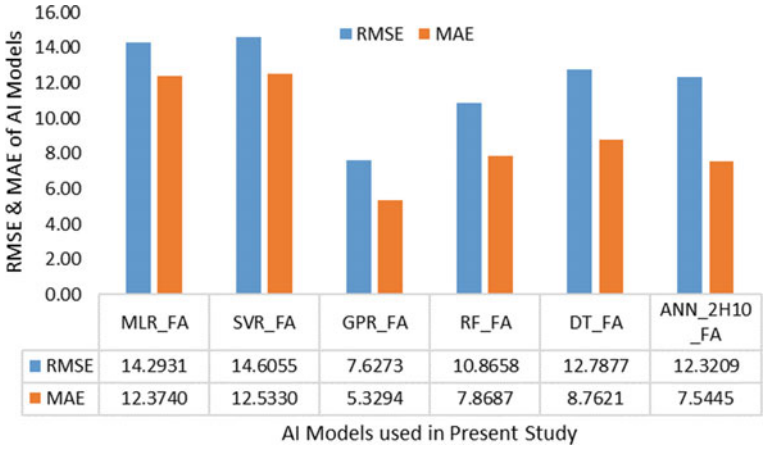

	MLR_FA	SVR_FA	GPR_FA	RF_FA	DT_FA	ANN_2H10_FA
RMSE	14.2931	14.6055	7.6273	10.8658	12.7877	12.3209
MAE	12.3740	12.5330	5.3294	7.8687	8.7621	7.5445

Fig. 4.7 Comparison of RMSE and MAE performance of AI models

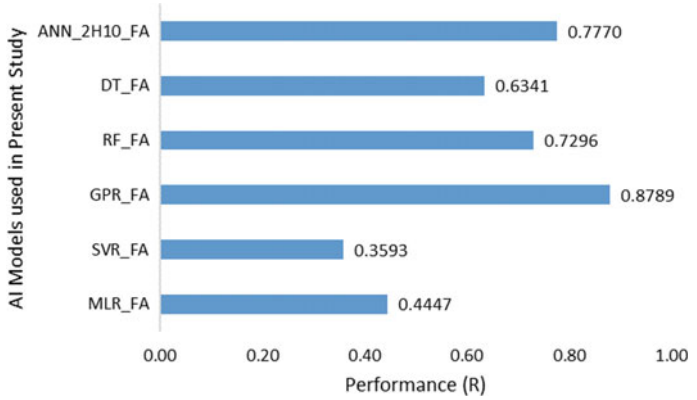

Fig. 4.8 Comparison of R performance of AI models

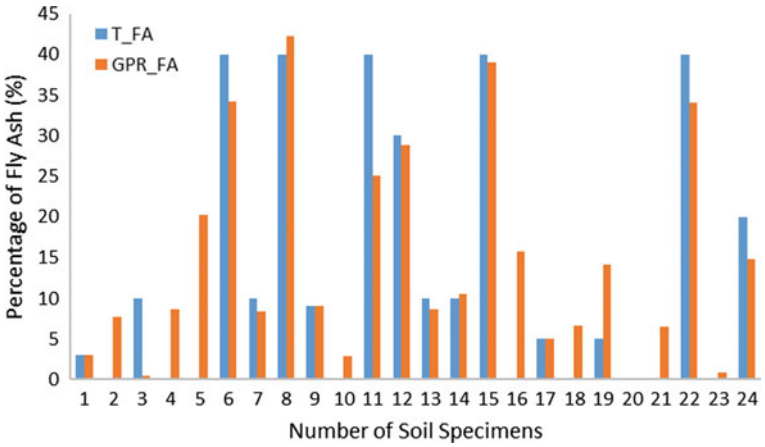

Fig. 4.9 Comparison of laboratory test and predicted results

Conclusions

The literature survey shows that the geotechnical properties of soil can be predicted using statistical approaches and machine learning. The regression analysis, support vector regression, Gaussian process regression, decision tree, random forest, and artificial neural network models were developed to predict the suitable percentage of fly ash for improving the geotechnical properties of black cotton soil. The following conclusions are mapped from the present study.

- The artificial neural network models were compared based on the performance, and the ANN_2H10_FA model was identified as the best architecture model.
- The performance of the ANN_2H10_FA model was compared with other AI models, and the GPR_FA model was identified as the optimum performance model.
- The GPR_FA model was predicted percentage of FA approximately equal to the actual percentage of FA.
- The GPR_FA model outperformed the other proposed AI model in the present research work, and it was also observed that the GPR_FA model performs better for small datasets than ANN.
- The present study shows that Gaussian process regression AI approach can predict the suitable percentage of fly ash for achieving the desired geotechnical properties of BC soil.

References

1. Arora KR (2004) Soil mechanics and foundation engineering, 6th edn. Standard Publisher Distributors, New Delhi, India
2. Ji-ru Z, Xing C (2002) Stabilization of expansive soil by lime and fly ash. J Wuhan Univ Technol 17(4):73–77
3. Edil TB, Acosta HA, Benson CH (2006) Stabilizing soft fine-grained soils with fly ash. J Mater Civ Eng 18(2):283–294
4. Hakari UD, Puranik SC (2012) Stabilization of black cotton soil using fly ash, Hubballi-Dharwad municipal corporation area, Karnataka, India. Global J Res Eng Civil Struct Eng 12(2)
5. Mehta A, Parate K, Ruprai BS (2013) Stabilization of black cotton soil by fly ash. International journal of application or innovation in engineering and management, special issue for national conference on recent advances in technology and management for integrated groth
6. Karthik S, Ashok KE, Gowtham P, Elango G, Gokul D, Thangaraj S (2014) Soil stabilization by using fly ash. IOSR J Mech Civil Eng 10(6):20–26
7. Rajak TK, Pal SK (2015) CBR values of soil mixed with fly ash and lime. Int J Eng Res Technol 4(2):763–768
8. Pallavi PT, Poorey PD (2016) Stabilization of black cotton soil using fly ash and Nylon fibre. Int Res J Eng Technol 3(11):1283–1288
9. Vahdani M, Ghazavi M, Roustaei M (2020) Prediction of mechanical properties of frozen soils using response surface method: an optimization approach. Int J Eng 33(10):1826–1841
10. Premarathne RPPK, Sawangsuriya A (2021) Prediction of unconfined compressive strength of cement stabilized pavement materials. In: International conference on road and airfield pavement technologies 2019, 10–12 July 2019, Malaysia, IOP Publishing, IOP Conference series: materials science and engineering, vol 1075, p 012008
11. Onyelowe KC, Bui Van D (2018) Predicting strength behaviour of stabilized lateritic soil-ash matrix using regression model for hydraulically bound materials purposes. Chin Soc Pavement Eng 11:875–887
12. Ahmed BS, Gadouri H, Ghrici M, Harichane K (2018) Best-fit models for predicting the geotechnical properties of FA-stabilise problematic soils used as materials for earth structures. Int J Pavement Eng 21(7):939–953
13. Rashidi M, Ashtiani RS, Si J, Izzo RP, McDaniel M (2018) A practical approach for the estimation of strength and resilient properties of cementitious materials. Transp Res Rec 2672(52):1–12
14. Sas W, Margielski J, Gluchowski A (2013) Estimation of mechanical properties of soil stabilized by hydratized lime addition, Annals of Warsaw University of Life Sciences—SGGW. Land Reclam 45(1):27–39
15. Shi X, Liu Q, Lv X (2012) Application of SVM in predicting the strength of cement stabilized soil. Appl Mech Mater 160:313–317
16. Trivedi JS, Nair S, Iyyunni C (2013) Optimum utilization of fly ash for stabilization of subgrade soil using genetic algorithm. In: Chemical, civil and mechanical engineering tracks of 3rd Nirma University international conference, Ahmedabad, Procedia Engineering, vol 51, pp 250–258
17. Kodicherla SPK, Nandyala DK (2019) Influence of randomly mixed coir fibres and fly ash on stabilization of clayey subgrade. Int J Geo-Eng 10(3):1–13
18. Bin-Shafique S, Edil TB, Benson CH, Senol A (2003) Incorporating a fly ash stabilized layer into pavement design—case study, Geo engineering program, University of Wisconsin-Madison 1415 Engineering Drive, Madison, WI 53706
19. Sahoo JP, Sahoo S, Yadav VK (2010) Strength characteristics of fly ash mixed with lime stabilized soil, Indian geotechnical conference—2010, IGC Mumbai Chapter & IIT Bombay, 16–18 Dec 2010, pp 429–432
20. Murmu AL, Dhole N, Patel A (2017) Stabilization of black cotton soil for subgrade application using fly ash geopolymer. Road Mater Pavement Design 21(3):867–885

21. Kulkarni PP, Mandal JN (2017) Performance assessment of stabilized soil with fly ash-nano material mixes. J Geotech Transp Eng 3(2):35–46
22. Vukicevic M, Maras-Dragojevic S, Jockovic S, Marjanovic M, Pujevic V (2013) Research results of fine-grained soil stabilization using fly ash from Serbian electric power plants. In: Proceedings of the 18th international conference on soil mechanics and geotechnical engineering, Paris, vol 307, pp 3267–3270
23. Sahu BK, Piyo PM (2002) Improvement in strength characteristics of white Kalahari Sands by fly ash, 174783667
24. Ratna Prasad R, Drga Kumar N (2015) CBR and strength aspects of fly ash-granular soil mixtures. Int J Eng Res General Sci 3(4):943–953
25. Senol A, Bin-Shafique, Edil TB, Benson CH (2002) Use of class C fly ash for stabilization of soft subgrade. In: Fifth international congress on advances in civil engineering, istanbul technical university, Istanbul, Turkey, 25–27 Sep 2002
26. Mohanty MK (2015) Stabilization of expansive soil using fly ash, MTech thesis, Department of Civil Engineering, National Institute of Technology, Rourkela, Odisha
27. Maheshwari S, Goliya SS (2016) Stabilization of black cotton soil for pavement using fly ash and lime. Int J Eng Develop Res 4(3):603–607
28. Smith GN (1986) Probability and statistics in civil engineering: an introduction. Collins, London
29. Singhatiya S, Ghosh S (2018) Soil properties prediction using ensemble regression technique. Int J Innov Res Comput Commun Eng 6(11):8733–8739

Chapter 5
Effect of Sample Disturbance on Compressibility Parameters

Lamsani Rajkumar, P. Arti Sudam, and Madhav Madhira

Introduction

Geotechnical properties of soil samples estimated from laboratory tests suffer from inevitable disturbances. It is important to know the degree of disturbance and its impacts on soil properties in both study and practice. Sources of sample disturbance have been extensively studied by many authors such as Hvorslev [4], Kallstenius [5], International Group of Soil Sampling (1971), and The Sub-Committee on Soil Sampling (1981). All the authors have found that the sample disturbance occurs during sampling, handling, shipping, storage, extrusion, specimen preparation and laboratory test processes Nhuan [9] that subsequently results in reduction of moisture content, damage to soil structure due to remolding and change in stress state from anisotropic to isotropic condition Chai et al. [2].

Various studies have established that sample disturbance effects are more in case of soft cohesive soils with high degree of sensitivity affecting the engineering properties such as permeability, compressibility and shear strength Santagata and Germaine [11], Karlsson et al. [6], Clayton et al. [3]. The degree of disturbances needs to be quantified to make the laboratory test results correspond to true in situ conditions of soil mass. Nagaraj et al. [7] predicted in situ compression curve based on laboratory compression curve and gave a method to estimate the degree of disturbance.

L. Rajkumar (✉) · P. Arti Sudam · M. Madhira
VNR Vignana Jyothi Institute of Engineering and Technology, Hyderabad 500090, India
e-mail: rajkumar999.857@gmail.com

P. Arti Sudam
e-mail: artisudam_p@vnrvjiet.in

K. Muthukkumaran (eds.), *Soil Behavior and Characterization of Geomaterials*,
Lecture Notes in Civil Engineering 296, https://doi.org/10.1007/978-981-19-6513-5_5

Methodology

Schmertmann [12] approach of developing true in situ compression curve based on laboratory compression curves and Quigley and Thomson [10] undisturbed compression curve using X-ray method were presented by Nagaraj et al. [7]. The true in situ, so-called undisturbed compression curves presented by Nagaraj et al. [7], is considered in the present study (Fig. 5.1).

In Schmertmann approach, true in situ compression line up to the preconsolidation pressure was drawn parallel to the rebound line. Beyond the preconsolidation pressure, the true in situ compression line was drawn up to the point 0.42 times of initial void ratio on the virgin compression line.

Casagrande [1] and Sridharan et al. [14] methods were applied to these curves to estimate the preconsolidation pressures of true in situ, laboratory undisturbed soil samples. Settlements and settlement ratios were estimated for layers of 5 m, 10 m, 15 m, and 20 m thicknesses for true in situ and so-called undisturbed samples as

NC soil:

$$S = \frac{c_c}{1 + e_0} * \log\log\left(\frac{p_0' + q}{p_0'}\right) * H \tag{5.1}$$

For OC soil:

For $p_0' + q > p_c'$

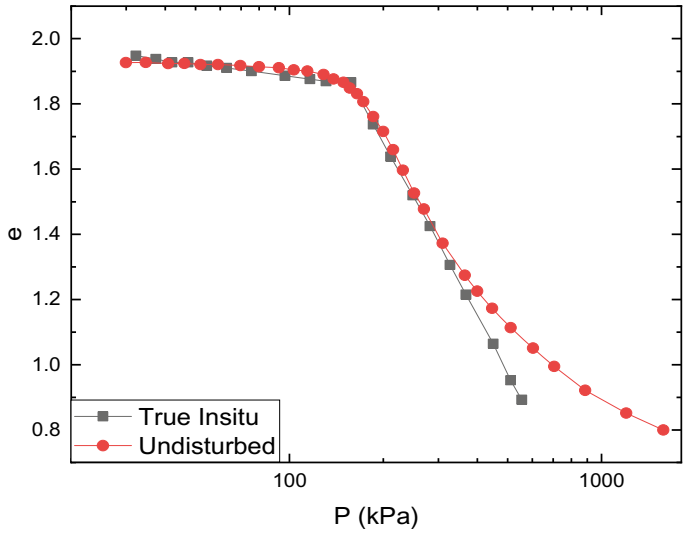

Fig. 5.1 e versus p—Schmertmann data

Table 5.1 Properties of soils from Schmertmann data

Thickness (m)	True——in situ				Undisturbed			
	5	10	15	20	5	10	15	20
p_0 (kPa)	23.63	39.07	54.52	69.97	23.63	39.07	54.52	69.97
c_s	*0.11*	*0.11*	*0.11*	*0.11*	*0.11*	*0.11*	*0.11*	*0.11*
c_c	*1.75*	*1.75*	*1.75*	*1.75*	*1.75*	*1.75*	*1.75*	*1.75*
p_c (kPa)	*159*	*159*	*159*	*159*	*155*	*155*	*155*	*155*
e_0	*1.95*	*1.95*	*1.95*	*1.95*	*1.95*	*1.95*	*1.95*	*1.95*
OCR	6.73	4.07	2.92	2.27	6.56	3.97	2.84	2.22

$$S = \frac{c_c}{1+e_0} * \log\log\left(\frac{p_0' + q}{p_c'}\right) * H + \frac{c_s}{1+e_0} * \log\log\left(\frac{p_c'}{p_0'}\right) * H \tag{5.2}$$

If $p_0' + q < p_c'$

$$S = \frac{c_s}{1+e_0} * \log\log\left(\frac{p_0' + q}{p_0'}\right) * H \tag{5.3}$$

where c_c is compression index, c_s—swelling index, p_c—preconsolidation pressure, e_0—initial void ratio, p'_0—effective overburden pressure, and q—the applied load.

Generally, preconsolidation pressure and overconsolidation ratio decrease with increase in disturbance. Preconsolidation pressure decreased to 155 kPa from 159 kPa (Table 5.1) for soil sample tested in the laboratory. Corresponding overconsolidation ratio also decreased, though the compression and swelling indices remain nearly the same for the true and the laboratory as predicted true in situ compression curve almost follows the laboratory compression curve (Fig. 5.2).

Quigley and Thomson [10] studied the so-called undisturbed compression curves using X-ray diffraction method and analysed sample disturbance effects of so-called undisturbed and remoulded soil samples and their behavior under different stresses. X-ray method was adopted on a block of sample from an open cut and observing soil particles orientation while performing consolidation tests at different stresses in case of both remoulded and so-called undisturbed soil samples. Nagaraj et al. [7] reworked on Quigley and Thomson [10] so-called undisturbed compression curve to get true in situ compression response.

Preconsolidation pressure decreased to 187 kPa from 230 kPa (Table 5.2) for the soil sample tested in the laboratory. Overconsolidation ratio decreased correspondingly. Swelling and compression indices reduced from 0.06 to 0.005 and from 1.04 to 0.71 for true in situ and undisturbed laboratory samples, respectively (Fig. 5.3).

Nagaraj et al. [7] approach neglects the compression up to the preconsolidated pressure in the field compression curve because of the cementing bonds between the soil particles. Beyond $\sigma_t = 10 * \sigma_c$, where σ_c is preconsolidation pressure, σ_t is equal to 10 times σ_c the field compression curve follows the rebound line. The field compression curve between σ_c and σ_t follows Eq. (5.1) where e_0 and e_t represent

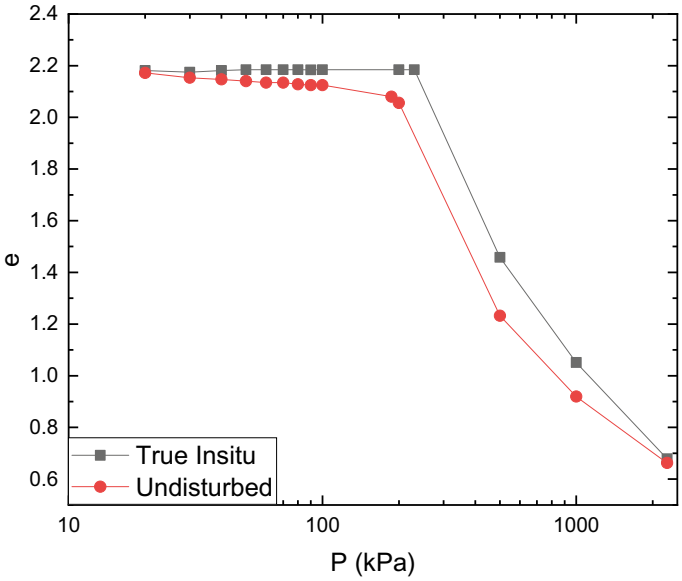

Fig. 5.2 e versus p—Nagaraj et al. approach for Quigley et al. Data

Table 5.2 Properties of soils—Nagaraj et al. Approach on Quigley et al. data

Thickness (m)	True in situ				So-called undisturbed			
	5	10	15	20	5	10	15	20
p_0 (kPa)	23.63	39.07	54.52	69.97	23.63	39.07	54.52	69.97
c_s	*0.005*	*0.005*	*0.005*	*0.005*	*0.06*	*0.06*	*0.06*	*0.06*
c_c	*1.04*	*1.04*	*1.04*	*1.04*	*0.71*	*0.71*	*0.71*	*0.71*
p_c (kPa)	*230*	*230*	*230*	*230*	*187*	*187*	*187*	*187*
e_0	*2.18*	*2.18*	*2.18*	*2.18*	*2.17*	*2.17*	*2.17*	*2.17*
OCR	9.73	5.89	4.22	3.29	7.91	4.79	3.43	2.67

void ratios at preconsolidation pressure and at σ_t, respectively.

$$e = A * (\log\log\sigma)^n + B \tag{5.4}$$

where A and B are constants, n obtained knowing conditions at (e_0, σ_c), (e_t, σ_t) and slope at σ_t. All the curves presented in Nagaraj et al. [7] are digitized and analysed. Preconsolidation pressure, compression index, swelling index, and overconsolidated ratio were estimated for the true in situ and the so-called undisturbed samples.

Preconsolidation pressure is 140 kPa in case of so-called undisturbed sample in contrast to 162 kPa for the true field in situ compression curve for Nagaraj et al. [7]

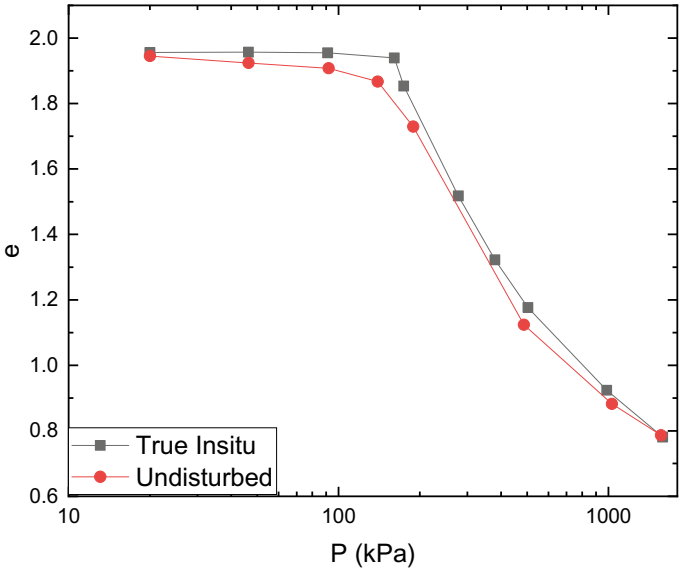

Fig. 5.3 *e* versus *p*—Nagaraj et al. approach

Table 5.3 Properties of soils—Nagaraj et al. [7] data

Thickness (m)	True in situ				So-called undisturbed			
	5	10	15	20	5	10	15	20
p_0 (kPa)	23.63	39.07	54.52	69.97	23.63	39.07	54.52	69.97
c_s	*0.02*	*0.02*	*0.02*	*0.02*	*0.09*	*0.09*	*0.09*	*0.09*
c_c	*0.87*	*0.87*	*0.87*	*0.87*	*0.74*	*0.74*	*0.74*	*0.74*
p_c (kPa)	*162*	*162*	*162*	*162*	*140*	*140*	*140*	*140*
e_0	*1.95*	*1.95*	*1.95*	*1.95*	*1.94*	*1.94*	*1.94*	*1.94*
OCR	6.86	4.15	2.97	2.32	5.93	3.58	2.57	2.00

data (Table 5.3). Compression and swelling indices are 0.87 and 0.74 and 0.02 and 0.09 for in situ and so-called undisturbed samples, respectively.

Results and Discussion

Settlement ratio (S_r):

Ratio of settlements based on parameters of so-called undisturbed and the true in situ samples is defined as

Table 5.4 Settlements for true in situ and so-called undisturbed sample for Schmertmann data

Load q (kPa)	True in situ settlements (cm), T				So-called undisturbed settlements (cm), U				Settlement's ratio U/T			
	Thickness (m)				Thickness (m)				Thickness (m)			
	5	10	15	20	5	10	15	20	5	10	15	20
50	9.20	13.34	15.81	17.46	9.20	13.34	15.81	17.46	*1.00*	*1.00*	*1.00*	*1.00*
100	13.40	20.56	25.30	60.96	13.40	20.56	25.30	73.26	*1.00*	*1.00*	*1.00*	*1.20*
150	26.77	67.36	123.29	193.83	29.85	73.51	132.52	206.13	*1.11*	*1.09*	*1.07*	*1.06*
200	59.37	127.81	207.82	299.37	62.45	133.96	217.04	311.67	*1.05*	*1.05*	*1.04*	*1.04*
50	9.20	13.34	15.81	17.46	9.20	13.34	15.81	17.46	*1.00*	*1.00*	*1.00*	*1.00*

$$S_r = S_{ud}/S_t \tag{5.5}$$

where S_{ud} and S_t are settlements based on undisturbed and true in situ soil parameters.

For Schmertmann [12] data, settlements based on true in situ and so-called undisturbed compression curves and the corresponding settlement ratios data are shown in Table 5.4. At 50 kPa loading, for all the strata thicknesses, S_r is 1.0 since the sum of effective overburden pressure and applied loading $(p'_0 + q)$ is less than preconsolidation pressure of both undisturbed (p_{cu}) and true in situ (p_{ci}) settlement cases where p_{cu} and p_{ci} are preconsolidation pressures of undisturbed sample and true in situ soil, respectively.

For loads from 50 to 100 kPa, S_r is estimated to be 1 (constant) for all layer thicknesses except 20 m as settlements are derived from the initial compression. In 20 m thick strata, loading from 50 to 100 kPa, S_r increases from 1.00 to 1.20 because $(p'_0 + q)$ is less than p_{ci} in the true in situ condition and $(p'_0 + q)$ is greater than p_{cu} in the so-called undisturbed condition. For loads from 150 to 200 kPa, the combination $(p'_0 + q)$ is greater than p_{cu} and p_{ci}. Therefore, for all thicknesses, the S_r is reduced from 150 to 200 kPa as settlements are more in virgin compression.

S_r for 200 kPa load is 1.05, 1.05, 1.04, and 1.04 (Table 5.4) for the strata thickness of 5 m, 10 m, 15 m, and 20 m, respectively, for Schmertmann [12] data. The results show that the predicted true in situ settlements differ only by 5% to 4% compared to those for so-called undisturbed sample.

Settlement ratios of true in situ and so-called undisturbed compression curves for Quigley and Thomson [10] data are presented in Table 5.5. Estimated the preconsolidation pressures are 230 kPa and 187 kPa for true in situ and so-called undisturbed sample, respectively. The settlements ratio for true in situ and so-called undisturbed sample for 5 m strata thickness for 150 kPa, 200 kPa, and 300 kPa loadings are 12.04, 22.42, and 1.41, respectively. S_r increased from 12.04 to 22.42 as at 200 kPa preconsolidation pressure (p_{cu}) was less than $(p'_0 + q)$ for so-called undisturbed sample. S_r was constant at 12.0 for strata thickness of 5 m from 50 to 150 kPa loading as $(p'_0 + q)$ was less than p_{cu} and p_{ci}. The settlement ratio variations with stress are presented in the Figs. 5.4, 5.5, and 5.6.

Table 5.5 Settlements of true in situ and so-called undisturbed sample for Quigley et al. data

Load q (kPa)	True in situ settlements (cm), T				So-called undisturbed settlements (cm), U				Settlement's ratio U/T			
	Thickness (m)				Thickness (m)				Thickness (m)			
	5	10	15	20	5	10	15	20	5	10	15	20
150	0.68	1.08	1.35	1.56	8.20	13.94	28.27	47.75	*12.04*	*12.95*	*20.87*	*30.52*
200	0.77	6.71	23.06	47.14	17.20	36.77	60.18	87.60	*22.42*	*5.48*	*2.61*	*1.86*
300	25.03	56.34	93.66	136.65	35.18	70.76	108.53	148.90	*1.41*	*1.26*	*1.16*	*1.09*

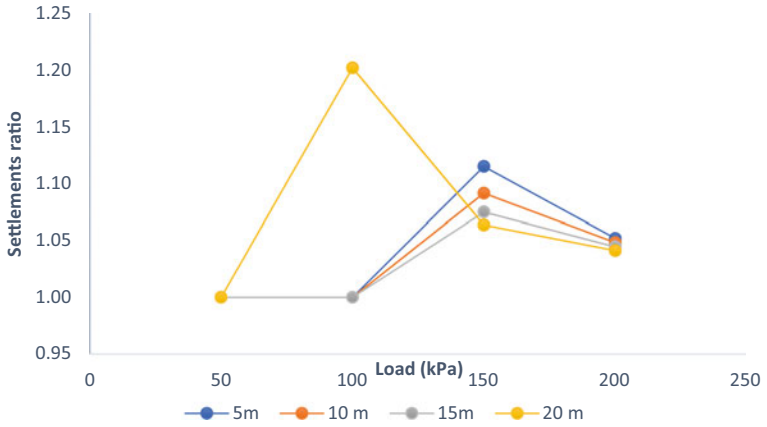

Fig. 5.4 Settlements ratio versus stress—effect of thicknesses for Schmertmann data

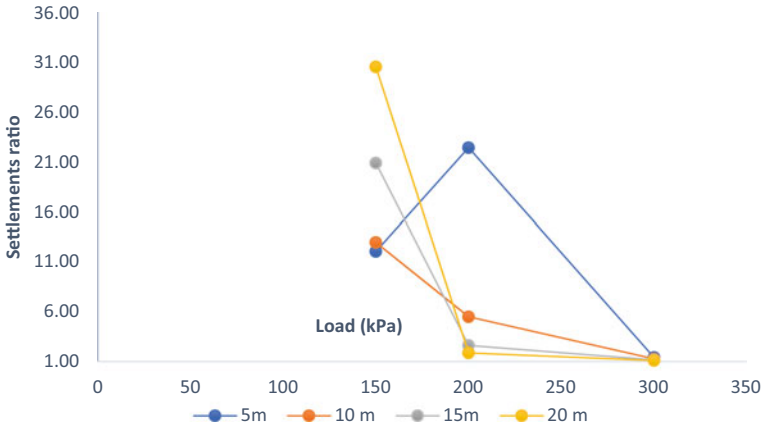

Fig. 5.5 Settlements ratio versus stress—effect of thickness for Quigley et al. data

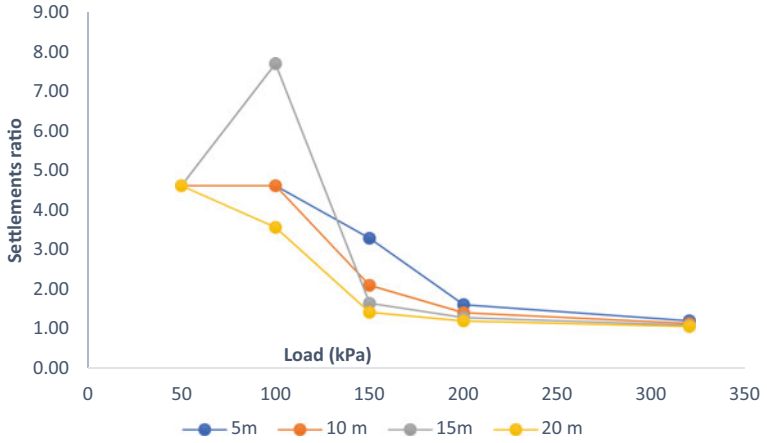

Fig. 5.6 Settlements ratio versus stress—effect of thickness for Nagaraj et al. data

For 300 kPa loading settlement ratios for 5 m, 10 m, 15 m, and 20 m are 1.41, 1.26, 1.16, and 1.09 respectively, indicating settlement of so-called undisturbed sample to be 9 to 41% higher than those for true in situ condition. For 200 kPa loading, S_r for 5 m, 10 m, 15 m, and 20 m thicknesses are 22.42, 5.48, 2.61 and 1.86 respectively.

For 200 kPa design load, so-called undisturbed sample settlement is estimated as 87.60 cm, whereas true in situ settlement is 47.17 cm. Settlement is overestimated by 1.86 times because of the sample disturbance.

Settlement ratios of true in situ and so-called undisturbed samples of Nagaraj et al. [7] data are presented in Table 5.6. Preconsolidation pressures are estimated as 162 kPa and 140 kPa for true in situ and so-called undisturbed sample, respectively. For 5 m strata thickness for 100 kPa, 150 kPa, and 200 kPa loadings, S_r is 4.62, 3.29, and 1.61, respectively. S_r for 5 m, 10 m, 15 m, and 20 m is 1.61, 1.41, 1.29, and 1.20 for 200 kPa loading, respectively. The overestimated settlements of so-called undisturbed sample range between 20 and 61%.

Settlement ratios for 5 m, 10 m, 15 m, and 20 m are 3.29, 2.10, 1.65, and 1.08 at 150 kPa loading respectively. Result confirms that the degree of disturbance overestimates the settlements if based on so-called undisturbed sample parameters.

Table 5.6 Settlements of true in situ and so-called undisturbed samples for Nagaraj et al. data

Load q (kPa)	True in situ settlements (cm), T				So-called undisturbed settlements (cm), U				Settlement's ratio U/T			
	Thickness (m)				Thickness (m)				Thickness (m)			
	5	10	15	20	5	10	15	20	5	10	15	20
100	2.44	3.74	4.60	17.18	11.25	17.25	35.41	61.26	*4.62*	*4.62*	*7.70*	*3.56*
150	7.25	23.88	49.37	82.92	23.86	50.19	81.37	117.64	*3.29*	*2.10*	*1.65*	*1.42*
200	23.38	53.79	91.18	135.13	37.69	75.84	117.24	162.41	*1.61*	*1.41*	*1.29*	*1.20*

Table 5.7 Degrees of disturbances for laboratory samples of Schmertmann, Quigley et al. and Nagaraj et al. data

Sample	Schmertmann data	Quigley et al. data	Nagaraj et al. data
The degree of disturbance for the laboratory undisturbed samples	2.51	18.69	13.75

Minimum sample disturbance gives the preconsolidation pressures and overconsolidation ratios of so-called undisturbed samples close to the true in situ values and settlement ratios close to unity. If sample disturbance is more, preconsolidation pressures and overconsolidation ratios of the so-called undisturbed samples differ significantly with the true in situ values. Settlement ratios are high for smaller applied loads proving that the settlement ratios are sensitive to the degree of sample disturbance (Table 5.7).

So-called undisturbed soil samples collected from block sampler experienced 10–35% of degree of disturbance. The degree of disturbance was less for the so-called undisturbed samples as per Schmertmann [12] approach as the predicted in situ compression curve is close to the so-called undisturbed compression curve.

Settlement ratios vs load plots of Schmertmann [12], Quigley and Thomson [10] and Nagaraj et al. [7], is presented in Figs. 5.4, 5.5, and 5.6, respectively.

Conclusions

Void ratio versus effective stress curves of so-called undisturbed soil samples is analysed to predict the true in situ behaviour by Nagaraj et al. [7] and Schmertmann [12] methods. Settlements are estimated for the so-called undisturbed samples and the predicted true in situ compression curves. Settlement ratios and degree of disturbance are estimated. Settlement ratio (S_r) is constant for the initial compression up to the preconsolidation pressure of so-called undisturbed sample (p_{cu}). If the sum of effective overburden pressure and the applied load is greater than the preconsolidation pressures of both the so-called undisturbed sample (p_{cu}) and the true in situ sample (p_{ci}), the settlement ratio (S_r) decreases with increase of applied stress. If the settlement ratio is more than unity, then the predicted settlements are higher than that of true settlements that are occurring at the site. If the settlement ratio is less than unity, then the settlements are underpredicting compared to the field settlements.

References

1. Casagrande A (1936) The determination of the preconsolidation load and its practical significance. In: Proceedings of 1st international conference on soil mechanics, vol 3. Cambridge, pp 60–64
2. Chai JC, Miura N, Zhu HH, Yudhbir A (2002) Compression and consolidation characteristics of structured natural clay. Can Geotech J 41(6):1250–1258
3. Clayton CRI, Hight DW, Hopper RJ (2002) Progressive destructing of Bothkennar clay implications for sampling and reconsolidation procedures. Can Geotech J 42(2):219–239
4. Hvorslev MJ (1949) Subsurface exploration and sampling of soils for civil engineering purposes. Report on a research project of ASCE, U.S. Army Engineer Experiment Station, Vicksburg, pp 1–57
5. Kallstenius T (1971) Mechanical disturbances on clay samples taken with piston sampler. Royal Swed Geotech Inst 16:1–74
6. Karlsson M, Emdal A, Dijkstra J (2002) Consequences of sample disturbance when predicting long-term settlements in soft clay. Can Geotech J 53(12):1965–1977
7. Nagaraj TS, Murthy BRS, Vatsala A, Joshi RC (1990) Analysis of compressibility of sensitive soils. J Geotech Eng 116(1):105–118
8. Nan J, Changming W, Wu Q, Li S (2002) Article influence of structure and liquid limit on the secondary compressibility of soft soils. J Marine Sci Eng 627(8):1–25
9. Nhuan BD (1981) The effect of sample disturbance on the geotechnical properties of soft clays. Swed Geotech Inst 69:1–54
10. Quigley RM, Thomson CD (1966) The fabric of anisotropically consolidated sensitive marine clay. Can Geotech J 3(1):61–73
11. Santagata MC, Germaine JT (2002) Sampling disturbance effects in normally consolidated clays. J Geotech Geoenviron Eng 128(12):997–1006
12. Schmertmann JH (1953) Estimating the true consolidation behavior of clay from laboratory test results. Trans Am Soc Civil Eng 118:311–1–311–25
13. Shogaki T, Kaneko M (2002) Effect of sample disturbance on strength and consolidation properties of soft clay. Jpn Soc Soil Mech Found Eng 36(3):1–10
14. Sridharan A, Abraham BM, Jose BT (1991) Improved technique for estimation of preconsolidation pressure. Geotechnique 41(2):263–268

Chapter 6
A Critical Review on Potential Use of Iron Ore Tailings as Structural Fill Material

S. Athira and Sridhar Gangaputhiran

Introduction

India, second largest populated country in the world whose economy relies mainly on three sectors, namely agriculture, industry and services. In the industry sector, mining is a core sector which drives Indian infrastructure development. Mining activities are crucial because of extensive mining and attraction to mining industries. Contribution of India in production of Iron ore was estimated around 206 million tonnes and was ranked 4th in the world ranking system according to British Geological Survey of World mineral production 2014–2018 [1]. Large quantity of mine waste has piled up in exploration, beneficiation, and extraction process of mineral ores. Because of advent of technologies, treatment of low-grade and complex ores has also piled up generating high volume waste in the country [2]. The characteristic of mine tailings depends upon the ore and varies according to minerals. They also depend on the physical and chemical process involved in the extraction of product. The tailings in its slurry form are disposed in a large structure called tailing dam or tailing storage facility (TSF) or also stored as backfill in underground at mined out voids, which helps in preventing subsidence [3]. Its disposal releases toxic heavy metals creating economic and environmental health issues to public [4]. Hence, it is very important to handle mine tailings and reduce its quantity by reusing effectively in engineering application. One of the potential ways to utilize them in large quantity is adopting it as a backfill material in structural fill which is an existing method, but still an under-utilized practice in our country. This paper highlights the review on mineralogical composition and current utilization of tailings in engineering application such as pavement, concrete, and retaining structures.

S. Athira (✉) · S. Gangaputhiran
Department of Civil Engineering, National Institute of Technology, Surathkal, Karnataka 575025, India
e-mail: athusatish@gmail.com

K. Muthukkumaran (eds.), *Soil Behavior and Characterization of Geomaterials*,
Lecture Notes in Civil Engineering 296, https://doi.org/10.1007/978-981-19-6513-5_6

Table 6.1 Production of iron ore tailing (IBM-statistical profile, 2018–19)

Parameter	2014–2015	2015–2016	2016–2017	2017–2018	2018–2019
Quantity (Th. tonnes)	129,321	158,108	194,584	201,426	206,446
Value (Rs.'000)	276,636,789	223,206,636	252,291,800	347,131,039	451,841,360

Iron Ore Waste and Tailings

Due to excessive usage and transportation, there is large-scale depletion of natural resource like sand creating environmental issues. Restriction is imposed on river sand quarrying and many sand mining industries have to look for alternative materials. To investigate for a better sustainable, easily available alternative for sand, research is needed [5].

Iron ores are types of rocks or raw material from which iron is extracted. 98% of extracted iron is converted to pig iron, which is an important constituent in manufacture of steel. According to Indian bureau of mines statistical report [6], India has total recoverable reserve of 22,487 million tonnes of hematite and 10,789 million tonnes of magnetite.

Yearly iron ore production is increasing, and with time, its resource will decline. Therefore, in future, iron ore tailings might be valuable resource. Production of iron ore tailings is shown in Table 6.1. Accumulation of mine waste takes place in each process of mining. Topsoil, overburden, waste rock, tailings, and processed leftover all come under the category of mine waste [7]. Figure 6.1 shows the schematic process of different mine waste generated at sites. Mine tailings get contaminated with lot of heavy metals; sulphur compounds can lead to environmental pollution if not properly handled [8]. Usual practice is to dispose these into tailing dam, which requires construction of dam in the vicinity of mine site to reduce transportation. But the location and site requirements are the major limitation. They are transported in slurry form, and it consolidates by own weight and get compacted, to form tailing dams [9]. Other than disposal options, tailings can be reused and recycled in various applications. Presently utilization of tailings can be categorized into two—recovery of iron from tailings and its use as a raw material. Due to depletion of high-grade iron ores, maximum utilization of low-grade ore is taking place. Many beneficiations processes have been applied to increase the Fe% in the ore. Broad classification of beneficiation methods involves mechanical separation and float flotation methods [10]. Lottermoser [11] has mentioned various reuse recycle option for tailings, processing waste, generate at mine sites.

State of the Art on Utilization of Iron Ore Tailings

The two prominent methods for mine wastes management or storage are dams and dumps, according to Blight [12]. Mine tailing impoundments and dam failures are

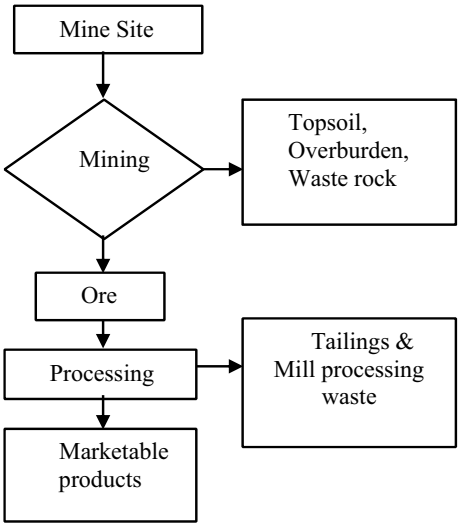

Fig. 6.1 Flowchart showing mine waste generation (BRGM [7])

very common, and many literatures have reported this [13, 14] as a cause due to the geotechnical behaviour of tailings. The Fundao dam failure in 2015 [15], Brumadinho dam disaster at Corrego do Feijao iron ore mine in 2019 [16] are the recent cases of catastrophic failures leading to human loss and environmental damage. These incidents created a renewed thoughts of urgency in society regarding the risk and failure potential associated with it.

Another approach of utilizing iron ore tailings (IoT) was seeking attention all over the world. It mostly includes land reclamation [17], recovery of iron, or other metals using modern technology [18–20], and as raw ingredients in construction material, backfilling materials, and fertilizers [21, 22].

Mineralogical Composition

The characterization of iron ore tailings differs greatly on the ore type, beneficiation process, and clay mineralogy. Therefore, a comprehensive analysis and testing is required before its application in structural fills. Iron ore tailings are finer material consisting of different chemical composition. Major minerals present are iron oxides (Fe_2O_3), silicon dioxide (SiO_2), alumina oxide (Al_2O_3), and other trace elements like oxides of Ca, Mg, P, Na, K, and S. Table 6.2 combines chemical composition of iron ore tailings from different literatures.

Detailed mineralogical study by Geremew 2013 has shown that tailings with high montmorillonite content showed greater resistance to cyclic loading than with kaolinite mineral [26]. The grain size distribution from different studies clearly shows that tailings generally come under silty sand classification, where more than 50%

Table 6.2 Chemical composition of iron ore tailings in percentage

SiO_2	Fe_2O_3	Al_2O_3	CaO	MgO	Na_2O	K_2O	SO_3	Reference
75.46	12.61	1.65	1.70	1.75	0.32	0.34	0.10	[23]
40.77	18.51	19.06	7.06	5.51	2.48	0.56	0.67	[24]
69.52	8.13	7.44	4.14	3.72	1.38	1.97	0.03	[25]

Table 6.3 Grain size distribution of iron ore tailings from literatures

Sand (%)	Silt (%)	Clay (%)	Reference
53.6	42.6	3.5	[27]
70.5	6.5		[28]
80	–		[29]
82.2	2.7		[30]

sand with very few percentages of clay. Table 6.3 shows grain size distribution of iron ore tailings from different studies. Lime and clay minerals are found in minimal amount, which makes it often cohesionless and granular, suitable for structural fill.

MSE Wall and Embankment

MSE wall has been a choice of retaining structures in many applications, and the most critical criteria are selection of backfill material and reinforcement. The criteria for backfill selection be it natural or recycled materials are established by regulatory agencies like American association of state highway and transport officials (AASHTO), federal highway administration (FHWA), and state department of transportation (DOTs) [31]. For long-term performance of wall, the reinforced fill must have high hydraulic conductivity to percolate water. The mechanical stability of wall depends on mechanical property of backfill possessing adequate friction angle to withstand the horizontal pressure imposed by soil mass. The excessive demand for granular soil makes construction expensive these days and identification of alternative, cheaper fill material is essential.

Iron ore tailings as structural fill in embankments and MSE wall has capacity to utilize them in large quantity and reduce its generation in state. Various geotechnical tests have been conducted to determine the shear strength parameters on iron ore tailings and also to obtain correlations with respect to other geotechnical parameters According to FHWA regulations, direct shear or triaxial testing is done to find the frictional angle. Das [32] considers triaxial setup as one of the reliable methods of finding sear parameters. Presotti [33] worked on four different samples of iron tailing from Agua Limpa Mine for which frictional angle was obtained in range of 35°–36°.

To study the fundamental geotechnical behaviour of tailings and to obtain data for scientific design, many literatures have studied the behaviour of coarse and fine

tailing. The coarse iron and copper tailings showed almost same values of frictional resistance and cohesion, whereas shear strength property of fines iron tailings was smaller to copper tailings [34]. The shear strength parameters required to meet the criteria can be enhanced by addition of various additives to iron ore tailing. The shear strength of lateritic soil improved with 8% optimal blend of iron ore tailings and was favourable in embankment application [35]. Addition of lime to iron tailing powder increased the shear energy dissipation which further enhanced the frictional force between iron ore tailing particles from 34.7° to 42.7° at 8–10% lime content [36]. On a similar trend, addition of polypropylene fibre enhanced the interfacial shear strength of iron tailing [37]. For the design of any MSE wall, FHWA [38] suggests to use maximum frictional angle value as 34° and never use design frictional value greater than 40°, even if measured value is higher.

Permeability characteristics of iron ore tailings are yet another important factor to be looked for stability aspect. It is affected by the amount of fine content and 40% was found to be the threshold value, i.e. coefficient of permeability started decreasing as fine content increased up to 40% and beyond 40% the coefficient of permeability tends to be stable [39]. Kudremukh iron ore tailings have coefficient of permeability of 0.011 cm/sec [40]. Study by Liming Hu reported average permeability of coarse iron ore tailings as 1×10^{-4} cm/sec. Permeability of fine iron tailing was around 1×10^{-5} to 1×10^{-6} cm/sec, which was greater than fine oil sand tailings from Wong et al. [41]. This depicted that metal tailing showed larger hydraulic conductivity compared to organic tailing [34]. According to FHWA, permeability is affected by amount of fine. If the soil has less than 3–5% fines, it is considered as freely draining material else proper drainage must be incorporated with soil in order to decrease the built up of pore pressure within reinforced soil mass [38]. The environmental feasibility of iron ore tailings by leaching and dissolution analyses has reported it as a class II-A non-dangerous and non-inert material [42]. Tailings from primary iron extraction processes have reported it as a non-hazardous inorganic solid waste [43].

To consider the usage of mine tailings in the embankment construction, the tailings can be blended with the other additives like fly ashes and cement. This enhances compaction characteristics and lowers the permeability of the entire mixture which fits its usage for the embankment construction. The effect of iron ore tailings on compaction properties of black cotton soil and lateritic soil improved with addition 8–10% iron ore tailings [44]. Iron ore tailing treated with 5% cement improved the bearing capacity, determined by California bearing ratio test, by 140% [45]. According to SUDAS, 2011 for subgrade, highway, and railway embankments, the compaction properties must have 95% proctor density with over 4% moisture content. For the strength and stability aspect, the soil should have CBR more than 10% [46]. These parameters are found based on ASTM standards and are considered to be good with heavy loading support capacity without any excessive deformation. Figure 6.2 shows a schematic view of embankment construction using mine waste according to Kuranchie [47].

Study was conducted to understand the mine waste behaviour subjected to uniformly distributed load. Retaining walls are constructed as model set up with mine waste as alternative fill along with bamboo reinforcement and steel grid fascia.

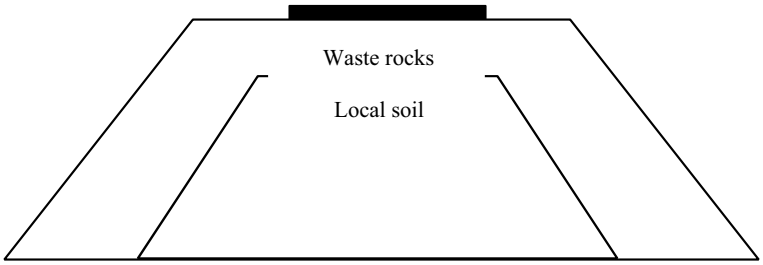

Fig. 6.2 Schematic view of embankment construction using mine waste [47]

For reinforcement of length 0.3 H, load at failure increased by 61.99% [48]. Similarly, to understand the load-settlement behaviour of strip footing resting on IoT as structural fill, model testing was done. Compared to local perth sand, tailing fill had 22 times the load bearing capacity and 13.5 times the stiffness [49].

From the above review, it can identify that iron ore tailings produced in large quantity in the country have limited application as structural fill in retaining structures. Fly ash was extensively considered in studies as alternate fill from early periods. Recent studies on coal wash, steel slag, compacted ash, and its combination are also worked out by researchers [50–52]. The characterization of iron ore tailings could satisfy most of the geotechnical design requirement for structural fill [53, 54].

Concrete and Pavements Applications

Another prominent method of minimizing the effect of iron ore tailings is utilizing it as backfill in pavements and ingredient in concrete. Concrete by volume comprises of 70% aggregate, which include both coarse and fine aggregate. Iron ore tailings can be considered as fully or partial replacement for natural aggregates, and parallelly, the scarce resources are protected by providing sustainable solution to handle tailings. The process of extraction and beneficiation of iron ore leads to particle size ranging from coarse to fine [55]. If they are segregated properly, both fine and coarse aggregate can be effectively obtained and utilized accordingly.

Presence of silica along with oxides of iron, alumina, and other trace minerals indicates their potential as aggregate for mortar and concrete [56, 57]. 100% replacement of fine aggregate with iron ore tailings drastically reduced the workability and compressive strength of concrete [58], whereas the mechanical behaviour of tailing mix was similar to control mix when replacement was up to 40%. Concrete with 50% iron ore tailings showed maximum compressive strength of 37.7 MPa at 28 days and flexural strength showed 17% improvement [59]. Technical feasibility of tailings as pavement material classified the material as class II A-not dangerous and not inert and was found to be more effective once chemically stabilized with cement [60]. When durability aspect of the concrete was studied using compressive strength test

under different curing period, 25% replacement of iron ore tailing with fine aggregate was considered as optimum and showed 13% improvement in compressive strength [61].

Many literatures have shown that the mine tailings stabilized with other additives were suitable for road construction. Bastos et al. 2016 used iron ore tailings stabilized with steel slag, cement, and lime. It showed that 5% cement was necessary to match the strength requirement for base course material for any traffic load and 7% lime with seven-day curing was needed for average traffic load. Slag additive was not recommended for subbase layer. Ojuri et al. [62] mixed iron tailings with lateritic soil and found that increase in tailing content improved the quality of soil for subgrade material. MDD increased and OMC decreased with addition of lime–cement binder to it. 8% binder with 30% tailing were found suitable satisfying the codes and environmental evaluation. The Golgohar mine tailings were stabilized with cement and bentonite for road construction. 10 and 15% cement were needed to satisfy the strength requirement for rigid and flexible pavement as base course layer [63]. IoT played a significant contribution as major constituent in subbase layer in pavements and significantly improved the structural behaviour of Brazilian tropical soil [64]. 8% iron ore tailings and lime were recommended for subbase material on black cotton soil. Leaching potential of iron from the mixture falls within the permissible value of not greater than 0.3 mg/l as per WHO [65].

Conclusion

With the advent of sustainability concepts integrated to engineering practices, it has become critical to develop a long-term sustainable structures with the use of waste materials which otherwise is detrimental to the environment. The paper mainly focused on application of tailings in engineering practices namely in mortars, concrete, pavements, and retaining structures. Experimental research on 100% replacement of fine aggregate with iron ore tailing in concrete has shown reduced workability and compressive strength. 25–50% partial replacement has shown significant improvement on compressive strength of concrete. Iron ore tailing stabilized with 5–15% of other additives such as cement and lime is found to be suitable for subbase and base layers in pavements. Structural fill could be the best application where huge quantity of tailing can be utilized. Even though few literatures have shown iron ore tailing as suitable material for structural fill, detailed research on its material and engineering behaviour is required in its comprehensive utilization.

References

1. World mineral production data compiled from World Mineral Production, 2014–2018. Brit Geol Surv
2. Mudd GM (2004) One Australian perspective on sustainable mining: declining ore grades and increasing waste volumes. In: Proceedings of the 11th international conference on tailings and mine waste'04. pp 359–369
3. Chapter 4.5 Mine wastes management.pdf
4. Tayebi-Khorami M, Edraki M, Corder G, Golev A (2019) Re-thinking mining waste through an integrative approach led by circular economy aspirations. Minerals 9(5):286
5. Bederina M, Makhloufi Z, Bounoua A, Bouziani T, Quéneudec M (2013) Effect of partial and total replacement of siliceous river sand with limestone crushed sand on the durability of mortars exposed to chemical solutions. Constr Build Mater 47:146–158
6. IBM (2002) Statistical profiles of minerals 2018–2019. Indian Bureau of Mines, Ministry of Mines, Government of India, Issued by Controller General, p 35: 11–16; 76: 23–24
7. BRGM (2001) Management of mining, quarrying, ore processing wastes in the European Union. p 79, RP-50319-F
8. Walsichuk M (1978) Disposal of mine wastes into the sea. Mar Pollut Bull (United Kingdom) 9(6)
9. Wills BA, Finch JA (2016) Chapter 16—tailings disposal, wills' mineral processing technology 8th edn. Butterworth-Heinemann, pp 439–448
10. Sahin R (2020) Beneficiation of low/off grade iron ore: a review. Int J Res-Granthaalayah 8(8):328–335
11. Lottermoser BG (2011) Recycling, reuse and rehabilitation of mine wastes. Elements 7(6):405–410
12. Blight G (2009) Geotechnical engineering for mine waste storage facilities. CRC Press, Taylor & Francis Group
13. Azam S, Li Q (2010) Tailings dam failures: a review of the last one hundred years. Geotech News 28(4):50–54
14. Rico M, Benito G, Salgueiro AR, Díez-Herrero A, Pereira HG (2008) Reported tailings dam failures: a review of the European incidents in the worldwide context. J Hazard Mater 152(2):846–852
15. do Carmo FF, Kamino LHY, Junior RT, de Campos IC, do Carmo FF, Silvino G, Mauro ML, Rodrigues NUA, de Souza Miranda MP, Pinto CEF (2007) Fundão tailings dam failures: the environment tragedy of the largest technological disaster of Brazilian mining in global context. Perspect Ecol Conserv 15(3):145–151
16. Rotta LHS, Alcantara E, Park E, Negri RG, Lin YN, Bernardo N, Mendes TSG, Souza Filho CR (2020) The 2019 Brumadinho tailings dam collapse: possible cause and impacts of the worst human and environmental disaster in Brazil. Int J Appl Earth Obs Geoinf 90:102119
17. Maiti SK, Nandhini S, Das M (2005) Accumulation of metals by naturally growing herbaceous and tree species in iron ore tailings. Int J Environ Stud 62(5):593–603
18. Yu J, Han Y, Gao P, Li Y, Yuan S, Li W (2018) An innovative methodology for recycling iron from magnetic preconcentrate of an iron ore tailing. Physicochemical Probl Miner Process 54
19. Rao KH, Narasimhan KS (1985) Selective flocculation applied to Barsuan iron ore tailings. Int J Miner Process 14(1):67–75
20. Li C, Sun H, Bai J, Li L (2010) Innovative methodology for comprehensive utilization of iron ore tailings: part 1. The recovery of iron from iron ore tailings using magnetic separation after magnetizing roasting. J Hazard Mater 174(1–3):71–77
21. Zhang SH, Xue XX, Liu X, Duan P, Yang H, Jiang T, Wang D, Liu R (2006) Current situation and comprehensive utilization of iron ore tailing resources. J Min Sci 42(4):403–408
22. Borges PHR, Ramos FCR, Caetano TR, Panzerra TH, Santos H (2019) Reuse of iron ore tailings in the production of geopolymer mortars. REM-Int Eng J 72:581–587
23. Tang C, Li K, Ni W, Fan D (2019) Recovering iron from iron ore tailings and preparing concrete composite admixtures. Minerals 9(4):232

24. Peng L, Jiao BQ, Xu GJ, Huang X (2015) Research on stimulating the activity of the iron tailings by alkali fusion. Mater Res Innovations 19(sup8):S8-237
25. Huang X, Ranade R, Li VC (2013) Feasibility study of developing green ECC using iron ore tailings powder as cement replacement. J Mater Civ Eng 25(7):923–931
26. Geremew AM, Yanful EK (2013) Dynamic properties and influence of clay mineralogy types on the cyclic strength of mine tailings. Int J Geomech 13(4):441–453
27. Costa G, Villar LF (2021) Obtaining resistance parameters in iron ore tailing from field (SPT and CPTu) and laboratory tests. In: MATEC web of conferences, vol 337. EDP Sciences, p 04011
28. Kuranchie FA, Shukla SK, Habibi D (2015) Electrical resistivity of iron ore mine tailings produced in Western Australia. Int J Min Reclam Environ 29(3):191–200
29. Sreekutty S, Jacob K Experimental study on iron ore tailings and bottom ash as fine aggregates in concrete
30. Moreira DDC, dos Santos CAS, Mesquita ALA, Moreira DC (2020) Influence of particle size distribution of iron ore fines on liquefaction during marine transportation. Powder Technol 373:301–309
31. Vibha S, Divya PV (2020) Mechanically stabilized earth walls with alternate backfills for highway structures. In: Conference: international conference on geoenvironment and sustainability, pp 229–236
32. Das BM (2011) Geotechnical engineering elements. Thomson learning, 6th edn. São Paulo, SP
33. Presotti ES (2002) The iron content influence on iron ore tailings resistance parameters. M.Sc. essay, UFOP, Ouro Preto, MG, Brasil
34. Hu L, Wu H, Zhang L, Zhang P, Wen Q (2017) Geotechnical properties of mine tailings. J Mater Civ Eng 29(2):04016220
35. Ishola K, Ijimdiya TS, Yohanna P, Osinubi KJ (2020) Evaluation of shear strength of compacted iron ore tailings treated lateritic soil. Platform: J Eng 4(3):48–58
36. Jiang P, Qiu L, Li N, Wang W, Zhou A, Xiao J (2018) Shearing performance of lime-reinforced iron tailing powder based on energy dissipation. Adv Civ Eng 2018
37. Jiang P, Lv S, Wang Y, Li N, Wang W (2019) Investigation on direct shear and energy dissipation characteristics of iron tailings powder reinforced by polypropylene fiber. Appl Sci 9(23):5098
38. Berg RR, Christopher BR, Samtani NC (2009) Design and construction of mechanically stabilized earth walls and reinforced soil slopes–volume I. Federal High Way Administration (FHWA)
39. Gan D, Yang X, Zhang Y (2019) Experimental analysis on permeability characteristics of iron tailings. Math Probl Eng
40. Savaraja HG (2020) Synthesis of Kudremukh iron ore tailing based geopolymer coarse aggregate using fly-ash as precursor in the construction industry. i-Manager's J Civ Eng 10(3):1
41. Wong RCK, Mills BN, Liu YB (2008) Mechanistic model for one-dimensional consolidation behavior of nonsegregating oil sands tailings. J Geotech Geoenviron Eng 134(2):195–202. https://doi.org/10.1061/(ASCE)1090-0241
42. Fontes WC, Fontes GG, Costa ECP, Mendes JC, Silva GJB, Peixoto RAF (2018) Iron ore tailings in the production of cement tiles: a value analysis on building sustainability. Ambiente Construído 18:395–412
43. Pappu A, Saxena M, Asolekar SR (2007) Solid wastes generation in India and their recycling potential in building materials. Build Environ 42(6):2311–2320
44. Yohanna P, Sani RO, Ishola K, Ijimdiya TS, Eberemu AO, Osinubi KJ (2021) Effect of iron ore tailings on the plasticity and compaction properties of selected tropical soils. In: IOP conference series: materials science and engineering, vol 1036, no 1. IOP Publishing, 012040
45. de Oliveira TM, Generoso FJ, da Silva TO, Sant'Anna GL, de Carvalho Silva CH, Pitanga HN (2019) Geomechanical properties of mixtures of iron ore tailings improved with Portland cement. Acta Sci Technol 41:e38038–e38038
46. SUDAS (2011) Statewide urban design and specifications. www.iowasudas.org Accessed: 10th June 2012

47. Kuranchie FA (2015) Characterisation and applications of iron ore tailings in building and construction projects
48. Kandolkar SS, Mandal JN (2013) Behaviour of reinforced mine waste model walls under uniformly distributed loading. Electron J Geotech Eng 18:1351–1365
49. Kuranchie FA, Shukla SK, Habibi D, Kazi M (2016) Load–settlement behaviour of a strip footing resting on iron ore tailings as a structural fill. Int J Min Sci Technol 26(2):247–253
50. Indraratna B, Nutalaya P, Koo KS, Kuganenthira N (1991) Engineering behaviour of a low carbon, pozzolanic fly ash and its potential as a construction fill. Can Geotech J 28(4):542–555
51. Indraratna B, Gasson I, Chowdhury RN (1994) Utilization of compacted coal tailings as a structural fill. Can Geotech J 31(5):614–623
52. Prasad PS, Ramana GV (2016) Feasibility study of copper slag as a structural fill in reinforced soil structures. Geotext Geomembr 44(4):623–640
53. Chiaro G, Indraratna B, Tassalloti SMA, Rujikiatkamjorn C (2013) Optimisation of coal wash-slag blend as a structural fill. In: Ground improvement, final paper published online ahead of print, pp 1–12
54. Trivedi A, Sud VK (2007) Settlement of compacted ash fills. Int J Geotech Geol Eng 25(2):163–176
55. Kuranchie FA, Shukla SK, Habibi D (2016) Utilisation of iron ore mine tailings for the production of geopolymer bricks. Int J Min Reclam Environ 30(2):92–114
56. Yellishetty M, Karpe V, Reddy EH, Subhash KN, Ranjith PG (2008) Reuse of iron ore mineral wastes in civil engineering constructions: a case study. Resour Conserv Recycl 52(11):1283–1289
57. Da Silva FL, Araújo FGS, Teixeira MP, Gomes RC, Von Krüger FL (2014) Study of the recovery and recycling of tailings from the concentration of iron ore for the production of ceramic. Ceram Int 40(10):16085–16089
58. Zhao S, Fan J, Sun W (2014) Utilization of iron ore tailings as fine aggregate in ultra-high-performance concrete. Constr Build Mater 50:540–548
59. Shettima AU, Ahmad Y, Hussin MW, Muhammad NZ, Babatude OE (2018) Strength and microstructure of concrete with iron ore tailings as replacement for river sand. In: E3S web of conferences, vol 34. EDP Sciences, p 01003
60. Bastos LADC, Silva GC, Mendes JC, Peixoto RAF (2016) Using iron ore tailings from tailing dams as road material. J Mater Civ Eng 28(10):04016102
61. Shettima AU, Hussin MW, Ahmad Y, Mirza J (2016) Evaluation of iron ore tailings as replacement for fine aggregate in concrete. Constr Build Mater 120:72–79
62. Ojuri OO, Adavi AA, Oluwatuyi OE (2017) Geotechnical and environmental evaluation of lime–cement stabilized soil–mine tailing mixtures for highway construction. Transp Geotech 10:1–12
63. Barati S, Tabatabaie Shourijeh P, Samani N, Asadi S (2020) Stabilization of iron ore tailings with cement and bentonite: a case study on Golgohar mine. Bull Eng Geol Environ 79:4151–4166
64. Dantas AAN, Mendes TA, Posse AJA, Ribeiro LFM, Gurjão CMC (2017) Analysis of compaction and California Bearing Ratio (CBR) test results of a mixture of iron ore tailings with Brazilian tropical soil in different proportions for road construction purposes. In: Bearing capacity of roads, railways and airfields. CRC Press, pp 21–25
65. Etim RK, Eberemu AO, Osinubi KJ (2017) Stabilization of black cotton soil with lime and iron ore tailings admixture. Transp Geotech 10:85–95

Chapter 7
New Correlation System for Compressibility and Expansivity of Clays

S. Vijaya Raj and V. K. Stalin

Introduction

Of the civil engineering construction material, soil is unique in being a natural material, most often engineered, as it exists, unlike other processed material like concrete or steel. Hence, property characterization of the soil is an important aspect of geotechnical engineering practice. The determination of engineering properties of soil by testing often needs to be supported by predictions mainly because of two reasons. Firstly, the volume of soil that can be tested in any project within the time constraints and economical feasibilities is only a very small fraction of the total volume of soil involved. Secondly, the present-day construction practice is such that the cost savings for elaborate testing may be outweighed by savings in time by prediction with accuracy acceptable at engineered level. Studies has been made on compressibility and swelling characteristics of soil-bentonite mixtures [1]. Bain [2] developed a Plasticity chart to identify and assess the industrial clays and clay minerals. Manimegalai [3] analysed and predicted the compressibility, swelling and shear strength of soil available empirical correlations.

In the plasticity chart, the 'CH' type of soils most often would be high expansive in nature [4], even though higher initial water content leads to more compressibility on one side and lower initial water content leads to more swellability on the other side. Array of empirical correlation is available, independently, to predict the compressibility of fine-grained soils and swellability of expansive soils even though they coexist [4]. Hence, an attempt is made in this paper to correlate the compressibility and swell properties of six natural soils (LL varies from 62 to 73%) and synthesized soils (LL varies from 122 to 389%).

S. Vijaya Raj (✉) · V. K. Stalin
Division of Soil Mechanics and Foundation Engineering, Department of Civil Engineering, College of Engineering Guindy, Anna University, Chennai, Tamil Nadu, India
e-mail: vijayarajsvr42@gmail.com

K. Muthukkumaran (eds.), *Soil Behavior and Characterization of Geomaterials*, Lecture Notes in Civil Engineering 296, https://doi.org/10.1007/978-981-19-6513-5_7

Properties of Soils

The various natural soils are collected from Chennai area, i.e. West Mambalam, T. Nagar (1), T. Nagar (2), OMR near Indira Nagar, Velachery, and Thiruvanmiyur. Natural soils collected which exhibits extreme plasticity characteristics (low to very high). The soil samples collected was subjected to evaluation of index, engineering, and swelling properties. The same has been used for the chart relating compressibility and swellability. Commercially available expansive clay mineral, bentonite (LL = 350%), was used to prepare synthetic soils like clay mixing with non-clay (silt or sand) or kaolinitic clay of different properties such that they exhibits low to very high compressibility and also swellability. The liquid limits of natural soils varied from 62 to 73%. The plasticity index of natural soils varied from 42 to 50%. The differential free swell index of these soils varied from 150 to 330%. Based on the Indian Standard Soil Classification [5], the natural soils are classified as clay of high compressibility (CH) (Table 7.1).

As the liquid limits of natural soils collected fall less than 100%, synthetic soils (sodium bentonite + clay mixtures) and soil samples from various literatures were used for the purpose of new extended plasticity chart. In order to have soil whose liquid limit greater 100%, synthetic soils were used for the development of extended plasticity chart. For this purpose, commercially available sodium bentonite was selected whose liquid limit is 389%, plastic limit is 48%, and plasticity index is 341%. Sodium bentonite was mixed with the natural soils at certain amount of trial proportions varying from 22 to 28%, and thus, all the index and engineering properties of synthetic soils were obtained. The synthetic soils showed a drastic increase of the liquid limits and expansivity nature of the soil. This variation is because of differences in the liquid limit in respective natural soils. The liquid limits of synthetic soils are varied from 122 to 276%, and for the sodium bentonite, it was found to be 389%. The plasticity index of synthetic soils is varied from 82 to 226%, and for the sodium bentonite, it was found to be 341%. The differential free swell index of these synthetic soils varied from 387 to 566%, and for the sodium bentonite, it was found to be 911%. Based on Indian Standard Soil Classification [5], the synthetic soils are classified as clay of high compressibility (CH) (Table 7.2).

Table 7.1 Index and engineering properties of natural soils

Description	Soil 1	Soil 2	Soil 3	Soil 4	Soil 5	Soil 6
Liquid limit, W_L (%)	69	73	62	68	68	67
Plasticity index, I_P (%)	46	50	42	44	48	48
DFSI (%)	330	220	211	150	323	234
Classification (IS)	**CH**	**CH**	**CH**	**CH**	**CH**	**CH**
Compression index, (C_c)	0.40	0.41	0.32	0.42	0.45	0.36
% of swell or swell potential (S_P) in %	25.63	32.19	23.73	27.14	31.11	30.61
Swell pressure, (P_S) in kN/m^2	3.60	3.87	2.46	3.51	3.54	3.42

Table 7.2 Index and engineering properties of synthetic soils

Description	Bentonite (Na)	Soil 1 + 24% Na-B	Soil 2 + 28% Na-B	Soil 3 + 26% Na-B	Soil 4 + 22% Na-B	Soil 5 + 26% Na-B	Soil 6 + 28% Na-B
Liquid limit, W_L (%)	389	262	126	122	136	276	124
Plasticity index, I_P (%)	341	226	94	93	97	235	82
DFSI (%)	911	560	427	438	387	566	446
Classification (IS)	**CH**	**CH**	**CH**	**CH**	**CH**	**CH**	**CH**
Compression index, (C_C)	2.55	1.74	0.84	0.76	0.84	1.87	0.78
% of swell or swell potential (S_P) in %	321	206	92	91	95	225	81
Swellpressure, (P_S) in kN/m^2	16.32	10.43	4.24	4.10	4.68	11.22	4.12

Correlation Between Liquid Limit and Free Swell Index

A new correlation chart is made between liquid limit, W_L, and differential free swell index to classify or group the soils based on the swelling or the expansivity nature of the soils as shown in Fig. 7.1. From the relationship made between liquid limit, W_L, and differential free swell index, liquid limit ranges between 0 and 30% can be represented by the symbol NE—non-expansive clays, and for the liquid limit, ranges between 30 and 50% can be represented by the symbol ME—medium expansive clays, for the liquid limit, ranges between 50 and 100% can be represented by the symbol HE—highly expansive clays, and for the liquid limit, ranges 100% and above can be represented by the symbol VHE—very highly expansive clays.

Empirical Correlations

A number of correlations is made between liquid limit and swell pressure, liquid limit and swell potential, compression index and swell potential, compression index and swell pressure of natural soils which are presented in the following section. The liquid limit values corresponding to the respective swell pressure and swell potential values and the compression index values corresponding to the respective swell pressure and swell potential values of the collected natural soil are plotted in the chart. For getting the more accuracy in the empirical equations, more numbers of data are needed. For getting the approximation of all these values, the following general equation of straight-line was used to obtain the empirical equations.

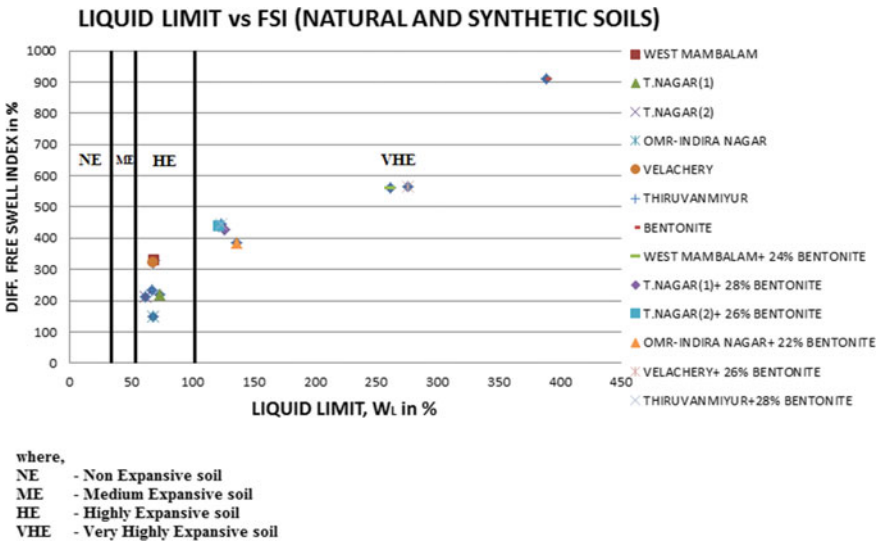

Fig. 7.1 Correlation chart for W_L and DFSI (a proposed chart)

$$y = mx + c \tag{7.1}$$

where

m	slope of the line
c	y intercept of the line (constant)
y and x	variables.

Correlation Between Liquid Limit and Swell Pressure

A correlation is made between liquid limit and swell pressure of natural and synthetic soils values as shown in Fig. 7.2. The liquid limit of the sodium bentonite is found to be 389%, and the corresponding swell pressure is 16.32 kN/m^2. The liquid limit of the natural and synthetic soils ranges between 62 and 262%, and the corresponding swell pressure values ranges between 2.46 kN/m^2 and 11.22 kN/m^2, respectively. From the correlation made between liquid limit (W_L) and swell pressure (P_S) for the natural and synthetic soils, the following empirical equation is developed.

$$P_S = 0.0392\ W_L + 0.2865 \tag{7.2}$$

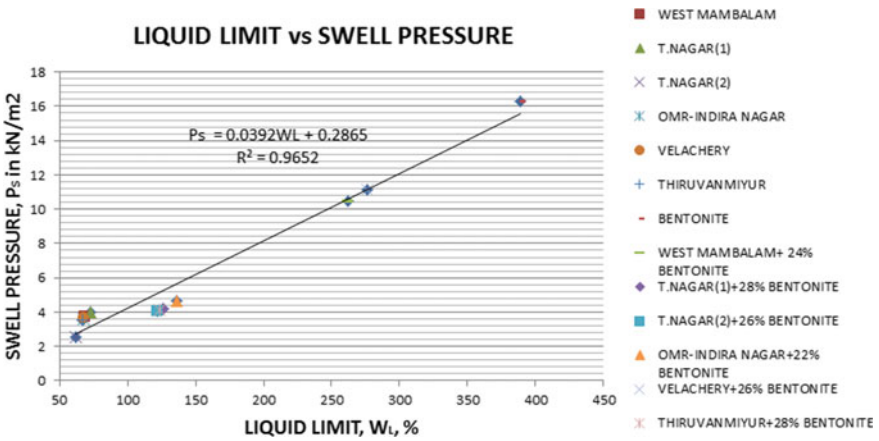

Fig. 7.2 W_L and P_S relationship for natural and synthetic soils

Correlation Between Liquid Limit and Swell Potential

A correlation is made between liquid limit and swell potential of natural and synthetic soils as shown in Fig. 7.3. The liquid limit of the sodium bentonite is found to be 389%, and the corresponding swell potential is 321%. The liquid limit of the natural and synthetic soils ranges between 62 and 262% and the corresponding swell potential values ranges between 23.73% and 225%, respectively. From the correlation made between liquid limit (W_L) and swell potential (S_P) for the natural and synthetic soils, the following empirical equation is developed.

$$S_P = 0.9791\ W_L - 35.316 \tag{7.3}$$

Correlation Between Compression Index and Swell Potential

A correlation is made between compression index and swell potential of natural and synthetic soils as shown in Fig. 7.4. The compression index of the sodium bentonite is found to be 2.55, and the corresponding swell potential is 321%. The compression index of the natural and synthetic soils ranges between 0.32 and 1.74, and the corresponding swell potential values range between 23.73% and 225%, respectively. From the correlation made between compression index (C_C) and swell potential (S_P) for the natural and synthetic soils, the following empirical equation is developed.

$$S_P = 141.09\ C_C - 27.903 \tag{7.4}$$

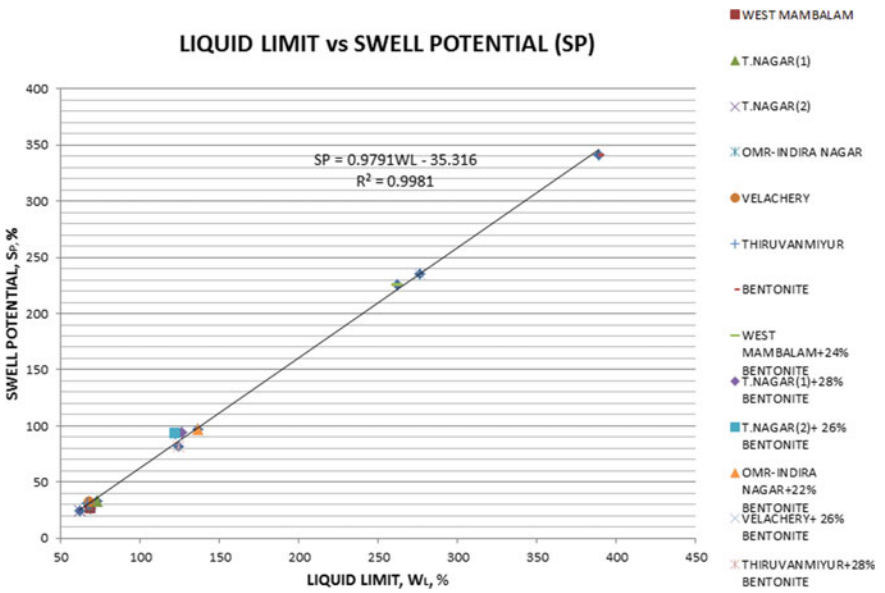

Fig. 7.3 W_L and S_P relationship for natural and synthetic soils

Correlation Between Compression Index and Swell Pressure

A correlation is made between compression index and swell potential of natural and synthetic soils as shown in Fig. 7.5. The compression index of the sodium bentonite is found to be 2.55, and the corresponding swell pressure is 16.32 KN/m^2. The compression index of the natural and synthetic soils ranges between 0.0.32 and 1.74, and the corresponding swell pressure values ranges between 2.46 kN/m^2 and 11.22 kN/m^2, respectively. From the correlation made between compression index (C_C) and swell pressure (P_S) for the natural and synthetic soils, the following empirical equation is developed.

$$P_S = 5.669\ C_C + 0.5711 \tag{7.5}$$

Conclusions

Based on the analysis of liquid limit, differential free swell index, compression index, swell pressure and swell potential of different natural soils, synthetic soils, and data collected from literature, the following conclusions are drawn.

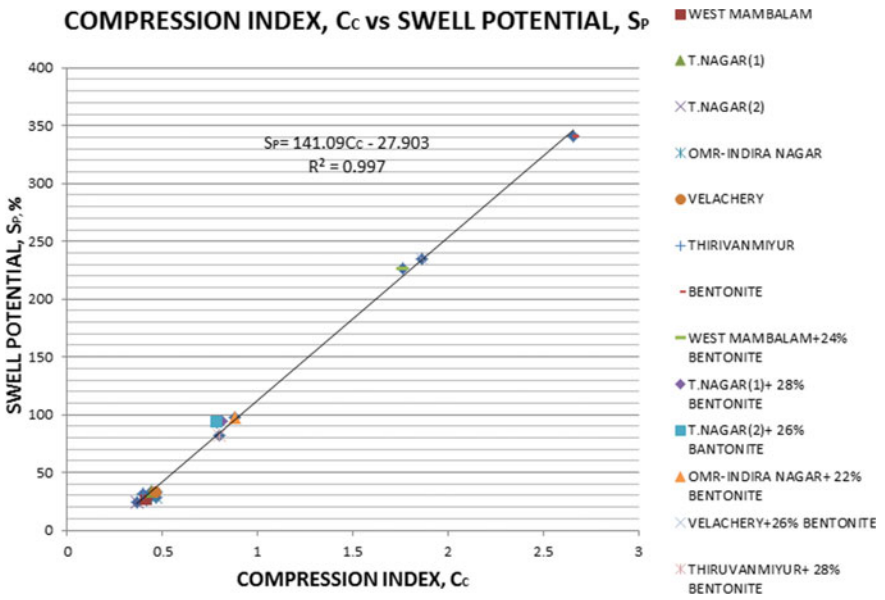

Fig. 7.4 C_C and S_P relationship for natural and synthetic soils

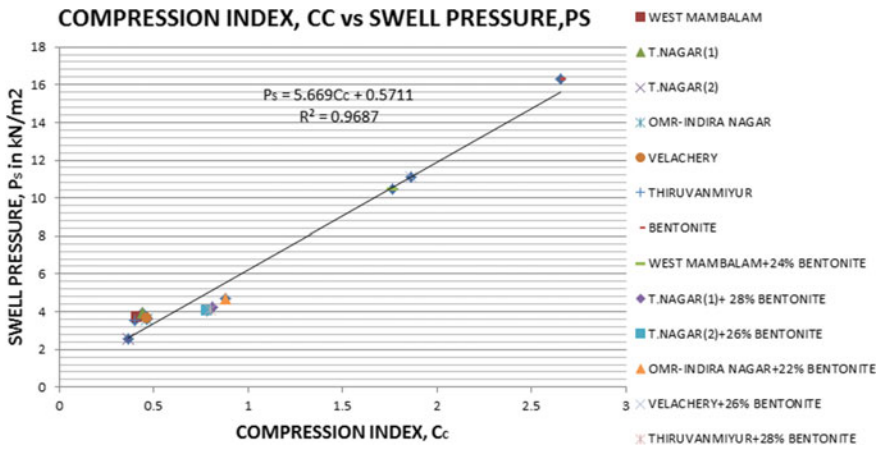

Fig. 7.5 C_C and P_S relationship for natural and synthetic soil

1. Based on the correlation chart developed between liquid limit, W_L and differential free swell index, the following classification symbols are proposed.

   (i) Liquid limit, W_L, between 0 and 30% is classified by a symbol **NE—**non-expansive soil.

(ii) Liquid limit, W_L, between 30 and 50% is classified by a symbol **ME**—medium expansive soil.
(iii) Liquid limit, W_L, between 50 and 100% is classified by a symbol **HE**—highly expansive soil.
(iv) Liquid limit, W_L, more than 100% is classified by a symbol **VHE**—very highly expansive soil.

2. The following empirical equations are proposed based on the index and swell properties of various soils.

(i) A correlation made between liquid limit, W_L, and swell pressure, P_S, is

$$P_S = 0.0392\ W_L + 0.2865$$

(ii) A correlation made between liquid limit, W_L, and swell potential, S_P, is

$$S_P = 0.9791\ W_L - 35.316$$

(iii) A correlation made between compression index, C_C, and swell pressure, P_S, is

$$P_S = 5.669\ C_C + 0.5711$$

(iv) A correlation made between compression index, C_C, and swell potential, S_P,
is

$$S_P = 141.09\ C_C - 27.903$$

where
W_L—Liquid limit, %
P_S—Swell pressure, kN/m^2
S_P—Swell potential, %
C_C—Compression index.

References

1. Muntohar AS (2003) Swelling and compressibility characteristics of soil—bentonite mixtures, Jurusan Teknik Sipil, Fakultas Teknik Sipil dan Perencanaan—Universitas Kristen Petra, Dimensi Teknik Sipil 5(2):93–98
2. Bain JA (1970) A plasticity chart as an aid to the identification and assessment of industrial clays, clay minerals group and the basic science section of the British ceramic society. Clay Miner 9(1):1–17

3. Manimegalai S (2008) Analysis of empirical correlations for the prediction of compressibility, swelling and shear strength of soil. M.E. thesis submitted to Anna University, Chennai
4. Das B M (2016) Principles of Geotechnical Engineering Cenage learning, USA
5. Indian Standards (Reaffirmed 2006) Classification and identification of soils for general engineering purposes, IS 1498–1970

Chapter 8
Analysis of Particle Breakage for Blasted Rockfill Material Under Large Size Triaxial Testing

Uday Bhanu Chakraborty, Sandeep Dhanote, and N. P. Honkanadavar

Introduction

Rockfill dams are reasonably accepted because of the flexibility of rockfill material, ability to soak up high seismic energy, and pliability to any foundation circumstances, and the rockfill dam also can be built even in rough weather condition. Rockfill is naturally available construction materials which are being used in various civil structures like dams, embankments, road, etc. Modern heavy earthmoving equipments and local accessibility of rockfill material make an easy and economical option for construction of large dam. In the current scenario, it has been increasingly used in the hydropower projects. Over the last two decades, lots of earth core rockfill dams (ECRD)/concrete face rockfill dams (CFRD) were constructed in India with height larger than 200 m and even reaching 300. Rockfill is the main constituents used in dam body. Hence, a significant amount of stress is subjected to rockfill material due to these increases in dam height. Particle breakage of rockfill material in a high ECRD/CFRD dams significantly increases. Therefore, it becomes crucial to study the characterization of the behaviours of rockfill materials.

An application of load, the load at the surface energy, is transformed into the new broken particles, and this process is called particle breakage [1]. Particle breakage is one of the important issues for rockfill material. Many researchers have been studied on particle breakage analysis basically for pre and post of the shear test. Therefore, this behaviour of rockfill material has quiet appealing for increasing consideration of researchers [1–6]. To know the effect of particle breakage on the shear strength parameters and deformation behaviours of rockfill material, different laboratories, and numerical studies, including the cyclic/static, large/medium, size triaxial test/hollow cylinder test/simple shear test were carried out on rockfill samples with different initial void ratios/relative densities [7–9]. It was also highlighted by various

U. B. Chakraborty (✉) · S. Dhanote · N. P. Honkanadavar
Central Soil and Material Research Station, New Delhi, India
e-mail: uday401133@rediffmail.com

K. Muthukkumaran (eds.), *Soil Behavior and Characterization of Geomaterials*,
Lecture Notes in Civil Engineering 296, https://doi.org/10.1007/978-981-19-6513-5_8

researcher that particle breakage would decrease with enhance of the strength of individual rockfill material [10]. A hyperbolic stress–strain relationship was established by many researchers [5, 7, 11–13] to relate the degree of particle breakage with the axial/shear strain or by the application of plastic strain. Two types of factors are responsible for particle breakage. Various physical properties were also described to considerably impact the breakage quantity of rockfill material apart from the mechanical factors. The quantum of particle breakage has decreased with the decreasing of coefficient of uniformity, C_u [14] when the other conditions like relative densities were unchanged. However, the influence of original density/void ratio on the breakage properties of rockfill material was uncertain. A trend for decreasing initial void ratio with increasing the degree of particle breakage was found in [15], while a reverse trend was highlighted [4] due to high stress concentration of the sharp portion of angular particles.

In this study, nine numbers of large size triaxial tests under different confining pressures and maximum particle sizes were performed by consolidated drained (CD) condition on blasted rockfill material to examine particle breakage under control strain method. Also, nine numbers of relative density test with three different maximum particle sizes were carried out. Relationship among the particle breakage, particle size, and confining pressure was studied.

Experimental Investigations and Discussion

Material Used

The blasted quarried rockfill material from one of the project sites of northern part of India (Fig. 8.1) has been considered for this study. The rock is represented by poorly graded metamorphic, viz. schist, phyllite, and quartzite. Prototype rockfill sample consists of graded particle of different sizes, angular to subangular in shape. Maximum grain size (d_{max}) of prototype rockfill material for this study considered is 600 mm. Laboratory testing for such large size of rockfill material is not feasible to test. Various modelling techniques are used to scale down maximum size of the prototype rockfill material so that the specimen can be prepared by using modelled size of particle but it should not be small 1/6 or 1/5 of the maximum particle size; otherwise, scale effect may be occurred. Parallel gradation technique [16] by John Lowe (1964) is mostly used due to simplicity and worldly accepted by engineering community. Based on the prototype gradation curve, modelled gradation curves with d_{max} of 25, 50, and 80 mm were developed by using parallel gradation technique, and the modelled rockfill material was collected.

Fig. 8.1 After the test, observation the pattern of failed specimen. **a** 25 mm particle under 0.6 MPa confining pressure. **b** 80 mm particle under 1.8 MPa confining pressure

Test Setup

Drained Triaxial Tests

Three different initial gradings of maximum particle size (d_{max}) 25, 50, and 80 were defined as materials 1, 2, and 3, respectively. Figure 8.1 shows the gradation of modelled and prototype rockfill material used in this consultancy job, whereas for this study, only modelled material was used. The following standards IS 2720 (Part 14), ASTM D4253-14 [17], and ASTM D4254-14 [18] are used to determine the minimum, maximum, and average packing densities of the same. Table 8.1 highlights the values of the maximum and minimum densities, coefficient of uniformity (C_u), and maximum (d_{max}) and minimum particle size (d_{min}) for each graded of rockfill material. The minimum (γ_{max}) and maximum (γ_{min}) densities of the material indicated as No. 1 are highlighted as 1.87 g/cm^3 and 2.22 g/cm^3, and material No. 2 was determined as 1.85 g/cm^3 and 2.21 g/cm^3, respectively, whereas the material indicated as 3 is 1.85 g/cm^3 and 2.18 g/cm^3, respectively. The packing density in triaxial test specimen (size 381 mm × 831 mm) for all the modelled rockfill materials was prepared by using minimum and maximum dry densities corresponding to 87% relative density; confining pressures, i.e. 0.6, 1.2, and 1.8 MPa, were used for each modelled rockfill material for conducting the test.

Table 8.1 Physical characteristic of the rockfill materials

Material no	γ_{min} (gm/cc)	γ_{max} (gm/cc)	d_{min} (mm)	d_{max} (mm)	C_u
1	1.87	2.22	0.075	25	57
2	1.85	2.21	0.075	50	70
3	1.82	2.18	0.075	80	75

Table 8.2 shows amounts of various fractions of material by mass used for preparing specimens for different maximum sizes of modelled rockfill. Collected rockfill material of different sizes was first washed, air-dried, and then weighed. Specimens were prepared by mixing and then dividing into six equal parts [17].

The specimens were made in split mould in six equal layers with two rubber membranes (1 mm inner and 3 mm outer). The sample was compacted by standard automated vibratory compactor. The tests were conducted in three stages, i.e. saturation, consolidation, and shearing. In first stage, specimen was saturated by facilitating water to seep through the base of the triaxial cell. A top drainage method was adopted for removing air voids. In the second stage, the specimen was consolidated under required confining pressure. In the third stage or shearing stage, the specimens were sheared till failure or 20% of axial strain. Post-failure of the specimen under different criteria is shown in Fig. 8.1a and b. After each test of shearing, the specimen was sieved and weighed as per the standard ASTM D4253-14 [17]. Figures. 8.2, 8.3 and 8.4 represent the particle breakage of different graded materials by sieve analysis of before and after the test. From the graph, it has been noticed that after shearing test, the gradation curves were shifted towards the left side from the original grading as smaller size of the particles was produced.

Results of major and minor principal stress have been expressed in Table 8.3.

Table 8.4 shows modelled rockfill particle retained (in percentage) at each sieve size before and after the shearing. It has been observed that a significant mass of material reduction occurred in larger sized of particles, i.e. Material 3 (80–50 mm) and Material 2 (50–25 mm), noticed a considerable amount of breakage. Though material of 25–10 mm size (material 1), a small quantity of material breakage occurred. Therefore, it can be considered that a smaller size of particle is generated due to the breakage and the supplement of particles induced (by particle breakage) from the upper size of particle ranges. Besides, a noticeable amount of increase in particles mass is observed in the range of 2–0.075 mm, while a small quantity of particle breakage raise has been observed for the particle of 10–4.75 mm and 4.75–2 mm.

The unique techniques and indices were first introduced by Marsal and Lee and Farhoomand to quantify the degree of breakage of particles. Marsal and his team observed that a high degree of particle breakage occurred during large size triaxial testing on rockfill materials. To address the phenomenon of breakage developed, a parameter called particle breakage factor (B_f). This technique needs the different in total particle size distribution of rockfill material before and after the testing. From the particle size distributions curves, the material differences can be calculated on

Table 8.2 Preparation of sample by different graded rockfill materials

Material No.	RD (%)	Packing density gm/cc	Total mass (Kg)	Mass of each size range (Kg)					
				80–50 mm	50–25 mm	25–10 mm	10–4.75 mm	4.75–2 mm	2–0.075 mm
1	87	2.17	201.63			62.50	40.32	36.29	62.50
2	87	2.16	200.11		48.02	46.02	36.02	24.01	46.02
3	87	2.13	197.33	31.57	41.44	45.38	29.59	17.75	31.57

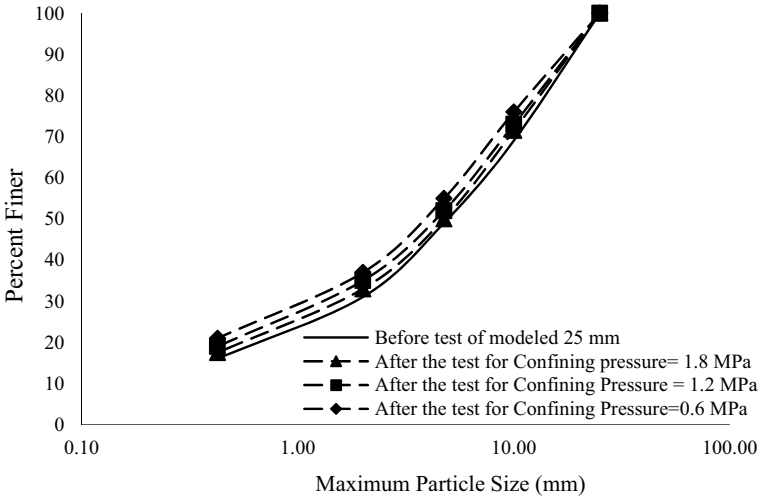

Fig. 8.2 Gradation of the rockfill material 1 before and after test with three different confining pressures

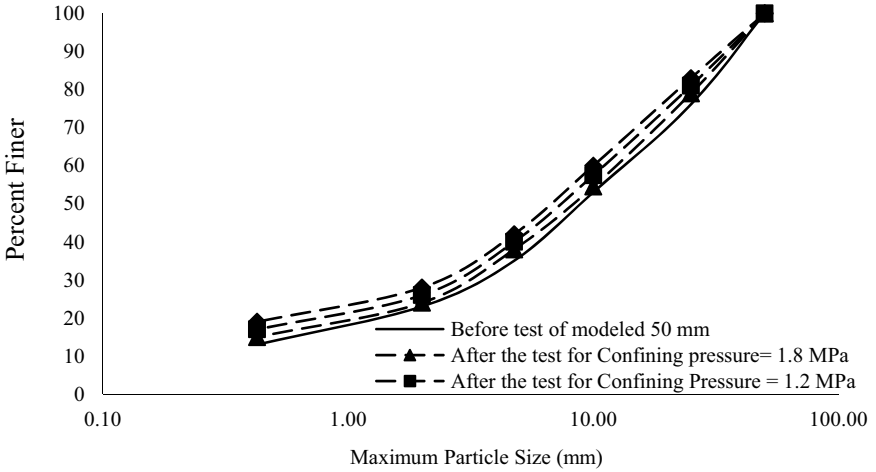

Fig. 8.3 Gradation of the rockfill material 2 before and after test with three different confining pressures

each sieve (in percent) as followed:

$$\Delta W_{\mathrm{s}} = \Delta W_{\mathrm{si}} - \Delta W_{\mathrm{sf}} \tag{8.1}$$

where ΔW_{si} represents the material retained on each sieve size 's' (in percent) before the test and ΔW_{sf} represents the per cent of material retained on the same sieve size,

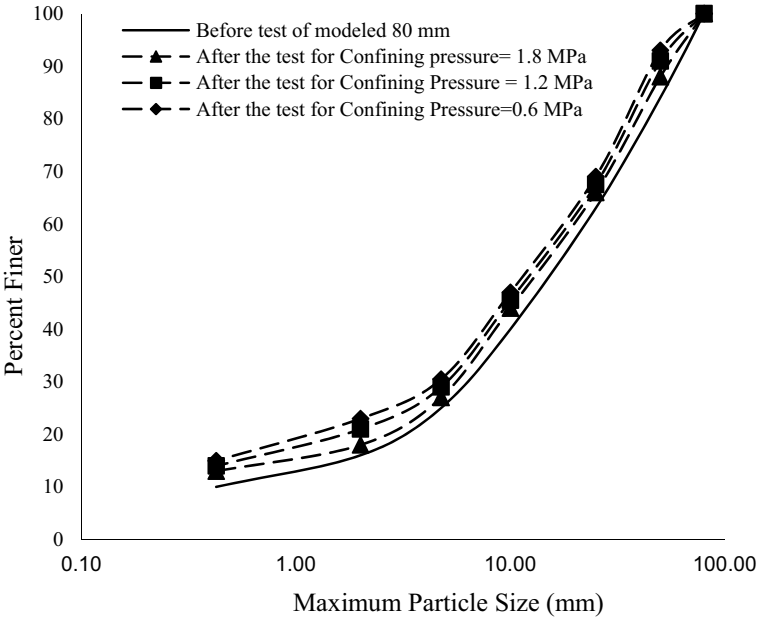

Fig. 8.4 Gradation of the rockfill material 3 before and after test with three different confining pressures

Table 8.3 Results of the triaxial test

Minor principal stress (σ_3), MPa	Deviator stress (σ_1–σ_3), MPa	Major principal stress (σ_1), MPa	Mean stress (σ_m), MPa	$p = (\sigma_1 + \sigma_3)/2$, MPa	$q = (\sigma_1 - \sigma_3)/2$, MPa
For maximum particle size 25 mm					
0.6	3.2	3.8	1.67	2.2	1.6
1.2	6.0	7.2	3.2	4.2	3.0
1.8	8.6	10.4	4.67	6.1	4.3
For maximum particle size 50 mm					
0.6	3.3	3.9	1.7	2.25	1.65
1.2	6.1	7.3	3.23	4.25	3.05
1.8	8.7	10.5	4.7	6.15	4.35
For maximum particle size 80 mm					
0.6	3.3	3.9	1.7	2.25	1.65
1.2	6.4	7.6	3.3	4.40	3.20
1.8	8.9	10.7	4.7	6.25	4.45

Table 8.4 Particle breakage factor (B_f) of different graded rockfill materials

Sample material no	Confining pressure (MPa)	Test state	Percentage retaining on each sieve size (%)						Breakage factor
			80–50 mm	50–25 mm	25–10 mm	10–4.75 mm	4.75–2 mm	2–0.075 mm	
1	0.6	Before			31	20	18	31	3.50
		After			28.5	21.5	17	33	
	1.2	Before			31	20	18	31	5.00
		After			27	21	17	35	
	1.8	Before			31	20	18	31	7.00
		After			24	21	18	37	
2	0.6	Before		24	23	18	12	23	5.00
		After		22	22	18	16	22	
	1.2	Before		24	23	18	12	23	7.00
		After		18.50	24	17.50	16	24	
	1.8	Before		24	23	18	12	23	9.00
		After		17	24	16	17	26	
3	0.6	Before	16	21	23	15	9	16	6.00
		After	12	22	22	17	9	18	
	1.2	Before	16	21	23	15	9	16	9.00
		After	9	23.5	22	16.5	8	21	
	1.8	Before	16	21	23	15	9	16	11.50
		After	7	24	22	16.5	7.5	23	

i.e. 's' after the test. Further, breakage index or called as particle breakage factor is the sum of all negative or the positive values of ΔW_s. Marshal's breakage index is presented below (in percentage):

$$B_f = \sum(-\Delta W_s) = \sum(+\Delta W_s) \quad \text{(take all positive or negative values)} \tag{8.2}$$

Additionally, a normally lesser B_f has been observed in material No. 1 (as mentioned in Table 8.1) which has a comparatively lesser coefficient of uniformity, signifying that well-graded rockfill material break/crush/rupture less. Superior quality of rockfill material which is well graded in nature may have the value of coefficient of uniformity (C_u) about to 15 or greater. When the value C_u is extremely higher, it indicates that the larger size of particle present in sample is very large quantity in contrast of lower size of particle. The same results were observed on railway ballast material and sand particle by researchers.

Conclusions

Particle breakage of rockfill material is dependent on the strength of different distinct particles [15], the particle size distribution curve [16], and the stress level on the material. The strength of distinct particles is interrelated not only to the mineral composition but also to the shape of the particle. B_f of blasted rockfill materials increases with increase of particle size. It is known from various research papers that the number of contact points decreases with increases of particle size which leads to higher contact pressure and increased B_f. Rockfill materials have shown increase in B_f with the increase of confining stress for all sizes/graded of the particles. It has been predicted that with the increase of confining stress causes increase in contact stresses leading to increase in B_f. From the postgraduation of crushed rockfill material, it has been observed that all the gradings of the material after test were shifted away from the initial grading curve. Therefore, it was observed that smaller size of particles was generated. Further, it has been observed that the particles with bigger size that appeared to crush were more than the smaller sized of particles.

References

1. Honkanadavar NP (2010) Testing and modelling the behaviour of modelled and prototype rockfill materials. Ph.D. thesis, I.I.T. Delhi
2. de Bono J, McDowell G (2016) Particle breakage criteria in discrete-element modelling. Géotechnique 66(12):1014e27
3. Einav I (2007) Breakage mechanics e part I: theory. J Mech Phys Solids 55(6):1274e97

4. Honkanadavar NP, Gupta SL, Ratnam M (2012) Effect of particle size and confining pressure on shear strength parameter of rockfill materials. Int J Adv Civ Eng Archit I(I):49–63
5. Honkanadavar NP, Sharma KG (2013) Testing and modeling the behaviour of riverbed and blasted quarried rockfill materials. Int J Geomech (ASCE) 14(6):04014028-1–11
6. Honkanadavar NP, Kumar N, Ratnam M (2014) Modeling the behavior of alluvial and blasted quarried rockfill material. Int J Geotech Geol Eng 1–15
7. McDowell GR, Bolton MD (1998) On the micromechanics of crushable aggregates. Géotechnique 48(5):667–679
8. Lackenby J, Indraratna B, Mcdowell G, Christie D (2007) Effect of confining pressure on ballast degradation and deformation under cyclic triaxial loading. Géotechnique 57(6):527e36
9. Zhang C, Nguyen GD, Kodikara J (2016) An application of breakage mechanics for predicting energy–size reduction relationships in comminution. Powder Technol 287:121e30
10. Coop M, Sorensen K, Freitas TB, Georgoutsos G (2004) Particle breakage during shearing of a carbonate sand. Géotechnique 54(3):157e63
11. McDowell GR, Li H Discrete element modelling of scaled railway ballast under triaxial conditions. Granular Matter 18:6. https://doi.org/10.1007/s10035-016-0663-8
12. Winter MJ, Hyodo M, Wu Y, Yoshimoto N, Hasan MB, Matsui K (2017) Influences of particle characteristic and compaction degree on the shear response of clinker ash. Eng Geol 230:32e45
13. Xiao Y, Liu H, Chen Y, Jiang J (2014) Bounding surface plasticity model incorporating the state pressure index for rockfill materials. J Eng Mech 140(11):04014087. https://doi.org/10.1061/(ASCE)EM. 1943–7889.0000802
14. Griffith AA (1921) The phenomena of rupture and flow in solids. Philos Trans R Soc London, Ser A 221(582–593):163–198
15. Lade PV, Yamamuro JA, Bopp PA (1996) Significance of particle crushing in granular materials. J Geotech Eng 122(4):309e16
16. Lowe J (1964) Shear strength of coarse embankment dam materials. In: Proceedings 8th international congress on large dams, vol 3, pp 745–761
17. ASTM D4253-14 (2014) Test methods for maximum index density and unit weight of soils using a vibratory table. ASTM International, West Conshohocken, USA
18. ASTM D4254-14 (2014) Standard test methods for minimum index density and unit weight of soils and calculation of relative density. ASTM International, West Conshohocken, USA

Chapter 9
Elemental Assessment of Pond Ash for Evaluating Its Application as a Subbase Material for Hardstand Construction

Aditya Shankar Ghosh and Tapas Kumar Roy

Introduction

Typically, the TPP produces two types of ash materials, namely bottom ash (BA) and fly ash (FA). These are collected, water mixed, and stored in ash lagoons. The major problem faced by these plants is the disposal of this residual waste stored in the ash ponds, which in this investigational work is termed as pond ash (PA). The deposition process of the slurry segregates the ash mixture [20, 22]. The one settling at or near the inflow point is the coarser and heavier one, with some distinct physicochemical differences than the ones drifting away towards the outflow point owing to their fineness and light weight. This leads to the formation of two different material types in the same ash pond deposition site. India is one of the leading producers of PA, which occupies 65,000 acres of valuable land as disposal site [17, 40]. However the disposal problem cannot be effectively addressed as the current levels of efforts are able to meet only 77.5% utilization in 2018–19 when compared to the target of 100% utilization of this residual waste [44].

The appreciated availability of PA, along with its increasing geotechnical usage [20], has called forth for evaluating its engineering properties as an alternative granular subbase material for hardstand in dockyards, where it can find bulk usage with low environmental impact. Under the National Perspective Plan (NPP) of Sagarmala, six mega ports with lakhs of square meter area are scheduled for construction of hardstand [46]. In addition, the Indian government has condemned mass use of sand for foundation purpose by imposing strict regulatory regime on large-scale sand mining. This came into effect after the declaration made by the Supreme Court of

A. S. Ghosh (✉) · T. K. Roy
Department of Civil Engineering, Indian Institute of Engineering Science and Technology, Shibpur, Howrah 711103, India
e-mail: adityaghosh369@gmail.com

T. K. Roy
e-mail: tapash@civil.iiests.ac.in

K. Muthukkumaran (eds.), *Soil Behavior and Characterization of Geomaterials*,
Lecture Notes in Civil Engineering 296, https://doi.org/10.1007/978-981-19-6513-5_9

India about imposing sustainable sand mining management guideline, to prevent extensive sand mining that was causing ecological imbalance [51]. Henceforth, this is a good opportunity to put PA into substantial usage as a subbase material.

Therefore, this paper focuses towards performing a thorough study on shear strength, bearing strength and other geotechnical properties of the representative PA samples, in order to portray their distinctive geotechnical characteristics under the mentioned conditions, and draw a comparison with the natural soil. This study also provides outcomes of effectively incorporating PA into viable layers of hardstand foundation as subbase after checking for its surface deflection.

Hardstand Foundation Layer Practice

Alike the flexible pavement foundation layer [53], the foundation layer of a hardstand is multilayered and functions as a multilayered structure with subgrade, unbound, and bound layer preceded by the surfacing course [28]. Unbound granular materials like moorum, natural sand, gravel, and crushed stones together form the subbase layer [8]. This multilayered elastic model has been described to be the most successful pavement design model by certain researchers [3].

Opportunities for Replacing Conventional Materials by CCA Products

A plenty of investigational works had been carried out suggesting successful utilization of coal combustion ash (CCA) as partial replacement for soil stabilization in roadway pavements [9]. It has also been used as structural fill [14] and embankment material [43]. Has found application as partial replacement of cement [15] in injection grouting [25] and subsidence control of embankment [32]. It has been used to prepare consolidated backfill materials for coal mines [39].

Investigational works carried out on port pavements revealed use of CCA as cost effective low maintenance binder for hydraulically bound mixtures of base and subbase [27]. Researchers have mentioned using small graded granular materials for subbase course which may vary country-wise in accordance to national standards [53].

Literature Review

Researchers have conducted various analysis of coal combustion ash (CCA) where the chemical analysis revealed presence of Si, Al, Fe, Ca, Mg, and Na making it

pozzolanic in nature [1]. Several experimental investigations carried out till date by researchers analysing the geotechnical characteristics of CCA determined its suitability as a subbase material [7].

Investigational works have revealed that PA has a specific gravity (G) ranging within 2.03–2.27 [52]. Research works also showed PA samples collected from ash pond inflow point has higher G than the outflow point samples, indicating heavier particle settlement near inflow point [20, 22, 52]. However, the FA particles have lower G owing to the presence of considerable amount of hollow particles than most solid particles [23, 26, 29, 41].

Liquid limit (LL) and plastic limit (PL) data of CCA samples collected by researchers from plants located in different countries showed the LL ranges from 18.5% to as high as 66%; however, the data showed the FA to be non-plastic [5, 13, 47].

Experiments were performed by researchers using PA and soil mixed with PA where the samples were compacted for increasing its strength and decreasing its settlement potential. The data obtained showed the optimum moisture content (OMC) ranging 18.01%-32.2% and the maximum dry density (MDD) ranging 1.093–1.322 g/cc [51]. Similar results are also obtained by other researchers [5, 13, 47] which is stated to be within specified permissible limits of IRC: SP: 58–2001 [19].

The hydraulic conductivity data obtained by the investigators for PA spanned the range of 10^{-4}–10^{-7} cm/sec [5]. They considered the uniform gradation of the ash to be instrumental for higher porosity values and suggested the bulk density of the PA ranges 1.081–1.275 gm/cc [52].

The database compiled by the researchers based on physical and geotechnical properties of CCA, primarily from the direct shear tests or consolidated drained triaxial tests, addressing mostly the drained cases showed CCA derives its shear strength from the friction between the particles and cohesive strength on moisture exposure with subsequent curing [12, 32, 49, 50]. However, investigators have also concluded that BA having an internal friction angle ranging 25°–43° improves strength characteristics [5]. Researchers conducted direct shear test for studying the shear strength of BA and recorded an internal friction angle over a wide range of 35°–55° [16].

Morphological analysis performed by scanning electron microscope (SEM), and photomicrographs published by several investigators showed PA particles to be unevenly shaped with composite pore structures. Further zooming showed it to be agglomerations of smaller ash particles [20, 22, 52]. X-Ray diffraction (XRD) results published by the researchers after analysing the mineralogy of PA revealed them to be highly crystalline minerals that are non-reactive at ordinary temperatures [20, 52].

Physical, chemical, morphological, and mineralogical analysis of coal combustion ash revealed its compatibility to be effectively used as a roadway subbase material [16].

Research Gap-Rationale

The above literature reviews reveal several successful outcomes of FA being used as a material of replacement for unbound base and subbase layers of pavement along with various additives. However, a miniscule amount of work has been done by researchers [22, 52] on the variability in behavioral pattern of the PA from inflow and outflow points of an ash lagoon. Much work is yet to be done to characterize their various properties and find out proper utilization technique as subbase material for the foundation layers of hardstand within confinement structure in port area. This is the need of time due to the restrictions imposed on extensive use of sand which till date has been the go to CGM for hardstand foundation subbase layer. The pozzolanic property of PA is sure to impart stability to subbase layer, in addition to its hydrophobic characteristic that will provide greater potential to absorb and release water improving its permeability, which is an essential requirement for hardstand foundation. However, it will be interesting to see whether the characteristic difference between the inflow and outflow type affects their performance.

Experimental Investigations

Ashes from TPPs are collected in the ash pond by wet disposal system, causing distinct segregation into two different material type at inflow and outflow points. Coarser particles are heavier ones settling immediately as they get discharged at the inflow point, the finer lighter particles drift away settling near outflow point.

The PA samples used in this investigational work were collected from both the inflow and outflow point of Kolaghat Thermal Power Station (KTPS) ash pond number 4 in West Bengal, India. The samples are denoted as PA_i and PA_o representing ash samples from inflow and outflow points, respectively. Sand was locally collected and is denoted as LS. The present study consists of thorough characterization, i.e. chemical, physical, mineralogical, and morphological properties of PA_i and PA_o. Detailed study of the geotechnical properties of the LS is also performed. Static strength characteristics of the materials are studied in details using consolidated drained triaxial tests.

Material Characterization

Specific gravity (G), bulk density (ρ), and loss on ignition (LOI) are determined for PA_i, PA_o and LS sample represented by Table 9.1. It shows the G values of PA_i are 2.585 which is comparatively higher than PA_o 2.103. However, G values of PA_i and PA_o are considerably lower than LS sample whose G value is 2.675. Similar results were obtained by other researchers [20, 22, 52], which was explained due to the higher

Table 9.1 Physical properties of inflow and outflow pond ash materials

	Specific gravity (G)	Bulk density (ρ) (g/cc)	Loss on ignition (%)
PA_i	2.585	1.49	3.03
PA_o	2.103	1.23	1.50
LS	2.675	1.77	–

Table 9.2 Chemical composition of KTPS pond ash from inflow and outflow points

Chemical composition (%)	PA_i	PA_o
Silica (SiO_2)	70.00	78.00
Alumina (Al_2O_3)	1.20	1.08
Iron oxide (Fe_2O_3)	12.70	10.00
Lime (CaO)	2.50	1.50
Magnesia (MgO)	1.40	0.70
Sulphate (SO_3) + Soda (Na_2O) + Potash (K_2O)	9.17	7.22

Fe_2O_3 presence in PA_i (12.7%) than PA_o (10%). The aforementioned percentages are obtained from chemical analysis of the samples. This further indicates the heavier particles settle near the inflow point immediately after getting discharged, whereas the outflow particles owing to its light weight drift further and settle near the outflow point [20]. The LOI representing unburnt carbon values for PA_i (3.03%) and PA_o (1.50%) are lesser than the maximum limit for class F fly ashes [2]. The ρ values in Table 9.1 shows PA_i is higher than PA_o [52].

Table 9.2 representing the chemical composition of ashes shows a little disparity in chemical composition of PA_i and PA_o. The findings are at par with other researchers [4, 20, 47, 52] where oxides of silica, alumina, and iron together form the considerable portion of the ash. The reasons behind this slight change in chemical composition is considered to be the soluble chemical that may have varying concentration at the inflow and outflow points. Besides, the PA_o can be produced from remote coals and is different as compared to PA_i which may be produced from the lately used coals [52]. Low LOI value for both the PA types ensures cutting off the self-heating or unprompted heating risk if used as filling material.

Nature of Particles

Morphological analysis performed to understand the shape and surface characteristics of samples using FESEM has been represented by the photomicrographs of Fig. 9.1.

PA_i shows irregular shaped complex pore structures (Fig. 9.1a), which are agglomerations of smaller ash particles (Fig. 9.1b). On the contrary, PA_o is observed to be

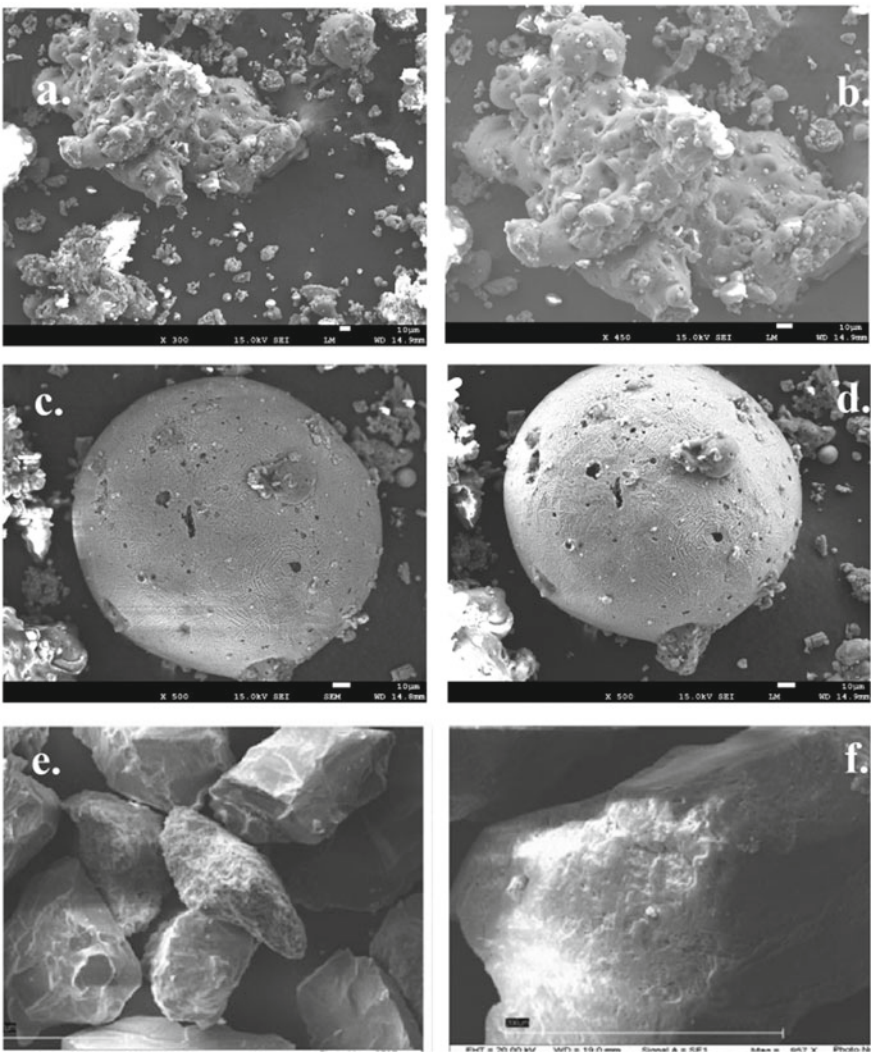

Fig. 9.1 Field emission scanning electron micrographs of representative sample particles

conglomerations of smaller spherical shaped particles of different sizes, having intra-particle voids (Fig. 9.1c, d) [52]. As for the LS, the SEM photomicrographs from the study of Suthar and Aggarwal 2016 revealed presence of solid particles without any intraparticle voids for the Yamuna Sand sample used by the researchers and matched closely with the LS sample used in this study (Fig. 9.1e, f).

Table 9.3 Grain size characteristics of KTPS PA_i, PA_o and LS

Properties	PA_i	PA_o	LS
Coarse and medium sand size (4.75–0.425 mm), %	4.6	0.3	46.35
Fine sand size (0.425–0.075 mm), %	89.5	45.9	53.65
Silt size (0.075–0.002 mm), %	5.9	53.8	0
Clay size (<0.002 mm), %	0	0	0
Uniformity coefficient, CU	3.926	1.306	2.0
Coefficient of curvature, CC	0.676	0.867	1.095
D10, mm	0.135	0.062	0.25
D30 size, mm	0.22	0.066	0.37
D60 size, mm	0.53	0.081	0.50

Grain Size Distribution

Grain size distribution was performed by sieve analysis followed by hydrometer analysis shown by Table 9.3. The PA_o samples are silt size, and PA_i samples are in the range of fine sand alike LS [20–22]. The particle size distribution represents that the ash samples are well graded within the available particle size range.

Atterberg Limits

The liquid limit (LL) and plastic limit (PL) of PA_i and PA_o could not be obtained by Casagrande's method indicating they are non-plastic [5, 20].

Compaction Characteristics

The PA_i, PA_o and LS samples are tested for compaction characteristics using standard and modified Proctor tests as per IS specifications. The MDD of compacted PA samples was found to be lower than LS due to lower G values and presence of intraparticle voids [20, 21]. Table 9.4 shows densities of the PA_i higher than PA_o due to higher G values. Both the ash samples although exhibit similar behavior like LS the PA_i compaction behavior are comparatively more akin to LS [5, 11, 20, 52] and satisfy the suitability in embankment constructions as specified by IRC: SP: 58-2001 [19].

Table 9.4 Compaction characteristics of the PA_i and PA_o materials

Material tested	Standard proctor		Modified proctor	
	MDD (gm/cc)	OMC (%)	MDD (gm/cc)	OMC (%)
PA_i	1.53	23.00	1.67	19.30
PA_o	1.18	27.86	1.58	25.86
LS	1.71	12.50	2.15	13.62

Table 9.5 CBR strength test result for soaked and unsoaked samples of PA_i and PA_o materials

Material tested	California bearing ratio (%)			
	Standard compaction		Modified compaction	
	Unsoaked	Soaked	Unsoaked	Soaked
PA_i	16.63	13.83	28.27	23.55
PA_o	17.19	14.22	29.23	24.17
LS	25.08	19.39	42.64	32.96

Strength Characteristics

The PA_i, PA_o and LS samples were tested for their strength characteristics using CBR test as per IS specifications for unsoaked and soaked conditions. To carry out the test, the samples were compacted in CBR mould using standard and modified compaction method respectively as per IS specifications. Table 9.5 represents result of the CBR test.

The test results indicate 17% decrease in strength index PA_i and PA_o for both standard and modified compaction under soaked condition. However, the decrement is 23% for LS under similar condition. This is due to the presence of lesser voids in finer PA samples when compared to the LS. Further, PA samples have components exhibiting cohesiveness when compared to the cohesionless LS. Table 9.5 shows the CBR value for finer PA_o sample is more than the coarser PA_i sample under both conditions which is due to the lesser voids in the finer counterpart. From the observations, it can be said that PA_o sample should find preference over PA_i sample while constructing hardstand subbase as it follows the specifications by MORD [34] and MORTH [35].

Permeability Characteristics

Coefficient of permeability (k) for PA_i and PA_o was determined by falling head permeability test. Standard Proctor method was used to compact them according to their MDD and corresponding OMC. The results are tabulated in Table 9.6.

Table 9.6 Values of permeability characteristics for PA materials and LS

Material description	Coefficient of permeability (k) m/sec
PA_i	2.26E−5
PA_o	1.57E−6
LS	7.44E−5

The results revealed the k value of PA_i is closer to LS sample due to the presence of more voids. However, the k value for finer PA_o sample falls within the range of silt materials forming denser counterpart of the PA [5, 11, 20, 22, 33, 54].

Shear Behaviour

Determination of the strength and shear characteristics of the samples was done by consolidated drained (CD) triaxial tests. PA_i, PA_o and LS samples were tested at 95% of proctor MDD to study the influence of density. The specimen was prepared using static compaction technique using 38 mm diameter and 78 mm height mould by moist tamping method, providing consistent desired densities as well as ensures uniformity of the sample [6, 20, 30, 56]. The sample was compacted in three layers using OMC. Hydraulic jack was used to extrude the compacted specimen onto the porous stone followed by mounting on cell pedestrian. This was followed by draining it with water. Volume change device was connected to the top drainage line, and volume change in specimen is monitored. After confirming no further volume change, the sample was ready for shearing. The recorded data has been tabulated in Table 9.7.

The LS shows no cohesion (c); however, it has the highest angle of friction (φ). The PA_i has a slight amount of c value compared to LS although decreases in φ. The PA_o sample shows a considerable increase in c value; however, its φ is only better than PA_i sample but lower than LS. Researchers have found out that φ depends on the angularity of the particles [21, 38]. The LS having more angular particle provides better resistance to particle rearrangement for sustainable shearing. However, the presence of more pozzolanic components in PA_o sample provides it with better c and φ values when compared to the PA_i sample.

Table 9.7 Effective strength parameters of various materials from CD tests

Material	State	Strength parameters	
		Cohesion, c (kPa)	Angle of friction, φ (°)
PA_i	Dense	11.60	31.17
PA_o	Dense	86.30	32.00
LS	Dense	0.00	40.00

Mineralogy Analysis

The mineralogy analysis of the PA_i and PA_o samples was carried out by X-Ray diffraction test (XRD) and Fourier transform infrared spectroscopy (FTIR). Detailed discussions along with respective outcomes are presented in the following sections.

X-Ray Diffraction (XRD) Test. The ULTIMA IV X-RAY DIFFRACTOMETER (RigakuKyowaglas-XA made in Japan) was used for XRD. The machine was automated with Cu-Kα radiations. Back loading technique is used for minimizing preferred orientation while preparing specimens for XRD. Incident beam with Soller slit 2.5°, width 0.8 mm and diffracted beam with Soller slit 4°, anti-scatter width 8 mm was used. Air scatter screen module was positioned 1–2 mm above the sample. The readings were taken in vertical Bragg–Brentano (ɵ–ɵ) geometry between 10° and 80° at 0.02° step size at 1 step/second, giving a total measurement time of 36 min/scan. The X-ray tube generator was operated at 40 kV and 40 mA. The results are presented in Fig. 9.3.

XRD pattern of the sample shows main mineralogical phases present in the form of mullite (M), quartz (Q) along with bunch of magnetite (G), hematite (H), sillimanite (S), calcium hydroxide (P), and calcium carbonate (K). The Q, M, and H are the crystalline substances present predominantly that are non-reactive at ordinary temperatures. XRD examination showed partly presence of silica in crystalline form of S and Q, additionally combined with alumina as M. Iron appears partly as oxide of M and minutely as H. Figure 9.2 shows the formation of peaks of P at 18.7° and K at 42.6° for PA_o sample which matched well with Joint Committee on Powder Diffraction Standards [18], respectively. However, K is absent in PA_i sample explaining its reduced pozzolanic nature [10, 52, 57].

Fourier Transform Infrared Spectroscopy (FTIR). The collection of high spectral resolution data over a wide range of spectrum is the main advantage of FTIR. Here PA_i and PA_o are pressed into KBr pellets by mixing 1 mg of the powdered sample with 100 mg KBr powder. Then quantitative FTIR analyses are done in Nicolet 7199 FT-IR. Such spectra are quantitatively analysed by curve analysis program which is employed to synthesize the IR spectra. It uses a basic set of absorption peaks shown in Fig. 9.3 identified with various functional groups. The spectra were obtained in 4000–450 cm^{-1} range at 4 cm^{-1} resolution with an average 64 scans per measurement. This aided in getting a good chemical structure understanding of the products from various stages of the PA hydration process.

The sample spectra of PA_i and PA_o shown in Fig. 9.3 compare the change in FTIR spectra of dry and hydrated PA after 7 days curing. O–H stretching, O–H bending, C–O stretching, and Si–O/S–O stretching vibrations are taken into consideration for comparing PA_i and PA_o FTIR spectra difference. Wavenumbers showing absorbance ranging 3000–3750 cm^{-1} represent stretching of O–H, and 1570–1750 cm^{-1} represents O–H bending [36, 58]. C–O stretching constitutes 1350–1570 cm^{-1}. The Si–O stretching due to the form of Silica in PA samples is observed centering around 1083 cm^{-1} and ranging from 850 to 1350 cm^{-1} [58]. This further transforms into

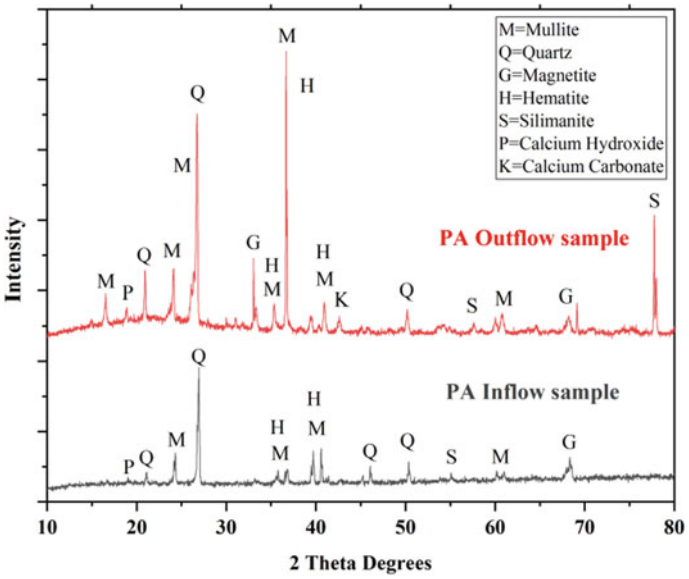

Fig. 9.2 XRD results for the representative samples

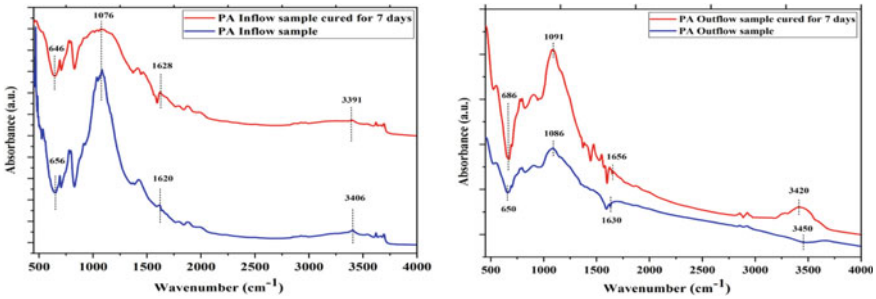

Fig. 9.3 FTIR spectra peaks for PA_i, PA_o and hydrated PA_i, PA_o after 7 days curing

Si–O–Al bonds of Poly-Sialate around 912 cm^{-1}. Figure 9.3 shows the magnitude of the peak shifts for respective stretching and bending for both PA samples, for dry state and hydrated state after 7 days curing, indicating on the degree of polymerization. Figure 9.3 clearly shows broader peaks covering more area for PA_o than PA_i. However, there is a decrease in O–H stretching region for PA_o than PA_i. The initial broader peaks and the decrease in the O–H stretch clearly indicate towards the comparatively more pozzolanic nature of the PA_o sample [24].

Deflection Analysis Using Light Falling Weight Deflectometer

Deflection analysis of the samples was done using DYNATEST 3031 LWD, developed by Dynatest Denmark A/S. This is a portable device with approximate weight 22 kg and a 10 kg drop weight falling from a 850 mm height impacting on bearing plate via 2 rubber buffer pad stacks can be effectively used to measure dynamic soil modulus. This produces a load pulse which is in the range of 0–25 kN in $15 \geq 30$ ms. Deflection caused by the mass impact on loading plate is measured by the center velocity transducer sensor. 300-mm-diameter loading plate has been used in this study. Investigators have satisfactorily used this instrument for quality control and quality assurance of compacted unbound materials for subgrade and subbase to obtain peak surface deflection and impact force [37, 48]. It has also found effective use in measuring deformation modulus of soil under a static loading condition [31, 32, 42, 45, 55]. Boussinesq solution was used for deflection measurement at center of the plate for calculating the dynamic deformation moduli (E_{LFWD}) as:

$$E_{\mathrm{LFWD}} = \{k(1 - v2)\sigma R\}/\delta c$$

where $k = \pi/2$ or 2 for rigid and flexible plates, respectively; δc = centre deflection; σ = applied stress; v = Poisson's ratio and R = radius of the plate.

Result and Discussions of LFWD Test

Data obtained from LFWD test has been organized and analysed using software LWDmod. Figure 9.4 represents the surface deflection modulus (E_{SURF}) and the peak surface deflection (μm) respectively for the number of drops. It shows PA_i, PA_o and LS closely follow each other as the magnitude of their E_{SURF} does not change much. However, PA_i and LS have more similar E_{SURF} value due to similar grain size distribution, than PA_o which have the highest value.

Although the μm of PA_i and LS is almost same, comparatively it is 1342 μm for PA_i which is lesser than LS which is 1350 μm. This is due to c value of PA_i. However, the PA_o sample with the highest c' value gives the lowest μm of 1327 μm.

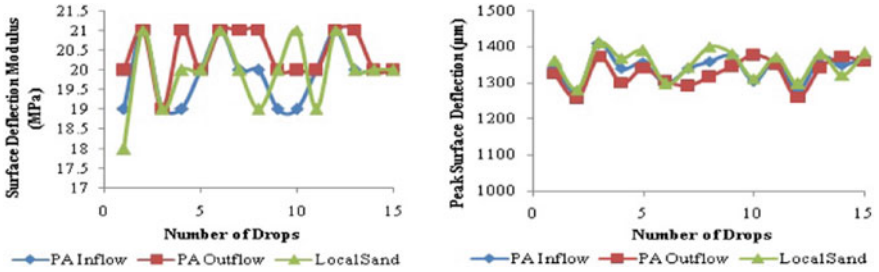

Fig. 9.4 Surface deflection modulus (E_{SURF}) and peak surface deflection (μm) of the representative samples under LFWD test

Conclusion

This study was carried out for testing different properties of PA_i and PA_o within same ash pond and its utility as a supplementary subbase material for hardstand construction. The G value of PA_i is 2.585 higher than PA_o having 2.103 due to higher Fe_2O_3 content. The grain size analysis shows PA_i particles are predominantly fine sand size and PA_o are silt size. Atterberg limit test determined PA to be non-plastic. The compacted MDD of PA_i is higher than PA_o and lower than LS due to lower G value and higher intraparticle voids. The PA_i sample exhibits higher permeability than PA_o sample which is comparable to that of the silt materials. CBR test showed value of PA_o sample 17.19% in unsoaked condition for standard compaction and 24.17% in soaked condition for modified compaction, which is almost up to the specified values of MORD and MORTH respectively for subbase construction material. The PA_o sample shows comprehensive increase in c' value 86.30 kPa when compared to the other two samples used in the study. The φ' values for PA_i and PA_o samples are almost similar with PA_o 32° showing a slight rise over PA_i 31.17° due to its cohesive nature. Chemical analysis result showed the integrated amount of SiO_2, Al_2O_3 and Fe_2O_3 exceeds 70% in the PA samples.

Special morphological characteristics analysed by FESEM displayed the irregular shape of the PA_i particles with complex pore structures and, spherical shaped PA_o particles with smooth surface but varying sizes. Mineralogical characteristics obtained from XRD analysis shows M and Q are the predominantly present in both PA_i and PA_o samples. The higher degree of silica polymerization present in the PA shows FTIR spectra for hydrated PA_i and PA_o after 7 days curing shifted to higher wavenumbers. The broader peaks covering more area in the spectra of hydrated PA_o sample and simultaneous decrement of its O–H stretch gives a clear indication towards the PA_o sample being comparatively more pozzolanic than PA_i.

The LFWD test revealed that all the three samples behave identically under the application of the drop weight. They show almost similar E_{SURF} values owing to their similar grain size distributions and irregular particle shape. PA_o sample shows lesser average μm of 1327 μm which is 1.7% lower than LS. The results from the study sum up that PA_o sample collected from the outflow point in ash ponds has better

geotechnical properties than PA_i collected from inflow point. However, the PA itself has a huge potential as a subbase layer material in the foundation construction of a hardstand which is very similar to that of the pavement layer construction.

References

1. Adriano DC, Page AL, Elseewi AA, Chang AC, Straughan I (1980) Utilization and disposal of fly ash and other coal residues in terrestrial ecosystems: a review. J Environ Qual 9:333–344
2. ASTM C 618-08a (2008) Specifications for fly ash and raw or calcined natural pozzolana for use as a mineral admixture in Portland cement concrete
3. Barber SD, Knapton J (1989) Structural design of block pavements for ports. J Univ Newcastle, UK 141–149
4. Bera AK, Ghosh A, Ghosh A (2007) Compaction characteristics of pond ash. J Mater Civ Eng 19(4):349–357
5. Bhatt A, Priyadarshini S, Mohanakrishnan AA, Abri A, Sattler M, Techapaphawit S (2019) Physical, chemical and geotechnical properties of coal fly ash: a global review. Case Stud Constr Mater
6. Chan CK (1985) CKC E/P cyclic loading triaxial system users manual. Soil Engineering Equipment Company, San Francisco
7. Chand SK, Subbarao C (2007) Strength and slake durability of lime stabilized pond ash. J Mater Civ Eng 19(7):601–608
8. Chakroborty P, Das A (2003) Principles of transportation engineering. Prentice Hall of India, New Delhi
9. Chu TY (1995) Soil stabilization with lime-fly ash mixtures: preliminary studies with silty and clayey soils. Highw Res Board Bull 108:102–112
10. Chung FH, Smith DK (2014) Industrial applications of X-ray diffraction. Taylor and Francis, pp 566–567. 13:978-0-8247-1992-0
11. Das SK, Yudhbir L (2005) Geotechnical characterization of some Indian fly ashes. J Mater Civ Eng 17(5):544–552
12. Datta M (1998) Engineering properties of coal ash. In: Proceedings of Indian geotechnical conference, Delhi, vol 2, pp 41–46
13. Dev T, Pal SK (2014) Effect of fly ash on geotechnical properties of local soil-fly ash mixed samples. Int J Res Eng Technol 3(5):507–516
14. DiGioa AR, Nuzzo WL (1972) Fly ash as structural fill. J Power Div 98(1):77–92
15. Gopalan MK, Haque MN (1986) Strength development of clinically cured plain fly ash concretes. Proc Aust Road Res Board 13(5):27–33
16. Huang HW (1990) The use of bottom ash in highway embankments, subgrade and subbases. Joint highway research project, Final Report, FHWA/IN/JHRP-90/4, Purdue University, West Lafayette, Indiana
17. HVFAC (2005) Fly ash status summary report in India. High volume fly ash concrete technology project, CIDA. http://www.hvfacprojectindia.com/Summary_Report.pdf. Assessed 9 Sept 2020
18. International centre for diffraction data/Joint committee for powder diffraction standards (ICDD/ JCPDS), JCPDS File No. 44-1482 and JCPDS File No. 85-1108. Newton Square
19. IRC SP 58 (2001) Guidelines for use of fly ash in road embankments. Indian Roads Congress, New Delhi
20. Jakka RS, Ramana GV, Datta M (2010) Shear behaviour of loose and compacted pond ash. Geotech Geol Eng 28(6):763–778
21. Jakka RS, Datta M, Ramana GV (2010) Liquefaction behaviour of loose and compacted pond ash. Soil Dyn Earthq Eng 30(7):580–590. https://doi.org/10.1016/j.soildyn.2010.01.015

22. Jakka RS, Ramaiah BJ, Ramana GV (2011) Dynamic characterization of settled pond ash using measured shear wave velocity (V_s) and SPT-N values: correlation between V_s & N. Int J Geotech Earthq Eng 2(1):83–97
23. Joshi RC, Nagaraj TS (1987) Fly ash utilization for soil improvement. In: AA Balkema (ed) Proceedings of environmental geotechnics and problematic soils and rocks, Rotterdam, The Netherlands, pp 15–24
24. Jose A, Nivitha MR, Krishnan JM, Robinson RG (2020) Characterization of cement stabilized pond ash using FTIR spectroscopy. In: Construction and building materials. https://doi.org/10.1016/j.conbuildmat.2020.120136
25. Joshi RC, Natt GS, Wright PJ (1981) Soil improvement by lime-fly ash slurry injection. In: Proceeding of 10th international conference on soil mechanics and foundation engineering, Stockholm, vol 3, pp 707–712
26. Kim B, Prezzi M, Salgado R (2005) Geotechnical properties of fly and bottom ash mixtures for use in highway embankments. J Geotech Geoenviron Eng 131(7):914–924
27. Knapton J (2006) Concrete block paving as a surfacing material for container storage areas. In: Proceeding of 8th international conference on concrete block paving, California, pp 700–709
28. Knapton J, Barber SD (1979) The behavior of a concrete block pavement. Proc Inst Civ Eng London 66(1):277–292
29. Kumar V (2004) Compaction and permeability study of pond ash amended with locally available soil and hardening agent. J Inst Eng India 85:31–35
30. Ladd RS (1978) Preparing test specimens using undercompaction. Geotech Test J 1(1):16–23
31. Livneh M, Goldberg Y (2001) Quality assessment during road formation and foundation construction: use of falling weight deflectometer and light drop weight. Transp Res Rec 1755:69–77
32. Maser KR, Wallhagen RE, Dieckman J (1975) Development of fly ash cement mine sealing system, USBM, NTIS-PB-250611, open file report 26–76
33. McLaren RJ, DiGioa AM (1987) The typical engineering properties of fly ash. In: Geotechnical special publication no 13, ASCE, New York, pp 683–697
34. Ministry of rural development (2014) Specifications for road and bridge works, 1st revision. Indian Roads Congress, New Delhi
35. Ministry of road transport and highways (2013) Specifications for rural roads, 5th revision. Indian Roads Congress, New Delhi
36. Mollah M, Yu W, Schennach R, Cocke DL (2000) A fourier transform infrared spectroscopic investigation of the early hydration of Portland cement and the influence of sodium lignosulfonate. Cem Concr Res 30(2):267–273. https://doi.org/10.1016/S0008-8846(99)00243-4
37. Nazzal M, Abu-Farsakh M, Alshibli K, Mohammad L (2004) Evaluating the potential use of a potable LFWD for characterizing pavement layers and subgrades. In: Yegian MK, Kavazanjian E (eds) Geotechnical engineering for transportation projects: proceedings of geo-trans, Los Angeles, California. American Society of Civil Engineers, Reston, VA
38. Pal SK, Ghosh A (2009) Shear strength behaviour of Indian fly ashes. IGC, Guntur, India
39. Palariski J (1993) The use of fly ash tailings, rocks and binding agents as consolidated backfill for coal mines. In: Proceeding of mine fill. SAIMM, Johannesburg, pp 403–408
40. Parswal IS, Makan OP, Atrea AK (2003) Eco friendly ash management in the form of ash mounds. In: Proceedings CBIP 3rd international conference-fly ash utilizations and disposal, New Delhi, India, III, pp 10–16
41. Prakash K, Sridharan A (2009) Beneficial properties of coal ashes and effective solid waste management. Pract Period Hazard Toxic Radioact Waste Manage 13(4):239–248
42. Puppala A (2008) Estimating stiffness of subgrade and unbound materials for pavement design. NCHRP Synthesis 382. Transportation Research Board, Washington, DC
43. Raymon S (1961) Pulverized fuel ash as embankment material. ICE Proc 19:515–536
44. Report on fly ash generation at coal/lignite based thermal power stations and its utilization in the country for the year 2017–18, Central Electricity Authority. https://www.cea.nic.in/reports/others/thermal/tcd/flyash_201718.pdf. Assessed 10 Oct 2020

45. Ryden N, Mooney M (2009) Analysis of surface waves from the light weight deflectometer. Soil Dyn Earthq Eng 29:1134–1142
46. Sagarmala (2018) National perspective plan executive summary, Ministry of shipping, Government of India. http://sagarmala.gov.in/sites/default/files/NPP%20executive%20summary.pdf. Assessed 10 Oct 2020
47. Sarkar R, Abbas SM, Shahu JT (2012) A comparative study of geotechnical behaviour of lime stabilized pond ashes from Delhi region. Int J GEOMATE 3(1):273–279
48. Shivamanth A, Pramod KK, Sharma PS, Desai MK, Desai AK (2015) Study of the light weight deflectometer and reviews. Int J Eng Res General Sci 3(6):42–46
49. Singh SP, Panda AP (1996) Utilization of flyash in geotechnical construction. In: Proceedings of the Indian geotechnical conference, Madras, India, vol 1, pp 547–550
50. Sridharan A, Pandian NS, Rajasedhar C (1996) Geotechnical characterization of pond ash. In: Raju VS et al (eds) Ash pond and ash disposal systems. Narosa Publishers, Delhi, pp 97–110
51. Sustainable sand mining management guideline (2016) Ministry of environment, forest and climate change. http://environmentclearance.nic.in/writereaddata/SandMiningManagementGuidelines2016.pdf. Assessed 10 Oct 2020
52. Suthar M, Aggarwal P (2016) Environmental impact and physicochemical assessment of pond ash for its potential application as a fill material. Int J Geosynth Ground Eng https://doi.org/10.1007/s40891-016-0061-7
53. Thoresen CA (2003) Port designer's handbook: recommendations and guidelines. Thomas Telford, London, UK
54. Toth PS, Chan HT, Cragg CB (1988) Coal ash as structural fill, with special reference to Ontario experience. Can Geotech J 25(4):694–704
55. Vennapusa P, White D (2009) Comparison of light weight deflectometer measurements for pavement foundation materials. Geotech Test J 32(3):1–13
56. Yang SL, Sandven R, Grand L (2006) Instability of sand-silt mixtures. Soil Dyn Earthq Eng 26:183–190
57. Ylmaz H (2015) Characterization and comparison of leaching behaviors of fly ash samples from three different power plants in Turkey. Fuel Process Technol 137:240–249
58. Zhu W, Chen X, Struble LJ, Yang EH (2018) Characterization of calcium containing phases in alkali-activated municipal solid waste incineration bottom ash binder through chemical extraction and deconvoluted Fourier transform infrared spectra. J Clean Prod 192:782–789

Chapter 10
Effect of Moisture Content on the Shear Strength Parameters

A. Palani Kumar, Suresh Maurya, and Kuldeep Kalra

Introduction

The top of earth crust is filled with soil. The soil is the primary construction material for earth retaining structures, embankment dams and foundation of the civil engineering structures resting on the soil. In general, soil is a three-phase system which consists of soil, water, and air. All the phases may exist when structure has excess to fluctuating water level, like in embankments and below the foundation of civil engineering structures. Compaction (expulsion of air) happens during construction period by mechanical means to improve the density of soil mass, and consolidation (expulsion of water) is a gradual process which takes place during and after construction with passages of time due to weight of structure. In soil mass, 100% compaction and consolidation are not practically possible; there may be a pore voids which may get fill with water or air and sometimes may be filled by both. In soil mass below the groundwater level or phreatic line (see Fig. 10.1), the soil is fully saturated; i.e., there is presence of two-phase system in which pore voids are fully filled with water. Just above the groundwater table or phreatic line, there is a presence of capillary zone and is three-phase system. When top soil surface in the field does not have access to water, soil remains unsaturated. Moisture content of soil mass above the saturated zone may vary with seasonal variation with fluctuation of groundwater table and subsurface and surface flow of water.

Groundwater Level (GWL): Groundwater is an important natural resource in the earth crust, and its water level (see Fig. 10.1a) varies with climate changes, rainfall conditions, surface water infiltration, voids ratio, and permeability of soil, which are an important component to create a three-phase system making soil more complex. Groundwater seepage in pore of soil has great influence on engineering properties of soil. Soil mass below the groundwater level is in saturated state, in which soil pores

A. Palani Kumar · S. Maurya (✉) · K. Kalra
Ministry of Jal Shakti, Deptartment of WR, RD and GR, CSMRS, New Delhi 110016, India
e-mail: maurya_suresh@yahoo.co.in

K. Muthukkumaran (eds.), *Soil Behavior and Characterization of Geomaterials*,
Lecture Notes in Civil Engineering 296, https://doi.org/10.1007/978-981-19-6513-5_10

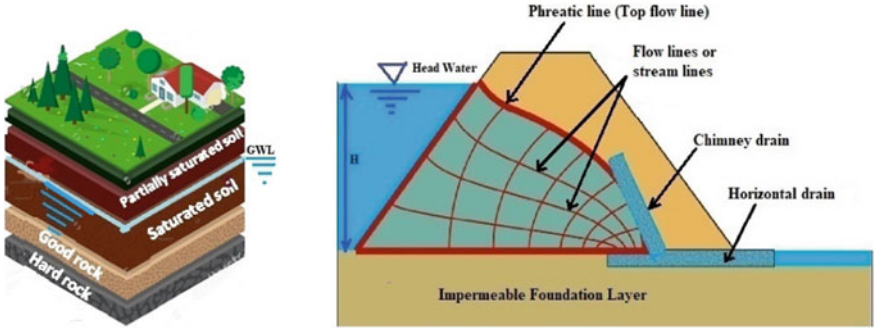

(a)Topography of earth (b) Homogeneous earth dam

Fig. 10.1 Earth structure with groundwater level and homogeneous dam with phreatic line

are filled with water (see Fig. 10.2a), whereas soil mass above the groundwater level is in partially saturated to unsaturated state, and therefore, its moisture content varies as shown in Fig. 10.2b, c.

Phreatic Line: Hydrostatic pressure in the embankment dam (see Fig. 10.1b) acts below the phreatic line, whereas atmospheric pressure exists above the phreatic line. The position of the phreatic line (top flow line) and flow lines below the phreatic line changes with the permeability characteristic of the soil. Phreatic line separates a saturated soil from an unsaturated soil. The soil mass below the phreatic line is fully saturated in which soil pores are filled with water (see Fig. 10.2a), whereas above the phreatic line, soil mass is in partially saturated to unsaturated state in which the degree of saturation varies from phreatic line to top of soil surface (see Fig. 10.2b, c).

Therefore, it is very much important to study the influence of the varying moisture content on the shear strength of the soil due to change in groundwater level or change in phreatic line.

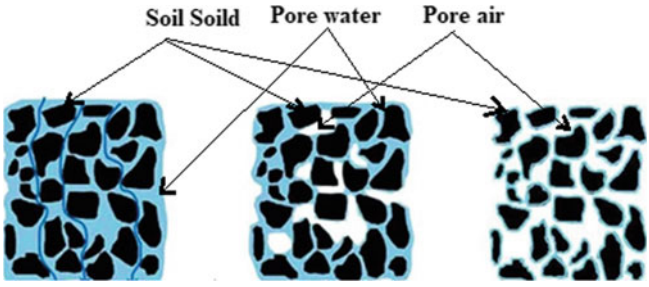

(a) Fully saturated (b) partially saturated (c) Unsaturated

Fig. 10.2 Phase diagram of soil

The maximum density of the soil mass can be achieved with optimum moisture content (OMC) by mechanical method. This moisture acts as a lubricant to hold the soil particles close to each other, and mechanical method expels air from the void spaces. Laboratory study to evaluate the shear strength of the compacted soil remoulded at 98% MDD under varying moisture content and further allowing compacted soil to undergo saturation may help to understand the similar condition of compacted field with fluctuating water levels. The shear strength parameters (c and ϕ) are influenced by soil type, density, drainage condition, etc. When clay is dominant in soil mass, the maximum shear strength is taken by cohesive force 'c', and when sand is dominant in soil mass, then the maximum shear strength is taken by angle of internal friction (ϕ).

Shear Strength and Factor Affecting the Shear Strength Characteristic

Shear Strength

In geotechnical engineering, the shear strength parameters are crucial for design work to produce safe structure design. Maximum resistance to shear stresses just before the failure is the shear strength of soil. The shear stress is the result from combination of self-weight from the soil mass and any external loads. When the shearing stress reaches its limit value due to the failure of a loaded soil mass, soil deformation is caused. With proper estimation, serious damage to property can be avoided. Shear strength is derived from cohesion 'c' and internal friction angle 'ϕ'. The origin cohesion is due to the cementing between the particles and chemical attraction between clay particles. Friction angle is due to interlocking between the particles. However, plastic undrained clay does not possess internal fiction.

There are many methods to evaluate shear strength of soil. The triaxial shear test is one of the versatile tests over other test method due to many reasons; i.e., failure occurs along the weakest plane; stress distribution on the failure plane is much more uniform, the triaxial machine has provision to stimulate the test with field conditions, complete control over the drainage is possible, it employs symmetrical three-dimensional stress over testing specimen, there is option to change the confining pressures (σ_3), precise measurement of pore water pressure, and volume changes during the test are possible. Triaxial shear test represent more realistically the stress conditions prevailing in the ground [1].

Factor Affecting the Shear Strength Characteristic

The shear strength is affected by moisture content, drainage condition, grain size, soil density, mineralogy composition, and shape of particle. When density is more, the shear strength tends to increase. Montmorillonite minerals in soil particles, increases cohesion 'c'. When clay content in high shear strength is taken by cohesive force and when soil mass is dominant by sand/granular material, then the value of angle of internal friction 'ϕ' is higher. The test results may vary and depend upon the condition of drainage, and therefore, simulating the field drainage in laboratory can bring best results.

The stress state that acts on a point can be represented graphically in a coordinate system. The Mohr circle can be constructed from the normal stress and shear stress and two principal stresses (σ_1 and σ_3) as shown in Fig. 10.3. The failure occurs when the stresses are such that Mohr circle touches the failure envelope [2]. This failure theory is the most practical theory applied in analysis of shear strength.

Failure envelope also known as strength envelope is represented and described by a straight-line in Mohr–Coulomb. Straight-line is by a linear function of the normal stress 'σ'. Here, the value of 'c' is the intercept on τ-axis and 'ϕ' is the angle which the envelope makes with the normal stress axis.

$$\text{Shear strength, } \tau = c + \sigma \tan \phi \tag{10.1}$$

Wang et al. [3] studied the effect of shear strength parameters from triaxial test under CD and CU drainage condition in loess soil. CD has shown smaller strength parameter as compared to CU test. He has shown the importance of plastic limit in test. When water content exceeds the plastic limit, cohesion reduces remarkably. Internal friction angle did not change significantly with the variation of water content.

Ghosh [4] plotted the shear strength curve for different compactions from the vane shear test which shows decrease in the shear strength with increase in water content.

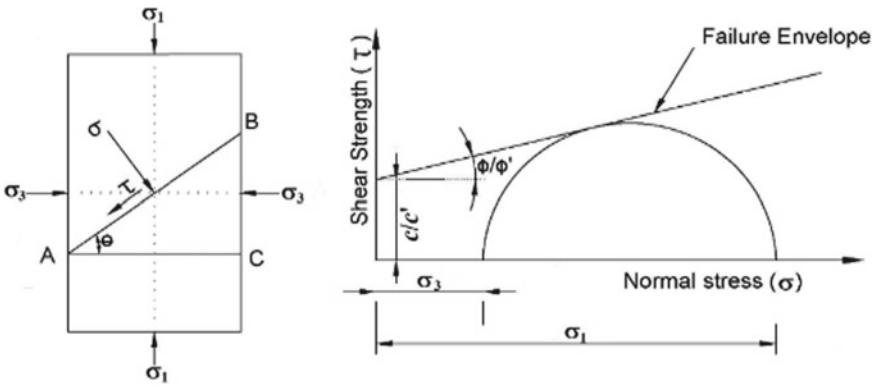

Fig. 10.3 Representation of principal stresses (σ_1 and σ_3)

Dafalla [5] studied from the direct shear test that both cohesion and angle of the internal friction decrease with the increase in moisture content in different proportions of clay content to sand.

Objective and Scope of Study

With the fluctuation in groundwater level, there is variation in moisture content in the ground. The shear strength of soil may be directly affected by these variations in moisture content. General information on application of laboratory tests to field problems is presented in Head, volume 3 [6]. Triaxial CU shear test is adopted to simulate the field condition in the laboratory. This test has complete control over the drainage functions, and specimen is free to fail along the poor plane. Two field conditions are modelled in laboratory study. In both the cases, specimens were remoulded at 98% MDD at varying moisture content.

(Case-I): Remoulded laboratory specimens were prepared with different moisture contents. As B-factor measured in machine was less than 0.9, it is in the partially saturated state. Further, no saturation of remoulded specimens was carried out with back pressure and the specimens were sheared to obtain shear strength parameters. This case represents the similar condition of soil mass above groundwater table or phreatic line.

(Case-II): In this case, laboratory specimen was remoulded at similar moisture content as done in case-I. Unlike case-I, specimens were further saturated with the help of back pressure system exhibiting B-factor greater than 0.9 [6], representing saturated state of the soil. This has allowed to replace the air voids in the specimen with water without altering the matrix of soil structure which has been formed during remoulding. This case represents the condition of soil mass coming in contact with water due to increase in water table which is in contrast of the case-I, having water table below the soil mass.

The study aims to understand the stress–strain characteristic and shear strength behaviour of partially saturated to saturated state of MI type of soil in the laboratory. The results of triaxial CU shear test are discussed in Sect. 10.5.

Material and Test Method

Material

The basic physical properties of soil are presented in Table 10.1. Three samples with different water contents were prepared from same soil to find out the effect of water content on shear strength. Samples were prepared keeping the water content as shown in Table 10.2.

Table 10.1 Physical properties of soil

Physical properties	Value
BIS classification	MI
Atterberg limit (LL, PL, PI)	(42.8, 29.2, 13.6)
Specific gravity (G)	2.73
Maximum dry density (MDD/γd(max))	1.65 g/cc
Optimum moisture content (OMC)	20.4%
Saturated moisture content (SMC)	25.18%

Table 10.2 Moisture content of samples

Sample no.	Moisture content, w (%) during remoulding of specimens
1	22.08
2	23.62
3	25.18

Preparation of Specimen

Three sample with above water content was divided into two different cases. In case-I, four identical specimens from each samples were remoulded at 98% of MDD into a cylindrical shape (size 38 $\times$ 76 mm) with H/D ratio of 2 as per IS: 2720-Part 12 [7]. Cylindrical specimen holding filter paper and porous stone are placed between rigid caps, enclosed with membrane and fasten with O-ring. Perspex cylinder is then fixed on a triaxial cell apparatus which is later filled with water (see Fig. 10.4). B-factor measurement for all the specimens was found to be less than 0.9, representing partially saturated state of soil. B-factor is the ratio of incremental pore water pressure to the increase in cell pressure.

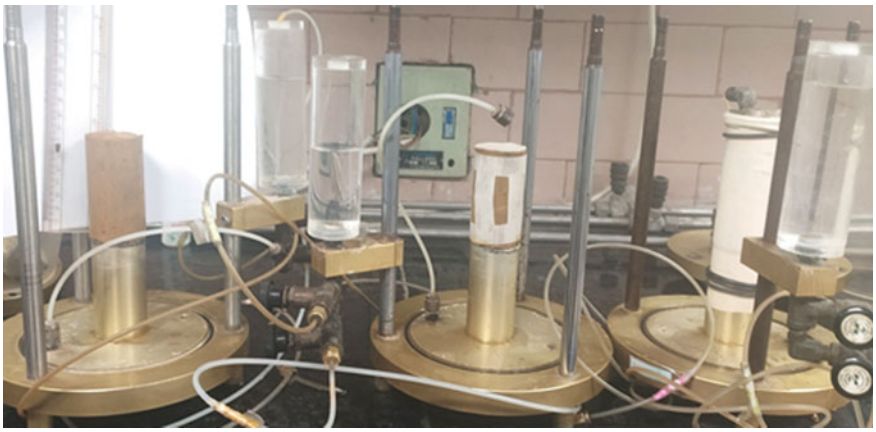

Fig. 10.4 Specimen preparation in triaxial cell

In case-II, laboratory specimens were remoulded and placed in a cell as done in case-I. Unlike case-I, specimens were further saturated with the help of back pressure system which exhibited B-factor greater than 0.9, representing saturated state of soil.

Test Method

To study the shear strength of soil in both the cases, specimens were tested in triaxial machine as shown in Fig. 10.5. CU tests were carried out with increasing confining pressures, σ_3 (1, 2, 3, and 4 kg/cm^2) to obtain deviator stress–axial strain curve. From the graph of results plotted, 'c' and 'ϕ' are determined from the best-fit line of failure envelope (see Fig. 10.6).

The top points of the Mohr circle correspond to the maximum stresses and are designated as 'p' and 'q' [8].

$$\text{where } p = \frac{(\sigma_1 + \sigma_3)}{2} \quad \text{and} \quad q = \frac{(\sigma_1 - \sigma_3)}{2} \tag{10.2}$$

Straight-line through points 1, 2, 3, and 4 make an angle 'α' with the p-axis and an intercept 'a' on the q-axis and has the straight-line equations as $q = a + p \tan \alpha$. From the coulomb equation of $\tau = c + \sigma \tan \phi$, the values of parameters 'c' and 'ϕ' are obtained from the intercept 'a' and the slope 'α', using below equations.

Fig. 10.5 Triaxial machine

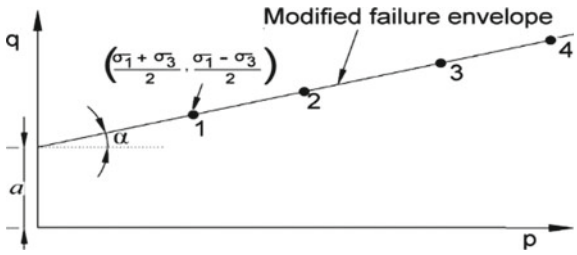

Fig. 10.6 *p-q* plot for modified failure envelope [8]

$$c = \frac{a}{\cos \emptyset} \quad \text{and} \quad \phi = \sin^{-1}(\tan \alpha) \tag{10.3}$$

Results and Discussion

Deviator stress–axial strain graphs achieved from experimental test for varying water content, w (%) at incremental confining pressures (σ_3) for both the cases are shown in Fig. 10.7. Each sample is tested at four different confining pressures of 1, 2, 3, and 4 kg/cm^2. Because of relative complexity of the test, inconsistent graphs were omitted and minimum three readings of different confining pressures were considered to plot the failure envelopes.

The deviator stress–axial strain curve with different, w (%), presents the characteristic of strain hardening behaviour under different confining pressures (σ_3) in all the cases. However, saturated samples show relatively flatter stress–strain curve as compared to partially saturated samples. At confining pressure of 4 kg/cm^2, the deviator stress (σ_d) to cause failure is observed in the range of 7.5–8.4 kg/cm^2 in case-I, whereas in case-II, at same confining pressure, the deviator stress (σ_d) to cause failure is observed in the range of 4.3–5.1 kg/cm^2. This shows that strain hardening takes place early in saturated specimens and the deviator stress to cause failure decreases significantly as compared to partially saturated specimens.

Maximum normal stress (p) and shear stress (q) values are calculated using Eq. 10.2, and failure envelopes for both the cases are plotted as shown in Fig. 10.8. Failure envelope of saturated samples exhibiting B-factor > 0.9 is more towards horizontal than partially saturated samples exhibiting B-factor < 0.9. This shows that when degree of saturation is increased with the help of back pressure, the shear stress to cause failure decreases and failure envelope tends to drop [9].

Strength parameters 'c' and 'ϕ' are achieved from the intercept 'a' and slope 'α' of modified failure envelopes using Eq. 10.3 and set out in Table 10.3.

Figure 10.9 implies that ϕ component plays an active role in controlling the shear strength of soil in both the cases (see impact of ϕ on τ in Table 10.3). In partially saturated state, cohesion, c, decreases continuously with increase in moisture content

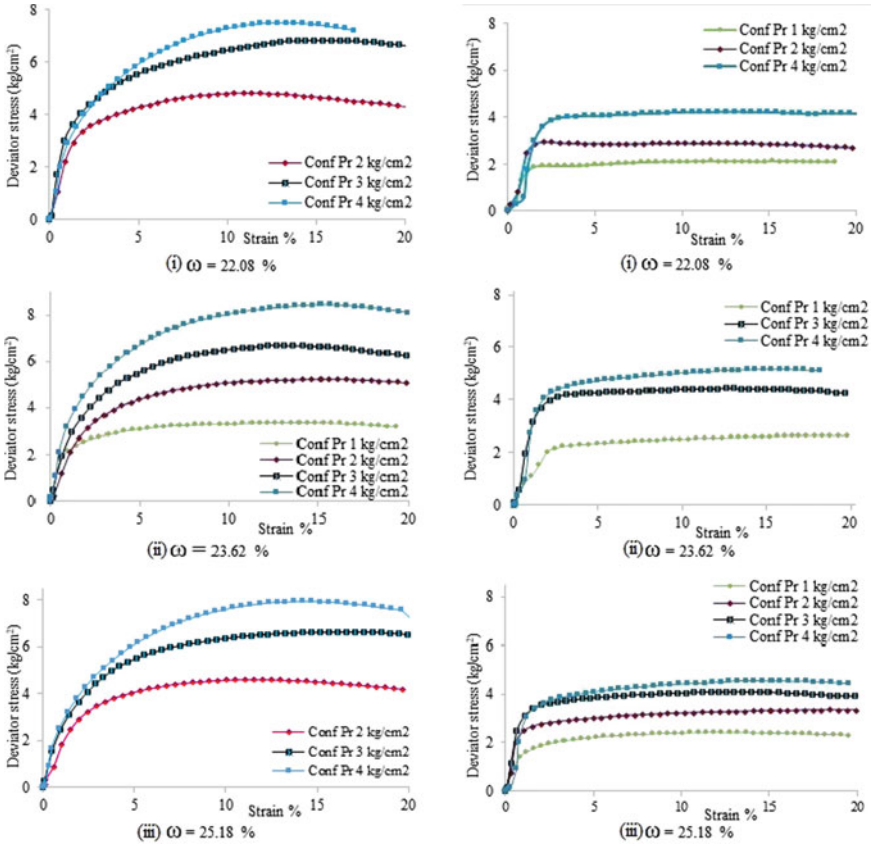

(a) Case I: Specimens exhibiting B-factor < 0.90 (Partially saturated state) (b) Case II: Specimens exhibiting B-factor > 0.90 (Saturated state)

Fig. 10.7 Deviator stress versus axial strain graph obtained for partially saturated and saturated samples at varying moisture content (i) 22.08%, (ii) 23.62%, and (iii) 25.18% with respect to B-factor

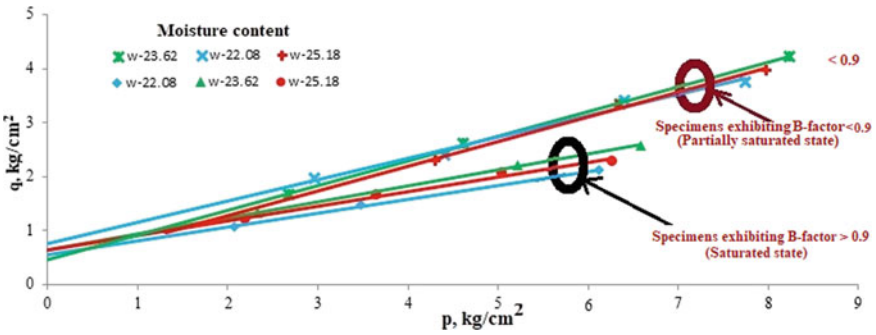

Fig. 10.8 '*p-q*' plot and modified failure envelope

Table 10.3 Obtained shear strength parameters

Sample no.	Moisture content, w (%)	Measurement of B-factor	c (kg/cm^2)	ϕ (Deg)	Assumed normal stress, σ_v (kg/cm^2)	Shear strength, τ (kg/cm^2)	Effect of ϕ on τ, (%)
1	22.08	< 0.9 (Partially saturated state	0.71	24	4	2.51	71.79
2	23.62		0.53	27		2.58	79.41
3	25.18		0.41	27		2.47	83.20
1	22.08	> 0.9 (Saturated state)	0.57	15	4	1.64	65.18
2	23.62		0.67	17		1.92	64.71
3	25.18		0.67	15		1.78	62.03

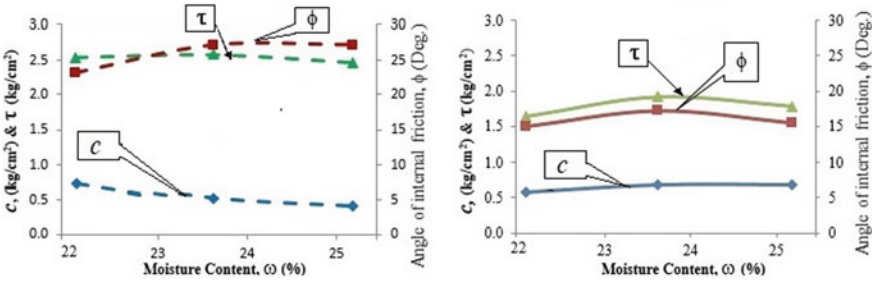

Fig. 10.9 Shear strength (τ), parameters (c and ϕ versus ω (%) plot. **a** Case-I: B-factor < 0.9, partially saturated state, **b** Case-II: B-factor > 0.90, saturated state

as shown in Fig. 10.9a, whereas in saturated state the change in cohesion is marginal as shown in Fig. 10.9b. The cohesion has little effect on the shear strength of soil.

Samples in saturated state loses its shear strength significantly as compared to partially saturated samples as shown in Table 10.3 (shear strength, τ is calculated using Mohr–Coulomb Eq. 10.1).

Conclusions

The water level in the field may fluctuate due to climate changes, rainfall conditions, surface water infiltration, and other man-made construction like water conveyance structure, etc. Two field cases (i.e. partially saturated and saturated state of soil) modelled in triaxial CU shear test from the same remoulded samples were studied. This paper characterizes the variation of shear strength parameters of MI type of soil at varying moisture content in both the cases under incremental confining pressures (σ_3). With the increase in moisture content, shear strength initially increases, and beyond critical moisture content, shear strength decreases. 'ϕ' curve follows

similar profile of shear strength, which implies that 'ϕ' component plays an active role in controlling the shear strength of soil in both the cases. There is significant decrease in the shear strength in saturated samples exhibiting B-factor > 0.9 as compared to partially saturated samples without back pressure, exhibiting B-factor < 0.9. Remoulded specimen exhibiting B-factor > 0.9 ensures that the air voids in the specimen is replaced by water without altering the matrix arrangement of soil particles. Therefore, it is important to test the sample in laboratory at its weakest state, i.e. at saturated condition having B-factor of preferably 1.0 but not less than 0.9 [7]. This will help to correctly select the minimum shear strength of soil mass in its saturated state, if field site has an access to water or any possibility of rise in groundwater level in near future.

References

1. Head KH (1994) Permeability, shear strength and compressibility tests. In: Manual of soil laboratory testing, vol 2, 2nd edn. Halsted Press (an imprint of Wiley), New York
2. Punmia BC, Jain AK, Jain AK (2017) Soil mechanics and foundation, 17th edn. Laxmi Publication, New Delhi
3. Wang Y, Xie W, Gao G (2019) Effect of different moisture content and triaxial test methods on shear strength characteristics of loess. In: IS-Glasgow 2019, E3S web of conferences 92, 07007. https://doi.org/10.1051/e3sconf/20199207007
4. Ghosh R (2013) Effect of soil moisture in the analysis of undrained shear strength of compacted clayey soil. J Civ Eng Constr Technol 4(1):23–31. https://doi.org/10.5897/JCECT12.070
5. Dafalla MA (2013) Effects of clay and moisture content on direct shear tests for clay-sand mixtures. J Adv Mater Sci Eng 2013, Article Id 562726. https://doi.org/10.1155/2013/562726
6. Head KH (1998) Effective stress tests. In: Manual of soil laboratory testing, vol 3, 2nd edn. Wiley, England
7. IS: 2720-Part 12 (2016) Determination of shear strength parameters of soil from consolidated undrained triaxial compression test with measurement of pore water pressure. Bureau of Indian Standards, New Delhi, India
8. Arora KR (2003) Soil mechanics and foundation engineering, 6th edn. Standard Publisher, New Delhi
9. Palani KA, Maurya S, Gupta M, Chitra R (2020) Degree of initial saturation and shear strength of soil in a triaxial loading. Int J Emerg Technol Innovative Res 7(4):805–812

Chapter 11
Compaction Characteristics of Fibre-Reinforced Expansive Soils—Plasticity Approach

Unnam Anil, H. S. Prasanna, S. Mahesh Kumar, and Mahalakshmi

Introduction

A large portion of land covers almost one-fifth of area of the Indian subcontinent being covered with expansive soil. Expansive soils exhibit high shrinkage and swelling characteristics connected with changes in moisture content, because of the inbuilt characteristics presented in the expansive soils having lesser strength, higher compressibility and swell–shrink behaviour due to change in moisture content. There are two important approaches used for the expansive soil stabilization that are mechanical modification and chemical modification. Chemical modification technique was useful in improving the cohesive nature (acted like binder) and strength of the expansive soil. The mechanical modification is involved in different rolling and reinforcement techniques. General reinforcement materials used are artificial or synthetic and fibres made from plants (natural). The reinforcement leads to increase in strength and decrease in deformation. The main advantage of fibres will make the arrangement of soil fabric in orientation that makes particles agglomerated. In this study, polyester (Recron 3s) fibres are used to prepare the composite soil. Natural fine-grained soils are mixtures of clay minerals and other than clay minerals. The engineering behaviour was controlled by the clay minerals presented in the expansive soil, i.e. especially physicochemical phenomenon. The present experimental research study focuses mainly on the fibre-reinforced expansive soils. The natural expansive soils having liquid limit range from 50 to 90% are carefully selected based on the clay mineralogical composition. The soils that are used fall under the IS classification of CH that is the soil of high compressibility. The CH type of soil is specifically used since these make treatment requisite for any construction activity. The fibres having different aspect ratios will be blended with soil based on design mix proportions with percentage variation of 0.5, 1, 1.5, 2, and 2.5%. The compaction and

U. Anil (✉) · H. S. Prasanna · S. Mahesh Kumar · Mahalakshmi
Civil Engineering, NIE, Mysuru 570008, India
e-mail: anil.nanna441@gmail.com

K. Muthukkumaran (eds.), *Soil Behavior and Characterization of Geomaterials*,
Lecture Notes in Civil Engineering 296, https://doi.org/10.1007/978-981-19-6513-5_11

unconfined compressive strength (UCS) tests will be conducted on the soils having different liquid limits and at the optimum fibre-reinforced soil for different energy levels like IS light and heavy compaction.

Literature Review

Kumar et al. [1] explained about the study of blending nylon fibres into the silty clay soil and comparing the relative strength parameters in the form of unconfined compression strength. The values of degree of compaction were affected the amount of fibre percentage in the soil. The samples having 93% of maximum dry density show the higher strength in peak and residual position when compared with higher density compaction, and also, the residual strength of soil with addition of fibres is higher when compared with the peak strength effect. There was an increase in amount of fibres, the stains at peak strength was increased.

Laskar et al. [2] evaluated that, the effect of waste plastic fibres on compaction and consolidation behaviour of reinforced soil. The fibres are used for reinforcing given clay soil of different aspect ratios (2, 4, and 8) and in different percentages (0, 0.25, 0.5, and 1%), respectively. The content of fibres in reinforced soil is defined as $W = W_f / W_s$, where W_f is the weight of plastic fibre and W_s is the weight of oven-dried soil sample. Plastic fibres have been added to soil with the optimum water content (OMC) and kept it in airtight bag in the laboratory at room temperature for 24 h; with the results obtained from compaction test, it is concluded that the magnitude of maximum dry density (MDD) is decreasing with increase in amount of fibre and OMC is independent because of no water absorption capacity for the fibre.

Viswanadham et al. [3] reported that the excessive swelling capacity of expansive soils was controlled or restrained by the distribution of discrete or random geofibres introducing in to the expansive soils. The reinforcement is added in to the soil in different aspect ratios ($l/b = 15, 30,$ and 45) and fibre percentages ($f = 0.25$ and 0.5%) on one-dimensional consolidation swell-consolidation test apparatus to analyse the swelling characteristics. There is a reduction in swelling pressure, and heave was observed at the both fibre contents of 0.25 and 0.5% (at low aspect ratio).

Phanikumar et al. [4] investigated that reinforcing the expansive soil with fibres becomes most useful technique than the other methods; these fibres can control the swell–shrink behaviour of expansive soil. Here, the nylon fibres were used with different percentages (0, 0.05, 0.10, 0.15, 0.20, 0.25, and 0.30%) and in different lengths of 15 and 20 mm. The heave, swell potential, and vertical swelling pressure were decreased with increase in fibre content up to 0.25%, and at $fc = 0.3\%$, they were increased, and they also decreased with increase in fibre length. The secondary compression decreases with increase in fibre content and length of a fibre.

Kar et al. [5] mentioned that the main subject of this project is to study the consolidation behaviour of compacted clay by reinforcing the fibres randomly of different lengths by dry weight of soil. The results of consolidation characteristics like coefficient of compression index (Cc) and coefficient of volume compressibility (Mv) were decreasing with increase in fibre content up to certain limit; thereafter, it is increasing, whereas with increase in fibre content, the values of coefficient of consolidation was increasing and the time of consolidation is decreasing with increase in fibre content of the soil.

Rajoria et al. [6] studied about the effect on the geotechnical properties of expansive soil using polymer stabilizer. The addition of polymer caused a significant modification in engineering properties. The polymer addition showed considerable improvement in strength, CBR, as well as swelling characteristics.

Kumar et al. [7] studied about the behaviour of black cotton soil in terms of CBR and compaction characteristics by adding the Recron 3s fibre. Generally, the soils are having sufficient shear strength and compression strength, and they are weak in tensile strength. The tensile strength factor is covered by the reinforcement in the soil through blending the fibres into the soil. The fibres were added in different cut lengths (6 and 12 mm) and percentages (0.5–4%) by taking dry weight of soil into consideration, and they were compacted at OMC and MDD. There is a reduction in OMC, and MDD was observed with addition of Recron 3s fibre to the soil.

Pasupalak et al. [8] studied about the expansive soils which are problematic soils, exhibiting swelling and shrinkage for change in moisture content. The polyester fibres are used in different lengths (3, 6, 9, and 12) and in different percentages (0.05, 0.10, 0.15, and 0.20) for reinforcement of soil. The maximum heave and swell pressure at equilibrium is decreased with increasing fibre content for a given length of fibre. Even so the behaviour of heave and swelling is different for a group length of fibres and after the optimum percentage, the heave and swelling pressure were increased.

Soltani et al. [9] reported the capacity of fibre to resist the swelling behaviour of expansive soil. The fibres were used as different percentages (0.5, 1, and 1.5) and different aspect ratios (15/2.5, 30/2.5 for fibre A and 15/7, 30/7 for fibre B). In the mentioned fibre particulars, the wider fibres are more efficient in resisting the swelling. For both fibre types, the optimum percentage of fibre is fc = 0.5%.

Materials and Method

Nearly, ten field soils were collected from various places around Mysuru and Chamarajanagar districts. Out of ten soils, three soils were finalized based on their liquid limit and free swell ratio [10]. The Atterberg limits were obtained by Casagrande method. Finally, the soils below mentioned were identified to be used in the present experiment.

1. Field soil 1 from Kuderu, Mysore district, which contains a dominant clay mineral, i.e. kaolinite montmorillonitic (K-M).
2. Field soil 2 from Kollegal, Chamarajanagar district, this soil having montmorillonitic (M) clay mineral dominance.
3. Field soil 3 from Kuntur, Chamarajanagar district, this soil having montmorillonitic (M) clay mineral dominance.

Recron 3s fibre is a type of polyester fibre which is made artificially, and it is collected from Reliance Industries.

Compaction Test

Standard and modified compaction tests were conducted on the natural and fibre-reinforced soils (Standard or Light Compaction) [11], and (Modified or Heavy Compaction) [12]. For the preparation of saturatedcompaction samples, there are around 6–9 samples were taken of each sample mass is 2.5 kg were mixed with different percentages of moisture contents for saturation. After putting the soil samples in saturation for required period, the proctor compaction tests were conducted on the soil samples to achieve maximum dry density (MDD) and optimum moisture content (OMC).

Unconfined Compression Test

In this test, a cylinder of soil without lateral support is tested to failure in simple compression, at a constant rate of strain. The compressive load per unit area is required to fail the specimen as called unconfined compressive strength (UCS) [13] of the soil. For the desired water content and the dry density, we calculate the weight of the dry soil required for preparing a specimen of 3.8 cm diameter and 7.5 cm long. In the present experimental study, the samples were compacted to the desired OMC and MDD in the split moulds for natural and fibre-reinforced soils. They were subjected to axial compression, and the loads corresponding to failure were recorded, and the variation of UCS values with percentage of fibre content was plotted for all the soils under study (Tables 11.1 and 11.2).

Table 11.1 Physical and index properties of soils

Soil properties	Soil 1	Soil 2	Soil 3
Specific gravity	2.69	2.87	2.72
Liquid limit (%)	58	74	85
Plastic limit (%)	27	26	28.5
Shrinkage limit (%)	17.6	8	16.7
Plasticity index (I_p)	31	38	56.5
Shrinkage index (I_s)	9.4	18	11.8
Activity (A)	1.291	1.461	0.94
Free swell ratio (FSR)	1.78	2.30	1.58
Grain size distribution			
Clay (%)	24	26	60
Silt (%)	48	52	31
Sand (%)	28	22	9
Dominant clay mineral present	K-M	M	M
IS classification	CH	CH	CH

Table 11.2 Properties of Recron 3s fibre

Particulars	Property
Density	0.91 g/cm^3
Cut length	12 mm
Diameter	0.034 mm
Water absorption	85%
Color	White
Humidity	< 0.1%
Acid resistance	Very good
Alkali resistance	Very good
Tensile strength	1400 MPa

Results and Discussion

Index Properties of Soil with Addition of Fibres

Figures 11.1, 11.2, 11.3, 11.4, 11.5 and 11.6 show that the variation of index properties with percentage variation of fibres of soils having different liquid limit ranges.

From Figs. 11.1, 11.2 and 11.3, it can be observed that the liquid limit of soils increasing with percentage variation in fibres for the soils having different liquid limit ranges. This is due to fact that the water absorption capacity of Recron 3s fibres (85%), i.e. with increase in fibre content, is leading to increase in moisture absorption

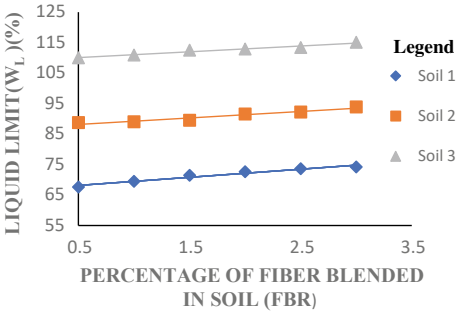

Fig. 11.1 Liquid limit variation with varying percentage of fibers of soils

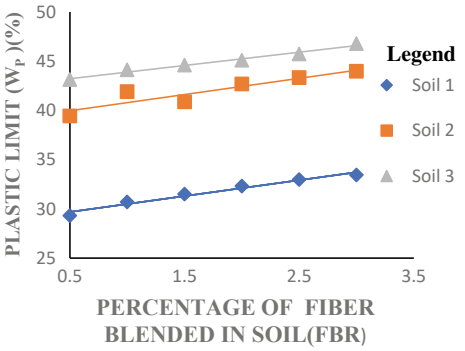

Fig. 11.2 Plastic limit variation with varying percentage of fibers of soils

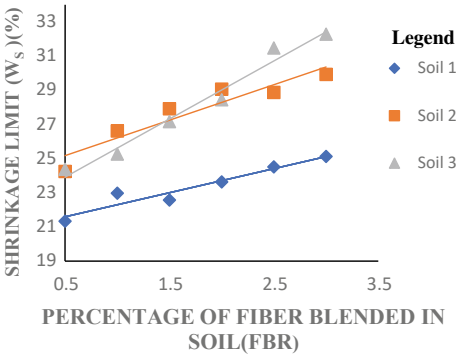

Fig. 11.3 Shrinkage limit variation with varying percentage of fibres of soils

fibres which were blended in the soil. Similar behaviour was observed for the plastic limit and shrinkage limit also for the soils under study. From Figs. 11.4, 11.5 and 11.6, it can be observed that the soils 1 and 3 are having less activity (A) and which is leading to increase in the values of I_s and I_p with variation of percentage of fibre, whereas for soil 2 which is highly active (A), it is leading to decrease in the values of I_s and I_p with increase in the percentage of fibre which was observed. This is due to the fact that the increase in percentage of clay fraction and montmorillonitic clay

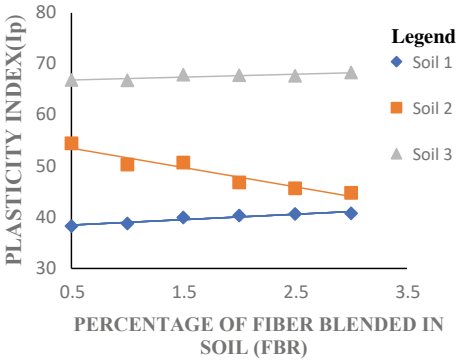

Fig. 11.4 Plasticity index variation with varying percentage of fibers of soils

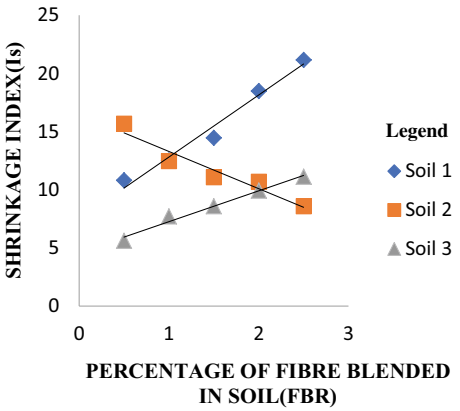

Fig. 11.5 Shrinkage index (*I*s) variation with varying percentage of fibers of soils

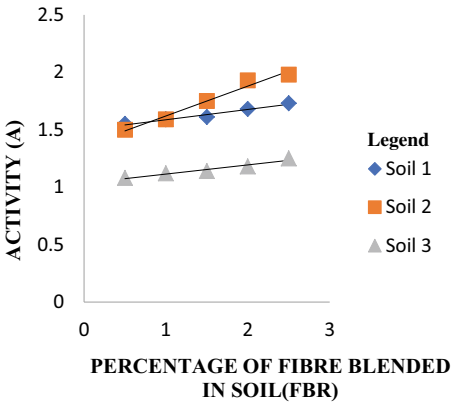

Fig. 11.6 Activity (*A*) with varying percentage of fibers of soils

mineral dominance was leading to increase in interparticle attraction which decreases the magnitude of particle flocculation and also the amount of void space available for water entrapment at liquid limit [Dispersed soil fabric structural arrangement, i.e. no face-to-face orientation] [14]. There is low magnitude of difference (23%) in plasticity characteristics of soil (W_L, W_P and W_S) for the Soil 1 and 2, whereas for the soil 3 it is higher (66%) with addition of fibres is leading to decrease in I_P, I_s and A when compared with soil 1 and 2. There is an improvement in the plasticity characteristics of expansive soils having liquid limit range from 58 to 74% with addition of Recron 3s fibres from 0.5 to 3% was observed, i.e. that the percentage of clay and silt fraction (fines) is having less particle size (high specific surface area) is influencing the more amount of water entrapment into soil voids, which intern leading to increase repulsive force of action between soil particles with increase in liquid limit of the soil, this is attributed to the behaviour of plasticity characteristics. This is due to fact that the soil having 74% liquid limit range can be considered as the optimum liquid limit range for improving the plasticity properties of expansive soil with addition of fibres.

Results of Compaction Characteristics with Varying Different Percentage of Fibres

Figures 11.7, 11.8, 11.9, 11.10, 11.11 and 11.12 shows that the variation of compaction characteristics (Optimum moisture content (OMC) and Maximum dry density (MDD) with addition of different percentage of fibres for the soils having different liquid limit ranges.

From Figs. 11.7 and 11.8, it can be observed that the magnitude of maximum dry density was achieved at 0.5% blending of fibre for light compaction and 1.5% blending of fibre for heavy compaction of the soil having liquid limit 58%.

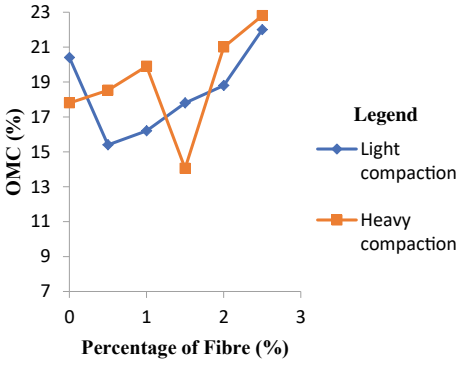

Fig. 11.7 Variation of OMC with different percentage of fiber for soil 1

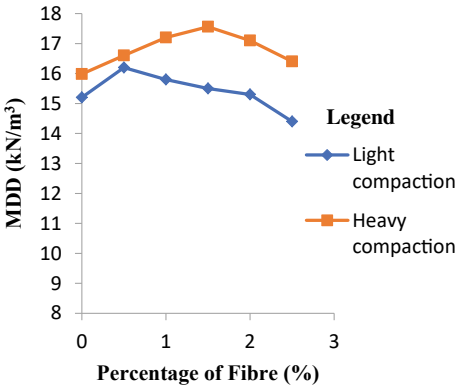

Fig. 11.8 Variation of MDD with different percentage of fiber for soil 1

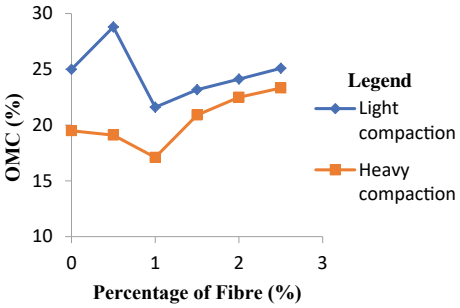

Fig. 11.9 Variation of OMC with different percentage of fiber for soil 2

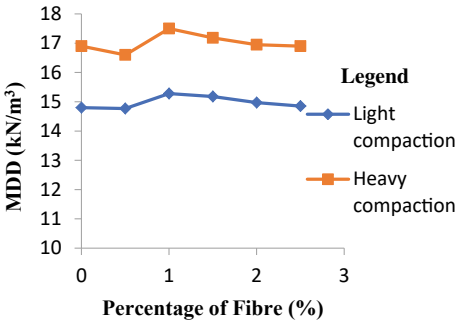

Fig. 11.10 Variation of MDD with different percentage of fiber for soil 2

From Figs. 11.9 and 11.10, it can be observed that the magnitude of maximum dry density was achieved at 1% blending of fibre for both standard proctor compaction and modified proctor compaction of the soil having liquid limit 74%.

From Figs. 11.11 and 11.12, it can be observed that the magnitude of maximum dry density was achieved at 2% blending of fibre for both standard and modified proctor compaction tests of the soil having liquid limit 85%.

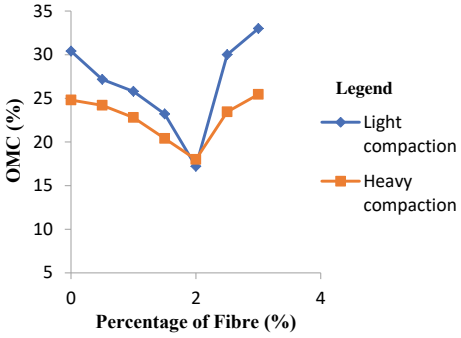

Fig. 11.11 Variation of OMC with different percentage of fibre for soil 3

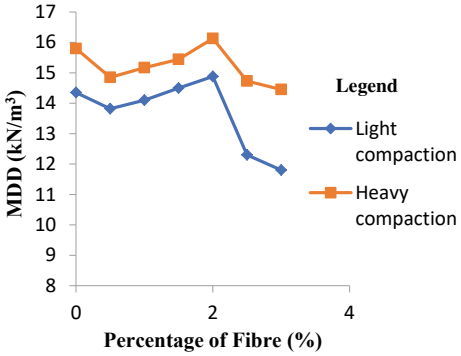

Fig. 11.12 Variation of MDD with different percentage of fibre for soil 3

From Figs. 11.7, 11.9 and 11.11, it is observed that there is a decrease in OMC up to optimum percentage of fibre, i.e. up to maximum magnitude of MDD. This behaviour can be attributed to the fact that according to Proctor's capillarity and lubrication theory [15], the water has a dual effect of capillarity (or suction) and lubrication. It is observed that, due to high capillarity, the dry density is lower for dry soil, and as water is added, the capillarity is reduced, and water also lubricates the particle interaction, giving rise to increased dry density up to the maximum dry density. The fibres blended in the soil are filling the intra-void spaces of the soil particles up to maximum dry density level. After the optimum fibre content, there is no sufficient internal flow channel to accommodate in the intra-void spaces for the additional fibres presented in soil fibre mixture. This will increase the interface between the fibre and soil particles and at the same time increase the surface area of soil which is leading to increase in optimum moisture content of the soil.

From Figs. 11.7, 11.8, 11.9, 11.10, 11.11 and 11.12, it can be also observed that, the variation of percentage of fibre to the soils having different liquid limit ranges, the optimum percentage of fibre with maximum value of MDD was increasing with increase in the liquid limit of the soil, i.e. from 0.5 and 1.5% for the soil having liquid limit 58% whereas for 74% and 85%, it is 1% and 2% respectively.

Variation of Unconfined Compression Strength (UCS) Behaviour with Addition of Fibres

Figures 11.13, 11.14 and 11.15 show the variation of UCS with addition of different percentages of fibres for soils having different liquid limit ranges.

From Figs. 11.13 11.14 and 11.15, it is observed that the variation of UCS is increasing up to 0.5% blending of fibre for both standard and modified proctor

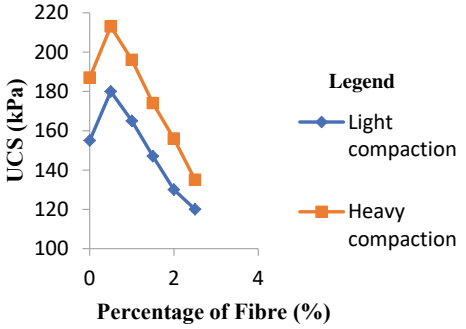

Fig. 11.13 Variation of UCS with different percentage of fibre of soil 1

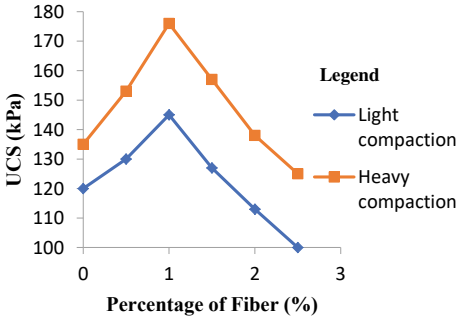

Fig. 11.14 Variation of UCS with different percentage of fibre of soil 2

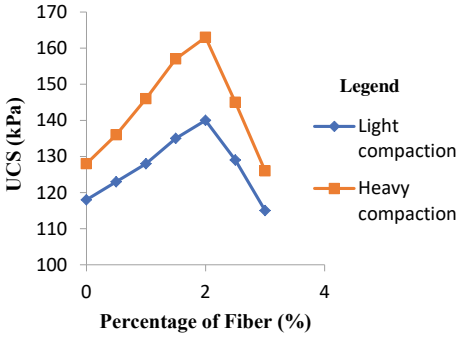

Fig. 11.15 Variation of UCS with different percentage of fibre of soil 3

compaction energy levels. It is due to the fact that the optimum percentage of fibre for soil 1 is 0.5%, whereas for soil 2 and soil 3, it is 1% and 2%, respectively. The optimum fibre content for maximum UCS increases with increase in the liquid limit of the soil.

From Figs. 11.7, 11.8, 11.9, 11.10, 11.11, 11.12, 11.13, 11.14 and 11.15, it can be observed that the strength characteristics (compaction and UCS) of soils having different liquid limit ranges with respect to addition of different percentage of fibres depend upon the optimum fibre content. The optimum fibre content depends upon the liquid limit of the soil; this is due to fact that it is leading to increase in water absorption of fibres that is effecting the increase in fibre content to be added to the soil.

Conclusions

The following conclusions can be made for the present experimental study:

- The plasticity characteristics of soils were increasing with percentage variation in fibres for the soils having different liquid limit ranges.
- The correlations made between the percentage of fibres and index properties of soils having different liquid limit ranges were accurate with R value ranging from 0.9 to 1.
- The soil having liquid limit (soil 2) (74%) is the optimum liquid limit range for improving the plasticity properties of expansive soil with addition of fibres.
- The optimum percentage of fibre (at maximum value of MDD and UCS) increases with increase in liquid limit of the soils.

References

1. Kumar S et al. (2003) Strength characteristics of silty clay reinforced with randomly oriented nylon fibers. Electron J Geotech Eng (EJGE)
2. Laskar A et al (2003) Effects of waste plastic fibers on compaction and consolidation behaviour of reinforced soil. Eur J Geotech Eng 18:1547–1558
3. Viswanadham BVS et al (2009) Swelling behaviour of a geo-fiber reinforced expansive soil. Geotext Geomembr 27:73–76
4. Phanikumar BR et al (2016) Swell-consolidation characteristics of fiber-reinforced expansive soils. Soils Found 56(1):138–143
5. Kar RK et al (2012) Consolidation characteristics of fiber-reinforced cohesive soil. Eur J Geotech Eng 17:3861–3874
6. Rajoria V et al. (2015) Effect of polymer stabilizer on the geotechnical properties of black cotton soil. In: 50th Indian geotechnical conference
7. Kumar PR et al (2017) Effect of CBR of black cotton soil reinforced with recron fiber. Imperial J Interdisc Res (IJIR) 3:1093–1097
8. Pasupalak S et al. (2017) Swell characteristics of expansive soil reinforced with polyester fibers. In: Indian geotechnical conference 2017-GeoNEst, pp 1–4

9. Soltani A et al (2017) Swell-compression characteristics of a fiber-reinforced expansive soil. Geotext Geomembr 46:183–189
10. Prakash K, Sridharan A (2004) Free swell ratio and clay mineralogy of fine grained soils. Geotech Test J ASTM 27(2):220–225
11. IS: 2720-Part 7 (1980) Indian standard methods of test for soils: determination of water content-density relation using light compaction (Second revision), Bureau of Indian Standards, New Delhi
12. IS: 2720-Part 8 (1983) Indian standard methods of test for soils: determination of water content-dry density relation using heavy compaction (Second revision), Bureau of Indian Standards, New Delhi
13. IS 2720-Part 10 (1991) Indian standard methods of test for soils: determination of unconfined compression strength, Bureau of Indian Standards, New Delhi
14. Sridharan A (1990) Engineering behaviour of fine grained soils: a fundamental approach. IGS Annual Lecture, pp 447–540
15. Proctor R (1933) Fundamental principles of soil compaction. Eng News Rec 111(9):245–248

Chapter 12
Parametric Study on Compaction Characteristics of Clay Sand Mixtures

C. Yogeshraj Urs and H. S. Prasanna

Introduction

Compaction is a process in which soil particles are densely packed mechanically by removing the air occupied in voids. Even though compaction appears to be a simple process of densification by the expulsion of air, it is not so in reality, particularly in fine-grained soils. Fine-grained soils predominately comprise sands, silts, and clay size fractions. The clay size fractions are just clay minerals, which form the active components of fine-grained soils.

The clay minerals have large variations in surface area and have surface charge; clay minerals have a variety of clay particle arrangements or can be termed clay fabric. The clay fabric together with the interparticle forces can be termed soil structure which determines the behaviour of clay soils. The clay size fraction that is present in natural soil can thus influence its behaviour depending upon its mineralogy. Thus, mineralogy can be considered fundamental to the understanding of geotechnical properties [1]. Activities such as the construction of embankments, pavements–highway, railway, and airfield pavements, earthen dams, preparation of the subsoil to receive the superimposed structural loads, reclamation of waste, and marginal lands and the like involve compaction of soils. These studies must consider the effect of clay mineralogical composition also to meet the reality. It may be inferred that it is of practical significance to study the compaction behaviour of fine-grained soils, with particular reference to the effect of soil clay mineralogy. In the present

C. Yogeshraj Urs (✉) · H. S. Prasanna
Department of Civil Engineering, The National Institute of Engineering, Mysuru 570008, India
e-mail: yogeshraj.urs@christuniversity.in

H. S. Prasanna
e-mail: prasanna@nie.ac.in

C. Yogeshraj Urs
Department of Civil Engineering, School of Engineering and Technology, Christ (Deemed to be University), Bangalore 560074, India

K. Muthukkumaran (eds.), *Soil Behavior and Characterization of Geomaterials*,
Lecture Notes in Civil Engineering 296, https://doi.org/10.1007/978-981-19-6513-5_12

experimental study two mix proportions, one with pure kaolinite clay containing various proportions of fine sand particles representing kaolinitic dominant soils and the second with pure bentonite clay containing various proportions of fine sand particles representing mont-morillonitic dominant soils were prepared artificially were tested and compared with natural soils representing kaolinitic and montmorillonitic dominance.

Literature Review

Dumbleton and West [2] developed a relationship between the Atterberg limits and the percentage clay content considering natural clay soils and artificially mixed clay soils containing clay minerals and quartz sand. The proposed relationship for montmorillonitic soils was reasonably agreeable, but there were larger deviations in the case of kaolinitic soils.

Blotz et al. [3] developed an equation for estimating maximum dry unit weight and optimum water content of clayey soils at any reasonable compaction effort E. Using liquid limit and a compaction curve, they concluded that a linear relationship exists between them.

Gurtug and Sridharan [1] correlated maximum dry density (γ_{dmax}) and optimum moisture content (OMC) with plastic limit (PL). The data were obtained from experimental work conducted on five natural soil samples with varying plasticity and data available in the literature. They concluded a good correlation exists between γ_{dmax}, OMC, and PL.

Sridharan and Nagaraj [4] developed correlation equations between index properties and compaction characteristics from the experimental conducted on five natural different pair of soils with nearly same liquid limit, and results from available literature were used. They concluded plastic limit bears a good correlation with compaction characteristics than liquid limit or plasticity index.

Sivrikaya et al. [5] proposed correlation equations that relate index properties with compaction characteristics obtained from standard proctor (SP) and modified proctor (MP) tests. They concluded that while optimum moisture content has the best correlation with plastic limit, maximum dry density can be estimated more accurately from optimum moisture content better than from the plastic limit. In addition, they proposed empirical methods including compaction energy (E) which can be used for estimating compaction characteristics of fine-grained soils.

Günaydın [6] developed statistical and ANN methods for estimation of the compaction parameters maximum dry density and optimum moisture content index properties like particle size, consistency limits, and specific density (Gs). The data were collected from the dam site in some areas of Nigde (Turkey). It was concluded that there exists a good correlation between grain size, consistency limits, Gs with OMC, and MDD. However, the liquid limit had more influence, in the estimation of OMC, and particle size had more influence in the estimation of MDD.

Cabalar and Mustafa [7] investigated the influence of sand grains content on the behaviour of sand–clay mixtures. The mixtures were prepared with sand contents varying from 0 to 50% by weight in a 10% interval. They concluded that the behaviour will depend on the quantity of the sand and clay samples. They concluded that as the sand quantity increased, dry unit weight increased and respective moisture content decreased.

Saikia et al. [8] developed regression models for predicting maximum dry unit weight (γ_{dmax}) and optimum moisture content of fine-grained soils in terms of their consistency limits. Forty natural low plasticity soil samples were tested for liquid limit (LL), plastic limit (PL), and compaction characteristics by IS light compaction test concluded that with the increase in LL or PL γ_{dmax} decreases and OMC increases. In terms of the regression coefficient, LL exhibits a good correlation with γ_{dmax} and OMC compared to PL.

Given the associated time and cost which is involved in the experimental study of compaction characteristics of natural fine-grained soils having different clay mineralogies around the globe, in the present experimental study, an attempt has been made to prepare the artificially available clay minerals representing kaolinite and montmorillonite which were mixed with fine sand in different proportions to replicate natural fine-grained soils. Atterberg limits and compaction characteristics were measured for different energy levels.

Materials

For the preparation of soil samples, three important soil types are used sand–natural river sand passing 425-μm, kaolinite clay–commercially available white clay or kaolin clay as the primary kaolinitic clay mineral ($Al_2Si_2O_5(OH)_4$), and montmorillonite clay–commercially available sodium bentonite used as montmorillonitic clay mineral ($Al_2H_2Na_2O_{13}Si_4$). The naturally obtained river sand is washed and treated if required to remove any impurities, then oven-dried, brought to room temperature, sieved through I.S. 425-μm sieve, and is collected and stored in plastic bins, kaolin and bentonite clay will be stored separately in airtight plastic bins. The details of the samples prepared are listed in Tables 12.1 and 12.2.

Table 12.1 Kaolinite–sand mix proportions (MP1)

Kaolinite (%)	Sand (%)	Sample designation
100	0	100K
90	10	90K
80	20	80K
70	30	70K
60	40	60K
50	50	50K

Table 12.2 Montmorillonite–sand mix proportions (MP2)

Montmorillonite (%)	Sand (%)	Sample designation
100	0	100M
90	10	90M
80	20	80M
70	30	70M
60	40	60M
50	50	50M

Methodology

The kaolinite–sand mixtures (MP1), montmorillonite–sand mixtures (MP2), and natural soil samples with more than 50% fines [9], representing kaolinitic or montmorillonitic and kaolinitic–montmorillonitic dominance, were tested to determine Atterberg limits like liquid limit [10], plastic limit [10], and shrinkage limit and compaction characteristics like maximum dry density (MDD) and optimum moisture content (OMC) at different energy levels like standard proctor (596 kJ/m^3) [11] and modified proctor (2682 kJ/m^3) [12]. The multivariable regression analysis was carried out on MP1, MP2 and a combination of MP1 and MP2 to generate correlation equations, which were used to predict and compare with the results obtained from the experimental study of natural soils.

Results and Discussion

Atterberg Limits

The variation of Atterberg limits of kaolinite–sand mixtures, montmorillonite–sand mixtures, and naturals soils with percentage fines is shown in Figs. 12.1, 12.2 and 12.3, respectively.

From Figs. 12.1, 12.2 and 12.3, it can be observed that as percentage fines increases, the Atterberg limits increase for both artificial and natural soils indicating artificial mixtures behave similar to that of natural soils.

Correlations Between Percentage Fines and Atterberg Limits

A multivariate regression analysis has been carried on the mix proportions MP1, MP2 and combination of MP1 and MP2; the correlation equations has been proposed between percentage fines and Atterberg limits obtained from artificial mix proportions, which is used to predict the values of natural soils. Table 12.3 presents the correlation equations developed.

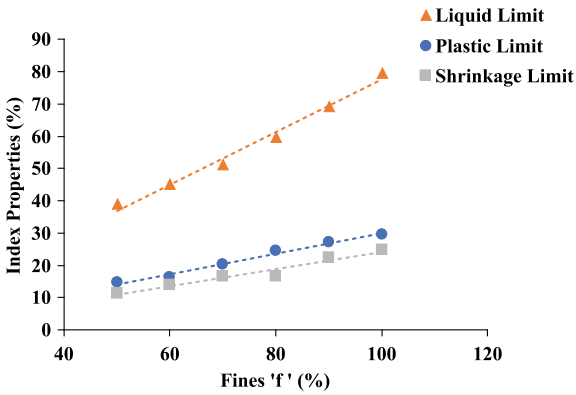

Fig. 12.1 Percentage fines versus Atterberg limits of MP1

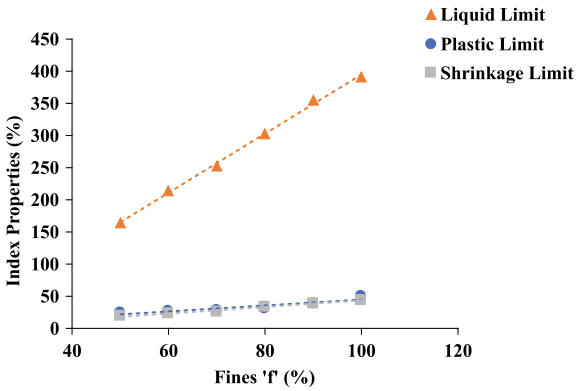

Fig. 12.2 Percentage fines versus Atterberg limits of MP2

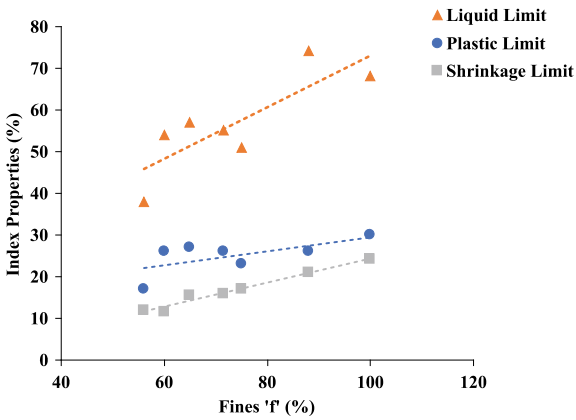

Fig. 12.3 Percentage fines versus Atterberg limits of natural soils

Table 12.3 Multivariate regression between percentage fines and Atterberg limits for mix proportion MP1 and MP2

Mix proportions	Equations	R^2	Multiple R
MP1	$F = 6.140603 + 3.127366\ W_p$	0.924	0.961
MP1	$W_L = -3.557143 + 0.811029\ F$	0.987	0.993
MP1	$W_p = -1.683810 + 0.316029\ F$	0.988	0.994
MP1	$W_s = -1.163310 + 0.325883\ W_L$	0.962	0.98
MP2	$F = 14.035690 + 0.217867\ W_L$	0.997	0.998
MP2	$W_L = -63.625238 + 4.579314\ F$	0.997	0.998
MP2	$W_p = 5.248390 + 0.917926\ W_s$	0.898	0.947
MP2	$W_s = -0.880335 + 0.112513\ W_L$	0.981	0.99
MP1 + MP2	$F = 18.521418 - 0.232135\ W_L + 3.974947\ W_s$	0.924	0.961
MP1 + MP2	$W_L = 51.285628 - 3.683445\ F + 16.361421\ W_s$	0.977	0.988
MP1 + MP2	$W_p = 5.628631 + 0.916799\ W_s$	0.933	0.966
MP1 + MP2	$W_s = -3.188318 + 0.229444\ F + 0.0595186\ W_L$	0.986	0.993

The following four correlation equations were used to predict the percentage of fines and Atterberg limits natural soil sample.

$$F = 18.521418 - 0.232135\ W_L + 3.974947\ W_s \tag{12.1}$$

$$W_L = 51.285628 - 3.683445\ F + 16.361421\ W_s \tag{12.2}$$

$$W_p = 5.628631 + 0.916799\ W_s \tag{12.3}$$

$$W_s = -3.188318 + 0.229444\ F + 0.0595186\ W_L \tag{12.4}$$

Equations 12.1–12.4 are used to predict percentage fines and Atterberg limits of natural soils. These predicted vs actual values are plotted as shown from Figs. 12.4, 12.5, 12.6 and 12.7.

From Figs. 12.4, 12.5, 12.6 and 12.7, it can be observed that Eqs. 12.1–12.4 can be used to predict the percentage fines (F) and Atterberg limits to a fair degree of accuracy for a given natural fine-grained soil sample having similar mix proportions.

Compaction Characteristics

The compaction characteristics optimum moisture content (OMC) and maximum dry density (MDD) for mix proportion MP1, MP2, and fine-grained natural soil samples are listed in Tables 12.4 and 12.5, respectively.

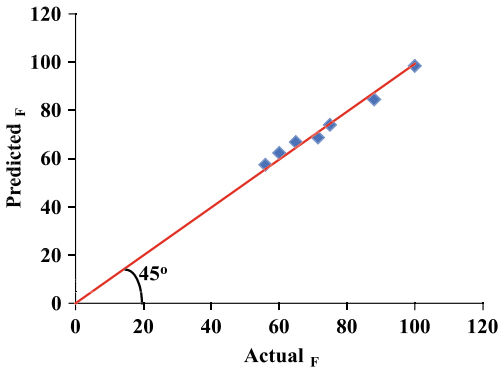

Fig. 12.4 Actual versus predicted plot of percentage fines (F) for natural soil samples

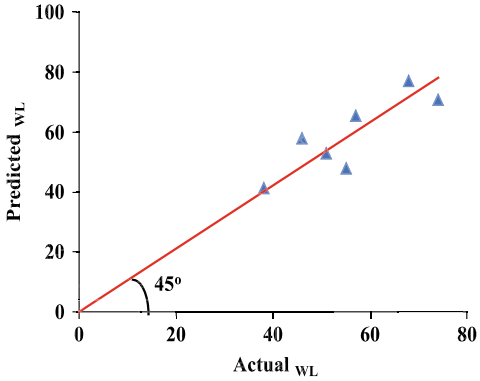

Fig. 12.5 Actual versus predicted plot of liquid limt (W_L) for natural soil samples

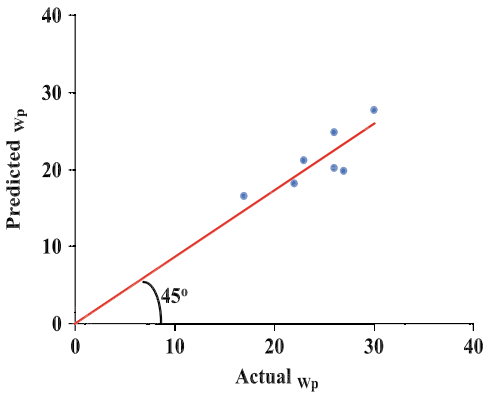

Fig. 12.6 Actual versus predicted plot of plastic limt (W_p) for natural soil samples

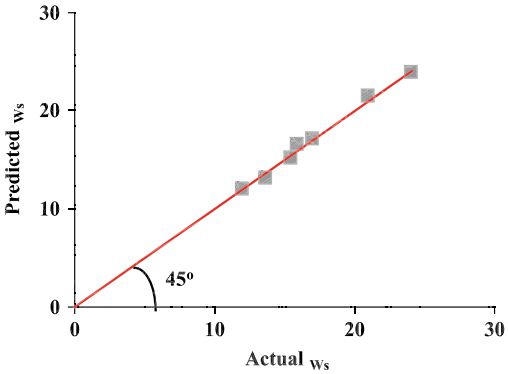

Fig. 12.7 Actual versus predicted plot of shrinkage limt (W_s) for natural soil samples

Table 12.4 Compaction characteristics of MP1 and MP2

Sample	SP (OMC)	SP (MDD)	MP (OMC)	MP (MDD)
100K	25.75	13.57	23.63	15.03
90K	24.08	14.47	20.52	16.15
80K	22.32	14.91	19.96	16.06
70K	20.93	15.7	18.61	16.92
60K	19.28	16.29	17.14	17.3
50K	18.19	16.77	16.03	18.01
100M	32.74	12.74	30.6	13.65
90M	31.42	13.14	30	14.1
80M	30.85	13.42	29.1	14.42
70M	30.05	13.7	28.05	14.85
60M	29.15	14.24	26.4	15.3
50M	27.71	14.68	25.2	15.8

Correlation Between Percentage Fines, Atterberg Limits and Compaction Characteristics

A multivariate regression analysis with a significance level (α) = 0.05 was performed between percentage fines, Atterberg limits and optimum moisture content (OMC); six equations were generated for both SP and MP energy levels for MP1, MP2 and a combination of MP1 and MP2; the results are shown in Table 12.6.

The above six equations were used to predict OMC for the natural soil samples. Equations 12.5 and 12.6 show fairly accurate results. The plot of actual and predicted values of OMC for natural soils is shown in Figs. 12.8 and 12.9.

$$\mathrm{OMC_{SP}} = 20.0 + 0.036\, W_L \tag{12.5}$$

Table 12.5 Compaction characteristics of natural soil samples

Sample	SP (OMC)	SP (MDD)	MP (OMC)	MP (MDD)
S1	17	16.19	13.7	18.74
S2	18.5	15.75	13.8	18.54
S3	23.2	15.79	17.4	17.29
S4	20.1	16.09	14.4	18.11
S5	28	14.05	20	16.33
S6	30.2	13.35	22.6	16.32
S7	34.5	13.15	21.2	15.61

Table 12.6 Multivariate regression analysis between percentage fines, Atterberg limits and optimum moisture content (OMC)

Sample	Equation	R^2	Multiple R
MP1	$OMC_{SP} = 11.02 + 0.18\ W_L$	0.99	0.99
MP1	$OMC_{MP} = 9.34 + 0.17 W_L$	0.97	0.98
MP2	$OMC_{SP} = 23.30 + 0.093\ F$	0.97	0.98
MP2	$OMC_{MP} + 0.15\ F - 0.084\ W_p$	0.98	0.99
MP1 + MP2	$OMC_{SP} = 20.0 + 0.036\ W_L$	0.88	0.94
MP1 + MP2	$OMC_{MP} = 17.41 + 0.038\ W_L$	0.89	0.95

$$OMC_{MP} = 17.41 + 0.038\ W_L \tag{12.6}$$

Similarly, multivariate regression analysis with a significance level (α) = 0.05 was performed between percentage fines, Atterberg limits, and maximum dry density

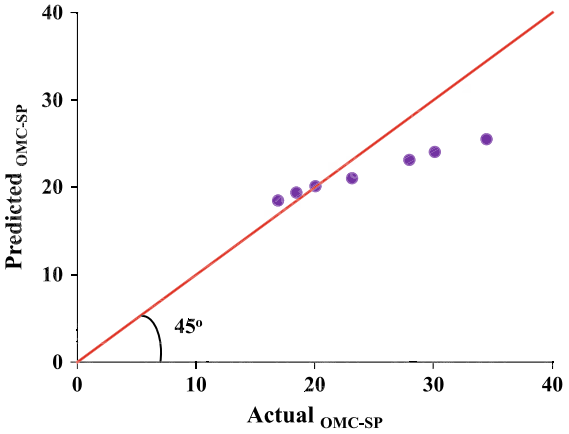

Fig. 12.8 Actual versus predicted optimum moisture content (OMC) at SP energy levels for natural soil samples

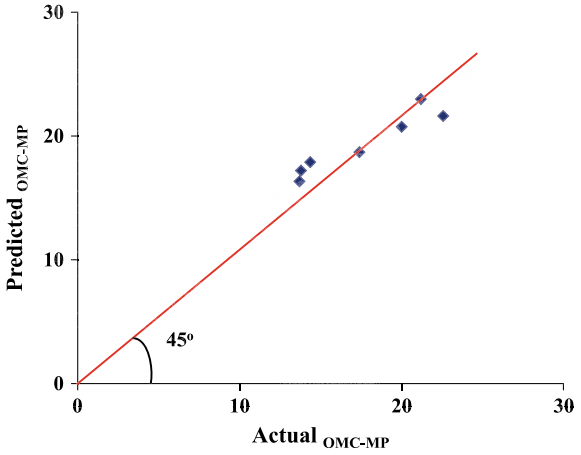

Fig. 12.9 Actual versus predicted optimum moisture content (OMC) at MP energy levels for natural soil samples

(MDD); six equations were generated for both SP and MP energy levels for MP1, MP2, and combination of MP1 and MP2; the results are shown in Table 12.7.

The above six equations were used to predict MDD for the natural soil samples. Equations 12.7 and 12.8 show fairly accurate results. The plot of actual and predicted values of MDD for natural soils is shown in Figs. 12.10 and 12.11.

$$\mathrm{MDD_{SP}} = 18.07 - 0.034\,F - 0.0062\,W_{\mathrm{L}} \tag{12.7}$$

$$\mathrm{MDD_{MP}} = 19.02 - 0.028\,F - 0.0076\,W_{\mathrm{L}} \tag{12.8}$$

From Eqs. 12.5 and 12.6, it can be observed that percentage fines, plastic limits, and shrinkage limits do not influence OMC. Similarly, from Eqs. 12.7 and 12.8, it can be observed that percentage plastic limit and shrinkage limit do not influence OMC. Observing Eqs. 12.5–12.8, we can say that the liquid limit has a major influence on the prediction of both OMC and MDD.

Table 12.7 Multivariate regression analysis between percentage fines, Atterberg limits and maximum dry density (MDD)

Sample	Equation	R^2	Multiple R
MP1	SP (MDD) = 19.75 − 0.078 W_{L}	0.99	0.99
MP1	MP (MDD) = 20.69 − 0.055 F	0.95	0.98
MP2	SP (MDD) = 16.95 − 0.067 F + 0.056 W_{s}	0.99	0.99
MP2	MP (MDD) = 17.85 − 0.042 F	0.99	0.99
MP1 + MP2	SP (MDD) = 18.07 − 0.034 F − 0.0062 W_{L}	0.86	0.93
MP1 + MP2	MP (MDD) = 19.02 − 0.028 F − 0.0076 W_{L}	0.9	0.95

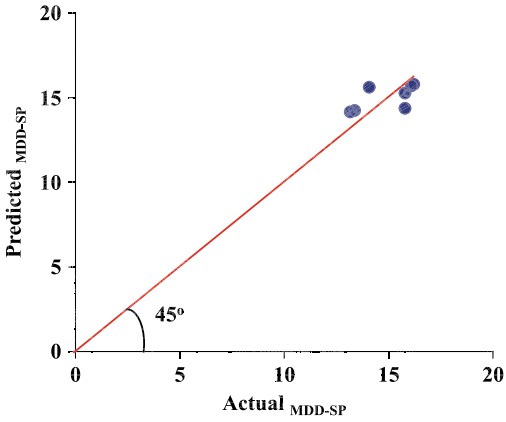

Fig. 12.10 Actual versus predicted maximum dry density (MDD) at SP energy levels for natural soil samples

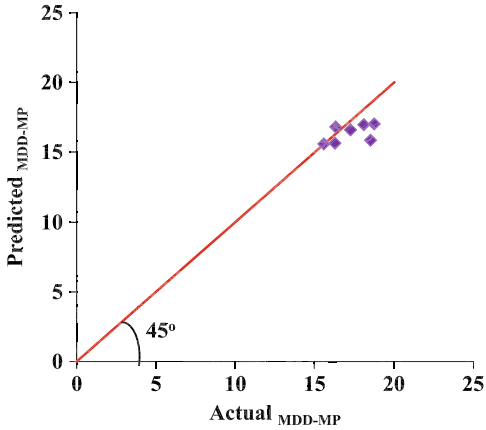

Fig. 12.11 Actual versus predicted maximum dry density (MDD) at MP energy levels for natural soil samples

Conclusions

Based on the experimental study, the following conclusions can be drawn.

- As the percentage fines increase, the Atterberg limit increases for both artificially prepared and natural soil samples.
- The predicted and actual Atterberg limits of natural soils can be correlated with a fair degree of accuracy.
- The correlation equation to predict optimum moisture content (OMC) for both SP and MP energy levels includes only liquid limit (W_L) as the main predictors, indicating a strong correlation between OMC and W_L exists.
- The correlation equation to predict maximum dry density (MDD) at both SP and MP energy levels includes percentage fines (F) and liquid limit (W_L) as the predictors, indicating a strong correlation between MDD, F and W_L exist.
- The artificial mix proportions depict the natural soil behaviour to a fair degree of accuracy in terms of Atterberg limits and compaction characteristics.

References

1. Gurtug Y, Sridharan A (2002) Prediction of compaction characteristics of fine-grained soils. Geotechnique 52(10):761–763
2. Dumbleton MJ, West G (1966) Some factors affecting the relation between the clay minerals in soils and their plasticity. Clay Miner 6(3):179–193
3. Blotz LR, Benson CH, Boutwell GP (1998) Estimating optimum water content and maximum dry unit weight for compacted clays. J Geotech Geoenvironmental Eng 124(9):907–912
4. Sridharan A, Nagaraj HB (2005) Plastic limit and compaction characteristics of fine grained soils. Proc Inst Civ Eng Ground Improv 9(1):17–22
5. Sivrikaya O, Togrol E, Kayadelen C (2008) Estimating compaction behavior of fine-grained soils based on compaction energy. Can Geotech J 45(6):877–887
6. Günaydın O (2009) Estimation of soil compaction parameters by using statistical analyses and artificial neural networks. Environ Geol 57(1):203
7. Cabalar AF, Mustafa WS (2017) Behaviour of sand–clay mixtures for road pavement subgrade. Int J Pavement Eng 18(8):714–726
8. Saikia A, Baruah D, Das K, Rabha HJ, Dutta A, Saharia A (2017) Predicting compaction characteristics of fine-grained soils in terms of Atterberg limits. Int J Geosynthetics Ground Eng 3(2):1–9
9. IS: 2720 (Part IV) 1985 (2006) Grain size analysis. Bureau of Indian Standards, New Delhi
10. IS: 2720 (Part V) 1985 (2006) Determination of liquid and plastic limit. Bureau of Indian Standards, New Delhi
11. IS: 2720 (Part VII) 1980 (2011) Determination of water content-dry density relation using light compaction. Bureau of Indian Standards, New Delhi
12. IS: 2720 (Part VIII) 1980 (2011) Determination of water content-dry density relation using heavy compaction. Bureau of Indian Standards, New Delhi

Chapter 13
Electrical Resistivity-Based Characterization of Geotechnical Properties of Mine Tailing

Vaishali Wayal, T. G. Sitharam, and Gali Madhavi Latha

Introduction

Growing demand for metals and minerals has led to the increased extraction of mineral resources by the mining industry, which generates an enormous amount of waste products such as mine tailings. The mine tailings are used for various civil engineering applications such as the manufacturing of geopolymer concrete, bricks, and ceramic tiles. However, the tailing materials are mostly stored in impoundments that are raised in various stages and each layer of impoundment may possess different material characteristics. Geotechnical characteristics of mine tailings depend on various parameters such as shape of particles, gradation, compaction density, and type of parent rock. These properties play a vital role in the determination of the stability of tailing impoundments.

In the past few years, numerous tailing dam failures were observed due to changes in bearing capacity, pore pressure, state of stress, and seepage conditions. Such failures lead to several environmental hazards and economic loss. Thus, to ensure the safety of tailing impoundments, a suitable testing technique is needed to evaluate the quality of construction and characteristics of in situ material. In such situations, conventional geotechnical testing methods may prove to be time-consuming, challenging, and costly. Non-destructive methods such as electrical resistivity technique can be effectively used for characterization of in situ subsurface which may help to monitor the condition of tailing dam and assessing the conditions that can lead to failure. Electrical resistivity technique is non-invasive method that allows evaluation

V. Wayal (✉) · T. G. Sitharam · G. M. Latha
Department of Civil Engineering, Indian Institute of Science, Bangalore 560012, India
e-mail: vaishaliw@iisc.ac.in

T. G. Sitharam
Indian Institute of Technology, Guwahati 781039, India

K. Muthukkumaran (eds.), *Soil Behavior and Characterization of Geomaterials*,
Lecture Notes in Civil Engineering 296, https://doi.org/10.1007/978-981-19-6513-5_13

of in situ soil characteristics rapidly. The resistivity of soil is affected by various factors such as porosity [2], compaction condition [4], pore fluid content and saturation [5, 7], fractional volume of water [10], soil mineralogy [8], percent of clay [11], pore fluid, and temperature. Previously, attempts were made by several researchers to develop correlation between electrical resistivity of soils and geotechnical properties [1, 9, 12, 13] very few studies had been carried out for electrical resistivity based assessment of mine tailing. Thus, present study attempts to relate the geotechnical characteristics of mine tailing with electrical resistivity through laboratory studies. In the present work, the resistivity of fine sand is also evaluated, and results are compared with the resistivity of mine tailings. The four-electrode and Wenner array methods, as described in ASTM G-57 standard [3], are used for electrical resistivity measurement in this work.

Present work consists of a series of experiments conducted in laboratory for assessing resistivity variation due to changes in geotechnical characteristics of tailings and fine sand. In first part of the study, the basic physical characteristics, viz., Atterberg limits, particle size distribution, and compaction characteristics of mine tailing and fine sand are determined using standard laboratory techniques. Following that, an electrical resistivity study was carried out using four-electrode method on tailing and fine sand with geotechnical properties that are dry density, water content, and degree of saturation. Also, an attempt is made to correlate the resistivity of saturated tailing samples with permeability by performing experiments in a modified falling head permeameter.

Materials and Methodology

Mine Tailing

Present study was carried out on the samples of mine tailings collected from mines located at Zawar, Rajasthan. The oven-dried samples were sieved through a 2 mm sieve to evaluate geo-electrical characteristics in the laboratory. Table 13.1 shows the various geotechnical characteristics, viz., liquid limit and compaction characteristics, specific gravity of tailing samples. Based on particle size distribution curve (see Fig. 13.1), the tailing samples can be classified as silty sand (SM) as per the Unified Soil Classification System (USCS). The tailing sample shows the traces of elements such as alumina (Al), silica (Si), and iron (Fe) based on analysis of energy-dispersive X-ray spectroscopy (EDS).

Table 13.1 Geotechnical characteristics of tailing samples

Property	Values
Specific gravity	2.67
% of sand	52.5%
% of silt	41.2%
% of clay	6.3%
Liquid limit (%)	26.54%
D10 (mm)	0.0055
D30 (mm)	0.051
D60 (mm)	0.097
Uniformity coefficient	17.4
Coefficient of curvature	4.9
Maximum void ratio	1.04
Minimum void ratio	0.43
Soil classification	SM

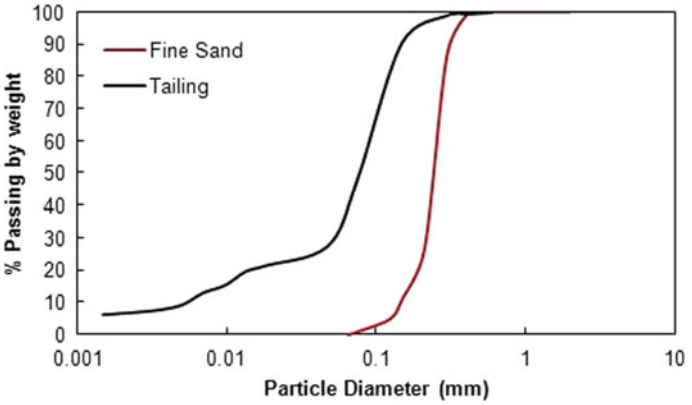

Fig. 13.1 Particle size distribution curves

Fine Sand

River sand collected from the Chikkaballapur, Karnataka, is used in the present work. Fine-sized sand (75–425 m) was obtained from the collected samples by thoroughly washing and sieving using a sieve shaker. Table 13.2 presents the geotechnical properties of fine sand. Based on analysis of the particle size distribution curve (Fig. 13.1) and USCS, fine sand is classified as poorly graded sand (SP).

Table 13.2 Geotechnical characteristics of fine sand

Properties	Value
Specific gravity	2.64
Minimum dry density (g/cc)	1.33
Maximum dry density (g/cc)	1.68
Coefficient of uniformity	1.75
Curvature coefficient	0.92
Effective size (mm)	0.16
Classification	SP

Experimental Setup and Method

Fabricated soil resistivity box

The resistivity box of cylindrical shape was fabricated using an acrylic sheet with dimensions internal length, 200 mm, and internal diameter, 40 mm. In the box, two stainless steel plates of thickness 3 mm are fitted for injecting current in the soil sample, and two metallic pins are (diameter 3 mm) fixed 126 mm apart for measuring the potential drop. The cylindrical resistivity box and experimental setup used in the study are shown in Fig. 13.2.

Modified rigid wall permeameter

The conventional rigid wall variable head permeameter [6] is fabricated using an insulating Perspex sheet and modified to enable the simultaneous measurement of electrical resistivity and permeability. The permeameter consists of the cylindrical mould of diameter, 80 mm, and height, 60 mm, base plate with porous plate, and top cap. The top cap was modified by fixing four electrodes (2 mm diameter stainless steel rods) at the spacing of 20 mm to form Wenner array for measuring electrical resistivity. Figure 13.3 shows the experimental setup and modified permeameter for permeability and resistivity measurements.

Fig. 13.2 Cylindrical resistivity box and experimental setup

Fig. 13.3 Experimental setup and modified permeameter

Result and Discussions

Study on Electrical Resistivity Variation with Geotechnical Properties

- **Variation of resistivity with water content**
  In mine tailing material, the electric current flows through pore fluid/water. As depicted from Fig. 13.4, with increased water content, electrical resistivity reduces due to enhanced ionic conduction. Also, at lower water content, electrical resistivity reduces rapidly for a given relative density, and beyond some critical value of water content, it decreases slowly. This is because, at higher water content, sufficient availability of water surrounding the soil particles improves the connectivity of pore fluid. As shown in Fig. 13.5, the resistivity values of fine sand are greater than those for the mine tailing. Due to the presence of particles of metallic traces in mine tailing, the corresponding resistivity values are lower.
- **Variation of electrical resistivity with density**
  Figure 13.6 shows the effect of dry density on the resistivity of compacted tailing at the different per cent of water. For a given pore fluid/water content, electrical resistivity increases with a reduction in density of soil sample. When particles obtain the densest state of packing, the changes in electrical resistivity values become negligible. Also, electrical resistivity changes with density are more noticeable at lower water contents. The resistivity variation of samples of fine sand with dry density is as depicted in Fig. 13.7.
- **Effect of degree of saturation**
  Figures 13.8 and 13.9 show that the electrical resistivity of mine tailing and fine sand reduces with the degree of saturation. However, it was observed that below a critical degree of saturation, the changes in resistivity values are rapid with the degree of saturation due to the partial formation of conducting phase surrounding

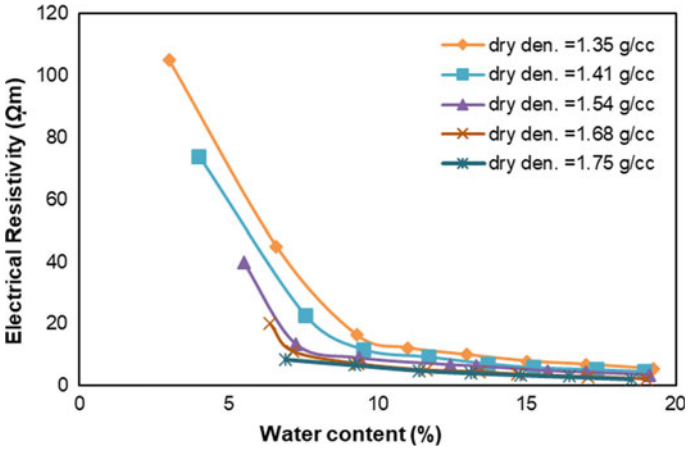

Fig. 13.4 Electrical resistivity versus water content plot for tailing

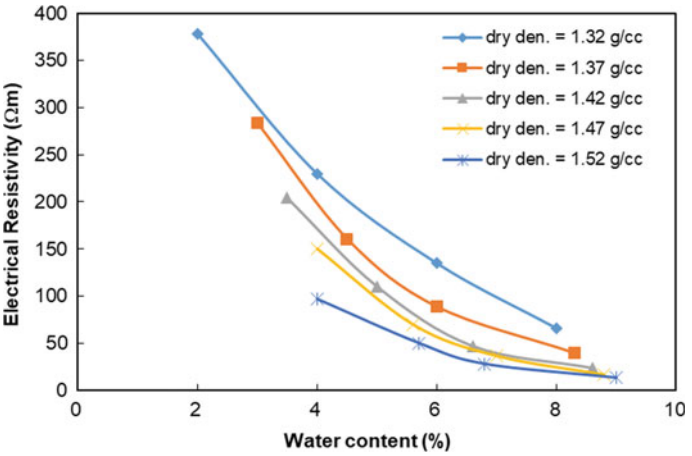

Fig. 13.5 Electrical resistivity versus with water content plot for fine sand

soil particles. With an increase in degree of saturation of soil, pore water continuity increases, which improves the ionic conduction in samples. However, resistivity varies slowly with increasing saturation beyond the critical saturation. The electrical resistivity can be correlated to degree of saturation by a power law as observed by various researchers

$$\rho = b_1 S^{-b_2}$$

where b_1 and b_2 are fitting parameters and S is degree of saturation.

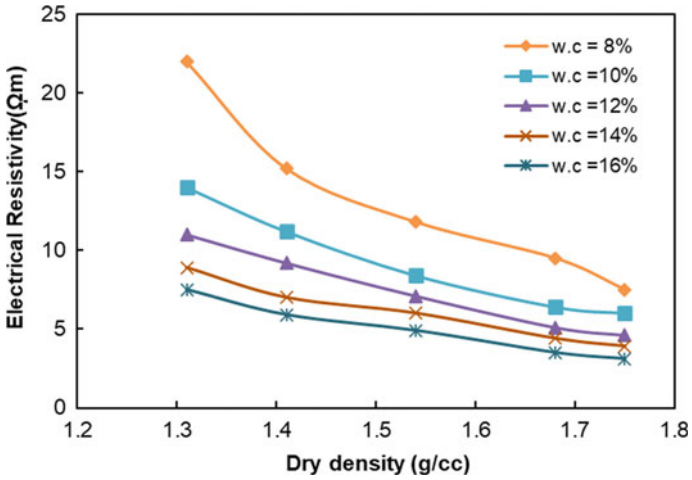

Fig. 13.6 Electrical resistivity variation of tailing with dry density

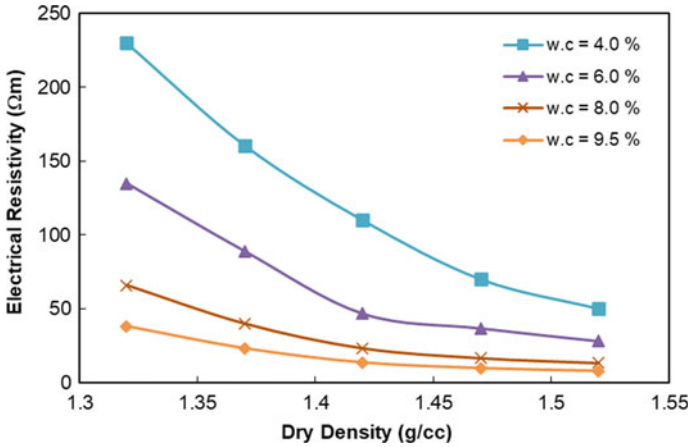

Fig. 13.7 Electrical resistivity variation of fine sand with dry density

- **Effect of porosity**

  With an increase in porosity of unsaturated soils, pore water connectivity decreases that resists the current flow and shows higher resistivity values. Figure 13.10 shows the changes in resistivity with porosity for the tailing samples at different moisture content. For a given moisture content, the samples with lower porosities show lower resistivity due to the enhanced interconnectivity of conducting phase that offers the continuous flow path for electric current flow. The effect of porosity on the resistivity of samples is more dominating at lower pore water. The higher

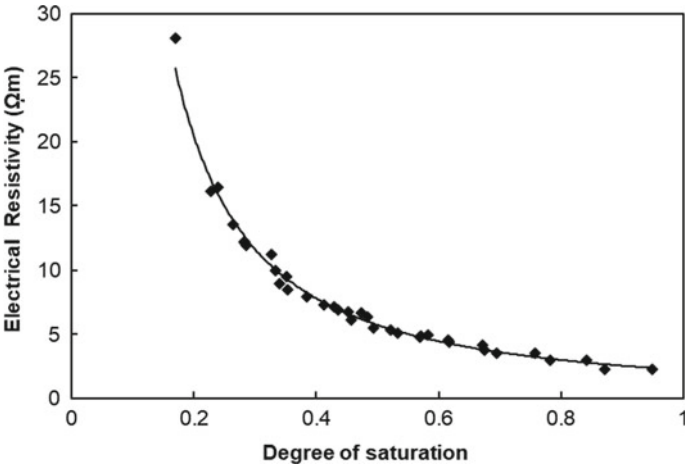

Fig. 13.8 Electrical resistivity versus degree of saturation plot for tailing

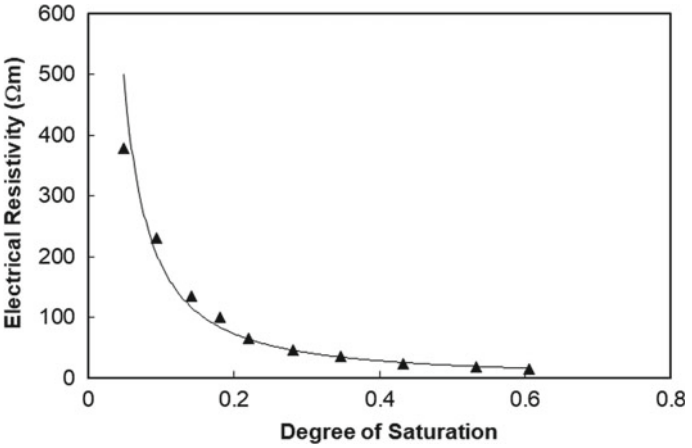

Fig. 13.9 Electrical resistivity versus degree of saturation plot for fine sand

resistivity is observed for fine sand compared to the tailing sample as shown in Fig. 13.11.

- **Effect of temperature and type of pore fluid**
  Figure 13.12 reveals that the resistivity reduces with an increase in temperature of the tailing sample. As the temperature rises, the ionic conductivity in soil pores increases, causing an increase in electrical conductivity and thus reducing the resistivity.

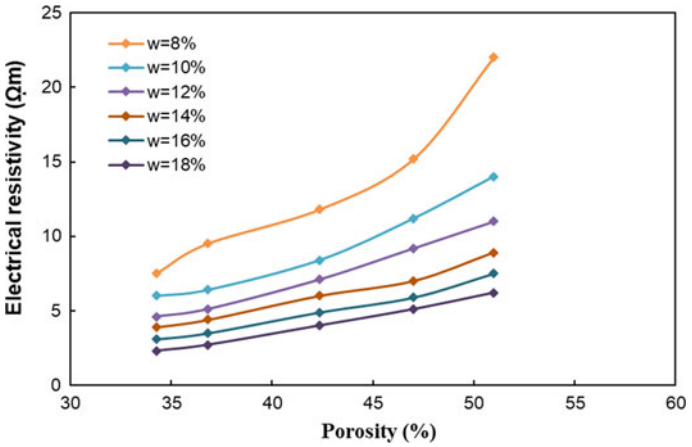

Fig. 13.10 Electrical resistivity variation of tailing with porosity

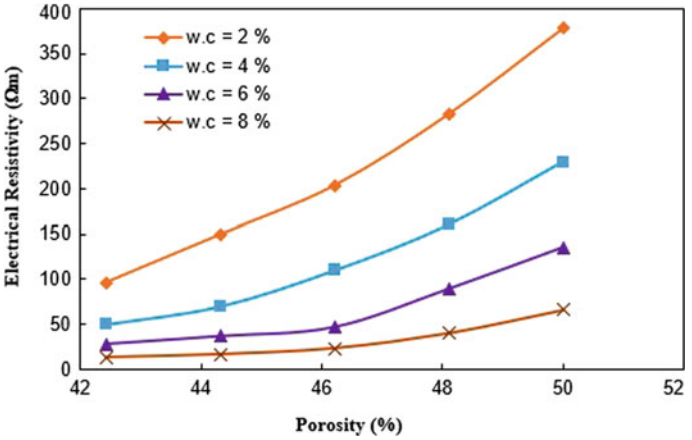

Fig. 13.11 Electrical resistivity variation of fine sand with porosity

Figure 13.13 shows that the resistivity of the samples with water as a pore fluid shows higher electrical resistivity compared to samples with the salt solution of 0.5 M NaCl as the pore fluid. Salt solutions possess more dissolved ions compared to water and thus are better conductors than water.

Electrical Resistivity Variation with Permeability

The electrical resistivity variations of saturated samples of tailing material and fine sand with permeability are presented in Figs. 13.14 and 13.15, respectively.

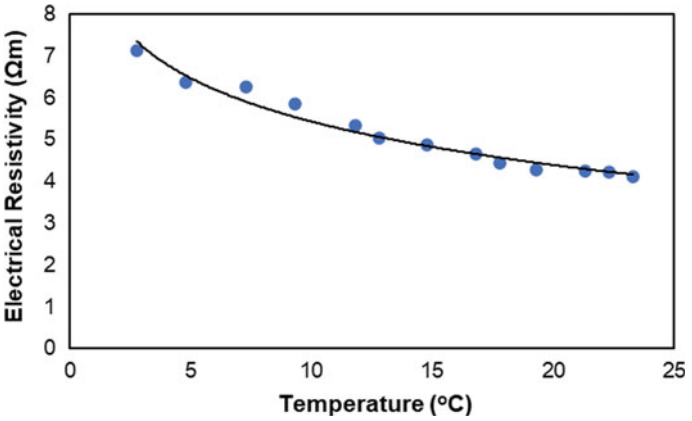

Fig. 13.12 Variation of electrical resistivity of tailing with temperature

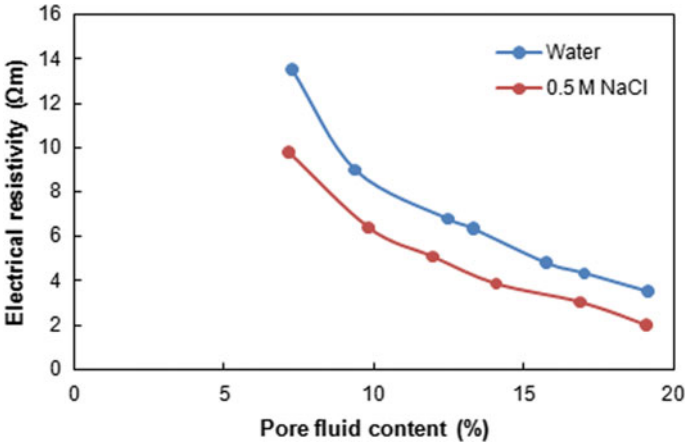

Fig. 13.13 Variation of electrical resistivity with pore fluid for tailing

As the permeability increases, the resistivity of saturated samples reduces due to enhanced ionic movement. The resistivity of soils can be correlated to permeability because, in both phenomena, water-filled pores play a key role. The relation between permeability and electrical resistivity can be presented as

$$\log k = a_1 \rho + a_2$$

where k = permeability of saturated tailing sample, ρ = electrical resistivity, a_1 and a_2 are fitting parameters. The correlation between saturated permeability and resistivity was found to match well with the study of Ward, 1990.

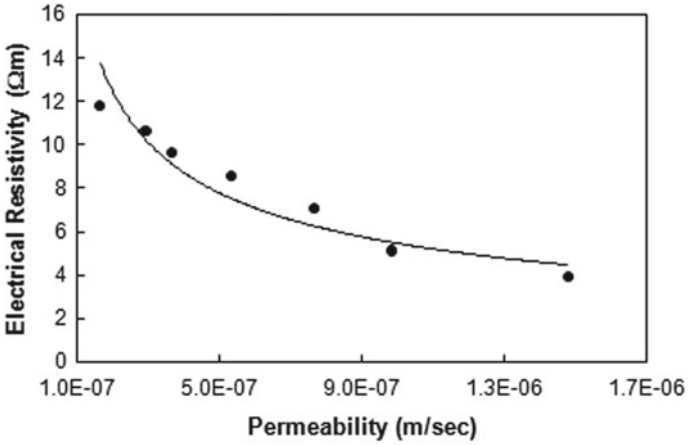

Fig. 13.14 Variation of electrical resistivity of tailing with saturated permeability

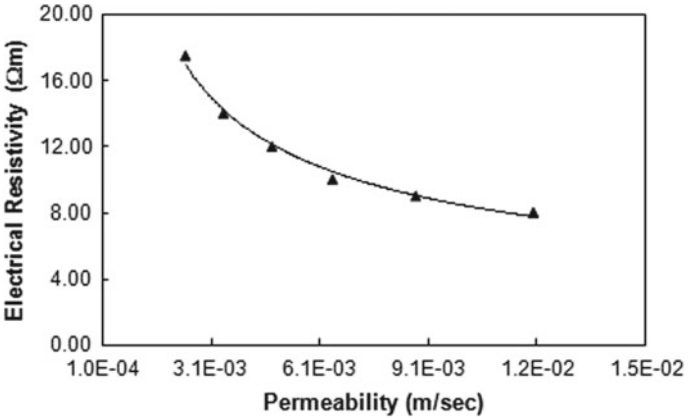

Fig. 13.15 Variation of electrical resistivity of fine sand with permeability

The results obtained from the experiments confirm that electrical resistivity values are dependent on geotechnical properties. Thus, this technique can efficiently identify the changes in in situ soil characteristics, which may indicate the presence of weak zones (low compacted zones), leakages (seepage or piping failure), and the presence of cavities in tailing dams. The continuous monitoring of changes in electrical resistivity may thus help in identifying the corresponding changes in geotechnical properties, which can be used for detecting the conditions leading to failure and accordingly adopt suitable measures for prevention of failure.

Conclusions

Under the partially saturated condition, the electrical resistivity of soil increases with the degree of saturation, relative density, and moisture fluid content. With increase in values of these quantities, resistivity values reduce due to enhanced pore fluid connectivity that improves the flow of current. Besides, the resistivity changes more rapidly at lower values of water content and densities. However, saturated samples compacted at higher density possess higher resistivity due to the associated lower saturated porosity, increased pore channel tortuosity, and packing of soil particles.

The resistivity of saturated soil reduces with permeability due to the presence of more water-filled pores. The obtained correlation between geotechnical properties and resistivity may help in the determination of the in situ characteristics of tailing material. Based on the above findings, the electrical resistivity of mine tailing shows significant changes with changes in geotechnical properties. It may thus help in identifying weak zones and seepage-associated failures such as piping failures.

References

1. Alsharari B, Olenko A, Abuel-Naga H (2020) Modeling of electrical resistivity of soil based on geotechnical properties. Expert Syst Appl 141:112966
2. Archie GE (1942) The electrical resistivity log as an aid in determining some reservoir characteristics. Trans AIME 146(01):54–62
3. ASTM G57-20 (2020) Method for measurement of soil resistivity using the Wenner four-electrode method. ASTM International, West Conshohocken, PA
4. Bai W, Kong L, Guo A (2013) Effects of physical properties on electrical conductivity of compacted lateritic soil. J Rock Mech Geotech Eng 5(5):406–411
5. Fukue M, Minato T, Horibe H, Taya N (1999) The micro-structures of clay given by resistivity measurements. Eng Geol 54(1–2):43–53
6. IS: 2720 (Part 17) (1986) Methods of test for soils, laboratory determination of permeability
7. McCarter WJ (1984) The electrical resistivity characteristics of compacted clays. Geotechnique 34(2):263–267
8. Mitchell JK, Soga K (2005) Fundamentals of soil behaviour, vol 3. Wiley, New York
9. Pandey LMS, Shukla SK (2018) Effect of state of compaction on the electrical resistivity of sand-bentonite lining materials. J Appl Geophys 155:208–216
10. Rhoades JD, Raats PAC, Prather RJ (1976) Effects of liquid-phase electrical conductivity, water content, and surface conductivity on bulk soil electrical conductivity. Soil Sci Soc Am J 40(5):651–655
11. Wayal V, Sitharam TG (2020) Geo-electric assessment of the compacted sand-bentonite mixes. Int J Geotech Eng 1–16
12. Yan M, Miao L, Cui Y (2012) Electrical resistivity features of compacted expansive soils. Mar Georesour Geotechnol 30(2):167–179
13. Zhou M, Wang J, Cai L, Fan Y, Zheng Z (2015) Laboratory investigations on factors affecting soil electrical resistivity and the measurement. IEEE Trans Ind Appl 51(6):5358–5365

Chapter 14
Geotechnical Properties of Soil Stabilized with Urea-Formaldehyde Polymer

Neelam Phougat, R. K. Bharti, Harendra Prakash, and Manish Gupta

Introduction

Polymers improve engineering properties of wide range of problematic weak soils by changing their mineralogy [1–5]. On sites, polymer application is widely used as an alternative to soil blending. Polymers act as cementing material which stabilizes the soil aggregate against the erosive forces by forming bond between clay minerals present in the soil and polar-end groups of polymer. Polymers are non-toxic, easy to apply, and inexpensive soil stabilizers which improve volume stability, strength, stress-strain behaviour, permeability, and durability of soil thus making it suitable for geotechnical application. Polymers are environmentally safe soil conditioners which do not change the pH of soil and do not cause any adverse environmental impact. In comparison to chemical stabilizer, relatively short curing time and small quantity of polymer are required for significant strength improvement. Danger of leaching of polymer to ground water is reduced due to use of very small amount of polymer for soil stabilization. Polymer used for soil stabilization should have high tensile, flexural, and compressive strengths, good adhesion to soil particles, and high resistance to chemicals and ultraviolet rays. Literature survey reveals that the long-term stability, modulus of elasticity, and strength of soil are improved with mixing of certain polymers which is further improved on increasing concentration of polymer and curing time. Improvement in strength of soil on mixing of polymer depends on the physical and chemical properties of the polymer, concentration of the polymer added, nature of soil, and degree of mixing of polymer with the soil.

For the present study, effect of urea-formaldehyde resin (UF-resins) on index properties and density of soil is being investigated. Urea-formaldehyde resins are thermosetting resins which are prepared by chemical reaction of urea and formaldehyde. The reaction of urea and formaldehyde to form urea-formaldehyde resin is a

N. Phougat (✉) · R. K. Bharti · H. Prakash · M. Gupta
Central Soil and Materials Research Station, New Delhi 110016, India
e-mail: neelamphougat@yahoo.com

K. Muthukkumaran (eds.), *Soil Behavior and Characterization of Geomaterials*,
Lecture Notes in Civil Engineering 296, https://doi.org/10.1007/978-981-19-6513-5_14

two-step process where alkaline methylolation is followed by acidic condensation. Urea-formaldehyde resins consist of some amount of monomers and mixture of linear or branched oligomers and polymers. Using different conditions of reaction of urea and formaldehyde, innumerable variety of condensed structures are possible. Unreacted urea present in urea-formaldehyde resins is helpful in better storage stability. Free formaldehyde present in urea-formaldehyde resins is necessary to induce the hardening reaction during curing. Depending on the reaction conditions used, UF resins contain methylene ether bridges ($–CH_2–O–CH_2–$) and methylene bridges ($–CH_2–$) in different proportions. Two formaldehyde molecules form one methylene ether bridge. At higher temperature, methylene ether bridges rearrange to methylene bridges with emission of one molecule of formaldehyde. It is recommended to minimize the proportion of methylene ether bridges in UF resins because methylene bridge is more stable than methylene ether bridge. Due to its low cost, high reactivity, ease of use under wide variety of conditions, low cure temperatures, water solubility, and dispersibility, urea-formaldehyde resin is widely used in various applications. After hardening, UF resins consist of insoluble three-dimensional network which cannot be melted or thermoformed again.

Methodology

To examine the effect of concentration of urea-formaldehyde resin on index properties and density of soil, it was mixed with soil samples collected from Rukni irrigation project, Cachar, India, and samples were cured for 14 days. For the present study, soil was dried, graded, and 1, 2, and 4% of urea-formaldehyde resins of the dry weight of the soil were mixed with soil samples using mechanical kneader. As per IS, specific gravity, Atterberg's limit, grain size analysis, and standard proctor compaction tests were done on these polymer-mixed soil samples. Permeability test was done on soil sample mixed with 1% of urea-formaldehyde resin of the dry weight of the soil. Effect of addition of lime on engineering properties of soil-polymer mixture was studied by conducting standard proctor compaction tests on soil sample prepared by mixing 5% of lime by dry weight of soil in soil having 4% of urea-formaldehyde resin. Data analysis and interpretation of result were done.

Results and Discussion

Results of standard proctor compaction tests are shown in Table 14.1 and Fig. 14.1. OMC of soil sample decreases with increasing concentration of urea-formaldehyde resin in soil sample. MDD of soil samples stabilized with different concentration of urea-formaldehyde resin increased with increasing resin content in soil sample and reached a maximum at 2% of resin content of dry weight of the soil, but MDD is slightly decreased on further increase in percentage of urea-formaldehyde resin up

Table 14.1 Results of MDD and OMC for soil mixed with urea-formaldehyde resin

Sample	MDD (g/cc)	OMC (%)
Soil + 0% urea-formaldehyde resin	1.90	12.6
Soil + 1% urea-formaldehyde resin	1.94	12.2
Soil + 2% urea-formaldehyde resin	1.95	11.6
Soil + 4% urea-formaldehyde resin	1.91	11.2

to 4% of the dry weight of the soil. MDD increased on increasing resin concentration up to 2% of the dry weight of the soil because with increasing polymer concentration up to 2%, more polymer molecules are available to form bond with soil particles, and due to small concentration of the polymer molecules, they are separated from one another and behave like free coils, but with increasing resin concentration to 4%, the polymer coils stop behaving like free coils and began to overlap and entangle with each other which diminishes bonding capacity of polymer with soil particles [6, 7]. OMC of soil resin mixer is decreasing on increasing resin concentration because increased bonding between soil particles and resin produced a durable hydrophobic material by filling the voids and making the stabilized soil samples impermeable to water [8]. Results of grain size analysis, Atterberg limit values, and specific gravity values of soil mixed with urea-formaldehyde resin are shown in Table 14.2. Results of grain size analysis are shown in Fig. 14.2. It is observed that on mixing of resin in soil, the proportions of larger particle size are increasing on increasing the concentration of urea-formaldehyde resin in soil. Formation of larger particles on mixing of resin in soil indicates the formation of chemical bond between resin and soil. Long polymer chains draw clay particles together and increase the size of particles thus enhancing the strength and improving engineering properties of the soil. It is reported that Fourier transform infrared spectroscopy studies confirmed the formation of clay mineral-polymer bond on mixing of polymer in soil [9, 10].

On mixing of urea-formaldehyde resin, soil got converted from non-plastic to plastic. Liquid limit and plastic index got reduced on increasing concentration of urea-formaldehyde resin in soil. Reduction of liquid limit and plastic index is an indication that an expansive characteristic of soil gets reduced on mixing of urea-formaldehyde resin to soil. PL and PI of soil are reduced on the addition of resin because these resins are effective in inhibiting the permeation of water into the soil. Specific gravity is getting decreased on mixing of urea-formaldehyde resin with soil which gets increased on further increasing the concentration of urea-formaldehyde resin. Soil sample with 1% urea-formaldehyde resin was tested to be impermeable.

Maximum dry density obtained by standard proctor compaction tests done on soil containing 4% of urea-formaldehyde resin and 5% of lime by dry weight of soil got reduced to 1.86 g/cc. As per literature survey, lime neutralizes formaldehyde. Neutralization reaction taking place between lime and formaldehyde fraction of urea-formaldehyde resin may be reducing the effective concentration of urea-formaldehyde resin in soil which might have reduced the degree of bonding

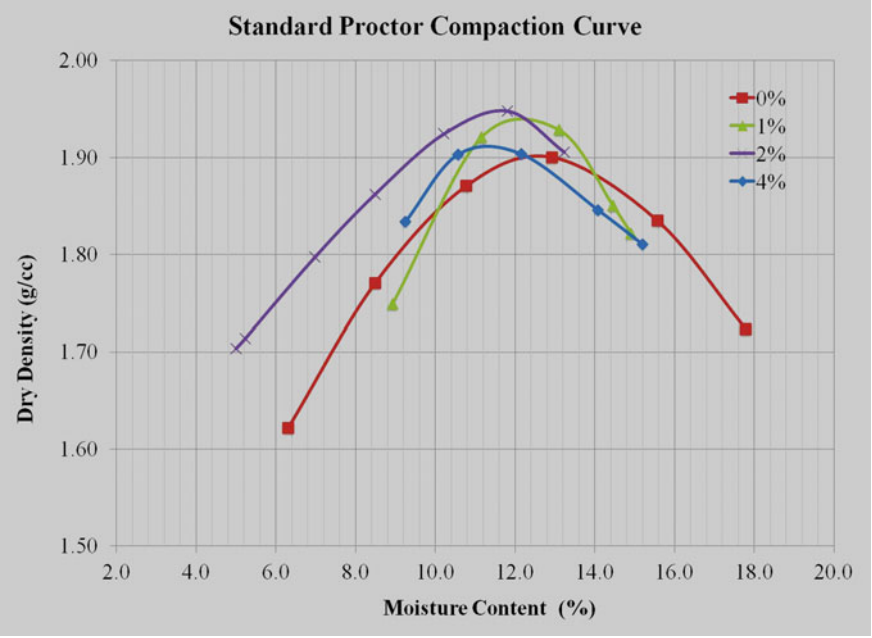

Fig. 14.1 Standard proctor compaction curves

of urea-formaldehyde resin with soil particles. Reduced effective concentration of urea-formaldehyde resin in soil due to neutralization reaction may be the reason for reduced value of maximum dry density [11].

Conclusion

These results indicate that the mixing of urea-formaldehyde resin in soil samples improves grain size distribution, maximum dry density, and specific gravity. Addition of the polymer agglomerates soil particles and increases cohesion, reduces volume of voids in the soil, and decreases affinity of the soil for water. It is reported that mixing of lime improves engineering properties of the soil and mixing of polymer with soil also improves engineering properties of soil, but in the present study, it is observed that it is not always having beneficial effect on engineering properties of soil to mix combination of polymer and lime in soil. Neutralization reaction between lime and formaldehyde fraction of urea-formaldehyde resin might have reduced the effective concentration of urea-formaldehyde resin in soil which in turn have reduced the degree of bonding of urea-formaldehyde resin with soil particles.

Table 14.2 Grain size distribution and specific gravity data

Material	Mechanical analysis						Atterberg limit (IS:425μ sieve)			Specific gravity
	0.002 mm and less	0.002–0.075 mm	0.075–0.425 mm	0.425–2.0 mm	2.0–4.75 mm	4.75 mm and above				
	Clay	Silt	Fine sand	Medium sand	Coarse sand	Gravel	LL	PL	PI	
Soil + 0%	19.8	34.8	45.2	0.2	0	0	24.0	NP	0.0	2.6
Soil + 1%	12.7	26.2	57.7	3.4	0	0	22.6	16.4	6.2	2.5
Soil + 2%	13.3	20.8	65.8	0.1	0	0	20.3	16.4	3.9	2.6
Soil + 4%	14.5	19.6	65.8	0.1	0	0	19.1	16.0	3.1	2.6

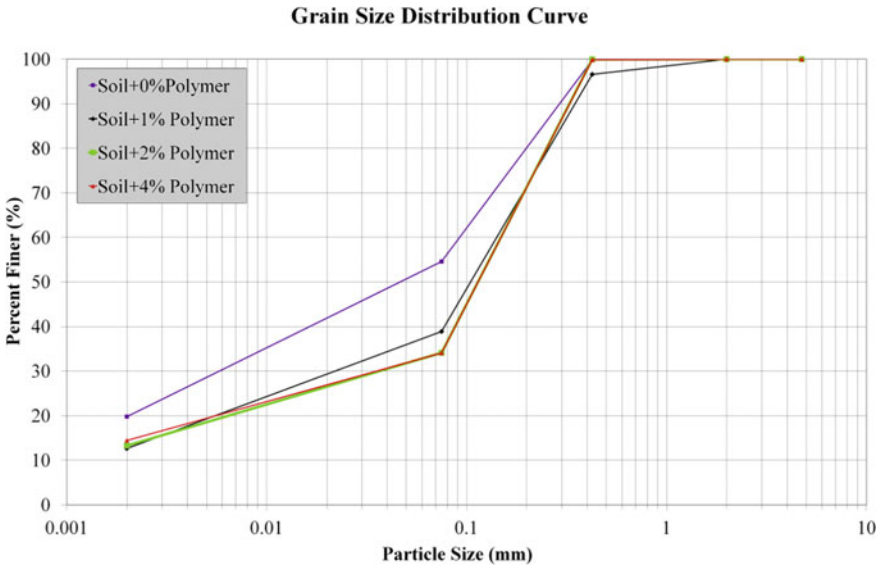

Fig. 14.2 Grain size distribution curves

Further studies will be done to examine the effect of urea-formaldehyde resin on strength properties, and an optimum polymer concentration to be mixed with soil to improve its engineering properties will be determined. FTIR studies and XRD analysis will be done to determine mechanism of interaction between urea-formaldehyde resin and the soil.

References

1. Bekkouche RS, Boukhatem G (2016) Experimental characterization of clay soils behaviour stabilized by polymers. J Fundam Appl Sci 8(3):1193–1205
2. Phougat N, Bharti RK, Khanna R, Dixit M, Chitra R (2019) Remediation of expansive soil by using polymer. In: Indian conference on geotechnical and geoenvironmental engineering. Motilal Nehru National Institute of Technology, Allahabad
3. Phougat N, Dixit M, Chitra R (2017) Remediation of expansive soil by using chemicals. In: 20th CRSI national symposium in chemistry, Gauhati University, pp 3–5
4. Phougat N, Dixit M, Chitra R (2016) Use of polymers for soil stabilization. In: 18th CRSI national symposium in chemistry, Punjab University, Chandigarh, pp 6–7
5. Phougat N, Vyas S (2007) Use of polymers for stablization dispersive soil. J Teach Res Chem 14(2):29–32
6. Naeini SA, Naderinia B, Izadi E (2012) Unconfined compressive strength of clayey soils stabilized with waterborne polymer. KSCE J Civ Eng 16(6):943–949
7. Phougat N (2021) Stablization of expansive soil. Water Energy Int 64/RNI(3):24–34
8. Hamed H, Hahid M, Andrady L, Hussain S (2013) Durability of LDPE nanocomposites with clay, silica and zinc oxide: part 1, mechanical properties of the nanocomposite materials. J Nanomaterials 1:1–6

9. Indraratna B, Mahamud M, Vinod JS, Wijeyakulasuriya V (2010) Stabilization of an erodible soil using a chemical admixtures. In: Bouassida M, Hamdi E, Said I (eds) ICGE'10: Proceedings of the 2nd international conference on geotechnical engineering, pp 45-54
10. Vinod JS, Indraratna B, Mahamud MA (2010) Stabilisation of an erodible soil using a chemical admixture. Proc Inst Civ Eng Ground Improv 163(1):43–52
11. Junkermann H, Schwab H (1978) Process for detoxification of formaldehyde containing wastewater. United States Patent 4104162

Chapter 15
Effect of Remoulding Water Content on Hydraulic Response of a Compacted Expansive Soil

M. Julina and T. Thyagaraj

Introduction

Depending on the design requirements of compacted clay liners for geotechnical engineering applications like brine ponds, waste impoundments, municipal and hazardous waste landfills, the natural clay soils when used are remoulded with pre-determined water content to obtain a pre-determined dry density. And the microstructure (macropores and micropores), volume change behaviour, and hydraulic conductivity of compacted expansive soils are controlled by the remoulding water content and compaction dry density [1–7]. For the same dry density along the standard Proctor compaction curve, the expansive soil has relatively larger macropores when compacted with remoulding water content on dry side of the optimum water content (OMC) than with water content on wet side of the OMC. Consequently, the hydraulic conductivity of expansive soil compacted with remoulding water content on dry side of the OMC at the swollen state remains relatively higher than the expansive soil compacted with remoulding water content on wet side of the OMC [1–3, 6]. Also, during swelling process, the magnitude of vertical swell of expansive soil compacted with remoulding water content less than the OMC remains relatively higher than the expansive soil compacted with remoulding water content higher than the OMC [4, 6, 7].

Basically, the swell-time plots of compacted expansive soil display different stages of swelling, i.e. initial, primary, secondary, and no swell regions [7–10]. The hydraulic conductivity of soils is determined at the end of swelling process in the secondary and no swell regions of time-swell plots [9, 10], whereas the infiltration rates of soils are determined during any stage of swelling process [9, 10]. Since the remoulding

M. Julina (✉) · T. Thyagaraj
Indian Institute of Technology Madras, Chennai 600036, India
e-mail: julina.lina15@gmail.com

T. Thyagaraj
e-mail: ttraj@iitm.ac.in

K. Muthukkumaran (eds.), *Soil Behavior and Characterization of Geomaterials*,
Lecture Notes in Civil Engineering 296, https://doi.org/10.1007/978-981-19-6513-5_15

water content of the compacted expansive soil significantly influences its hydraulic conductivity at complete saturation condition, it should also have a marked influence on the infiltration rates of soil during different stages of swelling. However, the effect of remoulding water content on the hydraulic response of compacted expansive soil is not studied in detail and needs examination.

Therefore, the present experimental study brings out the effect of remoulding water content on the hydraulic response of a compacted expansive soil during swelling process. To achieve this objective, two soil specimens compacted to the same standard Proctor compaction dry density at two different water contents corresponding to wet and dry sides of OMC were selected, and the infiltration tests using oedometric-infiltrometer test arrangement were carried out. The hydraulic response during swelling process is brought out in terms of inflow and outflow infiltration rates and hydraulic conductivity. And the scanning electron microscopy (SEM) images of as-compacted specimens are presented to bring out the microstructural differences, which aided in the interpretation of the test results.

Materials and Methods

Preparation of Compacted Soil Specimens

The processed natural expansive soil, with a plasticity index of 51%, was utilized in the present study (Table 15.1). The standard Proctor compaction curve of the expansive soil is shown in Fig. 15.1. The maximum dry density (MDD) and OMC of the soil were 1.34 Mg/m^3 and 28%, respectively.

To bring out the effect of remoulding water content on hydraulic behaviour of compacted specimens, two specimens (C1 and C2) corresponding to two points along the standard Proctor compaction curve, as shown in Fig. 15.1, were selected. The compacted dry density and remoulding water content of C1 specimen were 1.325 Mg/m^3 (98% of MDD) and 26.5% (dry of OMC), respectively. And the compacted dry density and remoulding water content of C2 specimen were 1.325 Mg/m^3 (98% of MDD) and 31% (wet of OMC), respectively. Prior to the static

Table 15.1 Properties of expansive soil ([9], [10])

Properties	Value
Sand fraction (%)	3
Silt fraction (%)	15
Clay fraction (%)	82
Liquid limit (%)	78
Plastic limit (%)	27
Unified soil classification system (USCS) symbol	CH
Specific gravity	2.71

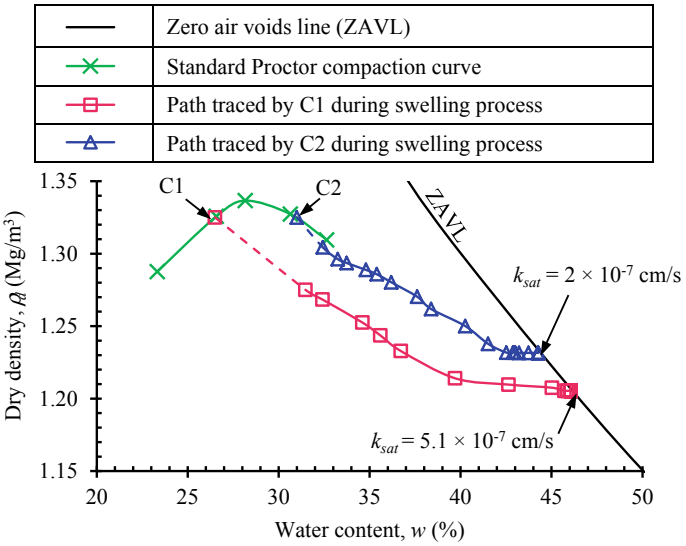

Fig. 15.1 Standard Proctor compaction curve of the expansive soil along with the paths traced by C1 and C2 specimens during swelling process

compaction of soil within the oedometric-infiltrometer ring, the soil was pre-wetted with distilled water (DW) to attain the desired water contents and stored properly for three days to attain the moisture equilibrium. The dimensions of the both the specimens, C1 and C2, at the as-compacted states were 75.4 mm diameter and 20 mm height.

The microstructure of compacted specimens at the as-compacted state was examined using SEM images which were acquired using Quanta 200. Small portions of the identical specimens at the as-compacted state of C1 and C2 were freeze-dried and then utilized for SEM analysis.

Infiltration Tests

Oedometric-infiltrometer test assembly, shown in Fig. 15.2, was used for carrying out the infiltration tests on compacted soil specimens [9, 10]. The test arrangement has a loading frame and oedometric-infiltrometer cell with modified oedometer ring and modified loading cap. The modified loading cap has two O-rings at its circumference and four connectors at the top to facilitate proper connection of two diagonally connected inflow tubes and two diagonally connected air vent tubes. Within the oedometric-infiltrometer cell, the compacted specimens sandwiched between the filter papers were further placed between a top porous stone and bottom acrylic disc with holes for infiltration testing. The inflow arrangement includes Mariotte tube,

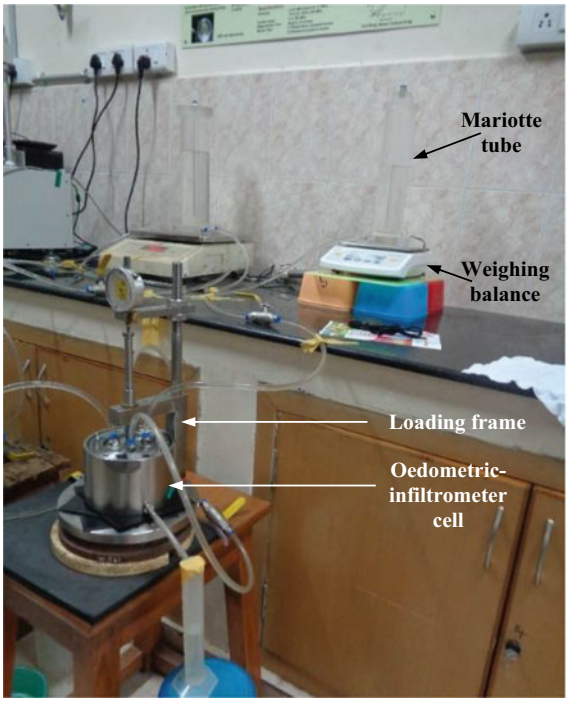

Fig. 15.2 Oedometric-infiltrometer test assembly for stage II testing

weighing balance with 0.01 g accuracy and, two semi-rigid and transparent inflow tubes with control valves. And the outflow arrangement includes two semi-rigid and transparent outflow tubes directed into a measuring jar placed above a weighing balance of 0.01 g accuracy.

During wetting of compacted specimens in oedometric-infiltrometer test arrangement, the percentage increase in vertical swell, inflow and outflow infiltration rates (I_{in} and I_{out}) occurring through the soil matrix, and hydraulic conductivity were measured. The inflow and outflow infiltration rates and hydraulic conductivity (k) were calculated using the following equations:

$$I_{in}(\text{cm/s}) = \frac{\text{Incremental inflow volume}}{\text{Area of oedometer ring} \times \text{Incremental time}} \tag{15.1}$$

$$I_{out}(\text{cm/s}) = \frac{\text{Incremental outflow volume}}{\text{Area of oedometer ring} \times \text{Incremental time}} \tag{15.2}$$

$$k(\text{cm/s}) = \frac{I_{in}}{\text{Hydraulic gradient}} \tag{15.3}$$

During stage I testing, the compacted specimens were inundated under an initial hydraulic gradient (i) of two, calculated solely based on the initial height of the

specimens at the compacted state, and under the applied vertical stress (12.5 kPa). After the attainment of steady-state condition (i.e. $I_{in} = I_{out}$), stage II testing was initiated. In the stage II testing, the compacted specimens were inundated under a hydraulic gradient of 22, calculated based on the swollen height of the compacted specimens at the end of stage I testing, and under the applied vertical stress (Fig. 15.2). The saturated hydraulic conductivity (k_{sat}) was determined at this stage of testing.

Results and Discussion

Effect of Remoulding Water Content on Swelling Behaviour

The SEM images at the as-compacted state of C1 and C2 specimens are presented in Fig. 15.3. It is evident from the SEM images that the expansive soil specimen compacted to 98% of MDD and dry of OMC (C1) has relatively larger pores than the specimen compacted to 98% of MDD and wet of OMC (C2). Upon wetting from the compacted state, both the specimens experienced volume increase in vertical direction. And the volume change behaviour during wetting of compacted C1 and C2 specimens in terms of time-swell plots is compared in Fig. 15.4b. As can be seen in Fig. 15.4b, the magnitude of vertical swell and rate of swelling of C1 specimen is relatively higher than C2 specimen. This behaviour is attributed to the lower remoulding water content of C1 specimen in comparison to C2 specimen. The SEM image analysis and volume change behaviour of C1 and C2 specimens are consistent with the results reported by Puppala et al. [4], Romero [5], Sivakumar et al. [6], Tripathy et al. [7], and others. In addition, the approximate time required for secondary swell region to start, identified in time-swell plots obtained from oedometric-infiltrometer testing, was about 300 and 800 min for the C1 and C2 specimens during swelling process, respectively.

Effect of Remoulding Water Content on Hydraulic Response

Figure 15.4a, b and c compare the variation of cumulative inflow and outflow volumes, infiltration rates (I_{in} and I_{out}) together with swell, and mean water content (w) and degree of saturation (S_r) with time of C1 and C2 specimens during swelling process in both stages of testing, respectively. It is evident from Fig. 15.4 that the remoulding water content of specimens at the as-compacted state not only influences the vertical swell magnitude during swelling process but also the infiltration rate and hydraulic conductivity during swelling process. During stage I testing, the compacted specimens inundated under an hydraulic gradient of two tend to swell in the vertical direction, and during this process, continuous inflow occurs as DW gets absorbed by the as-compacted expansive soil specimens continuously (Fig. 15.4a,

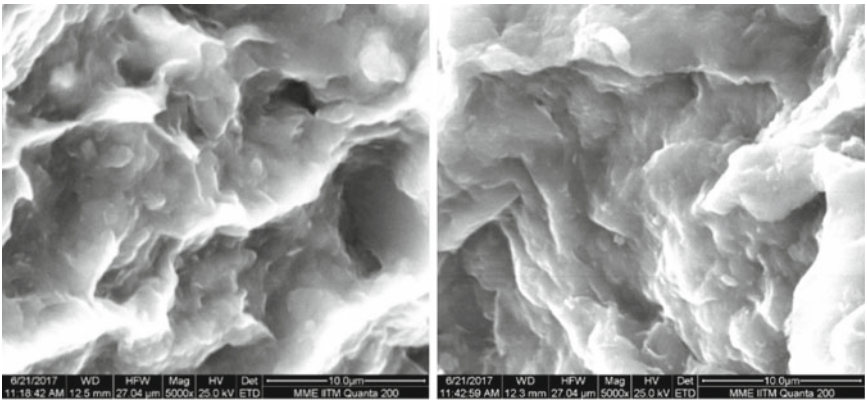

Fig. 15.3 SEM images of compacted soil specimens, C1 and C2

b). However, the cumulative inflow volume and inflow infiltration rate plots of C1 specimen were above the C2 specimen throughout stage I testing (Fig. 15.4a, b). This behaviour is attributed to the relatively lower remoulding water content at the as-compacted state and higher magnitude of vertical swell during wetting of the C1 specimen in comparison to C2 specimen.

Because of swelling of both the soil specimens, C1 and C2, the inflow infiltration rates gradually reduce with time (Fig. 15.4b). It should be noted here that for the first few minutes (6 min) of testing, the cumulative inflow volume and inflow infiltration plots cannot be plotted because of the absorption of infiltrating water by both the top porous stone and the soil specimen during this time period (Fig. 15.4a, b). The gradual decrease in the inflow infiltration rates in stage I testing of both the specimens, C1 and C2, approaches an approximate constant value (with $S_r > 97\%$; Fig. 15.4c) of 4.6×10^{-6} cm/s and 1.7×10^{-6} cm/s, respectively. This behaviour was observed at about 1000 min and 2600 min during swelling of C1 and C2 specimens, respectively (Fig. 15.4b). The attainment of approximate constant inflow infiltration rates occurred in the secondary swell region of time-swell plots during swelling in both the specimens (Fig. 15.4b). In addition, the water starts to permeate through the soil matrix, at the swollen state, of both the C1 and C2 specimens in the secondary swell region (Fig. 15.4b). And the outflow infiltration rates also attained an approximate constant value very close to the inflow infiltration rates (approximate steady state condition) at about 1000 min and 2600 min for the C1 and C2 specimens, respectively (Fig. 15.4b). In spite of having higher magnitude of swell during wetting, permeation outflow during wetting of C1 specimen occurred early with higher infiltration rates. This behaviour is attributed to the relatively porous microstructure of C1 specimen at its as-compacted state in comparison to C2 specimen.

Based on the time taken for the permeation outflow to start and attainment of approximate steady state condition, the infiltration rate and cumulative volume plots of compacted specimens are divided into two distinct regions namely: no outflow and

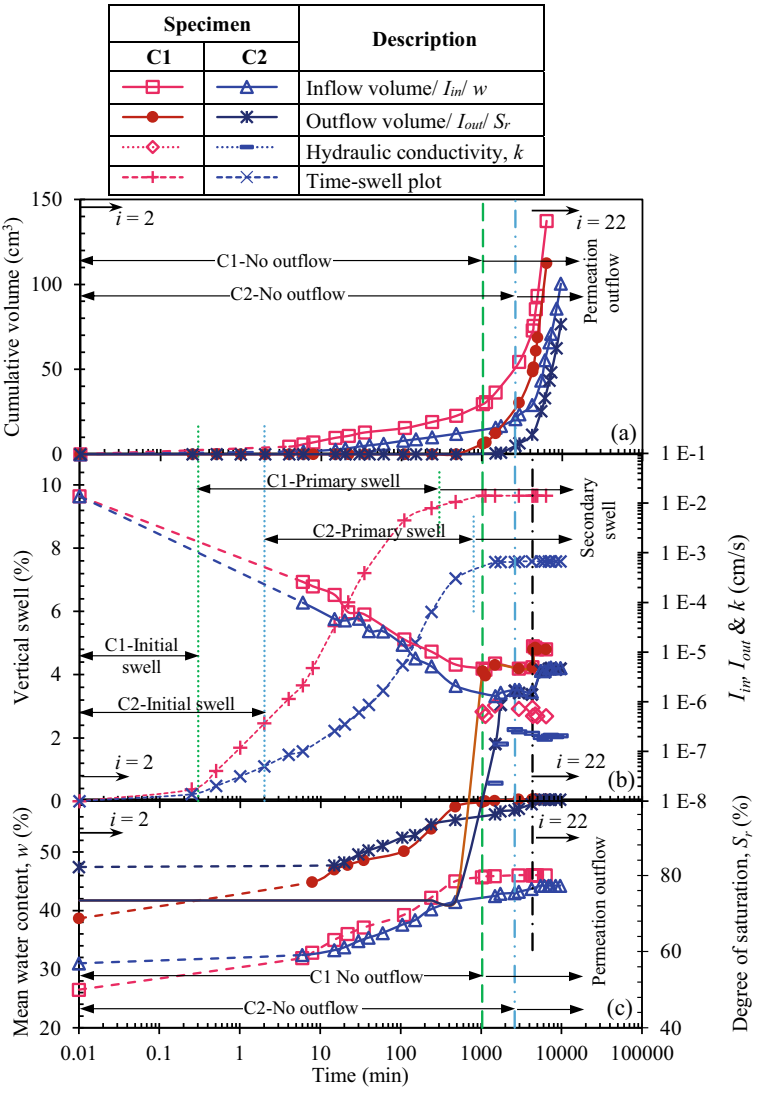

Fig. 15.4 Comparison of: **a** cumulative inflow and outflow volumes, **b** infiltration rates (I_{in} and I_{out}), hydraulic conductivity (k), and swell, and **c** mean water content (w) and degree of saturation (S_r) with time of C1 and C2 specimens during swelling process

permeation outflow regions (Fig. 15.4; [9]). For both the specimens, C1 and C2, the no outflow region occurred throughout the initial and primary swell regions and also occurred in the initial part of secondary swell region of the time-swell plot, whereas the permeation outflow region occurred in the secondary swell regions of the time-swell plot. Also, the infiltration rates approached steady-state condition ($I_{\text{in}} = I_{\text{out}}$)

in the permeation outflow region which also falls in the secondary swell region of the time-swell plot. It should be noted here that the no outflow region of C2 specimen during swelling also includes the data points with outflow infiltration rates lower than 1.7×10^{-6} cm/s (i.e. the region where approximate steady-state condition was not observed). The cumulative inflow and outflow volumes, and thus the corresponding inflow and outflow infiltration rates increased substantially because of the sudden increase in hydraulic gradient in stage II testing (Fig. 15.4a, b). As expected, the infiltration rates (both I_{in} and I_{out}) of the C1 specimen were higher than C2 specimen in stage II testing also (Fig. 15.4b).

The variation of hydraulic conductivity (k) with time during wetting of both the C1 and C2 specimens is also shown in Fig. 15.4b. The hydraulic conductivity of C1 specimen in the permeation outflow region was higher than the C2 specimen (Fig. 15.4b). And the saturated hydraulic conductivity of C1 and C2 specimens calculated in the steady-state condition in stage I testing as well as at the end of stage II testing was 5.1×10^{-7} cm/s and 2×10^{-7} cm/s, respectively (Figs. 15.1 and 15.4b). As expected, the water content of the C1 specimen ($w = 46.1\%$ at end of testing) at the swollen state was higher than the C2 specimen ($w = 44.3\%$ at end of testing) (Fig. 15.4c). The variation of hydraulic conductivity and swollen water content of the specimens, C1 and C2, are inconsistent with the existing literature [1, 3, 6].

In the present oedometric-infiltrometer testing, the volume and water content (presented in Fig. 15.4c) of the tested specimens can be derived from vertical swell and inflow and outflow infiltrating volume measurements, respectively. Utilizing the calculated volume and corresponding water content, the changes in dry density and water content during the swelling process of the C1 and C2 specimens were traced, and it is also presented in Fig. 15.1. Throughout the swelling process, the dry density of C2 specimen was higher than the dry density of C1 specimen. Similar observations can be found in the test results reported by Sivakumar et al. [6]. And because of the higher dry density of C2 specimens throughout the swelling process, the infiltration rates and hydraulic conductivity of C2 specimen were relatively lower than C1 specimen though out the swelling process.

Conclusions

The microstructural difference of compacted specimens due to the difference in the remoulding water contents not only influences the volume change behaviour but also influences the hydraulic response of the specimens during swelling process. As the specimen compacted with dry of optimum water content (C1) had relatively larger macropores, the C1 specimen exhibited higher hydraulic conductivity, magnitude of vertical swell, and rate of swelling during any stage of swelling process than the specimen compacted with wet side of optimum water content (C2). In addition, the infiltration tests on C1 and C2 specimens reveal that though the C1 specimen had higher magnitude of vertical swell, the specimens attained steady-state condition

much earlier with higher infiltration rates than the C2 specimen. Coincidentally, the dry density of C2 specimen was higher than the dry density of C1 specimen throughout the swelling process, which also resulted in reducing the infiltration rates and hydraulic conductivity of C2 specimen.

References

1. Benson CH, Trast JM (1995) Hydraulic conductivity of thirteen compacted clays. Clays Clay Miner 43:669–681
2. Daniel DE, Wu YK (1993) Compacted clay liners and covers for arid sites. J Geotech Eng 119(2):223–237
3. Lambe TW (1955) The permeability of fine-grained soils. In: Subcommittee R (ed) Symposium on permeability of soils. ASTM International, West Conshohocken, PA, pp 56–67
4. Puppala AJ, Manosuthikij T, Chittoori BC (2013) Swell and shrinkage characterizations of unsaturated expansive clays from Texas. Eng Geol 164:187–194
5. Romero E (2013) A microstructural insight into compacted clayey soils and their hydraulic properties. Eng Geol 165:3–19
6. Sivakumar V, Anderson C, Solan B, Rankin B, Mackinnon P (2015) Influence of testing on permeability of compacted fine soils. Proc Inst Civ Eng Geotech Eng 168(5):422–438
7. Tripathy S, Subba Rao KS, Fredlund DG (2002) Water content-void ratio swell-shrink paths of compacted expansive soils. Can Geotech J 39(4):938–959
8. Rao SM, Thyagaraj T, Thomas HR (2006) Swelling of compacted clay under osmotic gradients. Geotechnique 56(10):707–713
9. Julina M (2018) Effect of wet-dry cycles and interacting fluid on volume change and hydraulic behaviour of compacted clay liners. Ph.D. thesis India, Indian Institute of Technology Madras, 453
10. Julina M, Thyagaraj T (2021) Effect of hydraulic gradient on swell and hydraulic response of desiccated expansive soil–a experimental study. Int J Geotech Eng. https://doi.org/10.1080/19386362.2021.1902117

Chapter 16
GIS Mapping and Geostatistical Analysis of Dredged Soil Properties of Mangalam Reservoir

S. Athira and E. A. Subaida

Introduction

A considerable quantity of soil is needed for the construction of earth structures like embankments. Since the natural hills are the borrowed sources of the earth for such construction, alternative sources and materials must identify to avoid the exploitation of these natural resources. Bulk quantities of sediments dredged from reservoirs, and the suitability of using this material in earth structures is a sustainable and economical alternative to natural soil [1]. Therefore, assessing properties and enhancing the engineering properties of dredged soil has a good scope of research.

However, sediment properties from water bodies vary widely over distance-time and depend on numerous complicated natural and artificial processes. Soil deposited at various sites and times has varying engineering qualities. The results of laboratory tests are too localized and lack the simplistic heterogeneity of the total extended area [2, 3].

A database of geotechnical characteristics of reservoir sediments is significant to reuse the deposit in construction practices. In addition, this data helps to adopt proper treatment of soil and better engineering improvement. "Soil surveyors are aware of the regional diversity of soil qualities; standard soil maps do not depict it" [4, 5]. Traditional soil examination and interpretation are complex, time-consuming, and costly. As a result, geostatistical techniques (kriging) are commonly used in land resource inventories (Hengl et al. 2004). Soil properties are documented at an accessible location and attributed to regional mapping units. The present study aims

S. Athira (✉) · E. A. Subaida
A P J Abdul Kalam Technological University, Kerala, India
e-mail: aathirasmurali@gmail.com

E. A. Subaida
e-mail: subaidaea@gectcr.ac.in

K. Muthukkumaran (eds.), *Soil Behavior and Characterization of Geomaterials*,
Lecture Notes in Civil Engineering 296, https://doi.org/10.1007/978-981-19-6513-5_16

to trace the geotechnical properties of sediments from the Mangalam reservoir using soil samples and presentation of geotechnical data based on GIS and Inverse Distance Weighted Spatial Interpolation (IDW) techniques. Using Arc GIS, a sediment soil map was prepared, which displays the heterogeneity of soil types [6, 7]. GIS maps of soil sediments can help to make quick decisions on soil suitability for earthwork projects.

Study Area

Mangalam Dam is one reservoir constructed across the Cherukunnam River (a tributary of Mangalam River), which joints the Gayathri River and then the Bharathapuzha River. The network of the canal system has to irrigate 3440 ha of land. The reservoir is located between 10° 30′ N latitudes and 76° 32′ E longitude. The water spread area of the dam is 3.96 km^2 and 25.344 Mmm^3 at FRL of +77.88 mm. Sediment yield of the catchment results from the natural erosion process caused by water, wind, reservoir shore degradation, and landslides. Based on WGS (1984) data, the base maps were projected on UTM Zone 42. The GIS application used to develop polygon vector and point vector shape files of the base map of the reservoir with specified sampling points.

Materials and Methods

The study area was divided into random grids using a point shapefile, and the latitude and longitude of each grid point were documented. Figure 16.1 illustrates the watershed area and soil sampling points from Mangalam Dam. The reservoir is located between 10° 30′ N latitudes and 76° 32′ E longitude. The interval for both axes is 10° 00′. The samples (disturbed and undisturbed) were collected from the study area for clayey and C–Ø soils, respectively. The samples were subsequently oven-dried, crushed, and tested in the geotechnical laboratory as per Indian Standard 2720.

Spatial Interpolation of Soil Properties from Mangalam Reservoir

Spatial interpolation can forecast properties at non-sampled or non-data sites using limited data points. Due to the inaccessibility of sediments, regular soil testing is impossible. It is important to note that the geotechnical properties of soil vary with depth and width. Interpolating geotechnical data and anticipating data at unknown sites were employed to achieve this. Suppose each adjacent measured value has a

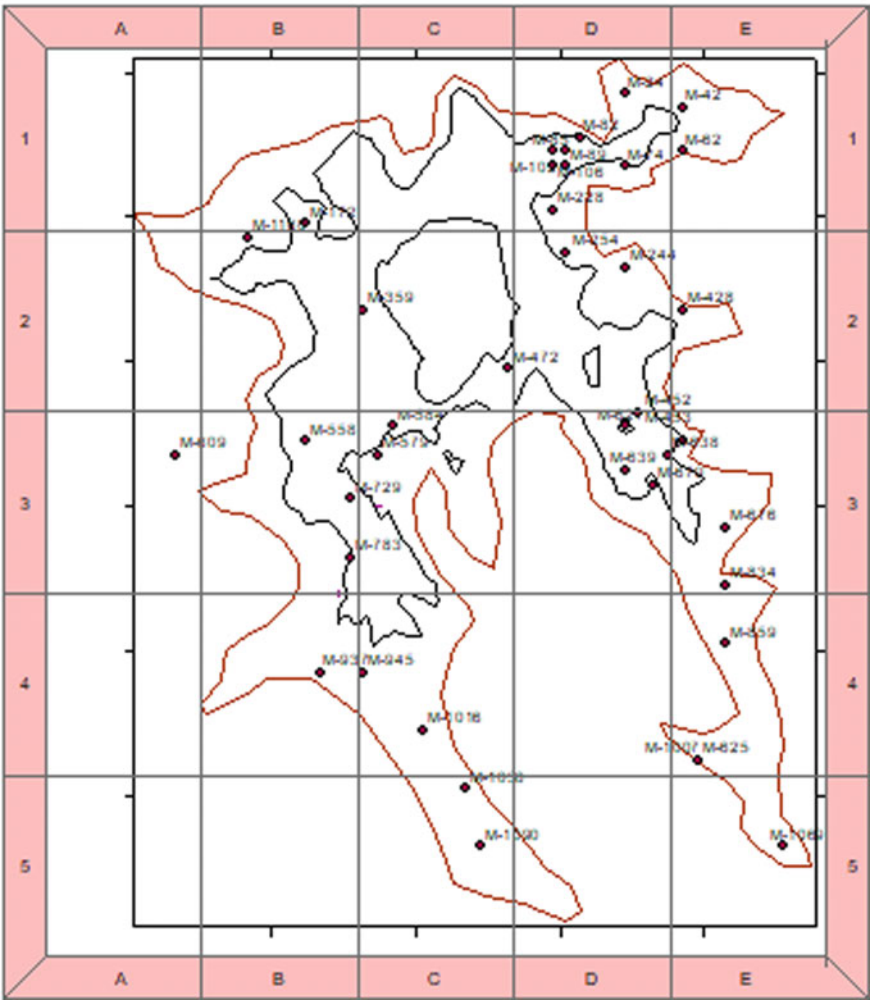

Fig. 16.1 Watershed area of Mangalam Dam and locations of soil samples

weight. In that case, an inverse distance weighted method can determine the unknown value (inversely proportional to the distance between each measured value and each unknown value). The IDW interpolation forecasts each soil property as a continuous map on the screen. As a result, sensitive soils can be identified anywhere in the region.

Assessment of Suitability of Soil Sediments in Embankment Construction

To assess the suitability of reservoir dredged soil in embankment construction, samples collected from two reservoir regions were tested for compaction parameters. Sandy silt and clayey silt soils were selected from two areas using a GIS map. Fly ash was used stabilizer to enhance the compaction properties of clayey silt.

Result and Discussion

Based on the laboratory test results, spatial variation in the percentage of clay and liquid limit of soil from locations were studied. Fifteen samples were tested, and an Excel database linked to the Arc map program was developed. Point data in the grid core at that position correspond to the soil parameters at that site. By the IDW technique, soil properties of nearby locations are interpolated. Thus, the IDW method generates continuous fields of characteristics at all points by employing the same set of parameters at all times.

Tables 16.1, 16.2 and 16.3 show the experimental results of samples (gradation, Atterberg limits, specific gravity and organic matter) named R1–R15. By analysing the initial characteristics of the soil samples, the clay-sized particle percentage ranges from 0.25 to 21%. The samples collected can be classified as low, intermediate, and high compressible silt and silty sand soil. The specific gravity ranges from 1.3 to 2.37. The liquid limit variation is found to range from 16.5 to 70.3%.

Distribution of Percentage Variation of Clay from Water Spread Area

Figure 16.2 illustrates the spatial variation of the percentage of clay. It varies from 15.7 to 20.93% *t* and is concentrated in the north-western (10.506° N and 76.544° E) and south-western (10.508° N and 76.536° E) regions. According to the spatial map of clay percentage, the dredged sediments collected at the study sites contain almost 40% sand and 45–50% of silt and clay. Due to a large percentage of silt and clayey silt soil in the northwest region, soil from this zone has poor engineering properties.

Table 16.1 Properties of the dredged soil

% of particle in soil	Sample R-1	Sample R-2	Sample R-3	Sample R-4	Sample R-5
IS classification	MI	SM	SM	SM	SM
Depth (m)	0.5	0.2	0.5	1.12	0.5
Clay percentage	21	11.21	11.04	12	18
Silt percentage	35.56	14.4	38.6	40.2	42
Fine sand percentage	16.5	28.2	14.8	14.8	7.91
Percentage of medium sand	23.6	33.7	38.6	26	27.5
Percentage of coarse sand	3.36	10.2	11.04	5.4	1.875
C_u and C_c values	4.5 and 1	6 and 1	10.25 and 1	6.2 and 2	4.33 and 1.02
Liquid limit (W_l)	40.41	43.63	38.73	45.06	45.635
Plastic limit (W_p)	32.95	23.33	29	31.13	32.95
Plasticity index (I_p)	7.46	20.3	9.73	13.93	12.685
Specific gravity (G)	1.6	2.37	2.09	2.12	2.15
Organic matter (%)	0.33	1.566	3.33	5.13	2.33

Table 16.2 Soil properties of collected samples

% of particle in soil	Sample R-6	Sample R-7	Sample R-8	Sample R-9	Sample R-10
IS classification	ML	ML	SM-SC	SM-SC	SC
Depth (m)	1.22	1.16	1	0.5	0.5
Clay percentage	9.780	12.100	12	6.63	12.32
Silt percentage	66.89	41.42	31.75	23.08	33.324
Fine sand percentage	10.55	22.080	20.206	15.8	26.03
Percentage of medium sand	11.94	23.782	28.489	9.402	23.003
Percentage of coarse sand	0.580	0.613	6	40.18	5.27
C_u and C_c values	–	6 and 1.5	–	–	10 and 1.6
Liquid limit (W_l)	40.8	34.93	36.004	33.944	43.56
Plastic limit (W_p)	36.81	32.95	29.22	28.609	32.5
Plasticity index (I_p)	4	1.98	6.784	5.335	11.06
Specific gravity (G)	1.7	1.3	2.05	1.61	1.6
Organic matter (%)	0.5	1.2	4.3	2.4	1.8

Table 16.3 Properties of soil samples

% of particle in soil	Sample R-11	Sample R-12	Sample R-13	Sample R-14	Sample R-15
IS classification	SM	SP	SW	MH	SM-SC
Depth (m)	0.5	1.15	0.68	1.5	0.77
Clay percentage	4.452	0.249	3.516	14.98	6.96
Silt percentage	46.28	1.413	9.73	83.05	46.29
Fine sand percentage	23.82	39.058	31.01	1.325	30.25
Percentage of medium sand	15.12	36.565	53.507	0.641	46.29
Percentage of coarse sand	4.608	14.127	0.057	0	1.5
C_u and C_c values	–	–	7.6 and 1.2	–	9 and 1.3
Liquid limit (W_l)	40.41	16	16.51	70.3	31.91
Plastic limit (W_p)	32.95	0	0	47.62	32.95
Plasticity index (I_p)	7.46	0	0	22.68	4.46
Specific gravity (G)	2.07	2.53	1.96	1.7	1.73
Organic matter (%)	0.53	0.2	0.6	3.2	6.2

Analysis of Liquid Limit Variation of Sediments from Water Spread Area

Figure 16.3 demonstrates the spatial distribution of liquid limit variation using IDW interpolation. Soil from the northwest region of the watershed area has the highest liquid limit ranging from 50 to 70%. The specific gravity of this region ranges from 1.3 to 1.62. The percentage of liquid limit ranges from 15 to 30%, and specific gravity ranges from 1.7 to 2.53 around the northeast region.

Suitability of Soil Sediments in Embankment Construction

To study the suitability of reservoir dredged soil for embankment construction, soil samples collected from two regions of the reservoir were tested for compaction

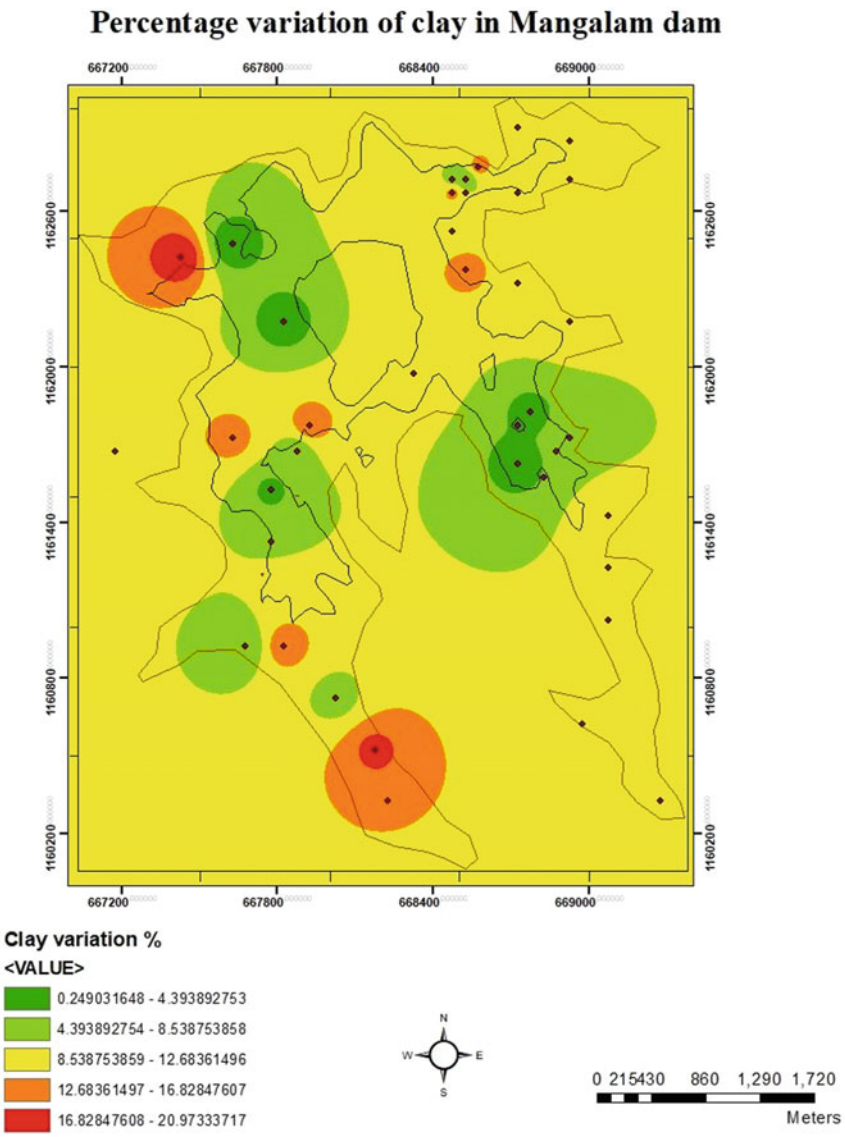

Fig. 16.2 Variation of clay percentage

parameters sample R2 from the southeast region and R10 from the northwest region. R2 is a sandy silt sample, and R10 is clayey silt. Maximum dry density and optimum moisture content obtained for sample R2 are 2.35 g/cc and 11.05%, respectively (Fig. 16.4). Therefore, this soil can be used for earthwork constructions without further treatment.

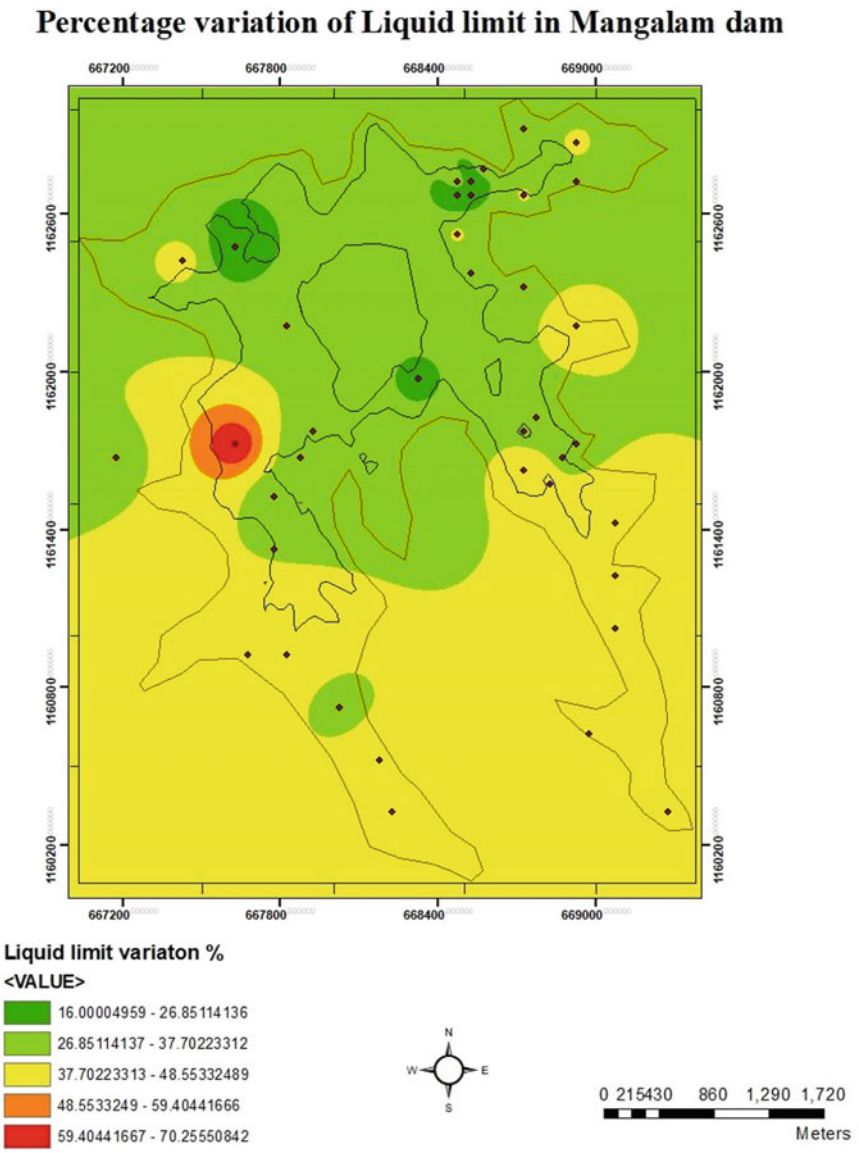

Fig. 16.3 Spatial variation in the liquid limit of Mangalam sediment

Sample R10 contains a higher percentage of clay. The test result shows that maximum dry density is 1.8 g/cc and optimum moisture content is 19.52% (Fig. 16.5 and Table 16.4). The potential of enhancement of compaction parameters using fly ash was tried on this soil sampl [4]. Class C fly ash was used as the stabilizing agent. Three percentages of fly ash (5, 10 and 15%) were added to the sample R10, and

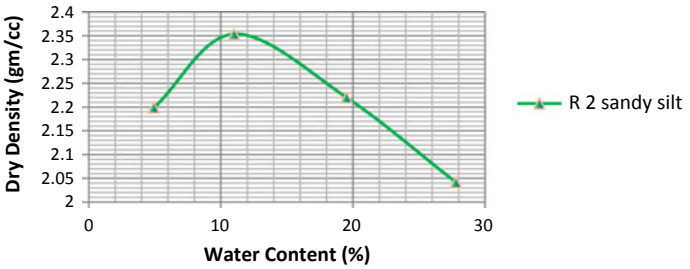

Fig. 16.4 Compaction curve of sample R2

the maximum dry densities and optimum moisture contents obtained are presented in Fig. 16.5. The results show that maximum enhancement was obtained by adding 10% of fly ash. The maximum dry density increased to 2.13 g/cc, and OMC reduced to 8%. The result indicates that significant improvement is possible by way of fly ash stabilization for clayey silt dredge.

The investigation shows that reservoir dredged soil is suitable for earthwork constructions like embankments with or without stabilization, depending upon the soil type. The GIS map developed provides an idea regarding the nature of the soil in different locations of the reservoir. Accordingly, the work can be planned as to

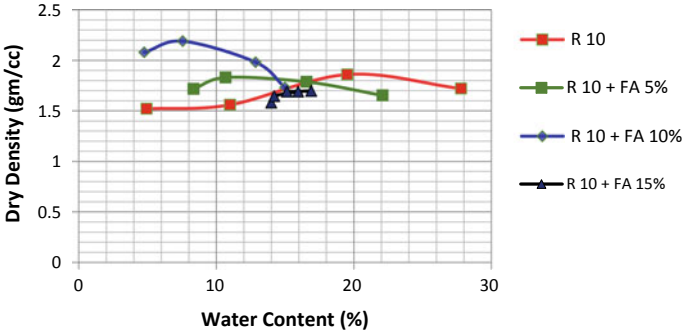

Fig. 16.5 Compaction curves of sample R 10

Table 16.4 Compaction properties

Sample	Dry density (gm/cc)	OMC (%)
Raw dredged soil (**R-10**)	1.8	19.52
R-10 + 5% class C fly ash	1.83	10.67
R-10 + 10% class C fly ash	2.18	8
R10 + 15% class C fly ash	1.7	16.9

whether the soil can be directly used for earth structures or stabilization is required. However, a further detailed study is necessary to assess the engineering properties of dredge soil for specific uses.

Conclusions

The following conclusions are derived from the study.

1. The IDW technique can be successfully used to create GIS maps of soil parameters in a reservoir. Digital soil maps are more detailed than hand-drawn data.
2. These maps are helpful to identify the nature of sediments at different locations of the reservoir. In addition, the locations of dredge suitable for earthwork constructions can be selected using the map.
3. The major part of sediment in Mangalam Dam is classified as intermediate compressible silt and sandy silt.
4. Sandy silt dredge can be used for earthwork construction without treatment.
5. Dredge from the clayey silt-type sediment zone can be effectively utilized for earthwork construction after stabilization using fly ash.

Acknowledgements All India Council for Technical Education (AICTE) granted the scholarship for this research (AICTE Doctoral Fellowship).

References

1. Bhairappanavar S, Liu R, Coffman R (2018) Beneficial uses of dredged material in green infrastructure and living architecture to improve resilience of Lake Erie. Infrastructures 3(4):1–16
2. Robinson TP, Metternicht G (2006) Testing the performance of spatial interpolation techniques for mapping soil properties. Comput Electron Agric 50(2):97–108
3. Vieira VA, Mello CR, Lima JM (2007) Spatial variability of soil physical attributes in a small watershed. Cienc Agrotecnol 31(5):1477–1485
4. Jalal FE, Xu Y, Jamhiri B, Memon SA, Graziani A (2020) On the recent trends in expansive soil stabilisation using calcium-based stabiliser materials: a comprehensive review. Adv Mater Sci Eng 2020
5. Heuvelink GBM, Webster R (2001) Modelling soil variation: past, present and future. Geoderma 100(3–4):269–301
6. Singh A, Noor S, Chitra K, Gupta M, Vel T (2015) GIS applications in geotechnical engineering—some case studies. Int J Latest Trends Eng Technol 5(2):36–42
7. Shit PK, Bhunia GS, Maiti R (2016) Spatial analysis of soil properties using GIS-based geostatistics models. Model Earth Syst Environ 2(2):1–6
8. Shao MA (2013) Spatial variability of soil physical properties in a region of the Loess Plateau of PR China subject to wind and water erosion. Land Degrad Dev 24(3):296–304
9. Tomislav Hengl a, Gerard B.M. Heuvelink b, Alfred Stein (2004) A generic framework for spatial prediction of soil variables based on regression-kriging Geoderma 120:75–93

Chapter 17
Correlating Relative Density and Particle Distribution at Specific Compaction Energy of Cohesionless Soil in Ahmedabad Region

Shyamkumar N. Marsonia and Mayur G. Vanza

Introduction

Relative density represents denseness of cohesionless soil and large extend of engineering properties of cohesionless soil directly related to it. Holts and kovacs [1] suggest that for soil having fines less than 12%, then field compaction quality is better indicated by relative density (D_r) than relative compaction (R_c).

In present study, an attempt was made to carryout correlation by multiple linear regression between relative density (at specified compaction energy) and same soil index properties (F_c%, D_{10}, D_{30}, D_{50}, D_{60}, C_u, C_c, G_s). Multiple linear regression analysis is done by SPSS 16.0. Compaction test on soil in laboratory is done by standard proctor test (light compaction) and modified proctor test (heavy compaction). By concluding void ratio at maximum dry density from compaction test, a model develop for prediction of relative density at corresponding energy (593 Kn m/m^3 and 2698 Kn m/m^3) prior to work exhibits in field. Relative density (D_r) of soil represents relative position of void ratio e_o with its maximum void ratio (e_{max}) and minimum void ratio (e_{min}). relative density (D_r)% defines by equation as

$$D_r\% = \frac{e_{max} - e_0}{e_{max} - e_{min}} \times 100 \tag{17.1}$$

Youd [2] observed that particle shape, particle size range, variance in gradation curve influence more than only particle size. Youd develop relation between e_{max} and e_{min} to C_u by taking particle angularity (A) as parameter. Cubrinovski and Ishihara [3] investigate characteristics of sand's maximum and minimum void ratio. In study, author concludes that key advantages of void ratio range (e_{max}–e_{min}) over conventional material parameters such as F_c and D_{50}. As per author, void ratio range is

S. N. Marsonia (✉) · M. G. Vanza
Applied Mechanics Department, L. D. College of Engineering, Ahmedabad, India
e-mail: shyam.maronia@gmail.com

K. Muthukkumaran (eds.), *Soil Behavior and Characterization of Geomaterials*,
Lecture Notes in Civil Engineering 296, https://doi.org/10.1007/978-981-19-6513-5_17

indicative of overall grain size composition of given soil and gives general basis for comparative evaluation of material properties. Gunaydin [4] investigates correlation between soil compaction parameter and soil classification properties by using statistical analyses and artificial neural networks. Author gets good correlation results ($r^2 = 0.70$ - 0.95). Das [5] tries to correlate relative density and relative compaction based on laboratory and field test. Various tests on soil as classification, density index test, filed density, standard and modified compaction test are investigated on 185 soil sample. Multiple linear regression is carried out to correlate relative compaction and relative density, maximum (e_{max}) and minimum void ratios (e_{min}), and express e_{max} and e_{min} in terms of median grain size (D_{50}) and uniformity coefficient (C_u) where 95% confident interval achieved.

The presented literature review is motivated for the current research, wherein study tries to conclude an empirical equation for relative density (D_r) at specific compaction energy based on index properties of soil.

Soil Sample Collection

Total 30 samples are collected from Ahmedabad region. The sample collection location selected such in manner that soil of that location is of cohesionless in nature. Various location of Sabarmati river or other location are selected. Collection of sample is done in group of three number at different nearby places of main location. Major locations are Amobod village (Sabarmati river), Sadra village (Sabarmati river), Vautha village (Dhodka) (Vatrak river). Other locations are Limbdi, Valad, Simalkhedi, Piplaj, Rohisa, and Kaniz.

Experimental Program

Following laboratory experiment is done on collected sample for get particle size distribution, specific gravity, maximum and minimum void ratio, and void ratio at different compaction energy. Table 17.1 represents all test results.

Particle Size Analysis

Mechanical grain size distribution is used to identify present of different size particle in tested soil. Oven dry samples were taken for sieve analysis. In test set of different sizes of sieves as follows: 4.75 mm, 2 mm, 1 mm, 600 μ, 425 μ, 300 μ, 212 μ, 150 μ, 75 μ are used. F_c%, D_{10}, D_{30}, D_{50}, D_{60}, C_u, C_c all are input variable getting from the test. Figure 17.1 characterize all grain size distribution curve.

Table 17.1 All test results of 30 samples

No	F_C %	D_{10}	D_{30}	D_{50}	D_{60}	C_u	C_c	G_s	e_{max}	e_{min}	e_s	e_m
1	1.500	0.255	0.510	0.725	0.887	3.478	1.150	2.661	0.690	0.381	0.530	0.436
2	6.000	0.127	0.257	0.379	0.469	3.693	1.109	2.535	0.681	0.441	0.552	0.483
3	7.400	0.176	0.486	0.730	0.890	5.057	1.508	2.649	0.763	0.513	0.616	0.549
4	9.000	0.084	0.305	0.509	0.591	7.036	1.874	2.536	0.845	0.546	0.621	0.559
5	6.300	0.160	0.305	0.698	0.820	5.125	0.709	2.535	0.691	0.432	0.527	0.450
6	1.143	0.247	0.405	0.549	0.660	2.672	1.006	2.637	0.747	0.458	0.573	0.504
7	2.234	0.166	0.387	0.720	1.170	7.048	0.771	2.618	0.553	0.315	0.415	0.360
8	0.792	0.234	0.368	0.510	0.585	2.500	0.989	2.637	0.672	0.376	0.488	0.413
9	1.723	0.160	0.297	0.568	0.800	5.000	0.689	2.646	0.701	0.381	0.548	0.412
10	1.578	0.160	0.297	0.550	0.800	5.000	0.689	2.635	0.642	0.321	0.470	0.348
11	1.013	0.185	0.400	0.700	1.136	6.141	0.761	2.604	0.588	0.311	0.428	0.367
12	1.158	0.171	0.400	0.800	1.653	9.667	0.566	2.682	0.530	0.273	0.427	0.290
13	3.836	0.218	0.677	1.257	1.620	7.431	1.298	2.537	0.621	0.336	0.443	0.379
14	3.476	0.116	0.401	1.368	2.029	17.491	0.683	2.622	0.497	0.296	0.389	0.334
15	2.444	0.246	0.387	0.541	0.671	2.728	0.907	2.642	0.776	0.479	0.599	0.534
16	4.571	0.165	0.375	0.545	0.701	4.248	1.216	2.688	0.732	0.483	0.581	0.520
17	1.767	0.319	0.770	1.120	1.488	4.665	1.249	2.558	0.529	0.272	0.361	0.283
18	1.574	0.319	0.721	1.212	1.547	4.850	1.053	2.568	0.586	0.306	0.419	0.343
19	2.010	0.228	0.613	0.950	1.260	5.526	1.308	2.572	0.524	0.291	0.378	0.317
20	1.429	0.251	0.462	0.558	0.641	2.554	1.327	2.654	0.789	0.503	0.607	0.542
21	0.972	0.235	0.471	0.965	1.178	5.013	0.801	2.593	0.566	0.276	0.371	0.316
22	2.557	0.270	1.021	2.000	2.450	9.074	1.576	2.589	0.481	0.230	0.334	0.275
23	4.209	0.200	0.738	1.800	2.400	12.000	1.135	2.587	0.482	0.245	0.347	0.286
24	2.547	0.380	1.510	2.289	2.750	7.237	2.182	2.585	0.546	0.255	0.376	0.305
25	5.647	0.120	0.300	0.503	0.906	7.550	0.828	2.574	0.575	0.354	0.446	0.384
26	0.640	0.356	0.789	1.380	1.700	4.775	1.029	2.609	0.548	0.293	0.407	0.350
27	1.377	0.230	0.318	0.421	0.717	3.117	0.613	2.602	0.598	0.345	0.431	0.376
28	2.051	0.291	0.599	0.920	1.250	4.296	0.986	2.565	0.608	0.332	0.457	0.392
29	3.582	0.200	0.267	0.340	0.390	1.950	0.914	2.697	0.843	0.542	0.632	0.559
30	2.991	0.233	0.449	0.900	1.250	5.365	0.692	2.582	0.596	0.310	0.443	0.368

Specific Gravity of Soil Solids

Determining as per IS 2720 Part-3 [6] section (1). 50 ml density bottle used to find specific gravity of soil. A vacuum desiccator used to remove air from bottle by using vacuum pump. Specific gravity is also used as input variable in regression analysis.

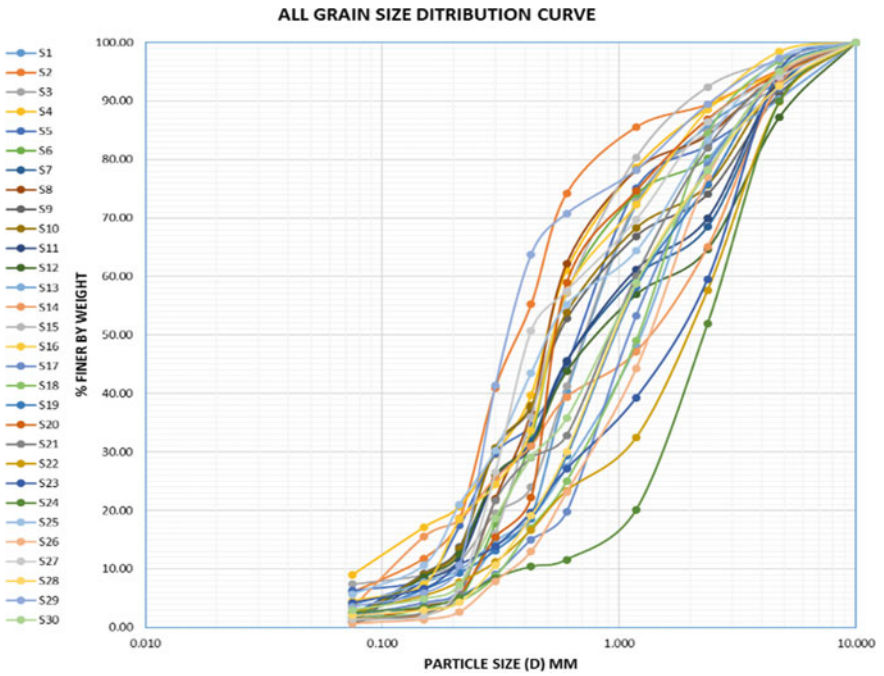

Fig. 17.1 All 30 sample grain size distribution curves

Density Index Test

Density index test [7] used find minimum and maximum density at dry state of cohesionless soil. It is used to derive maximum and minimum void ratio (range of void ratio). Test is divided into two stages as follows:

Determination of Minimum Dry Density

An oven dry sample of soil was taken to determine the minimum density (maximum void ratio) of cohesionless soil. The minimum density is determined by filling dry soil into a mould (3000 cm^3) with a special hopper as per IS: 2720 part—14 [7], and adjusting the spout of the hopper device so that the free fall level not more than 25 mm. Maximum void ratio (e_{max}) at minimum dry density is calculated by following equation.

$$e_{max} = \frac{G_s * \gamma_w}{\gamma d_{min}} - 1 \tag{17.2}$$

Determination of Maximum Dry Density

After determining minimum dry density, same loose fill soil mould is attached to vibration table. Surcharge load mounted on soil surface and table vibrate at 60–70 Hz frequency with amplitude range 0.05–0.65 mm, for 8 min to compact loose fill soil in mould. Compacted density is determined from soil mass dividing by reducing volume of compacted soil. Minimum void ratio ($e_{\min}$) at maximum dry density is calculated by following equation.

$$e_{\min} = \frac{G_s * \gamma_w}{\gamma d_{\max}} - 1 \tag{17.3}$$

Laboratory Compaction Test

Laboratory compaction test is used for determine maximum dry density of soil achieved by compaction, at specified compaction energy prior to work exhibit in field. For field compaction, specification up to 90–95% of density needs to achieved reference to laboratory compacted density. Two types of laboratory compaction test are used as standard compaction and modified compaction to find corresponding void ratio and derive relative density after compaction by comparing void ratio with maximum and minimum void ratio of same soil.

Standard Compaction

In test, soil was compacted into three equal layers in 1000 cm^3 mould, with each layer experiencing 25 hammer blows weighing 2.6 kg. The hammer falls from a height of 0.31 m with applied compaction energy of 593 Kn m/m^3. Void ratio (e_s) of compacted soil is calculated by equation, where γd_s represents maximum dry density at standard compaction.

$$e_s = \frac{G_s * \gamma_w}{\gamma d_s} - 1 \tag{17.4}$$

Modified Compaction

Same 1000 cm^3 mould is used for compaction. Soil is compacted by 4.89 kg hammer in total five layer with hammer drop of 0.45 m. In test, compaction energy 2698 Kn m/m^3 is applied on soil. Void ratio of compacted soil is calculated by following equation, where γd_m represents maximum dry density at modified compaction.

$$e_m = \frac{G_s * \gamma_w}{\gamma d_m} - 1 \tag{17.5}$$

Multiple Linear Regression Analysis

Multiple linear regression analysis carries out to develop model of (1) maximum void ratio (e_{max}), (2) minimum void ratio (e_{min}), (3) void ratio at standard compaction (e_s) and modified compaction (e_m), by help of F_c%, D_{10}, D_{30}, D_{50}, D_{60}, C_u, C_c, G_s as input variables. Multiple linear regression is carried out in SPSS 16.0. Quality of regression model concludes by following statistical features: (1) higher value of coefficient of determination (r^2), (2) having low value of SSE (sum of square due to errors), and (3) pass the F-test with preselected α significant values ($\alpha = 0.05$).

The coefficient of determination (r^2) is used to measure preciseness of regression model. The reduction in model error related with the use of independent variables is measured by the coefficient r^2, ranges from 0 to 1. The standard error of estimated SEE (square root of the mean squared error) is widely used to measure the regression model's prediction accuracy. As a result, a model with strong prediction ability will have a low SEE value.

From Table 17.2, all regression models possess higher value of R^2. SSE values are also lower. The model F-Significant is also less than 0.05 ($\alpha = 0.05$) to accept alternate hypothesis which means there is existence of relation between independent variables and independent variable. Tables 17.3 and 17.4 show information of numerical model for all regression model, which includes coefficient of variables, standard errors, t-statistics, and 95% confidence interval on coefficient of variable.

Figure 17.2 shows that predicted versus experimental maximum and minimum void ratios are in range of ±5% from 1:1 line. Figure 17.3 shows predicted versus experimental void ratio corresponding standard, and modified compaction is also within ±5% range. By using this regression model, a unique model develop to predict

Table 17.2 Regression model summary and ANOVA

Regression model		Model_1	Model_2	Model_3	Model_4
Dependent variable		e_{max}	e_{min}	e_s	e_m
Independent variable		F_c%, D_{10}, D_{30}, D_{50}, D_{60}, C_u, C_c, G_s			
Model summary					
R (correlation coefficient)		0.941	0.9634	0.945	0.956
R^2 (coefficient of determination)		0.886	0.9282	0.892	0.914
Adjusted R^2		0.843	0.901	0.852	0.881
Standard error of estimate		0.041	0.029	0.034	0.031
ANOVA					
Sum of square (ss)	Regression	0.2804	0.2320	0.2098	0.2164
	Errors	0.0359	0.0179	0.0253	0.0203
	Total	0.3164	0.2499	0.2352	0.2367
Model F-value		20.4754	33.9782	21.7056	27.9577
Model F-significates		2.81871E−08	2.54398E−10	1.66358E−08	1.61021E−09

Table 17.3 Coefficient table of regression models 1 and 2

	Model_1 (e_{max})						Model_2 (e_{min})					
	Unstandardized coefficients		t	P value	95.0% confidence interval for B		Unstandardized coefficients		t	P value	95.0% confidence interval for B	
	B	Std. error			Lower	Upper	B	Std. error			Lower	Upper
Const	−1.217	0.524	0.030	0.030	−2.306	−0.127	−1.518	0.370	0.001	0.001	−2.288	−0.748
F_c%	0.014	0.007	0.058	0.057	−0.001	0.029	0.023	0.005	0.000	0.000	0.013	0.034
D_{10}	0.440	0.376	0.254	0.025	−0.341	1.222	0.724	0.266	0.013	0.012	0.172	1.277
D_{30}	−0.172	0.252	0.504	0.049	−0.696	0.353	−0.138	0.178	0.447	0.044	−0.509	0.233
D_{50}	0.158	0.100	0.131	0.013	−0.051	0.367	0.091	0.071	0.216	0.021	−0.057	0.238
D_{60}	−0.221	0.122	0.084	0.085	−0.474	0.032	−0.196	0.086	0.033	0.032	−0.375	−0.017
C_u	0.002	0.010	0.861	0.074	−0.020	0.024	0.010	0.007	0.206	0.027	−0.006	0.025
C_c	0.106	0.067	0.133	0.012	−0.035	0.246	0.074	0.048	0.135	0.013	−0.025	0.173
G_s	0.691	0.195	0.002	0.002	0.286	1.096	0.670	0.138	0.000	0.000	0.383	0.956

Table 17.4 Coefficient table of regression models 3 and 4

	Model_3 (e_s)						Model_4 (e_m)					
	Unstandardized coefficients		t	P value	95.0% confidence interval for B		Unstandardized coefficients		t	P value	95.0% confidence interval for B	
	B	Std. error			Lower	Upper	B	Std. error			Lower	Upper
Const	−1.641	0.439	0.001	0.001	−2.553	−0.728	−1.524	0.394	0.001	0.001	−2.343	−0.705
F_c%	0.020	0.006	0.003	0.003	0.008	0.033	0.023	0.005	0.000	0.001	0.012	0.034
D_{10}	0.516	0.315	0.116	0.012	−0.138	1.171	0.818	0.283	0.009	0.009	0.230	1.406
D_{30}	−0.096	0.211	0.055	0.655	−0.535	0.343	−0.132	0.190	0.492	0.049	−0.527	0.262
D_{50}	0.072	0.084	0.039	0.394	−0.103	0.247	0.121	0.076	0.123	0.012	−0.036	0.278
D_{60}	−0.162	0.102	0.127	0.127	−0.374	0.050	−0.223	0.091	0.024	0.023	−0.413	−0.033
C_u	0.004	0.009	0.061	0.623	−0.014	0.023	0.011	0.008	0.185	0.185	−0.006	0.027
C_c	0.053	0.057	0.035	0.355	−0.064	0.171	0.064	0.051	0.219	0.022	−0.041	0.170
G_s	0.782	0.163	0.000	0.000	0.443	1.121	0.681	0.146	0.000	0.000	0.376	0.986

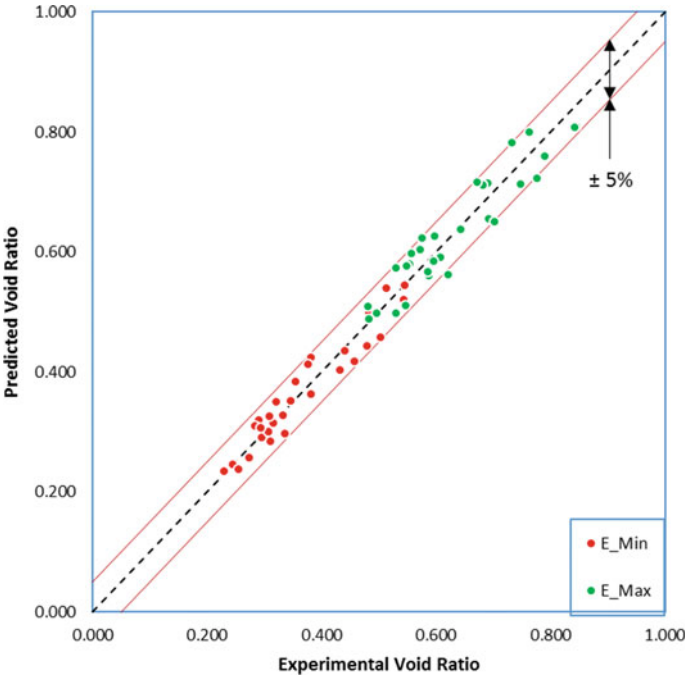

Fig. 17.2 Predicted versus experimental void ratio (e_{max} and e_{min})

relative density at two different compaction energy (593–2698 Kn m/m^3) is described in Sect. 3.4.

Prediction of Relative Density

Relative density in terms of void ratio is defined as Eq. 17.1. In present study, an attempt was made to predict relative density at two different compaction energy. The equation defines the predictive relative density as

$$D_{r(s)}\%(\text{predicted}) = \frac{e_{max}(\text{Predicted}) - e_s(\text{Predicted})}{e_{max}(\text{Predicted}) - e_{min}(\text{Predicted})} \times 100 \tag{17.6}$$

and

$$D_{r(m)}\%(\text{predicted}) = \frac{e_{max}(\text{Predicted}) - e_m(\text{Predicted})}{e_{max}(\text{Predicted}) - e_{min}(\text{Predicted})} \times 100 \tag{17.7}$$

e_{max}, e_{min}, e_s and e_m are predicted variables from regression models (Tables 17.3 and 17.4). Following are models of relative density concluded by Eqs. 17.6 and 17.7.

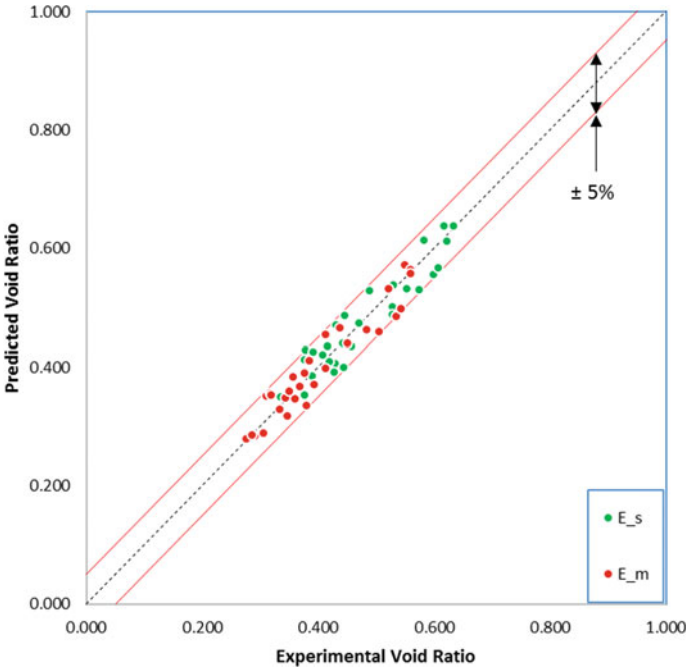

Fig. 17.3 Predicted versus experimental void ratio (e_s and e_m)

$$\begin{aligned} \boldsymbol{D}_{\mathbf{r(s)}}\% = {} & (152.212) + (-0.387 * F_c\%) + (25.676 * D_{10}) \\ & + (-15.629 * D_{30}) + (17.745 * D_{50}) + (-17.667 * D_{60}) \\ & + (-0.605 * C_u) + (10.431 * C_c) + (-37.951 * G_s) \end{aligned} \tag{17.8}$$

and

$$\begin{aligned} \boldsymbol{D}_{\mathbf{r(m)}}\% = {} & (104.904) + (-0.308 * F_c\%) + (-46.058 * D_{10}) \\ & + (-3.499 * D_{30}) + (-9.921 * D_{50}) + (10.364 * D_{60}) \\ & + (-0.936 * C_u) + (5.002 * C_c) + (-3.746 * G_s) \end{aligned} \tag{17.9}$$

Table 17.5 represents % relative error between predicted and experimental relative density.

Figure shows the % deviation in predicated versus experimental relative density with two ranges are ±5% and ±10% with reference to 1:1 line.

Table 17.5 represents the relative % error in of predictive model to actual value. In some few cases, error value reached up to ±15% in relative density at standard compaction energy, which occurs due large value change in few independent variable corresponding no or proposed less change in dependent variable, due to systematic or random error occurs during investigation. In case of relative density at modified

Table 17.5 % Relative error in predicted versus experimental relative density

No	$D_{r(s)}$ % (experimental)	$D_{r(s)}$% (predicted)	% error	$D_{r(m)}$% (experimental)	$D_{r(m)}$% (predicted)	% error
1	53.945	60.439	12.037	82.112	85.614	4.266
2	56.573	65.123	15.113	82.663	90.093	8.988
3	58.973	62.509	5.995	85.813	87.905	2.438
4	74.744	74.164	−0.776	95.700	92.415	−3.432
5	63.214	61.178	−3.220	92.881	85.437	−8.014
6	60.063	61.656	2.653	84.058	85.958	2.260
7	58.026	54.542	−6.003	81.239	87.836	8.120
8	62.203	62.186	−0.028	87.514	86.525	−1.129
9	54.356	56.487	3.921	90.223	87.702	−2.794
10	53.572	56.667	5.779	89.088	87.925	−1.305
11	57.548	55.489	−3.577	86.973	87.871	1.032
12	40.199	43.691	8.687	93.248	88.326	−5.278
13	62.452	61.482	−1.554	84.899	85.844	1.113
14	53.634	54.295	1.233	81.087	82.011	1.139
15	59.543	60.057	0.864	81.411	85.164	4.609
16	60.485	59.499	−1.630	84.956	88.630	4.325
17	62.357	60.185	−3.482	88.623	83.200	−6.119
18	59.760	59.147	−1.026	87.053	82.038	−5.761
19	69.043	61.702	−10.633	90.614	87.103	−3.874
20	63.636	63.870	0.367	86.364	86.833	0.543
21	60.651	59.503	−1.893	86.771	84.738	−2.343
22	58.456	58.144	−0.534	82.035	83.732	2.069
23	56.893	54.768	−3.736	82.870	83.813	1.137
24	58.306	58.033	−0.468	82.670	81.348	−1.600
25	58.300	56.804	−2.566	86.515	88.805	2.647
26	55.292	57.757	4.459	77.572	80.181	3.363
27	66.281	56.766	−14.356	87.840	86.205	−1.861
28	54.583	59.396	8.817	78.160	83.563	6.913
29	65.339	59.208	−9.383	94.549	87.012	−7.971
30	53.520	56.157	4.927	79.673	84.284	5.788

compaction, the relative error ranges between ±9% which gives good confident of correlation.

Conclusion

A laboratory test was conducted on 30 samples collected from the Ahmedabad region to develop regression model for prediction of relative density at a specific compaction energy, which corresponded to the standard, modified proctor compaction tests. A regression model of e_{max}, e_{min}, e_s and e_m, concluded by input variables (F_c%, D_{10}, D_{30}, D_{50}, D_{60}, C_u, C_c, G_s) with fair degree of accuracy indicated by higher value of R^2, low value of SSE, and F-significance less than 0.05. Value of predicated variables and experimental variables lies between ±5% range as shown in Figs. 17.3 and 17.4.

Final model is derived for relative density at standard compaction, where maximum relative errors in percentage occurs are +15.113 to −14.356 and 84% of total sample sizes are in range of ±5% form 1:1 line. For model of relative density at modified compaction, maximum relative errors in percentage are +8.988 to −7.977, where 87% of sample size falls in range of ±5% with reference to 1:1 line.

With fair accuracy on prediction, the model will help for compaction specification in field application and for getting idea about how soil behave under compaction.

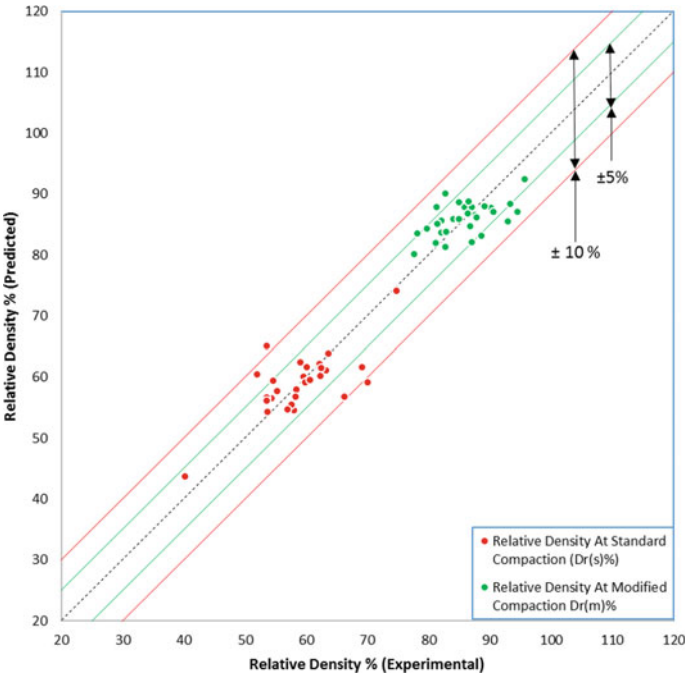

Fig. 17.4 Predicted versus experimental % relative density

References

1. Holtz, R.D., and Kovacs, W.M. (1981) An introduction to geotechnical engineering. Prentice Hall, New Jersey.
2. Youd TL (1973) Factors controlling maximum and minimum densities of sands. . ASTM, Digital Library/STP/STP523-EB/STP37866S
3. Cubrinovski M, Ishihara K (2002) Maximum and minimum void ratios characteristics of sands. Soils Found JGS 42(6):65–78
4. Gunaydın O (2008) Estimation of soil compaction parameters by using statistical analyses and artificial neural networks. J Environ Geol 1–13
5. Das BM (2019) Laboratory and field investigations in granular soils to correlate relative density, relative compaction and grain size. J S Afr Inst Civ Eng 62(2):12–21
6. IS: 2720—Part 3 (1983) Methods of test for soils "determination of specific gravity". Bureau of Indian Standards, New Delhi
7. IS: 2720—Part 14 (1983) Methods of test for soils "determination of density index (relative density) of cohesionless soil". Bureau of Indian Standards, New Delhi

Chapter 18
Geotechnical and Geophysical Characterization—Case Study of a Site with Steeply Dipping Rock

Ravi Sundaram, Sorabh Gupta, and Sanjay Gupta

Introduction

Initial geotechnical investigation for a multistoreyed residential complex in south Delhi indicated substantial variation in the depth to rock across the site. To evaluate the trend of the rock profile, seismic refraction tests were performed.

The paper presents the effective use of geophysical tests to characterize the stratigraphy for effective geotechnical assessment of the site.

Project Description

The project site covers an area of 1.93 acres approximately. The site is fairly level with ground levels varying from RL 224.0 to 222.2 from west to east. A railway track runs north of the site.

The development includes two residential towers (1 basement + stilt +12–13 floors). These towers are identified as Type V Quarters on the eastern side of the plot and Type VI Quarters on the west. In the open area between the towers, extended basement is planned for parking and utilities. The foundation was planned at about 4.5 m depth.

R. Sundaram (✉) · S. Gupta · S. Gupta
Cengrs Geotechnica Pvt. Ltd, Noida 201309, India
e-mail: ravi@cengrs.com

S. Gupta
e-mail: sorabh@cengrs.com

S. Gupta
e-mail: sanjay@cengrs.com

K. Muthukkumaran (eds.), *Soil Behavior and Characterization of Geomaterials*,
Lecture Notes in Civil Engineering 296, https://doi.org/10.1007/978-981-19-6513-5_18

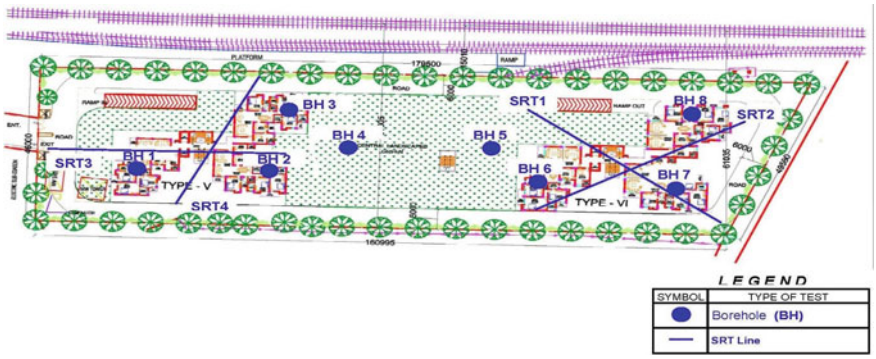

Fig. 18.1 Plan of field investigation

Scope of Geotechnical Investigation

The initial investigation at the site included eight boreholes through soil and rock. The borehole data indicated that the rock level varied from 7.5 to 12 m in the Type V Quarters. In the open area between the towers, the depth to rock is about 2.8–3 m. Moving further west, rock is met at 5–23 m depth in Type VI Quarters.

Reviewing the variation in the rock profile, it was decided to perform seismic refraction tests along four lines to evaluate the trends. The alignment of the seismic lines was selected to get maximum coverage below the tower foundations. A layout plan presenting the locations of the field investigation is illustrated in Fig. 18.1.

Site Conditions

Regional Geology

The overburden soils in the area belong to the Indo-Gangetic Alluvium and are underlain by the Delhi System of rocks. The quartzites of Delhi System are massive, compact, and hard. These quartzites are intruded by pegmatites. These pegmatites, on weathering, yield mica zones encountered in the area. A generalized description of geological formations encountered in Delhi [1] is given in Table 18.1.

Experience in different parts of Delhi has shown that the rock is highly folded due to which the depth to rock varies significantly. Variations in depth to rock have been seen over short distances. The rock has three sets of joints, one is nearly horizontal, the second is nearly vertical, and the third set is inclined at 30–50°. Preferential weathering has occurred along the joints due to flow of water.

Table 18.1 Geological succession in Delhi

Period	Formation	Description
Recent	Newer (younger) alluvium	Unconsolidated, interbedded lenses of sand, silt gravel and clay confined to flood plains of Yamuna River
Quaternary	Older alluvium	Consolidated interbedded, interfingering deposit of sand, clay and kankar, moderately sorted, thickness variable
Pre-cambrian	Pegmatite and quartz veins Quartzites and minor schist bands	Well stratified, thick-bedded brown to buff coloured hard and compact quartzite, intruded locally by pegmatite and quartz veins interbedded with mica schists

Boreholes

Boreholes were drilled using a hydraulic rotary drill rig as per IS: 1892-1979 [2]. While SPT was conducted in soil at every 1.5 m depth interval, rotary core drilling using a double tube core barrel was done through the rock. The boreholes were drilled from the existing ground surface. Figure 18.2 presents a photograph of a typical borehole in progress at the site.

Site Stratigraphy

Below the surficial fill that ranges from 1.5 to 6 m, the natural deposits at site consist of an alluvial overburden underlain by rock (quartzite). A pictorial summary of the borehole profiles is illustrated in Fig. 18.3.

The depth to rock varies substantially across the site as discussed below:

- Type V Quarters: Rock is encountered at 12 m depth (RL 211.4 m) on the western side (BH-1), rising to 7.5–9 m (RL 215.9–214.3 m) on the eastern side.
- Landscaped area between towers: Rock is met at 2.8–3.0 m depth (RL 221.2–220.5 m) at BH-4 and 5 in the level of the rock which rises rapidly from west to east with an anticline in the vicinity of BH-4 and 5.
- Type VI Quarters: Rock is met at 5 m depth (RL 218.4 m) at BH-6 in the vicinity of the anticline. Moving further east, rock dips downwards, and is encountered at 15 m depth (RL 207.2 m) at BH-7 and 23 m (RL 199.6 m) at BH-8.

Groundwater was not encountered at the borehole locations to the maximum explored depth of 27 m suggesting that it is quite deep in this locality.

Fig. 18.2 Borehole drilling in progress

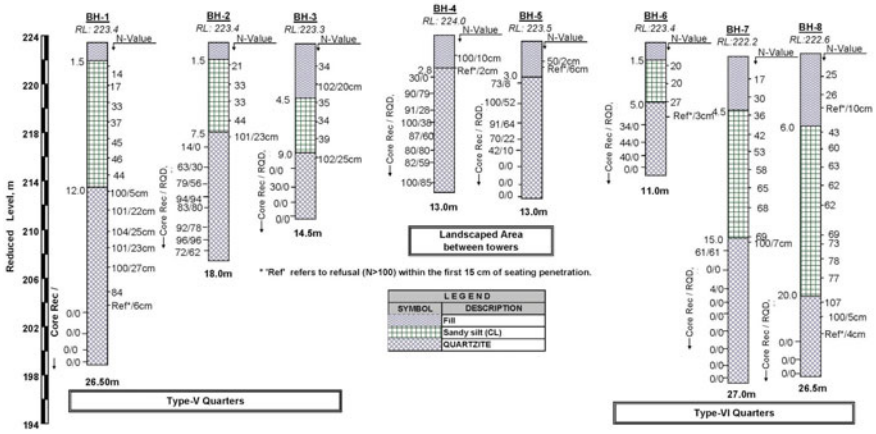

Fig. 18.3 Summary of borehole profiles

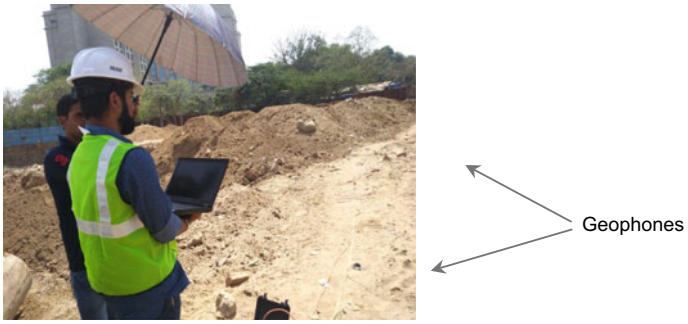

Fig. 18.4 Seismic refraction test—data acquisition in progress

Seismic Refraction Tests

Seismic refraction test (SRT) consists of recording the time taken for an artificially provoked surface vibration to propagate through the earth. By processing the data recorded at geophones placed along a line, absolute velocities, velocity contrasts, and the depths of the underlying layers are determined.

These results give information about the nature and thickness of overburden soils, depth to the top of bedrock, depth of weathering zones in the rock mass, faults or weak zones, etc. [3]. The seismic velocities are characteristic of the thickness, nature, and quality of the overburden soils and the underlying rock and may be used to identify the deposits in conjunction with the borehole data to effectively characterize the site [4].

To evaluate the trend of the rock profile, seismic refraction tests were performed along four selected lines. Two lines in the area of the Type V Quarters and two lines in the area of the Type VI Quarters as identified in Fig. 18.1 were investigated.

The tests were performed after excavation were done in the area of Type V Quarters to the planned basement level of 4.5 m. At the Type VI Quarters, excavation had not started, and the tests were done from ground level. Each line was 60 m long. Figure 18.4 shows data acquisition for the seismic test in progress using an array of geophones spaced 5 m apart.

Typical seismic refraction lines are illustrated in Fig. 18.5 (Type V Quarters) and Fig. 18.6 (Type VI Quarters). The borehole data are superimposed on the seismic profile to compare the stratigraphy.

Site Characterization

The boreholes and seismic refraction tests effectively confirm that the rock levels vary significantly across the site. The rock levels interpreted from the seismic refraction tests along the four selected lines are plotted in Fig. 18.7.

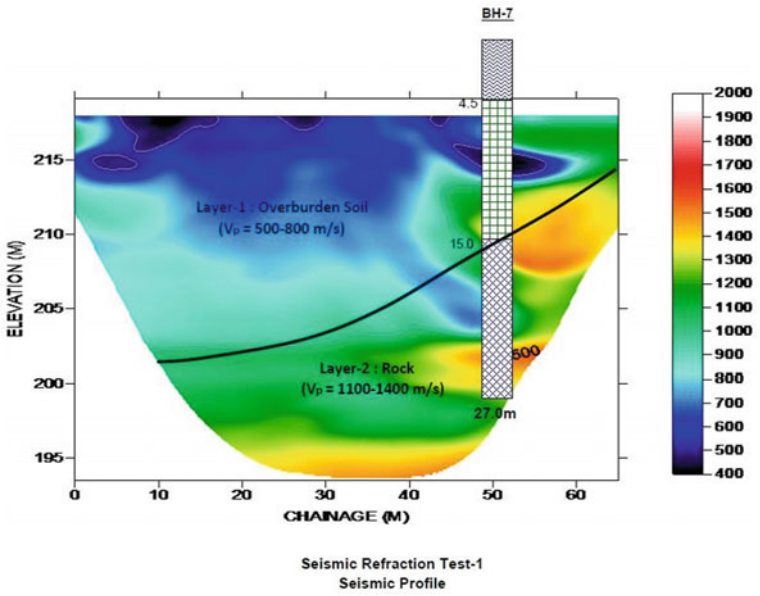

Fig. 18.5 Seismic profile along SRT-1 (Type V Quarters)

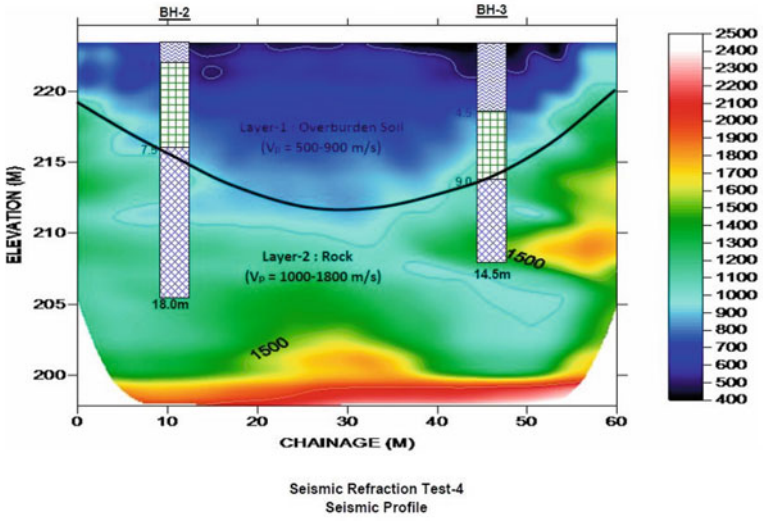

Fig. 18.6 Seismic profile along SRT-4 (Type VI Quarters)

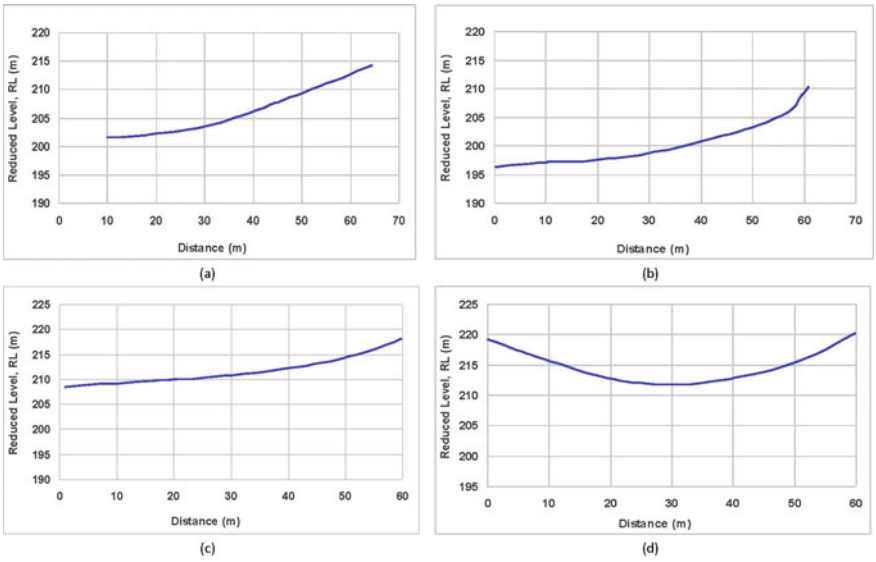

Fig. 18.7 Interpreted rock profile along seismic lines: Type V Quarters—**a** SRT-1 **b** SRT-2 Type VI Quarters—**c** SRT-3 **d** SRT-4

Seismic Line 1: On the northwest end of the line, rock is met at 15 m depth (RL 203 m). Towards the middle of the line, the rock level rises gently to about RL 203.5 m. It then rises steeply and is met at RL 214 m at the southeast end of the line. Rock level at BH-7 at 10 m depth below excavated level (RL 208 m) matches well with the seismic profile.

Seismic Line 2: Rock is met at 23 m depth (RL 196 m) on the northeast end of the line. Towards the middle of the line, the rock is met at about RL 200 m. It then rises steeply and is met at RL 210 m at the southwest end of the line. The rock level at BH-8 is at 19 m depth below excavated level which matches well with the seismic profile. At BH-6, rock is encountered at 1 m depth below excavated level (218.4 m). This also matches well-extrapolated seismic profile.

Seismic Line 3: Rock is at 14 m depth (RL 209 m) on the west end of the line. Towards the middle of the line, rock is at about RL 211 m, matching with BH-1. The rock then rises steeply and is met at RL 218 m at the east end of the line. The rock level at BH-2 at 7.5 m depth (RL 215.9 m) matches well with the seismic profile.

Seismic Line 4: Rock is at 3 m depth (RL 219 m) on the southeast end of the line. Towards the middle of the line, the rock dips steeply downward to about RL 211 m. The rock then rises steadily and is met at RL 220 m at the northeast end of the line, suggesting a synclinal fold. The rock level at BH-2 at 7.5 m depth (RL 215.9 m) and BH-3 at 9.0 m depth (RL 214.3 m) matches well with the seismic profile.

Reviewing the trend of rock as obtained from the boreholes and SRT lines, contours of rock level are illustrated in Fig. 18.8.

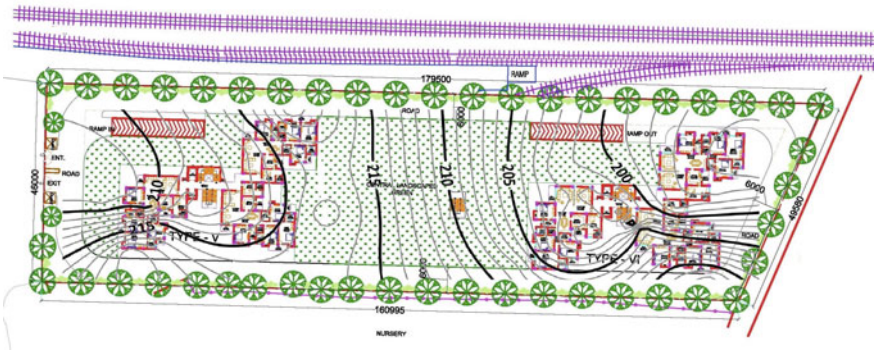

Fig. 18.8 Contours of rock level

These contours have been developed from the depth to rock observed at the borehole locations as well as the interpreted level of rock along the SRT lines. The building layout superimposed on the contours indicates rock-level variation of over 20 m over a 170 m distance. A synclinal basin is also observed at Type VI Quarters.

Foundation Design

Since one basement was planned, the raft foundation for the towers was planned at RL 219 m. The minimum and maximum depth of rock below the founding level was estimated from the trend of contours given in Fig. 18.8.

Since groundwater was not encountered to the maximum explored depth, the raft settlement is expected to be essentially immediate. The rock surface was treated as a rigid layer for the purpose of analysis. The immediate settlement was computed in accordance with Clause 9.2.3.2 of IS: 8009-1976 [5].

The raft foundation covering the whole area of the tower is expected to experience a net bearing pressure of 15 T/m^2 at the planned founding level (corresponding gross bearing pressure = 23 T/m^2). Table 18.2 presents the minimum and maximum depth to rock below foundation for the two towers together with settlement analysis for the following two cases:

- the best case (minimum thickness of soil overburden above rock): This will estimate the minimum settlement that may occur, and
- the worst case (maximum thickness of soil overburden above rock): This will estimate the maximum settlement that may occur

The difference between the best-case settlement and the worst-case settlement is an indicator of the differential settlement that could potentially occur.

Table 18.2 Depth of rock and estimated foundation settlement

Building	Analysis case	RL of rock m	Depth of rock below founding level (RL 219 m)	Estimated settlement, mm
Type V Quarters	Best	RL 215.9	3.1 m	Best case: 14 mm
	Worst	RL 211.4	7.6 m	Worst case: 31 mm
Type VI Quarters	Best	RL 218.4	0.6 m	Best case: 5 mm
	Worst	RL 199.6	19.4 m	Worst case: 40 mm

For both towers, the computed angular distortion was substantially less than 1/500 as permitted in IS: 1904-1986 [6]. Hence, the towers were judged to be safe under the planned applied bearing pressure.

Geotechnical Investigation on Sites with Varying Rock Profile

Where the depth to rock/hard strata varies across the site, the authors suggest that the geotechnical investigation programme should be coupled with a geophysical study to evaluate the trend of the depth to rock. Boreholes should extend at least 5 m into rock to confirm the continuity of the rock and to assess the rock characteristics. Rock drilling should be done using a hydraulic rotary drill rig and a double tube core barrel. In areas of weathered rock, triple tube core barrel may help in maximizing core recovery.

Static cone penetration tests as per IS: 4968 (Part 3)-1976 RA-2002 [7] may also be used to map the depth to refusal strata and to obtain additional data for foundation analysis.

The authors are of the opinion that boreholes and cone penetration tests should be supplemented by a geophysical investigation on sites with varying depth to rock in order to obtain the rock profile along selected lines. This may include:

- Seismic refraction tests
- MASW/SASW tests
- Electrical resistivity tests or electrical resistivity imaging.

Using a combination of these tests, the depth to rock all over the site should be properly mapped out. Contours of rock level should be prepared to assess the trends, and in areas where the variations are unusual, additional tests may be performed to identify the depth to rock and also identify anomalies, if any.

The foundation design should then be done structure-wise keeping the variations in view and ensuring that the total and differential settlements are within permissible limits.

Concluding Remarks

Geophysical tests in conjunction with borehole data are an effective way to characterize sites with varying rock profile. The case study illustrates an effective characterization of a site with folded and steeply dipping rock using seismic refraction tests.

The foundations were designed considering the variation in the rock level, and it has been ensured that the differential settlement due to the variation in the depth to rock across the site is within the permissible limits.

References

1. Krishnan MS (1986) Geology of India and Burma. CBS Publishers, New Delhi
2. IS: 1892 (1979) Code of practice for subsurface investigation for foundations. Bureau of Indian Standards, New Delhi (Reaffirmed 2002)
3. Whitley RJ (1994) Seismic refraction tests—a tutorial, geophysical characterization of sites. In: Woods RD (ed) Volume prepared by ISSMFE Technical Committee # 10. Oxford & IBH Publishing Co. Ltd., New Delhi, pp 45–48
4. Anomohanran O (2013) Seismic refraction method—a technique for determining the thickness of stratified substratum. Am J Appl Sci 10(8):857–862
5. IS: 8009 (1976) Code of practice for calculation of settlement of foundations, part 1: shallow foundations subjected to static vertical loads (Reaffirmed 2003)
6. IS: 1904 (1986) Design and construction of foundations in soils: general requirements. Bureau of Indian Standards, New Delhi (Reaffirmed 2006)
7. IS: 4968 (2002) Method for subsurface sounding for soils, part 3: static cone penetration test. Bureau of Indian Standards, New Delhi (Reaffirmed 2002)

Chapter 19
A Parametric Study of the Yield of Ring-Well—A Practical Approach

H. S. Prasanna, Shashank S. Shastry, B. Sharanprasad Rajesh, M. Shivaprasad, and L. Sanjay Raj

Introduction

Agriculture is vital part of the Indian economy as agriculture alone contributes about 15% to the Indian gross domestic product (GDP). In many developing countries, irrigation is a critical component of agricultural productivity. In developing countries, irrigated land provided two-fifths of crop production and about one-fifth of cultivated land in 1997–99. Also, the developing countries are responsive towards increasing agricultural yield in correspondence with increase in population. This demand is met by two ways, firstly, through increase in yield of rain fed agriculture, secondly, by importing, but irrigated agriculture is the main contributor. Irrigation improves agricultural land efficiency while also increasing production per acre. The provision of bulk water for irrigation places a burden on other water-using sectors, limits future water resource growth, and is hampered by inadequate maintenance. Canals, wells, tanks, and other irrigation systems are the most common forms of irrigation for agricultural land in the river basins lacking a primary source for irrigation relays on ring-wells. In such cases, the yield of ring-well directly influences the irrigation quality the crop receives. The yield of ring-well is higher in case of sandy soil as void ratio is higher, but this is not the case in clayey soils which have low void ratio. As a result of which the recuperation time increases, this causes inconvenience to farmers as the water may not be available in sufficient quantity for irrigating all the crops, also increased pumping of water causes subsidence around the ring-well. One of the main reasons for delayed recuperation is the number of entry points for water into the ring-well. In case of a normal ring-well without laterals, the number of entry points is only one, i.e. from the bottom of the ring-well. During this experimental study,

H. S. Prasanna · S. S. Shastry (✉) · B. Sharanprasad Rajesh · M. Shivaprasad · L. Sanjay Raj
Department of Civil Engineering, National Institute of Engineering, Mysore 570008, India
e-mail: shasshastry@gmail.com

H. S. Prasanna
e-mail: prasanna@nie.ac.in

K. Muthukkumaran (eds.), *Soil Behavior and Characterization of Geomaterials*,
Lecture Notes in Civil Engineering 296, https://doi.org/10.1007/978-981-19-6513-5_19

an attempt was made to increase the number of entry points into the ring-well by accessing the water stored by soil around the ring-well. From the study of drawdown curve, it was observed that the hydraulic gradient around the ring-well is higher than that observed inside the ring-well; therefore, by the introduction of slotted laterals into the ring-wells, the water around the ring-well flows into the ring-well through laterals resulting in increase of yield of ring-well.

The main implication of this experimental study is that it increases the yield of the ring-well by increasing the number of entry points in the form of laterals introduced at the bottom of the ring-well. Also, on continuous pumping out of water from the ring-well, the water in the vicinity of the ring-well is drawn from the bottom resulting in subsidence of the soil surrounding the ring-well, and also continuous drawing of water increases the recuperation time. On introduction of laterals as the influence area of the ring-well increases due to which subsidence is reduced and the recuperation time decreases. This also reduces dredging of soil and provides reinforcement to the soil at the bottom.

Literature Review

Sankalpa rural development society (SRDS), developed rainwater harvesting techniques that enhanced bore well discharge, allowing them to irrigate their crops even during the dry summer months.

Raphael [1] carried out a study on open well recharge programme based on rain water harvesting was conducted. In this study, the harvested rain water is either directed to an open well or directed to a recharge pit constructed next to open well.

Thangasalsrinivasarao et al. [2] worked on increasing yield of wells through hydro-fracturing technique. Increasing water well yield with hydro-fracturing is a process in which water is pumped into the fractures of rocks widening the cracks resulting in increase in the flow of water into the well. This technique is usually applied to low-yielding wells.

Patel et al. [3] attempted to assess the hydraulic performance of porous pipe used as a microirrigation lateral in a subsurface irrigation system by measuring the discharge from the lateral tube and came to the conclusion that the porous pipe tested lacked the qualities of a good microirrigation lateral.

Mayilswami et al. [4] studied on guidelines for augmentation of groundwater resources. Previously, ring-wells were used to obtain water, whereas presently, they are also used to raise the water level. To enhance the water table, recharge wells or ring-wells are being developed in 21 panchayats of Kaniyambadi block. The purpose of the recharge wells is to save rainwater while also increasing the water table. It is being tested in Kaniyambadi block as a pilot project. These wells will receive water from the stream. For one to two years, an impact study was conducted to examine how this aided in improving the water table. It was discovered that water does not flow directly into the river. Water reaches the lakes in the second year after the groundwater level rises and then flows into the river.

Prasanna et al. [5] carried out experimental study regarding increasing yield of ring-well through economical methods without increasing the diameter of the ring-well. This experiment was carried out for the sandy soil. This experimental study also focused on decreasing subsidence of the soil around the ring-well. The method proposed is cost-effective and can be executed without any complications.

Materials and Methods

The coordinates of the site selected for this study are (12.259162 N, 76.783340 E) which are about 20 km from the district of Mysore, Karnataka, India. The selected site is under influence of natural tank known as Duddgere tank. The undisturbed soil samples were collected from around the proposed location of ring-well, and tests to determine various index and engineering properties were carried out as per relevant IS codes.

The grain size analysis of soil carried out as per IS: 2720-Part 4-1985 shows that the soil mainly consists of 2% gravel, 48% sand, 46% silt, and 4% clay. Further analysing the type of clay through X-ray diffraction (XRD) test, it reveals that the principal clay present is montmorillonite. The specific gravity of the soil was determined as per IS: 2720-Part 3/section 2-1980, and the average value of specific gravity was obtained to be 2.79.

The liquid limit of the soil was determined using cone penetrometer as per IS: 2720-Part 5-1985, and it was found to be 52.25% through cone penetration method.

The dry density of soil was calculated as per IS: 2720-Part 29-1975 and was found to be 12.80 kN/m^3.

The shear parameters friction angle (φ) and cohesion (c) of the soil were determined and were found to be 27° and 12.5 kN/mm^2.

Double-ring infiltrometer test was carried out near the prototype to determine the infiltration rate of the soil as per ASTM D3385 and was found to be 2×10^{-2} mm/s.

Also, falling head permeability test was conducted in laboratory as per IS: 2720, and the average permeability was found to be 5.129×10^{-5} mm/s. Tables 19.1 and 19.2 show all the index and engineering properties of soil around the vicinity of the ring-well.

The location of the prototype ring-well is (12.258828 N, 76.782758 E). Ring-well prototype was 10 feet deep and 5 feet wide. During the excavation of the ring-well, undisturbed soil samples were collected for every 1-foot depth, and a scale model was modelled in laboratory. The model created consists of 2 cylindrical rings placed concentrically; the outer ring is made of iron sheet welded at bottom such that it is watertight. The second ring was made of iron mesh such that a ring with diameter of 2.5 feet and a height of 2.5 feet is obtained. Figure 19.1 shows photograph of the model. Similarly, a model of ring-well was made using PVC pipe of 4 in. diameter and having length of 1.5 feet, introduced with 4 galvanized iron pipe laterals of length 8 in. and having a diameter of 0.5 in. Similarly, 4 other galvanized iron pipe laterals of length 4 in. and having diameter 0.5 in. were introduced such that the 8 and

Table 19.1 Index properties of soil

Properties	Values
Density	12.80 kN/m^3
Grain size analysis	Gravel—2% Sand—48% Silt—46% Clay—4%
Specific gravity	2.79
Atterberg limits	Liquid limit—52.25% Plastic limit—22% Plasticity index—30.25%
IS classification	SM-SC

Table 19.2 Engineering properties of soil

Properties	Values
Shear parameters	Friction angle (φ)—27° Cohesion (c)—12.5 kN/m^2
Shear strength	228 kN/m^2
Coefficient of permeability (k)	5.129×10^{-5} mm/s

4 in. laterals are placed alternatively. The ring-well model is as shown in Fig. 19.2. The samples collected during excavation were sieved using 4.75 mm IS sieve and were filled around the ring-well model to achieve a density of 12.80 kN/m^3. Before placing the ring-well model at the centre of the rings, all perforated laterals were permanently sealed on the outer end and temporarily sealed from the interior edge using rubber bush; this enabled to control the discharge occurring through the laterals and to measure the water entering the ring-well through laterals. Further soil was filled into the second ring of the model according to the scale and the field density, as shown in Fig. 19.3. Water was filled in the outer ring in order to maintain a constant head for water to recuperate into the ring-well model, as shown in Fig. 19.4. For all laterals closed condition, volume of water recuperating into the ring-well from the bottom was measured every 40-min intervals, and the measurements were tabulated. Further, the rubber bush from two of the 8 in. laterals was removed allowing the discharge from the laterals; this resulted in increase in depth of water by 89.18 cm^3, i.e. an increase of 14%. Further, the same procedure was carried out by allowing discharge through all the 8 in. laterals, and the corresponding depth of water in the ring-well was noted. Now, all the 8 in. laterals were closed, and the above procedure was carried out by allowing discharge through 4 in. laterals in the order of 2 and 4 number of laterals one after the other. The results are given in Table 19.3.

For field implementation of the concept, laterals with length 7 feet were to be introduced into the ring-well prototype. The laterals introduced are as shown in Figs. 19.5 and 19.6. For ease of driving the laterals through ring-well from the

Fig. 19.1 Photograph depicting the laboratory model before filling sand

Fig. 19.2 Photograph depicting model of ring-well

interior of ring-well, it was decided that two 3.5 feet pipes coupled together would be used as single lateral. It was decided to use slotted laterals to reduce clogging of laterals and to minimize cost of fabrication. Meanwhile, galvanized iron pipe of length 3.5 feet each having diameter of 2 in was fabricated by introducing slots of length 8 cm each and threads at coupling ends. For the ease of driving laterals, pointed edge was designed. The slots were introduced on both the sides of the pipe alternatively at 3 in intervals measured centre to centre of slots along the length of the pipe. These fabricated laterals were introduced into the ring-well in the order of 2, 4, 6, and 8 providing an interval of 3 days on introduction of 2 slotted laterals. The yield measured after introduction of every two laterals is given in Table 19.4.

Fig. 19.3 Photograph depicting arrangement of model of ring-well

Fig. 19.4 Photograph depicting the model during yield measurement

Table 19.3 Average depth of water obtained for different laterals during laboratory trials

Length of active laterals (in.)	Number of active laterals	Depth of water (cm)
–	0	8
4	2	8.5
	4	8.8
8	2	9.1
	4	9.6
8 and 4	8 (4 + 4)	10.5

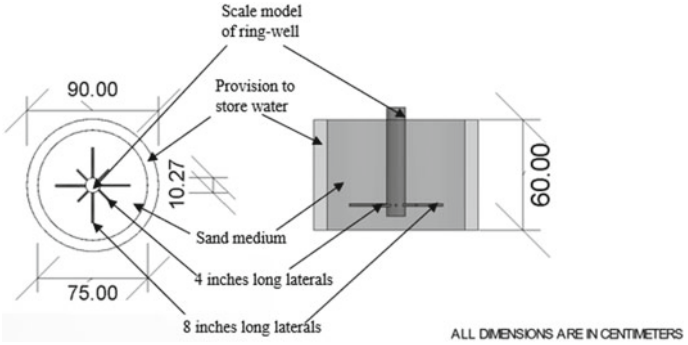

Fig. 19.5 Plan and sectional elevation of the model

Table 19.4 Average yield obtained for different laterals during field trials

Diameter of laterals (in.)	Length of each lateral (feet)	Number of laterals	Average yield (cm)
2	7	0	80
		2	92
		4	105
		6	120
		8	130

Fig. 19.6 Typical photograph showing laterals with collars and sharp driving edge

Results and Discussion

During the first trial, all the inlets were closed, and the yield entering the ring-well was measured. Later, two 4 in. laterals were activated by removing the rubber bush from the inside, and the height of standing water was measured. Similarly, all the 4 in. laterals were activated, the height of standing water was measured, and all results were tabulated. The results are as shown in Table 19.3. The variation of standing height of water with number of laterals for different combination of laterals for perforated laterals was plotted as shown in Fig. 19.7.

Further, all the 4 in. laterals were closed, two inlets of 8 in. were un-bushed, and the height of standing water was measured. This process was also carried out by un-bushing all the 8 in. laterals, the height of standing water was measured, and the results were tabulated. Further, correlation between the number of laterals versus the depth of water was plotted as shown in Fig. 19.8. Further, all the laterals were un-bushed, and the increase in the height of water in the ring-well was measured. Also, Fig. 19.9 shows the comparison between the 4 in. laterals and 8 in. laterals when two and four laterals are un-bushed, respectively (Fig. 19.10).

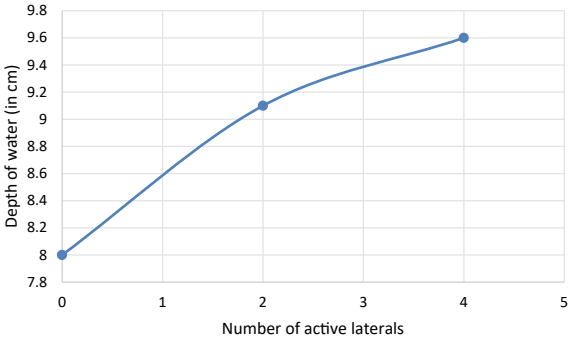

Fig. 19.7 Number of laterals versus depth of water for 4 in. laterals

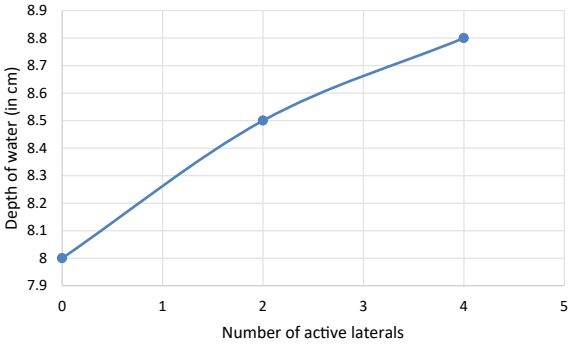

Fig. 19.8 Number of laterals versus depth of water for 8 in. laterals

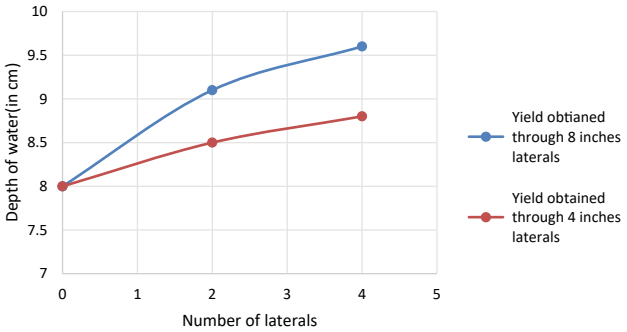

Fig. 19.9 Comparison between yields obtained through 4 in. and 8 in. laterals

Fig. 19.10 Increase in yield observed during field trials

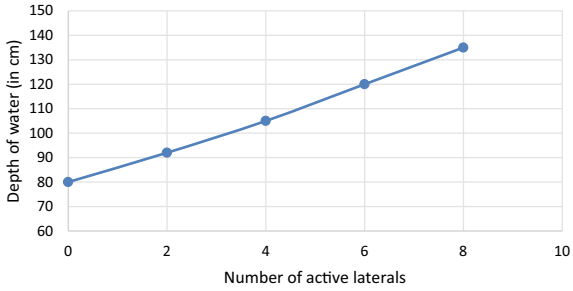

After the laboratory experimentation, the field trials were conducted by introducing 2 laterals at a time, the increase in depth of water was measured, and the measurements are as shown in Table 19.4.

The double-ring infiltrometer test was carried out in order to determine the permeability of the soil in field at various locations around the ring-well for different depths in order to compare the permeability obtained near prototype with that obtained from the model studies. Table 19.5 shows the permeability values, and Fig. 19.11 shows the correlation between the permeability obtained in laboratory and that obtained near prototype.

Figures 19.7 and 19.8 show the increase in depth of water for various conditions of 4 in. laterals and that of the 8 in. laterals. Figure 19.9 shows a comparison between

Table 19.5 Comparison between permeability obtained in laboratory and that obtained in field

Laboratory permeability (cm/s)	Field permeability (cm/s)
6.059×10^{-5}	2.52×10^{-4}
6.19×10^{-5}	4.41×10^{-4}
6.536×10^{-5}	6.68×10^{-4}
5.787×10^{-5}	7.81×10^{-4}
5.855×10^{-5}	8.83×10^{-4}

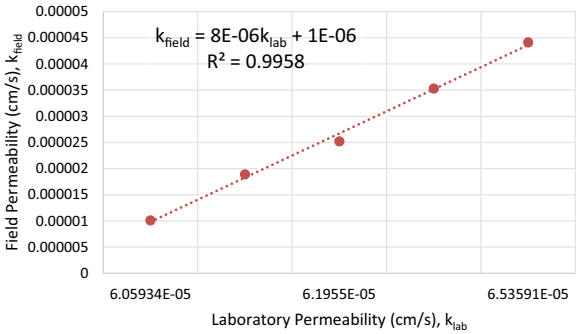

Fig. 19.11 Correlation between laboratory permeability and field permeability

the yield obtained from 4 in. laterals and that of 8 in. laterals. From the plot, it can be observed that there is an increase in yield of about 12% when discharge is allowed through all the 4 in. laterals. Also, it can be observed that the increase in yield of about 20% when discharge is allowed through all the 8 in. laterals. Figure 19.10 shows the increase in yield measured during field trials. The permeability correlation shows that the permeability variation in field and in laboratory model is considerably linear which directly signifies the reliability of the results.

Conclusion

From the above obtained results and their interpretations, few major conclusions which can be drawn as follows:

- The yield of ring-well can be increased by providing laterals which influences the permeability of soil. The increase in yield without increasing the diameter of the ring-well is economical and space conserving.
- The permeability obtained in field and that in laboratory shows that the variation of permeability is linear which increases the reliability of the method adopted.
- Provision of laterals decreases the subsidence of soil around the periphery of the ring-well.

Acknowledgements The successful implementation of the project involves the effort of many people. We received a lot of help and support from all quarters during the course of this experimental study; we take this opportunity to acknowledge all those involved. At the very outset, we convey our gratitude to **Dr. H. S. Prasanna,** Guide for this experimental study, for his guidance and uncompromising assistance throughout the study. We also express our gratitude for **Mr. Rajeev,** Founder of RR foundations, for giving us a wonderful opportunity to carry out this experimental study at his site. Also, we thank **Mr. Yogendra Prasad** for providing all the key assistance throughout the execution of this study. We convey our heart-felt thanks to our beloved principal **Dr. Ragavendra,** NIE, Mysuru, for giving us the support in our academic's progress. We express our heart-felt thanks to **Dr. K. C. Manjunath,** Head of the Department, Civil engineering, for their uncompromised technical and financial support.

References

1. Raphael J (2009) Mazhapolima wells in kerala for rain harvesting, Kerala, India. Raghunath HM (2007) Ground water. New Age International (P) Limited, New Delhi, India
2. Thangasalsrinivasarao et al (2010) Hydrofracturing, article: January 2010, Research Gate, Tamil Nadu, India
3. Patel GR et al (2011) Hydraulics performance evaluation of porous pipe (sub surface) irrigation system. IJAE 4(2):156–159
4. Mayilswami C et al (2013) Guidelines for augmentation of groundwater resources under climate change in Tamil Nadu. NICRA, Water technology center, Tamil Nadu Agricultural University, Coimbatore, India, ICAR collaborative network project
5. H S Prasanna, S C Harshavardhan, A R Chaitra, P K Pooja & P Beeresha (2018), Increasing the yield of ring wells by user friendly method, Indian Geotechnical Conference (IGC-2018), Bangalore, paper No: TH-01-005

Chapter 20
Using Laboratory Electrical Resistivity Testing to Estimate Geotechnical Properties of Some Bhubaneswar Region Soils

Raghava A. Bhamidipati, Lav Nayan, and Rinki Mahato

Introduction

The investigation of subsurface conditions is a very important step for almost all civil engineering projects. The traditional methods of soil and rock exploration involve operations like soil excavation and drilling. These methods offer the advantage of providing actual samples either in disturbed or in undisturbed state, for study. But these methods are generally costly and the take time to execute. The information provided from these tests is also localized. The use of geophysical testing methods like electrical resistivity testing can address some such issues. Electrical resistivity of a soil can be defined as a quantification of the resistance offered by a sample of soil towards the flow of electric current. Soil resistivity is normally measured by using a set of electrodes and a source of electric current along with a soil resistivity metre. The pore water composition, density, water content, temperature, and mineralogy of soil are some of the variables that influence the resistivity of soils. Electrical resistivity for most earth materials varies from 1 to 10,000 Ω-m [1].

In the past few decades, several researchers have investigated the electrical resistivity of soils and their relationships with geotechnical properties. Rhoades et al. [2] developed relationships which correlate bulk soil conductivity with volumetric water content, pore water conductivity and soil surface conductivity. Using a four-probe resistivity cell, Kalinski and Kelly [3] predicted the volumetric moisture content of a soil sample containing 20% clay. By using electrical conductivity testing, Kalinski and Vemuri [4] proposed a way to rapidly estimate the amount of compaction of a clayey soil. Guinea et al. [5] used electrical resistivity values to delineate commercially useful gypsum rock deposits in Spain. Syed and Siddiqui [6] correlated field electrical resistivity values of soil with their standard penetration test SPT-N values and moisture content in Malaysia.

R. A. Bhamidipati (✉) · L. Nayan · R. Mahato
C V Raman Global University, Bhubaneswar 752054, India
e-mail: jones.kgp@gmail.com

K. Muthukkumaran (eds.), *Soil Behavior and Characterization of Geomaterials*,
Lecture Notes in Civil Engineering 296, https://doi.org/10.1007/978-981-19-6513-5_20

Materials and Methodology

The materials used for undertaking this study were: a red lateritic soil, a sandy sample, and a greyish-brown clay sample. All the samples were collected from the Mahura region of south Bhubaneswar. The basic properties of these soils are shown in Table 20.1.

A rectangular resistivity box (20.5 cm in length, 11 cm in breadth and 9 cm in height) made out of glass was used for conducting the resistivity tests. The current electrodes at the end of the box were made out of metal plates [7]. The voltage electrodes were created by inserting two metal nails in between the box. The general guidelines of ASTM G-57 [8] were followed for carrying out these tests. Figure 20.1 shows the circuit and the testing setup. The mean indoor temperature during this study was 30 °C.

Test samples were prepared by mixing dry soil (sieved through a 4.75 mm sieve) with a calculated quantity of tap water to achieve the desired moisture content. These samples were placed in the soil box in three layers and compacted lightly using a tamping mechanism. A 25 V direct current (DC) source was used to pass electric current through the soil. One multimeter was used for measuring potential drop between the two inner electrodes (V). Another multimeter was used for measuring the current flowing in the circuit (i). The Wenner electrode configuration was used in which the spacing between all the four electrodes is equal. Resistivity (Ω-m) was calculated as the ratio of potential drop (V) and current (i), multiplied by the box geometry constant (k). The constant 'k' is obtained by dividing the cross-sectional area of the box with the electrode spacing. Figure 20.2 shows a resistivity

Table 20.1 Basic properties of the three soils tested

Soil	Fines %	Sp. gravity	Liquid limit (%)	Plastic limit (%)
Sand	3	2.61	–	–
Laterite	54	2.64	31	17
Clay	76	2.67	38	25

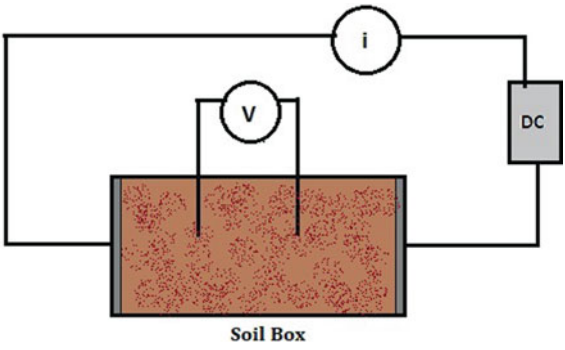

Fig. 20.1 Setup of soil resistivity testing

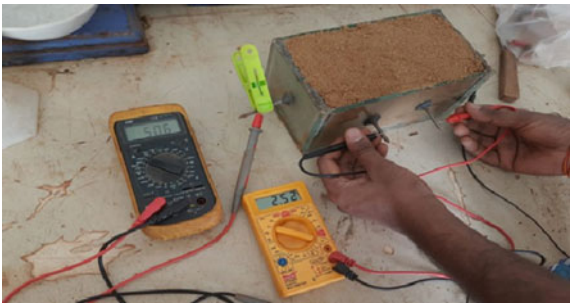

Fig. 20.2 Testing of a soil sample

measurement being made by using the test setup. For each sample, two resistivity measurements were made by passing the current in opposite directions. The mean value of resistivity from these two measurements was considered.

Testing and Results

The first set of tests was performed to study the relationship between moisture content and electrical resistivity. The moist samples were prepared as described in the previous section. The water and soil were thoroughly mixed in a tray and left covered for some time before being filled in the box. This was to ensure uniform distribution of moisture, especially for the clayey soils. Water content of the samples was varied from 5 to 25%. All the test samples were made in the dry density range of 1.2–1.3 g/cm^3. Figure 20.3 shows the plot between resistivity and moisture content. It is found that with increasing moisture content, resistivity reduces sharply. Sand has a higher resistivity compared to laterite and clay samples. The laterite sample however exhibited a higher resistivity at 5% moisture content. In general, electrical resistivity values of these samples ranged from 15 Ω-m at higher moisture to 300 Ω-m at lower moisture contents.

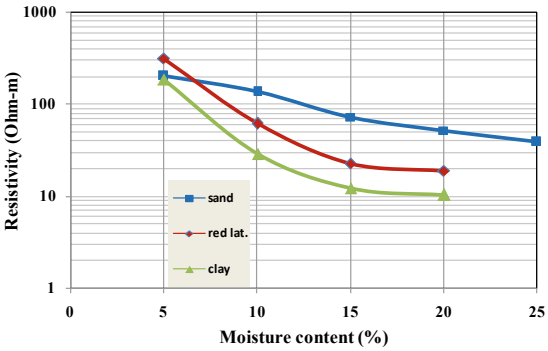

Fig. 20.3 Electrical resistivity versus moisture content for the three samples

Three soil types were then taken to study the relationship between dry density and resistivity. These were the sand, laterite, and a sample of a 50% sand and 50% clay mixture. The clayey sample was avoided because of the difficulty in compaction, especially at lower density. All the samples were prepared at a constant moisture content of 10%. The samples were compacted to different densities in the range of 1.0–1.7 g/cc. Resistivity values were measured for each sample, and it was shown that resistivity decreased with increase in dry density. The observed resistivity values for these conditions varied from 100 Ω-m to 280 Ω-m for sand, 60–250 Ω-m for laterite and 50 Ω-m to about 150 Ω-m for clayey sand. Laterite sample showed a high resistivity at low dry density, but resistivity decreased with increase in dry density, becoming comparable to that of clay above 1.3 g/cc (Fig. 20.4).

Next, the effect of clay content on the electrical resistivity of sand was studied. To accomplish this, the greyish-brown clayey soil was added to the sand in proportions of 25 and 50% by weight. The resistivity of the sand samples with addition of 0, 25 and 50% clay was studied with respect to change in moisture content (Fig. 20.5). The results indicate that resistivity of sand reduced greatly upon the introduction of clay. The sand sample had resistivity between 40 to 200 Ω-m, but the addition of clay lowered range to 10–100 Ω-m.

According to Samoulien et al. [1], the values of soil resistivity also depend on the resistivity of the pore water fluid. Since tap water was used in all the experiments, its

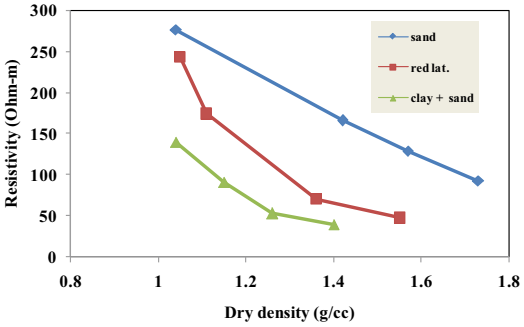

Fig. 20.4 Electrical resistivity versus dry density for three samples

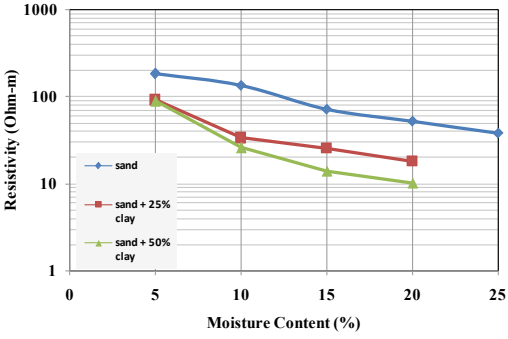

Fig. 20.5 Electrical resistivity versus moisture content for samples with different amounts of clay

resistivity was also measured using the soil box, by filling it with tap water instead of soil. The resistivity of tap water was observed to be 11.7 Ω-m.

The range of observed resistivity values for the laterite and sandy soils is seen to be in agreement with the findings of Choudhury et al. [9] who performed field resistivity measurements using vertical electrical sounding (VES) method in Niamey city, Niger, Africa, for the delineation of potential aquifer zones. The resistivity values of the sand samples are compared favourably with the findings of Hazreek et al. [10], who used the field electrical resistivity method to study gravelly sands and silty sand at two different sites in Malaysia. The resistivity values of clay are similar to the values observed by Duan et al. [11]. These researchers used three different field resistivity methods to study the electrical resistivity of marine clay in Ningbo city.

Regression Analysis

From the study, it was found that the resistivity of the soils decreased with increase in moisture content, density as well as clay content. Considering this aspect, an attempt was made to model resistivity as a simple linear function of these variables using the data analysis tool of MS Excel. Resistivity was the 'dependent variable', and moisture content, density and clay content were the 'independent variables'. Based on the data available, two different analyses were performed.

The first regression was resistivity as a linear function of water content (w%) and clay content (clay %). Here, 13 data points were selected with water content ranging from 5 to 20% and clay content ranging from 0 to 50%. The density of all the samples was kept between 1.2 and 1.3 g/cc. The outcomes of the multivariable regression analyses were as shown in Table 20.2.

The *p* values for both water content and clay were much below 0.05, indicating a strong relationship between resistivity and these parameters. Based on the outcome of the regression, the following multivariable regression equation was developed from these data:

$$\mathrm{ER} = 173.2 - 5.58(\mathrm{w}\%) - 1.48(\mathrm{Clay}\%) \tag{20.1}$$

Table 20.2 Regression statistics for first analysis

Parameter	Value
Observations	13
R-squared	0.82
Adjusted *R*-square	0.78
Standard error (Ω-m)	23.03
P value (water content)	0.00028
P value (clay content)	0.0008

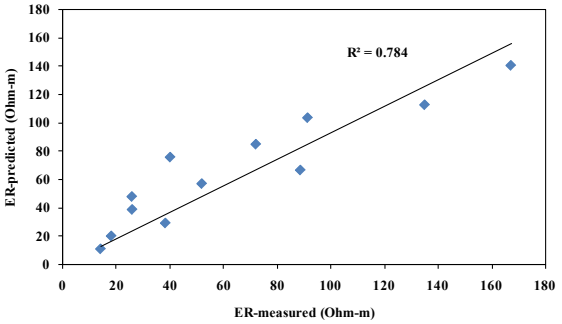

Fig. 20.6 Predicted versus actual resistivity values for Eq. 20.1

This equation was used to make a comparison of measured versus predicted values of resistivity for the above data. Figure 20.6. shows the plot of the predicted versus actual values for 12 points. The accuracy of the model is around 78% as seen from the *R*-squared value. It works fairly well in the moisture content range of 5–20%. The relationship holds well as long as the observed resistivity values are 15 Ω-m and above.

The next regression was performed on resistivity as a function of water content (w%) and dry density (dd) of soil measured in the units of g/cc. Here, 11 data points were selected with water content ranging from 5 to 20% and dry density was varying from 1 g/cc to 1.55 g/cc. In this case, the soil type was kept constant (a mixture of 50% sand and 50% clay). The outcome of this multivariable regression was as follows (Table 20.3).

Again in this case, the *p* values of water content and dry density were much below 0.05, showing a strong correlation between soil resistivity and these variables. The following equation was developed based on the regression output:

$$\mathrm{ER} = 302.2 - 3.46(\mathrm{w}\%) - 151.1(\mathrm{dd}) \tag{20.2}$$

This equation was used to make a comparison of measured versus predicted values of resistivity for the data. Figure 20.7 shows the plot of predicted versus actual values for 11 points. The accuracy of the model is around 87% as seen from the R-squared

Table 20.3 Regression statistics for second analysis

Parameter	Value
Observations	11
R-squared	0.87
Adjusted *R*-square	0.84
Standard error (Ω-m)	17.7
P value (water content)	0.014
P value (dry density)	0.0003

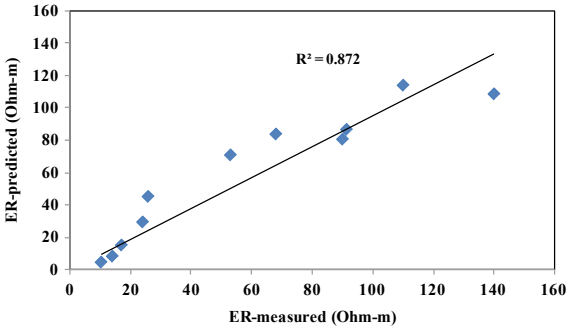

Fig. 20.7 Predicted versus actual resistivity values for Eq. 20.2

value. It works reasonably well in the moisture content range of 5–20% and dry density range of 1–1.5 g/cc.

Conclusion

Based on this study, it was found that electrical resistivity of the laterite, sand, and clay samples were influenced by factors like moisture content, density, and clay content. Sand had the highest resistivity of the three soils. Laterite and clay had lower resistivity, with clay having the lowest of the three soils. The lower resistivity of laterite could be a result of the presence of iron and aluminium oxides in the soil. An attempt was made to model resistivity as a function of more than one parameter, which included moisture content, dry density, and clay content using linear regression. The regression yielded satisfactory results with R-squared values ranging from 0.75 to 0.87, but the range of the prediction was limited because of the number of test samples available. There is a potential for incorporating larger variability in terms of experimentation by increasing the range of clay content and moisture content and the considering the effect of other parameters like soil plasticity, mineralogy, etc., on resistivity values. These relationships developed could then become useful for applications in field investigations, laboratory investigations and engineering projects.

References

1. Samouelian A, Cousins I, Tabbagh A, Bruand A, Richard G (2005) Electrical resistivity survey in soil science. Soil Tillage Res 173–193
2. Rhoades JD, Raats PA, Prather RJ (1976) Effect of liquid-phase electrical conductivity, water content and surface conductivity on bulk soil electrical conductivity. Soil Sci Soc Am J 40:651–655
3. Kalinski RJ, Kelly WE (1993) Estimating the water content of soils from electrical resistivity. Geotech Test J 323–329

4. Kalinski ME, Vemuri SC (2005) A geophysical approach to construction quality assurance testing of compacted soils using electrical conductivity measurements. Geotechnical Special Publication No. 133, American Society of Civil Engineers
5. Guinea A, Playa E, Rivero L, Himi M, Bosch R (2010) Geoelectrical classification of gypsum rocks. Surv Geophys 31:557–580
6. Syed A, Siddiqui I (2012) Use of vertical electrical sounding (VES) method as an alternative to standard penetration test (SPT). In: Proceedings of the twenty-second (2012) international offshore and polar engineering conference, Rhodes, Greece, pp 871–875. ISBN: 978-1-880653-94-4
7. Bhamidipati RA, Nayan L, Mahato R (2021) Electrical resistivity measurement of sand, red mud and clay using an inexpensive soil resistivity box. In: Proceedings of Veda Mladych-Science of youth 2021, Slovak University of Agriculture in Nitra
8. ASTM: G57–06 (2012) Standard test method for field measurement of soil resistivity using the Wenner Four-Electrode Method
9. Choudhury J, Kumar KL, Nagaiah E, Sonkamble S, Ahmed S, Kumar V (2017) Vertical electrical sounding to delineate the potential aquifer zones for drinking water in Niamey city, Niger, Africa. J Earth Syst Sci 126(91)
10. Hazreek ZAM, Rosli S, Chitral WD, Fauziah A, Azhar ATS, Aziman M, Ismail B (2015) Soil identification using field electrical resistivity method. J Phys: Conf Ser 622:12030
11. Duan W, Cai G, Liu S, Li K, Puppala AJ (2018) Comparison of different electrical resistivity measurement methods of soft marine clays. In: Proceedings: GeoShanghai 2018 international conference: multi-physics processes in soil mechanics and advances in geotechnical testing

Chapter 21
Geotechnical Investigations of Blended Borrow Area Materials for Suitability of Construction of Core for Proposed Earthen Dam

Rajesh Khanna, Manish Gupta, and R. Chitra

Introduction

There is a scarcity of water in some parts of Central India, and therefore due to initiative of project authorities, some irrigation schemes are proposed to cater the need of irrigation and drinking in that water-deficient area. In one of such areas, it is proposed to construct a small earthen dam across a stream in central part of India. The proposed dam would cater the drinking and irrigation requirements of that area.

For the construction of an earthen dam, large quantity of fine-grained soil and coarse soil are required. The core is constructed of fine-grained soil, and the shell is mainly constructed of coarse-grained soil. According to Gulati and Datta [1], Arora [2], Lambe and Whitman [3], the core of dam mainly provides imperviousness and shell mainly provides stability to the dam. Therefore, detailed borrow area and laboratory investigations were carried out to know the feasibility for the construction of this dam. The paper presents the results of geotechnical investigations of two different borrow area materials as collected and the results of different trials in various proportions of available soil samples as blended from these borrow areas for improving the index and engineering properties of soil.

Field Investigations

Depending upon the terrain and availability of suitable construction materials, three numbers of disturbed soil samples were collected from pits of size 3 m × 3 m × 3 m in gunny bags from two different borrow area locations in Jharkhand. Borrow area materials would be used as construction material of core of dam. Therefore,

R. Khanna (✉) · M. Gupta · R. Chitra
Central Soil and Materials Research Station, Hauz Khas, New Delhi 110016, India
e-mail: rajesh12khanna@yahoo.com

K. Muthukkumaran (eds.), *Soil Behavior and Characterization of Geomaterials*,
Lecture Notes in Civil Engineering 296, https://doi.org/10.1007/978-981-19-6513-5_21

it is necessary to evaluate the engineering properties and strength properties of soil for suitability as construction material. These borrow area samples were transported from site to the laboratory for extensive laboratory investigations.

Laboratory Investigations

Laboratory Investigations of Original Borrow Area Samples

Laboratory investigations of original borrow area samples were carried out, and the following results were determined as per BIS 2720, part 7 [4], 8 [5], 12 [6], and part 17 [7]. Different parameters were found: grain size distribution, soil type, consistency limits, maximum dry density, optimum moisture content, shear strength parameters, compressibility characteristics, and the permeability characteristics. Soil classification of samples shows that one soil sample each falls under SM (Silty Sand), SW–SM (Well-Graded Sand and Silty Sand) and CH (Clay with High Plasticity) groups as per Bureau of Indian Standard Soil Classification System. The Atterberg's limits of the tested soil samples indicate that out of the three tested soil samples, two soil samples (S1 & S2) possess low compressibility characteristics and exhibit non-plastic characteristics. And the results of the remaining one soil sample (S1) indicate that the soil sample possesses high compressibility characteristics and exhibits high plasticity characteristics. Coefficients of permeability of **S1** indicate soil of impervious nature. Consistency limits and design parameters of original soil samples are indicated in Tables 21.1 and 21.2, respectively.

Since soil samples collected from the potential borrow area were either non-plastic sandy soils or the highly clay material, these borrow area materials were not found suitable for the construction of the embankment dam.

On request from the project authorities and as there were no other option of identifying the alternate potential borrow areas at the project site, attempts were made to blend the three soil samples collected earlier and to arrive at a suitable blended borrow area material which can be used for the construction of the embankment dam.

Table 21.1 Consistency limits of original samples

Consistency limits				IS soil classification
Sample no.	Atterberg's limits			
	LL	PL	PI	
S 1	24.7	NP	NP	SM
S 2	34.7	NP	NP	SW-SM
S 3	60.6	24.8	35.9	CH

Table 21.2 Design parameters of original sample (S1)

Standard proctor test	
Maximum dry density (g/cc)	1.93
Optimum moisture content (OMC) (%)	10.5
Triaxial shear test	
Total cohesion (c) (kg/cm^2)	0.21
Total angle of shearing resistance (ϕ)	31.7
Effective cohesion (c') (kg/cm^2)	0.11
Effective angle of shearing resistance (ϕ')	33.4

Laboratory Investigations of Blended Soil Samples

Blend 1 was made with blending equal quantities (33% of total weight) of all three soil samples (S1, S2, and S3) collected from both the left and right sides of the dam location and based on the results of Blend 1, Blend 2 was fine-tuned by blending 25% of total weight each of the SM and SW-SM soil samples with 50% of the CH soil sample. The results of consistency limits of blended soil samples are presented in Table 21.3, and the design parameters of blended soil samples are presented in Table 21.4.

Table 21.3 Consistency limits of blended soil samples

Consistency limits				IS soil classification
Sample no.	Atterberg's limits			
	LL	PL	PI	
Blend 1 (33% S1 + 33% S2 + 33% S3)	26.3	15.8	10.5	SC
Blend 2 (25% S1 + 25% S2 + 50% S3)	33.9	18.4	15.5	CL

Table 21.4 Design parameters of blended soil samples

Standard proctor test	Blend 1	Blend 2
Maximum dry density	1.94	1.92
Optimum moisture content (OMC) (%)	13.2	14
Triaxial shear test		
	Trial 2	
Total cohesion (c) (kg/cm^2)	0.22	
Total angle of shearing resistance (ϕ)	26.4°	
Effective cohesion (c') (kg/cm^2)	0.11	
Effective angle of shearing resistance (ϕ')	31.1°	

The blended soil sample of Blend 2 was subjected to the laboratory permeability test using falling head method. The test was carried out on the material passing 4.75 mm sieve size compacted at 98% of the maximum dry density and at optimum moisture content. The coefficient of permeability value evaluated from the laboratory permeability test is found to be 2.303×10^{-7} cm/s which indicates that the tested blended soil sample of Blend 2 possesses impervious drainage characteristics.

Discussion of Test Results

Mechanical Analysis and Atterberg's Limits

By blending 33% each of SM and SW-SM soil samples with 33% of CH soil samples, the blended soil sample of Blend 1 falls under SC (Clayey Sand) group as per Bureau of Indian Standard Soil Classification System and possesses medium sand sizes followed by silt sizes, find sand sizes, and clay sizes and exhibits low compressibility characteristics having the plasticity index of 10.5 which is less than 12 (non-plastic). Therefore, the second trial was made with 25% each of the SM and SW-SM soil samples with 50% of the CH soil sample. The blended soil sample thus arrived was found to be falling under CL (Clays with Low Compressibility) group as per Bureau of Indian Standard Soil Classification System and possesses clay sizes followed by silt sizes, medium sand sizes and find sand sizes and exhibits low compressibility characteristics having the plasticity index of 15.5. Figure 21.1 shows grain size distribution curves of borrow area material and the blended material.

The liquid limit of the CH soil sample decreases by 59% for the blended soil sample of 33% each of SM and SW-SM soil samples with 33% of CH soil samples, Blend 1 and decreases by 41% for the blended soil sample of 25% each of SM

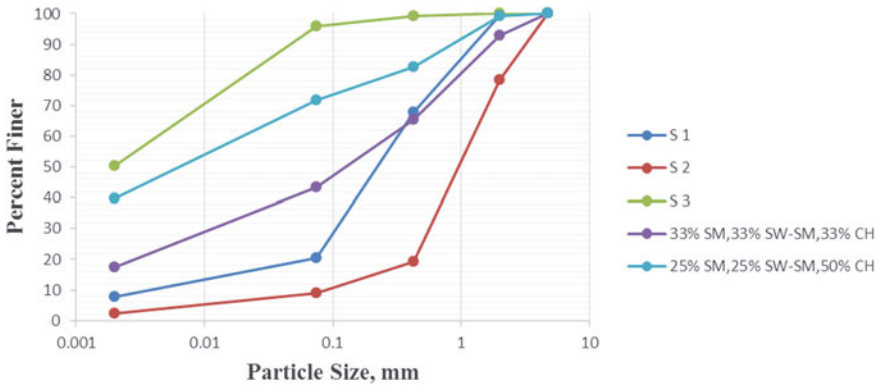

Fig. 21.1 Grain size distribution curves of borrow area material and the blended material

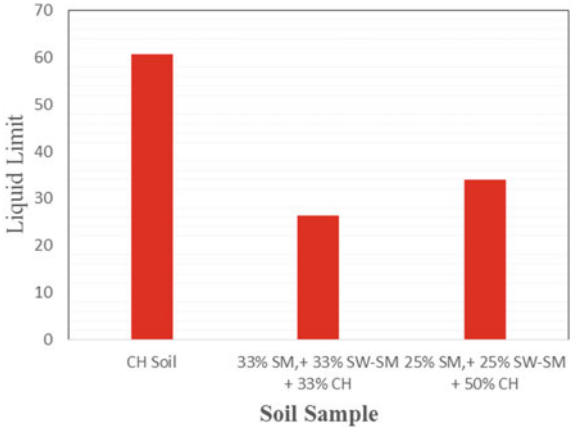

Fig. 21.2 Variation of liquid limit

and SW-SM soil samples with 50% of CH soil samples, Trial 2. Figure 21.2 shows variation of liquid limit.

The plastic limit of the CH soil sample decreases by 40% for the blended soil sample of 33% each of SM and SW-SM soil samples with 33% of CH soil samples, Blend 1 and decreases by 60% for the blended soil sample of 25% each of SM and SW-SM soil samples with 50% of CH soil samples, Blend 2. Figure 21.3. Variation of Plastic Limit.

The plasticity index of the CH soil sample decreases by 46% for the blended soil sample of 33% each of SM and SW-SM soil samples with 33% of CH soil samples, Blend 1 and decreases by 54% for the blended soil sample of 25% each of SM and SW-SM soil samples with 50% of soil samples, Blend 2. Figure 21.4 shows variation of Plasticity Index.

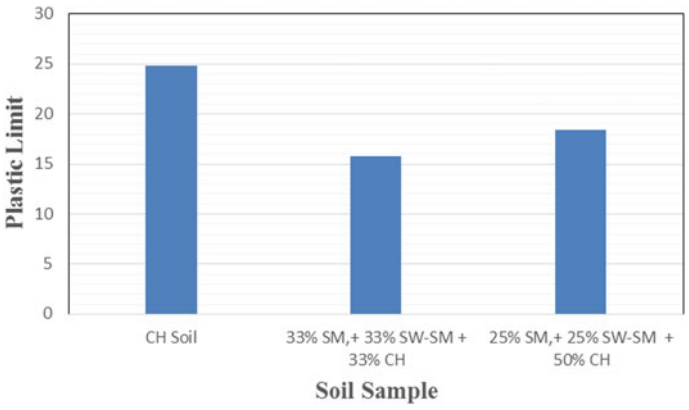

Fig. 21.3 Variation of plastic limit

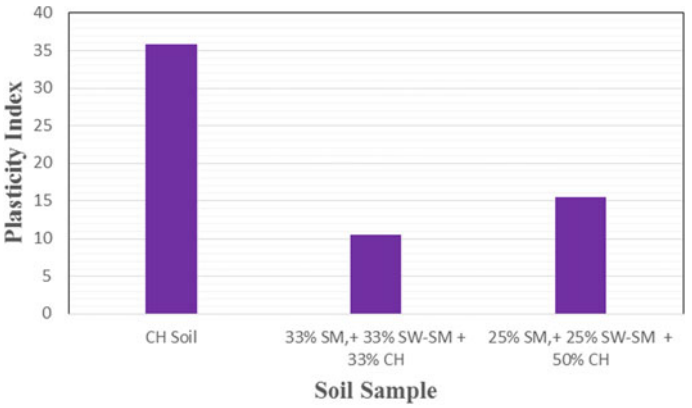

Fig. 21.4 Variation of plasticity index

Standard Proctor Compaction Test

Based on the results of the standard proctor compaction tests conducted on the blended soil samples, it is inferred that the maximum dry density remains almost the same with very marginal difference, whereas the optimum moisture content increases with the increase in the amount of CH soil sample and decreases in the SM and SW-SM soil samples. In original samples, MDD and OMC of only SI sample have been determined as shown in Fig. 21.5.

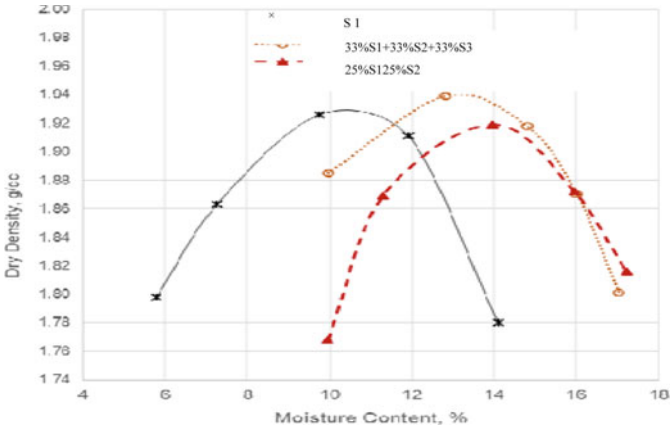

Fig. 21.5 Dry density versus moisture content

Conclusion

Based on the laboratory investigations carried out on the blended soils, it is recommended that the blended borrow area material arrived by mixing 25% each of the SM and SW-SM soil samples with 50% of the CH soil sample by weight is the most suitable material for the construction of the embankment dam. The significance of present paper is to find suitable solution with the available construction material by blending to get optimum engineering parameters, even if the quantity of borrow area material is not adequate for the construction of core of dam. The future scope of this research is that in addition to available borrow area materials; one can add other construction materials to improve the soil properties of borrow area material so that quantity is adequate for construction of dam.

References

1. Gulati SK, Datta M (2005) Geotechnical engineering. Tata McGraw-Hill, New Delhi
2. Arora KR (2000) Soil mechanics and foundation engineering. Standard Publishers, New Delhi
3. Lambe TW, Whitman RV (2000) Soil mechanics. Wiley, New York
4. IS:2720-Part 7 (1980) Standard proctor compaction. Bureau of Indian Standards, New Delhi
5. IS:2720-Part 8 (1983) Methods of test for soils—determination of water content—dry density relation. Bureau of Indian Standards, New Delhi
6. IS:2720-12 (1993) Triaxial shear test—CU test with PP measurement. Bureau of Indian Standards, New Delhi
7. IS:2720-17 (1986) Laboratory determination of permeability. Bureau of Indian Standards, New Delhi

Chapter 22
Experimental Investigation on Effect of Soil Consistency on Pullout Behavior of Plate Anchors in Reinforced Clay

Subramaniam Ravishankar, Subhadeep Banerjee, and Sarvesh

Introduction

Plate anchors are designed to transmit uplift forces of superstructure into the soil at a predetermined embedment depth below the ground surface. Plate anchors are widely used in both marine and land environments as an economical alternative to gravity anchors [1]. The ultimate pullout capacity of horizontal plate anchors in cohesive soil is represented in terms of non-dimensional breakout factors which depends maximum pullout load resisted by the anchor and undrained shear strength of clay. With respect to depth of embedment and failure conditions, the plate anchors are grouped into shallow and deep anchors. In shallow anchor conditions, the anchors are placed close to the surface of the soil and at the ultimate pullout, the tension cracks reaches the ground surface with considerable surface movements. When the anchor is placed at a higher embedment depth, the failure zone is localized around the anchor without any visible cracks at the ground surface.

At space constraint locations, introduction of geotextile reinforcement layer in soil above the plate anchor enhances the breakout resistance of anchor without altering the plate size and embedment depth. A review of existing literature shows that most of past research is focused on pullout capacities of anchor in reinforced granular soils. The present paper attempts to evaluate the behavior of horizontal plate anchors in reinforced cohesive soil and reports the influence of soil consistency on anchor pullout capacity.

S. Ravishankar (✉) · S. Banerjee
Department of Civil Engineering, IIT Madras, Chennai 600036, India
e-mail: sravishankariitm@gmail.com

Sarvesh
L&T Constructions, Chennai 600089, India

K. Muthukkumaran (eds.), *Soil Behavior and Characterization of Geomaterials*,
Lecture Notes in Civil Engineering 296, https://doi.org/10.1007/978-981-19-6513-5_22

Brief Review

In order to determine to the pullout capacity of plate anchors, several experimental investigations were executed by the researchers in the past. The majority of experimental studies were performed in the sand, and in clay such studies are limited. Experimental tests on plate anchors embedded in clay have been conducted by Davie and Sutherland [2], Das [3, 4], Rowe and Davis [5], Datta et al. [6], Das and Puri [7], Baba et al. [8], Singh et al. [9], Thorne et al. [10], Song et al. [11], and Das et al. [12]. The effect of soil consistency on pullout behavior of plate anchors was investigated by Singh and Ramaswamy [13], using a model plate anchor of 70 mm diameter embedded in soft clay, by varying the consistency index from 0.25 to 0.6.

However, the performance of plate anchors in reinforced cohesive soil is not well addressed. The small-scale laboratory model tests conducted on plate anchors buried in reinforced clays have been studied by Nene and Garg [14], Krishnaswamy and Parashar [15], and Saran and Rao [16]. Bhattacharya et al. [17] reported the effect of the inclusion of geosynthetic reinforcement in undrained clay on the pullout capacity of embedded plate anchors. The stress-controlled pullout tests were carried out in reinforced clay having undrained shear strength of 15 kPa. The improvement in pullout capacity of anchors due to the inclusion of geotextile reinforcement was quantified. In most of past research, the anchor capacity in reinforced clay was conducted at fixed undrained shear strength. But no attempts have been made in past studies to understand the effect of soil consistency on the pullout behavior of plate anchors in reinforced clay. In this paper, the pullout capacity of non-vented anchors in reinforced clay was determined, and their variation with embedment depth and consistency index is presented.

Experimental Procedures

Model Anchors

A 100 mm square plate made of mild steel is used as model plate anchors having a thickness of 6 mm. 8-mm-diameter anchor rod is used to connect the anchor plate and load cell. The anchor rod is connected to the anchor plate using a bolted joint arrangement.

Soil Used

Clay having a liquid limit of 73% and a plasticity index of 31% was used in the laboratory tests. The soil contains 90% of fines and classified as ‘CH’ as per Unified Soil Classification System (USCS).

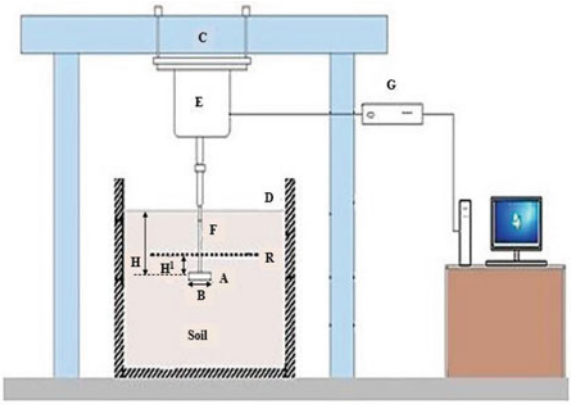

Fig. 22.1 Experimental setup

A	Plate anchor	G	Data acquisition system
B	Anchor width	H	Embedment depth of from top
C	Loading Frame		of plate anchor to soil surface
D	Testing Tank	H^1	Height of reinforcement above
E	Pneumatic actuator		Plate anchor
F	Connecting rod	R	Geotextile sheet

Geotextile

Woven geotextile fabric with mass per unit area 240 GSM (ISO 9864), tensile strength of (Warp/Weft), 52/40 kN/m, and maximum elongation at failure (Warp/Weft), 30/25% (ISO 10319) was used to reinforce the clay.

Experimental Setup and Loading Arrangements

The schematic representation of the experimental setup is shown in Fig. 22.1. The steel load frame of capacity 50 kN was used to facilitate the pullout tests. The horizontal steel beam is 2.3 m in height from floor level. A square tank of 1 m × 1 m × 1 m size, made of mild steel plates, was used to conduct the pullout tests. A load cell with a pneumatic actuator fixed at the center of the horizontal beam was used to apply vertical pullout load. The anchors were connected to the load cell by an 8-mm-diameter anchor rod. The anchor displacement is measured using Lvdt, connected to the actuator setup. The applied displacement and the corresponding pullout loads were captured and recorded using the data acquisition system.

Testing Procedure

The soil sample collected from the site is air-dried and pulverized. The pulverized clay was thoroughly mixed at the four different water contents (w) ($w = 67\%, 60\%,$

53%, and 48%) to achieve consistency index, $I_c = 0.15$, 0.25, 0.45, and 0.6. The corresponding undrained shear strengths of clay were found as 2.5, 4, 10, and 16 kPa. The mixed soil was stored in air tight containers for one week to achieve uniform moisture content. A similar technique was adopted by Datta et al. [6] to achieve homogenous soil mixture. Then the saturated soil was filled in the test tank in layers and lightly patted at the desired density. For stiff consistency ($I_c = 0.6$), the clay is uniformly compacted using a drop hammer. The clay bed thickness of 250 mm was kept as a soil cushion base for the plate anchor. Plate anchor was placed over the base layer and connected to the load cell through connecting anchor rod. A single layer of woven geotextile was fixed to anchor the rod using spec and spread horizontally above the top of the anchor plate at the desired location. The clay is filled up to the required embedment depth and kept undisturbed for 24 h. The soil in the test tank was covered with wet jute sheets to minimize the effect of evaporation.

The horizontal plate anchors are placed at embedment ratios (H/B) (1, 2, 3, 4 and 6), and the pullout tests are conducted in unreinforced and reinforced clay conditions. In reinforced soil condition, the width of geotextile was chosen as 4 times the width of the anchor plate, and the geotextile was positioned at a distance of 0.25 H, where H is the anchor embedment depth (Banerjee and Mahadevuni [18]). The static pullout tests were conducted at a fixed rate of loading 3.5 mm/min on embedded plate anchors. Tests were performed on four different consistencies of clay, and the load versus corresponding displacements were recorded in real-time at the proposed scan interval. Load displacement curves were plotted till there is a decrease in pullout load or the value of displacement equals to the size of anchor plate. The maximum pullout load resisted by anchor is termed as the ultimate pullout capacity of plate anchor.

Breakout Factor

In the present investigation, non-vented anchor plates were used to achieve immediate breakaway condition at different embedment depths. The ultimate pullout capacity of plate anchor in embedded in undrained clay is expressed in terms of non-dimensional breakout factor, N_c (Merifield et al. [19]).

$$q_u = C_u N_c \tag{22.1}$$

where $q_u = \frac{Q_u}{A}$ in which Q_u is the maximum pullout load resisted before failure and A anchor plate's plan area. Based on the above formulation, the breakout factors were calculated in reinforced and unreinforced clay at different embedment depths.

Result and Discussion

Influence of Geotextile Reinforcement on Pullout Capacity

The load displacement behavior of 100 mm model square plate anchor placed at embedment ratio 2 ($H/B = 2$) in saturated clay bed at $I_c = 0.15$ and 0.25 is shown in Fig. 22.2. The load displacement response of the anchors in both reinforced and unreinforced soils is in similar nature exhibiting nonlinear behavior. For both the soil consistencies, the ultimate pullout resistance is higher in reinforced soil compared to plate anchors embedded in unreinforced soil (Fig. 22.2). The frictional resistance between the soil and the geotextile reinforcement against anchor movement results in higher pullout capacity of anchor placed in reinforced soil. It was also observed that in unreinforced soil and reinforced soil, at failure condition, considerable upheaval was noticed at the surface. Table 22.1 gives a summary of ultimate pullout loads and corresponding displacement of 100 mm square anchor plate.

The maximum breakout factor obtained at different embedment ratios for model anchor placed in reinforced and unreinforced soil at $I_c = 0.45$ is shown in Fig. 22.3. Irrespective of embedment ratios, the breakout factors of anchors in reinforced clay are higher compared to anchors in unreinforced soil. In addition to this, it is also noted that the provision of geotextile reinforcement in soil is highly beneficial at lower embedment depths (Fig. 22.3).

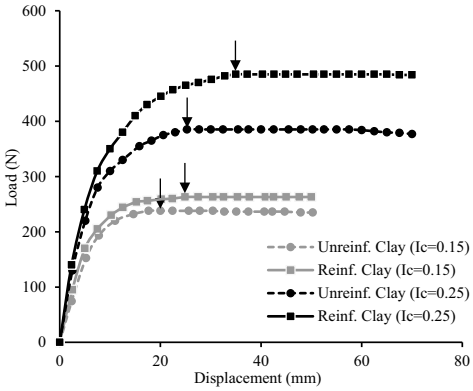

Fig. 22.2 Load displacement curve for anchor at $H/B = 2$

Table 22.1 Ultimate pullout load of 100 mm plate anchor at embedment ratio 2

Embedment depth	I_c	Unreinforced clay		Reinforced clay	
		Pullout load	Displacement	Pullout load	Displacement
200 mm	0.15	238 N	20	263 N	25
	0.25	385 N	25	485 N	35

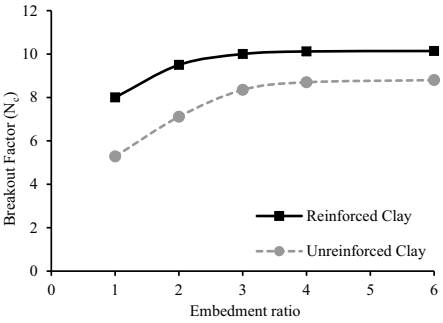

Fig. 22.3 Variation of N_c and embedment ratio at $I_c = 0.45$

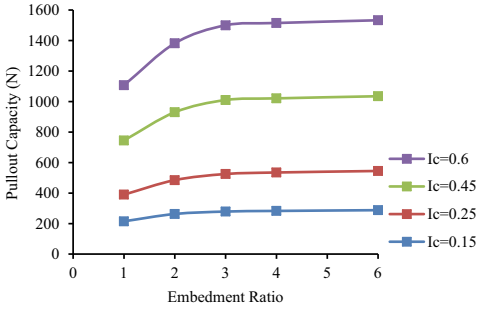

Fig. 22.4 Variation of anchor pullout capacity with embedment ratio

Effect of Embedment Ratio on Pullout Capacity

The value of breakout factors, of 100 mm square plate anchor embedded in unreinforced and reinforced soil, raises with the increase in embedment ratio. The value of breakout factor reaches the peak at an embedment ratio of three, beyond which there is no considerable change in breakout factor for given soil consistency (Fig. 22.3). Similarly, in Fig. 22.4, for all soil consistencies, it can be noted that the breakout factor increases steadily with the increase in embedment ratio, up to the embedment ratio of three, and it is almost constant with further increment in embedment ratio. This embedment ratio ($H/B = 3$) is termed as critical embedment ratio for the given soil, and it is the borderline separating the shallow and deep anchor behavior of the anchor. Similar observations were reported by Bhattacharya et al. [17] and Banerjee and Mahadevuni [18].

Effect of Soil Consistency on Pullout Capacity

Figure 22.4 plots the variation of ultimate anchor pullout load in reinforced soil with embedment ratio for different clay consistencies. It is seen that, at all embedment ratios, the anchor pullout capacity increases with the increase in the consistency

index of clay. This scenario is mainly due to the fact that, in undrained condition, at a higher consistency index (lower moisture content), the shear strength of clay is maximum, and hence the soil offers more resistance against the anchor movement. A similar kind of behavior is observed by Singh and Ramaswamy [13] in unreinforced soils. In the present investigation, the soil exhibits higher resistance against anchor displacement at consistency index and undrained shear strength, 0.6 and 16 kPa, respectively.

Effect of Soil Consistency in Reinforced Soil

Irrespective of the embedment depth, the inclusion of geotextile reinforcement above the anchor increases the pullout resistance of the plate anchors. The maximum percentage increase in ultimate pullout loads due to the inclusion of geotextile reinforcement, compared to unreinforced soil, is represented as pullout improvement percentage. Pullout improvement percentage is the ratio of the difference in ultimate pullout load resisted by the anchor in reinforced and unreinforced soil to ultimate pullout load of anchor in unreinforced soil, represented in percentage. The pullout improvement percentages of 100 mm × 100mm model anchor, placed in clay having consistency index of 0.6, for different embedment ratios are shown in Table 22.2. The pullout improvement percentage for embedment ratio 1 is the highest that indicates the fact that the maximum effect of reinforcement is achieved in shallow embedment depth.

Figure 22.5 represents the variation of pullout improvement percentage with embedment ratio for different consistency index of clay. It can be seen that the maximum increase in ultimate pullout load due to the inclusion of reinforcement is around 50% (at $H/B = 1$) for anchors placed in the soil with a consistency index of 0.6. In reinforced soil, for a given embedment depth, the maximum pullout improvement percentage is achieved at higher consistency index of soil. At a higher consistency index (less moisture content), the frictional force between the reinforcement and soil is higher, which results in increased reinforcement resistance against anchor movement.

Table 22.2 Pullout improvement percentage of reinforced soil

Embedment ratio	I_c	Unreinforced clay	Reinforced clay	Pullout improvement percentage (%)
		Ultimate pullout load	Ultimate pullout load	
1	0.6	740	1107	50
2		995	1382	39
3		1110	1500	35
4		1130	1515	34
6		1150	1533	33

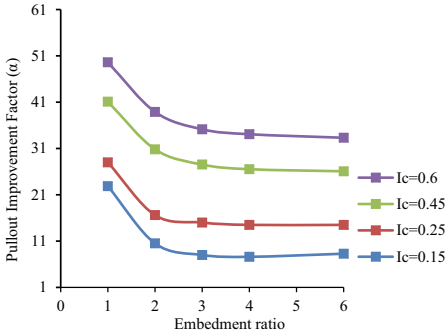

Fig. 22.5 Variation of pullout improvement factor with embedment ratio

Effect of Soil Consistency on Anchor Movement in Reinforced Clay

The displacement corresponding to ultimate pullout load for both reinforced and unreinforced soil conditions at different embedment ratios is determined from load displacement curves. The relative anchor displacement is represented as a non-dimensional pullout displacement factor (β). Pullout displacement factor is the ratio of anchor displacement corresponding to ultimate pullout load and the size of the plate anchor.

Figure 22.6 shows the variation of pullout displacement factor of reinforced clay for given soil consistencies. It is evident that for anchors embedded in soil with a higher consistency index (i.e. higher undrained shear strength), higher anchor displacement is required to achieve the peak pullout load. At failure load, in shallow anchors condition the soil is mainly stressed in bending, however in deep anchors, failure caused by substantial plastic deformation of the clay around the anchor before the complete collapse, which is clearly seen from the steady raise in pullout load along with an excessive anchor displacement at the peak.

In reinforced soil, the pullout displacement factor is higher for both soil consistencies due to the fact that a significant anchor displacement is required to mobilize the friction between geotextile and soil in reinforced soil (Fig. 22.7).

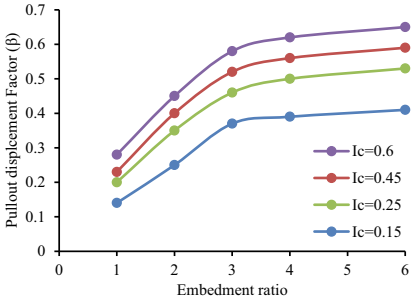

Fig. 22.6 Pullout displacement factor versus embedment ratio in reinforced soil

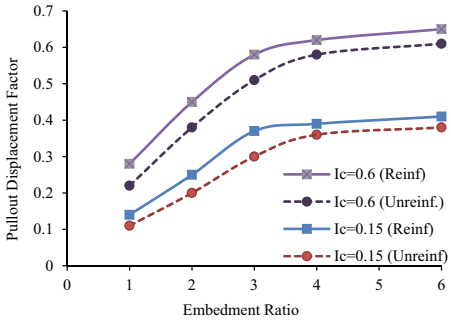

Fig. 22.7 Pullout displacement factor versus embedment ratio in reinforced and unreinforced soil

Conclusion

An attempt was made in the present study to investigate the behavior of horizontal plate anchors in unreinforced and reinforced cohesive soil during the vertical pullout. The pullout capacities of anchors placed at different soil consistencies were obtained by experimentation on model anchors. On the basis of experimental studies, several notable conclusions are listed below,

- The inclusion of geotextile reinforcement above the plate increases the ultimate pullout capacity of plate anchors at all embedment ratios. The breakout factors for anchors in reinforced soil increase with embedment depth and attain a constant value at the critical embedment ratio.
- The consistency of backfill soil plays a vital role in the behavior of plate anchors in unreinforced and reinforced soils. For higher soil pullout resistance, the consistency index of soil should be higher.
- The efficiency of geotextile on enhancing the resistance of soil against pullout is higher when the soil is stiffer (less moisture content). It signifies that, at a higher consistency index, the undrained shear strength of clay is maximum, and it is the predominant factor in determining the effectiveness of geotextile reinforcement against load resistance.

References

1. Bouazza A, Finlay TW (1990) Uplift capacity of plate anchors buried in a two-layered sand. Geotechnique 40(2):293–297
2. Davie JR, Sutherland HB (1977) Uplift resistance of cohesive soils. J Geotech Eng Div ASCE 103(9):935–952
3. Das BM (1978) Model tests for the uplift capacity of foundations in clay. Soils Found Jpn 18(2):17–24
4. Das BM (1980) A procedure for estimation of ultimate capacity of foundations in clay. Soils Found Jpn 20(1):77–82
5. Rowe RK, Davis EH (1982) The behaviour of anchor plates in clay. Géotechnique 32(1):9–23

6. Datta M, Gulhati SK, Achari G (1990) Behaviour of plate anchors in soft cohesive soils under cyclic loading. Indian Geotech J 20(3):206–224
7. Das BM, Puri VK (1989) Holding capacity of inclined square plate anchors in clay. Soils Found Jpn 29(3):138–144
8. Baba HU, Gulhati SK, Datta M (1989) Suction effect in plate anchors in soft clays. In: Proceedings of the 12th international conference on soil mechanics and foundation engineering, Rio de Janeiro 1, pp 409–412
9. Singh SP, Tripathy DP, Ramaswamy SV (2007) Estimation of uplift capacity of rapidly loaded plate anchors in soft clay. Mar Georesour Geotechnol 25(3):237–249
10. Thorne CP, Wang CX, Carter JP (2004) Uplift capacity of rapidly loaded strip anchors in uniform strength clay. Géotechnique 54(8):507–517
11. Song Z, Hu Y, Randolph MF (2005) Pull-out behaviour of inclined plate anchors in clay. In: Proceedings of the 11th international conference of the international association of computer methods and advances in geomechanics. Turin, Italy, pp 715–722
12. Das TK, Chattopadhyay BC, Roy S (2013) Pull-out capacity of plate anchors with coaxial geotextile reinforcement. Ann Pure Appl Math 5(1):53–63
13. Singh SP, Ramaswamy SV (2008) Effect of shape on holding capacity of plate anchors buried in soft soil. Geomech Geoeng Int J 3(2):157–166
14. Nene AS, Garg S (1991) Behaviour of plate anchors in reinforced cohesive soils. Indian Geotech J 21(4):327–336
15. Krishnaswamy NR, Parashar SP (1994) Uplift behaviour of plate anchors with geosynthetics. Geotext Geomembr 13(2):67–89
16. Saran S, Rao PP (2002) Uplift behaviour of horizontal plate anchors with geosynthetics. Ind Geotech J 32(2):329–338
17. Bhattacharya P, Bhowmik D, Mukherjee SP, Chattopadhyay BC (2008) Pull-out behaviour of square anchors in reinforced clay. In: Proceedings of the 12th international conference of international association for computer methods and advances in geomechanics (IACMAG), Goa, India, pp 3441–3447
18. Banerjee S, Mahadevuni N (2017) Pull-out behaviour of square anchor plates in reinforced soft clay. Int J Geosynthetics Ground Eng 3(3):25
19. Merifield RS, Lyamin AV, Sloan SW, Yu HS (2003) Three dimensional lower bound solutions for the stability of plate anchors in clay. J Geotech Geoenviron Eng 129(3):243–253

Chapter 23
Geotechnical and Geophysical Characterization of Vadodara Region, Gujarat, India

Payal Mehta, T. P. Thaker, Nagdeep Desai, Markana Paras, and Hirapara Jaydeep

Introduction

The 2001 Bhuj earthquake was an alarming seismic event for the state of Gujarat. The hazards caused by this event have enforced the researchers to think about various parameters that need to be considered while performing microzonation study. Seismotectonic setup, local geology, past earthquakes, soil characteristics are the basic inputs to study seismic hazard in any region. Seismic site characterization has been investigated out by many researchers at different parts of India considering different approaches. Geotechnical and geophysical studies of local soil have been carried out at various cities of India like Dehradun [1], Delhi [2], Bangalore [3], Chennai [4], Surat [5], Agartala [6], Kumaon Himalayas [7] with MASW tests. Hanumantharao and Ramana [8] have examined dynamic soil properties in terms of shear wave velocity by carrying spectral analysis of surface wave (SASW) test in capital of India, Delhi. Nath and Thingbaijam [9] have performed vertical electrical resistivity sounding (VES), drill holes, and microtremor surveys to investigate geotechnical and geophysical characteristics of Guwahati city. Anbazhagan et al. [10] have investigated geomorphology and site classification of Lucknow city by carrying MASW test at 47 locations and drilling boreholes at 23 locations. As per NEHRP classifications, Lucknow city belongs to site class D with C class site at very few locations.

In this study, attempt has been made to investigate detailed geotechnical and geophysical attributes for Vadodara region. Borelog data have been collected from various private and public sectors to prepare soil profiles at various locations of the

P. Mehta (✉)
Civil Engineering Department, Indus Institute of Technology and Engineering, Indus University, Ahmedabad, Gujarat, India
e-mail: payalmehta2910@gmail.com

T. P. Thaker · N. Desai · M. Paras · H. Jaydeep
Civil Engineering Department, School of Technology, Pandit Deendayal Petroleum University, Gandhinagar, Gujarat 382007, India

K. Muthukkumaran (eds.), *Soil Behavior and Characterization of Geomaterials*,
Lecture Notes in Civil Engineering 296, https://doi.org/10.1007/978-981-19-6513-5_23

city. Field investigations have been conducted to generate shear wave and compressional wave velocity models at various depths. Based on shear wave velocity profiles, subsoil classification has been done considering NEHRP standards for Vadodara region.

Study Region

Vadodara is the third populated city after Ahmedabad and Surat in state of Gujarat. Vadodara is located at 22.30° N 73.19° E and falling under seismic zone III as per IS:1893-2016. Vishwamitri River, passing through the complete city, is spreading free dregs along its bank. General soil profile of the city is alluvial type with loose sediments. Vadodara is the developing city and going to convert into 'Smart City'. Many constructions are going to be built under this 'Smart City Project'. Structural safety is the prime factor of any developmental project. The detailed seismic hazard study considering local soil effects is the need for structural surety of the project. Study region, Vadodara, is situated in Mainland Gujarat having threat from near-field and far-field seismic sources. Cambay rift zone and Narmada rift zone are near-field vulnerable tectonic sources, which had witnessed of earthquakes of magnitude more than 5. Kutch Mainland Fault, Island Belt Fault, and Allah Bund Fault are far-field seismic sources but associated with the earthquakes of magnitude 7 and above. Considering the vulnerability of seismic sources to upcoming constructions, geotechnical and geophysical attributes of local soil of Vadodara city have been examined.

Geotechnical Attributes of Study Region

Around 430 borehole data have been collected from various geotechnical laboratories of private and public sectors. These data are of varying depth from 10 to 30 m, which revealed that Vadodara city is having variety of soil profiles. Synthesization of borehole data has been done to examine the soil properties with varying depth. Total 24 sections have been considered, which are passing through the various locations of the city to prepare the soil profiles. Figure 23.1 shows 11 sections on east part of the river and 15 sections on the west part of the river.

Typical sections of soil profile of the study region have been presented in Fig. 23.2a–c. Figure 23.2a represents central part of the city, which covers Salatwada, Raopura, Nawabwada, Bajvada, Yukupura, and Vrundavan circle. In Salatwada, Raopura, and Nawabwada locations, silty sand is found up to 15 m depth with intervening layer of poorly graded sand and clay of intermediate plasticity at 6–12 m depth. Bajvada and Yukupura locations comprise of poorly graded sand and silt of low plasticity, respectively, and followed by clay of intermediate plasticity up to 10 m depth. The next layer consists of silty sand up to 15 m depth at both locations. Clay

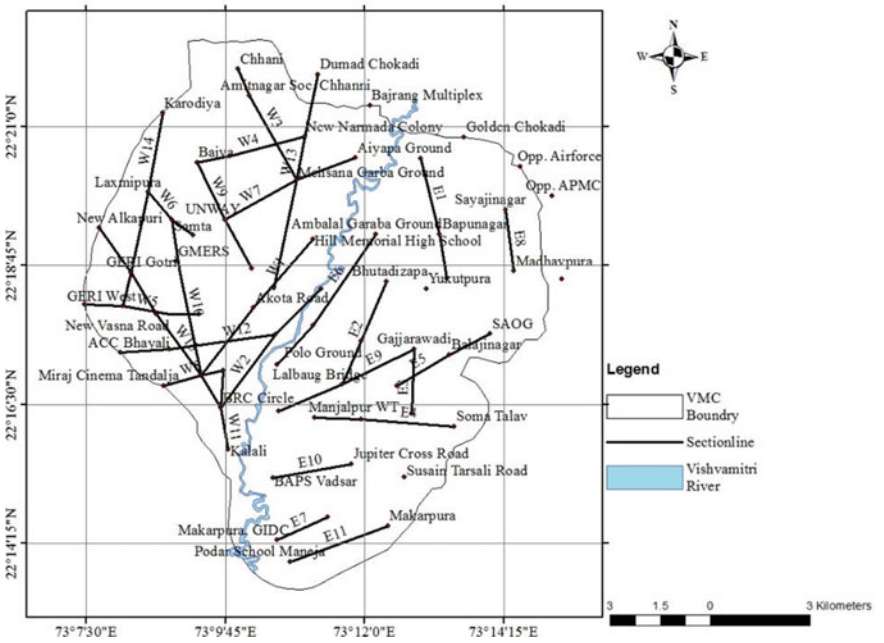

Fig. 23.1 Synthesization of borelog data for Vadodara region

of intermediate plasticity up to 8 m depth with intervening layer of low plasticity silt is encountered at Vrundavan circle and subsequent layer of silty sand from 8 to 15 m depth.

Northern section passes through Koyali, Eklavya Gorwa, and Chhani as depicted in Fig. 23.2b. Silt of low plasticity is found near Koyali, Eklavya Gorwa, and Chhani up to 10 m depth with intervening layer of silty sand. The Chhani location comprises of poorly graded sand from 10 to 15 m depth.

As shown in Fig. 23.2c, eastern section is passing through WC (borehole of Vishwamitri river front project), Nawabwada, Warsiya, New VIP road, and Sayajipura. At WC location, silt of low plasticity is found followed by silty sand up to 10 m depth. Clay of high plasticity is encountered from 10 to 15 m depth at same location. Nawabwada location is having silty sand up to 11 m depth with intervening layer of poorly graded sand of 2 m thickness at 5 m depth. Various kinds of soil layers are observed at Warsiya location. Silty sand is found up to13 m depth with two intervening layers of clayey sand and clay of intermediate plasticity at depth 2–5 m and 5–8 m, respectively. New VIP road comprises of silt of low plasticity, silty sand, and clayey sand up to 5 m, 7 m, and 9 m, respectively. The subsequent layer is of clay of intermediate plasticity from 9 to 15 m depth. Sayajipura location consists of clay of high and intermediate plasticity up to 10 m and 15 m depth, respectively.

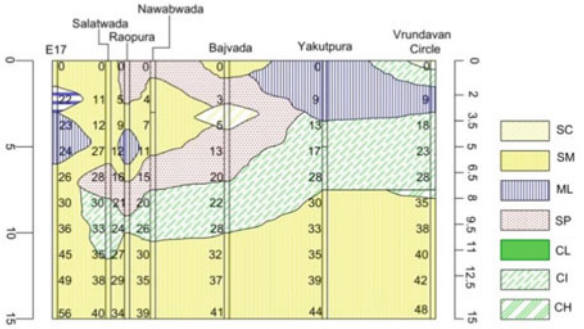

(a) Central section

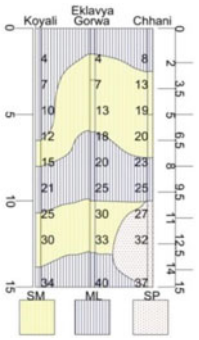

(b) Northern section

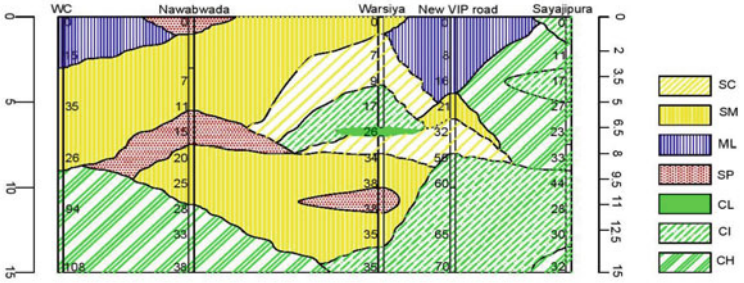

(c) Eastern section

Fig. 23.2 Geotechnical sections in various parts of Vadodara city (SP—poorly graded sand, SM—silty sand, SC—clayey sand, CL—silty clay of low plasticity, CI—silty clay of medium plasticity, CH—silty clay of high plasticity, ML—silty soil)

Geophysical Investigations

Shear wave velocity and compressional wave velocity are important geophysical attributes of local site, which need to be considered in detailed hazard study. Shear wave velocity of subsoil strata is an important parameter to increase ground motion

at surface level during an earthquake event. Multichannel analysis of surface wave (MASW) and seismic refraction (SR) are efficient methods to determine shear wave velocity and compressional wave velocity of local soil, respectively. In the present study, Vadodara region is divided into 2 × 2 km grid, and MASW and SR tests have been carried out at 67 locations in and around the study region.

Multichannel Analysis of Surface Wave (MASW) Test

MASW is a non-invasive method to generate shear wave velocity profiles of local soil. The 48-channelled engineering seismograph with 24 geophones of 4.5 Hz frequency has been used in testing programme. Total survey length is of 72 m with 3 m spacing between geophones. Offset distance is considered as 1.5 m. Total 25 shots have been made with sledge hammer of 10.5 kg. The data have been generated with triggered geophone and recorded in the seismograph. SeisImager/SW software has been used to analyse the acquired data. The detailed analysis of data is shown in form of flowchart in Fig. 23.3.

Shear wave velocity (V_s) models at depth of 5, 10, 15, 20, 25, and 30 m are depicted in Fig. 23.4a–f. In eastern part of the city, locations like Bapod, Pariwar Chowkadi, and Waghodia road possess the lowest velocity with a range of 165–215 m/s. The northeast, southeast, and central locations of the city have registered medium range velocity of 215–240 m/s at 5 m depth as depicted in Fig. 23.4a. The locations like

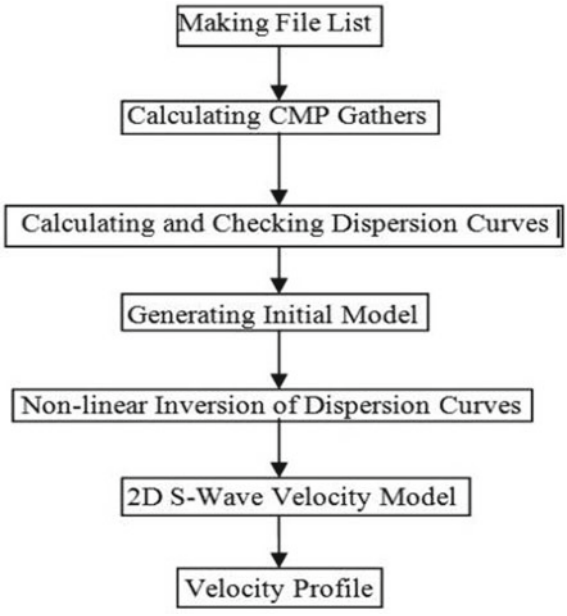

Fig. 23.3 Flowchart for analysis of MASW test

Alkapuri, Sayajigunj, Kalali, Vadsar, Sama, Akota have shear wave velocity in the range of 245–275 m/s and 275–310 m/s at 10 m and 15 m depth, respectively. The northwest locations like Gorwa, Karodiya are having the highest velocity of 285–325 m/s and 310–345 m/s at 10 m and 15 m depth, respectively. The areas like Gorwa, Gotri, Tandalja, Atladra, and Manjalpur have observed V_s of 285–325 m/s at same depths. It is observed from Fig. 23.4d–f that there is not much variation in V_s after 20 m depth as the soil is found to be medium to very stiff after 20 m depth.

Seismic Refraction (SR) Test

The seismic refraction (SR) test is performed to determine compressional wave velocity profile of study region. Refracted wave energy has been captured by seismic receivers. Seismic events have been recorded in form of raw seismic data which are called shot gather in engineering seismograph. This raw data have been analysed for picking up the first arrival times from each shot position through SeisImager/SW software. The result has been displayed in travel time versus distance graph, and velocities are calculated for the soil layers depth wise. The final output of this test comprises of P-wave velocity profiles of subsurface strata.

Data acquisition of seismic refraction test has been conducted through 48-channel seismograph with 24 geophones of 28 Hz natural frequency. These geophones are laid at 3 m space interval with 72 m total survey length. Seismic energy is generated with 10.5 kg hammer at an offset distance of 1.5 m. The source is shifted with 15 m interval at 4.5 m, 19.5 m, 34.5 m, 49.5 m, and 64.5 m, respectively, of the survey line.

The acquired data are analysed through SeisImager/SW software which consists of PickWin95, Plotrefa WaveEq, and Geoplot software package. The field data are imported into PickWin95 software, and the first arrival of refracted P-waves is picked manually or automatically on the waveforms in order to construct the travel time curves. These travel time curves are generated in the Plotrefa software. Travel time curves should be corrected and checked for the exact estimation of the P-wave velocity profile. Plotrefa software automatically checks reciprocal times for multiple-shot locations, and the root mean square (RMS) error should be less than 5%. The reciprocal method is used to obtain 2D velocity profile. Calculated and observed travel time curves are shown automatically after ray tracing has been completed. Two-dimensional P-wave velocity profiles are represented in Fig. 23.5a–f.

Figure 23.5a, b reveals that east, north, and some part of central locations of the city like Sayajipura, Bapod, Waghodia, Nizampura, Alkapuri, Akota, Sayajigunj have registered the lowest value of P-wave velocity (V_p) ranging from 435 to 610 m/s and 475 to 745 m/s at 5 m and 10 m depth, respectively. Locations like Gotri, Diwanpura, Kalali, Vadsar, Maneja, and Makarpura have encountered V_p of 610–710 m/s and 745–860 m/s at 5 m and 10 m depth, respectively. Highest V_p has been found at places such as Vasna, Tandalja, Atladra ranging from 710 to 1090 m/s and 860 to 1225 m/s at 5 m and 10 m depth, respectively. V_p values ranging from 850

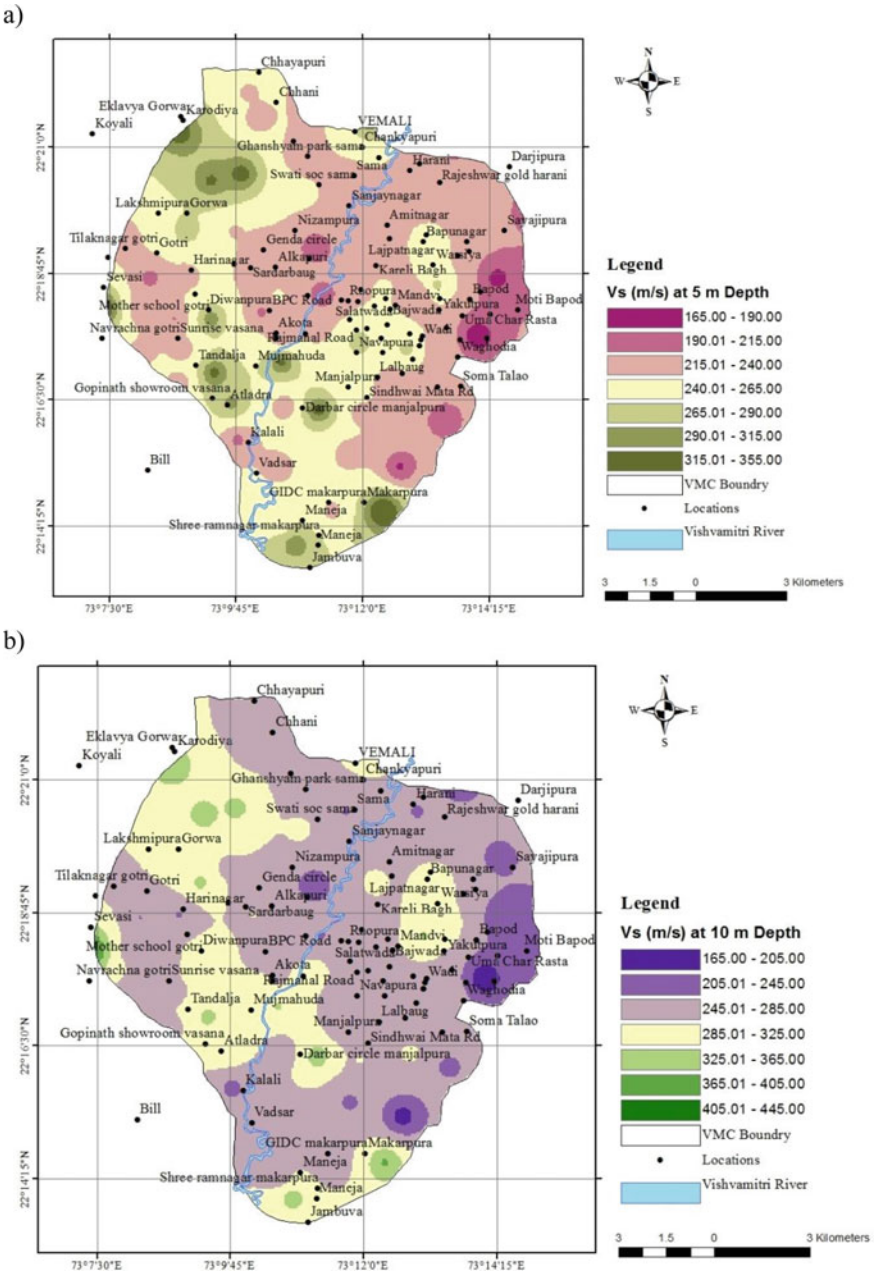

Fig. 23.4 Shear wave velocity profiles at **a** 5 m, **b** 10 m, **c** 15 m, **d** 20 m, **e** 25 m, **f** 30 m depths

c)

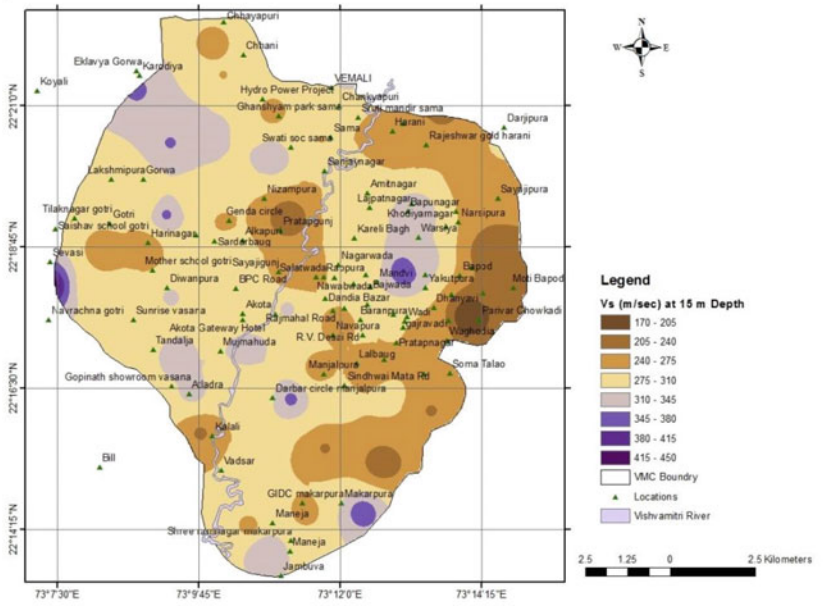

d)

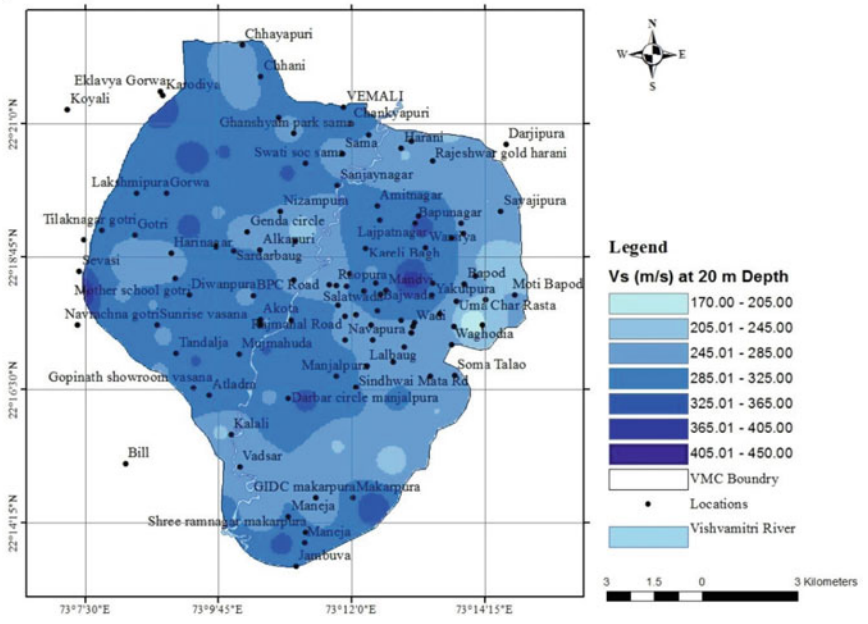

Fig. 23.4 (continued)

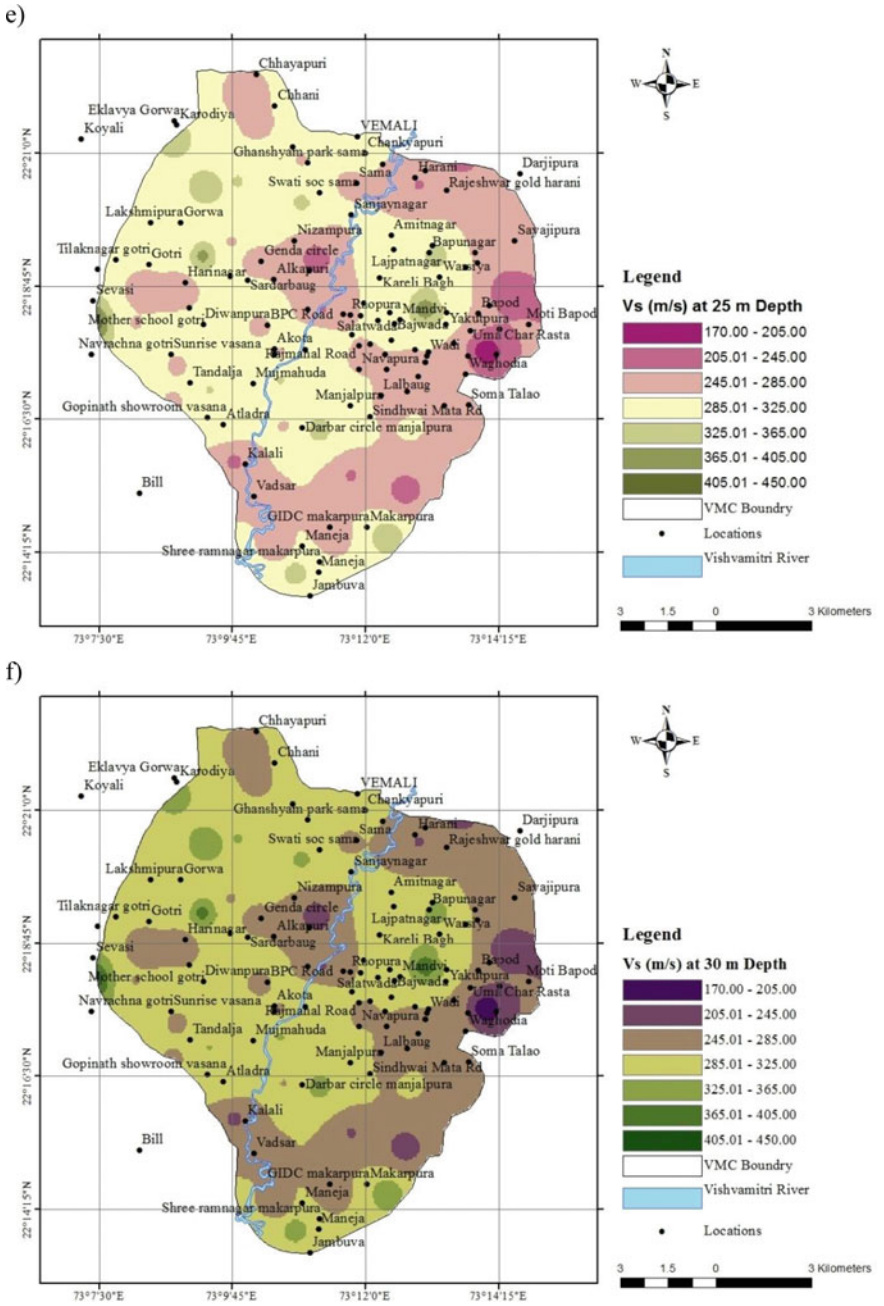

Fig. 23.4 (continued)

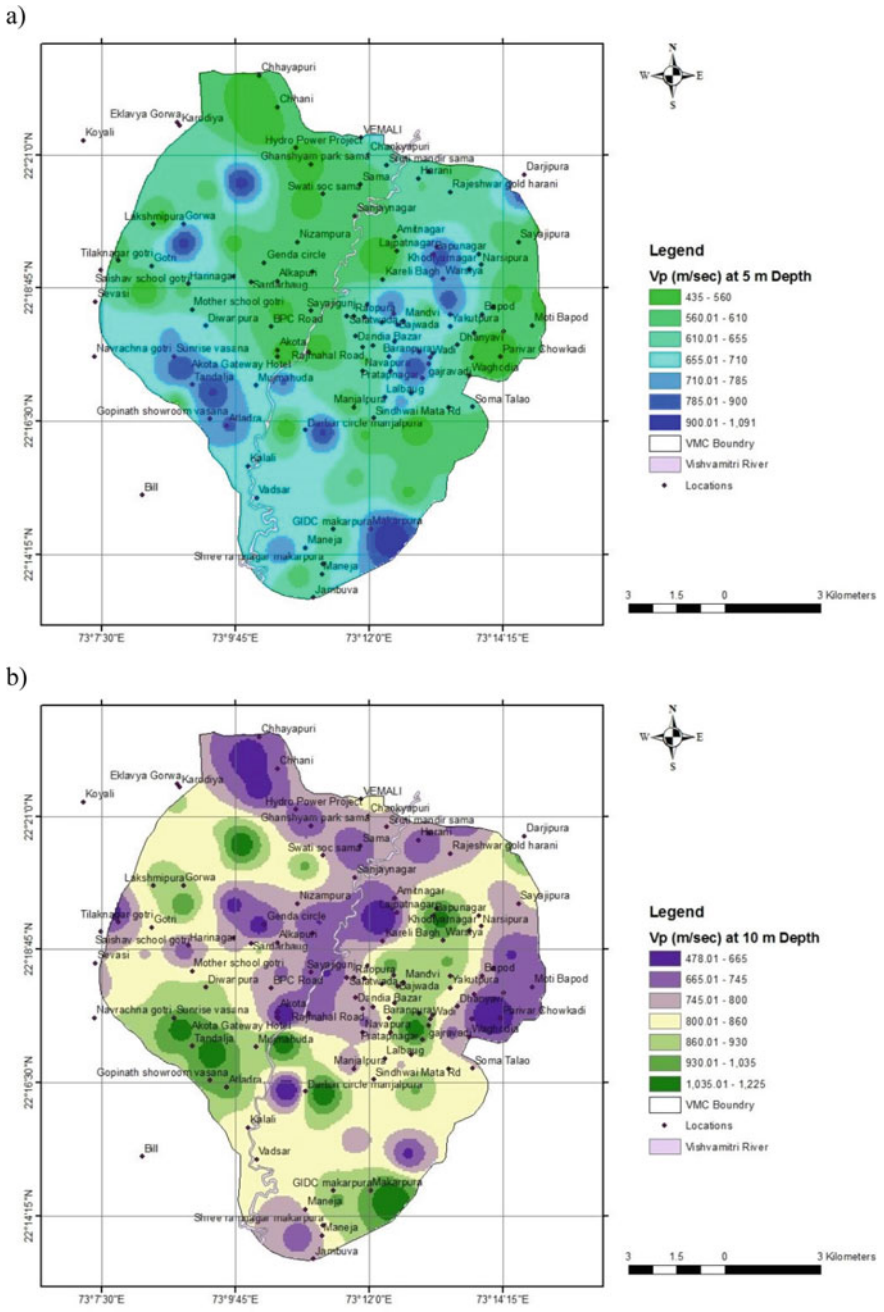

Fig. 23.5 Compressional wave velocity profiles at **a** 5 m, **b** 10 m, **c** 15 m, **d** 20 m, **e** 25 m, **f** 30 m depths

c)

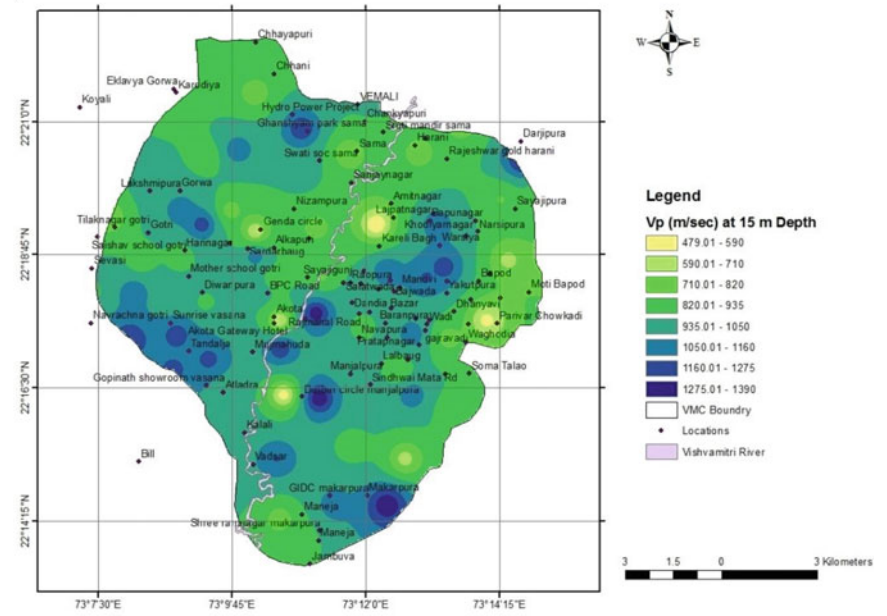

d)

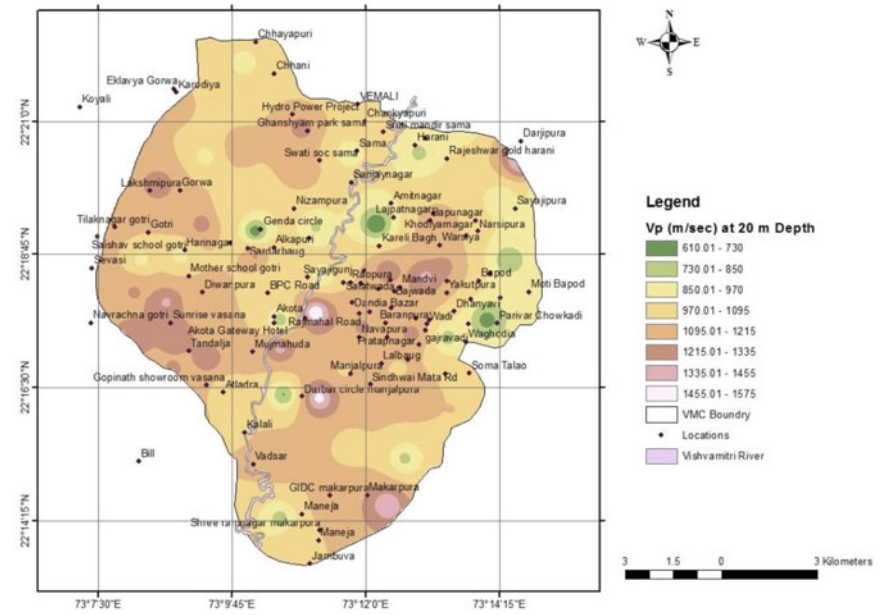

Fig. 23.5 (continued)

e)

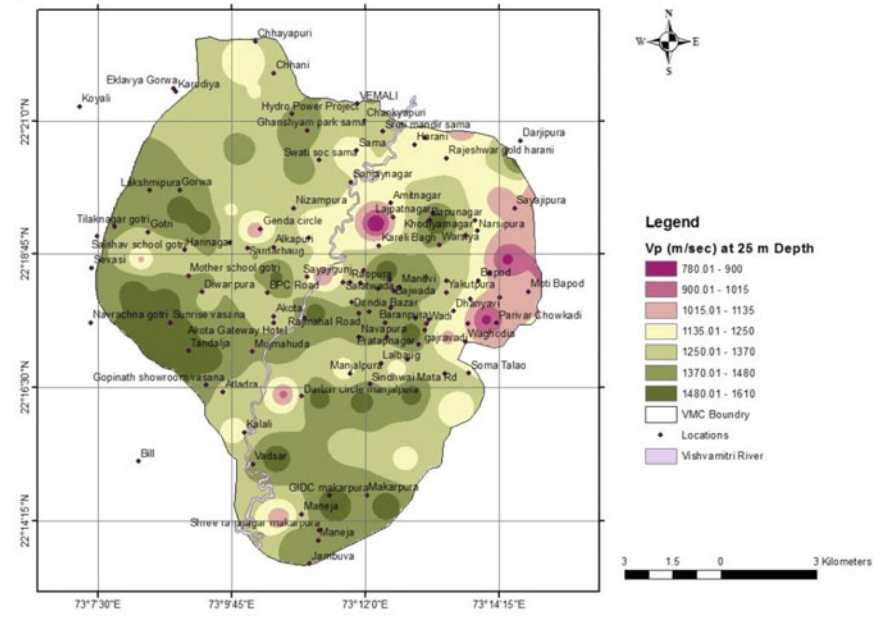

f)

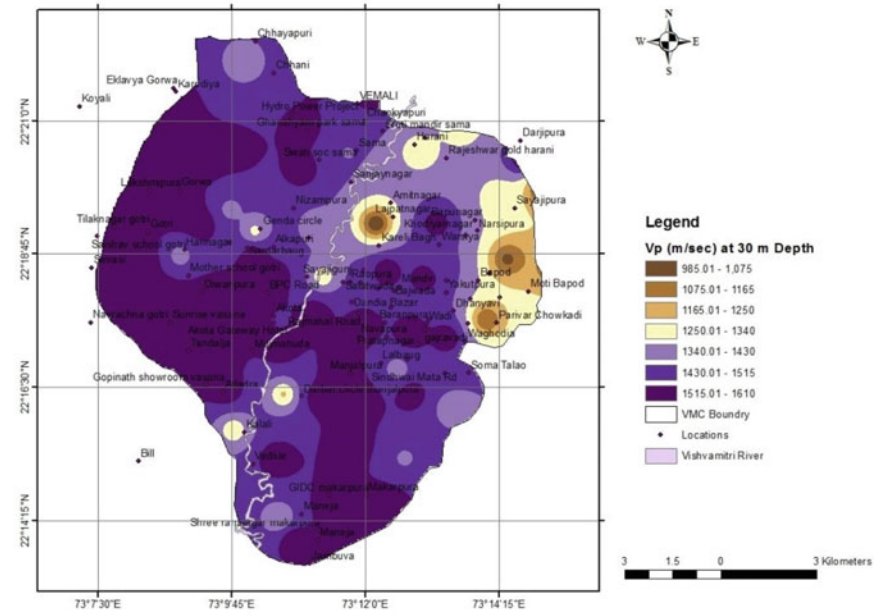

Fig. 23.5 (continued)

to 1335 m/s have been noticed at 20 m depth in 70% area of the city as depicted in Fig. 23.5d. Figure 23.5f reveals that east part of the city is having the lowest V_p (985–1165 m/s), central and southeast are having middle range of V_p (1340–1430 m/s), and western portion is having maximum range of V_p (1430–1610 m/s) at 30 m depth.

Conclusion

The present paper shows geotechnical and geophysical characteristics of the local soil of Vadodara region. Various geotechnical sections have been considered to study soil profiles of different parts of the city. Southern part of city comprises of deep black, and other parts of the city consist of alluvial sandy loam to sandy clay loam. Shear wave velocity (V_s) and compressional wave velocity (V_p) models have been generated in ArcGIS software to study geophysical characteristics of the region. Shear wave velocity ranges from 170 to 450 m/s at 30 m depth. As per NEHRP provisions, Vadodara city comes under NEHRP class C [$360 < V_{s30}$ (m/s) < 760] and NEHRP class D [$180 < V_{s30}$ (m/s) < 360] soil type. About 80% part of the city is having stiff soils (class C), and other portion consists of highly dense soils or soft rock (class D). The results are further useful for seismic ground response studies and also for seismic microzonation of the region.

References

1. Mahajan AK, Sporry J, Ray PKC, Ranjan R, Slob S, Van WC (2007) Methodology for site-response studies using multi-channel analysis of surface wave technique in Dehradun city. Curr Sci 92(7):945–955 (Research Article)
2. Neelima SD, Rao KS (2008) Seismic site characterization in Delhi Region using multi-channel analysis of shear wave velocity (MASW) testing. Electron J Geotech Eng 13(Bund. L):167–183
3. Anbazhagan P, Sitharam TG, Vipin KS (2009) Site classification and estimation of surface level seismic hazard using geophysical data and probabilistic approach. J. Appl Gephys 68(2):219–230
4. Maheshwari UR, Boominathan A, Dodagoudar GR (2010) Use of surface waves in statistical correlations of shear wave velocity and penetration resistance of Chennai soils. Geotech Geol Eng 28:119–137
5. Thaker TP, Rao KS (2012) Development of statistical correlations between shear wave velocity and penetration resistance using MASW technique. In: Pan-Am CGS geotechnical conference
6. Sil A, Sitharam TG (2013) Dynamic site characterization and correlation of shear wave velocity with standard penetration test 'N' values for the City of Agartala, Tripura State, India. Pure Appl Geophys
7. Joshi A, Bharadwaj P (2018) Site characterisation using multi-channel analysis of surface waves at various locations in Kumaon Himalayas, India. J Ind Geophys Union 22(3):265–278

8. Hanumantharao C, Ramana GV (2008) Dynamic soil properties for microzonation of Delhi, India. J Earth Syst Sci 117(S2):719–730
9. Nath SK, Thingbaijam KKS (2010) Assessment of seismic site conditions: a case study from Guwahati City, Northeast India. Pure Appl Geophys
10. Anbazhagan P, Kumar A, Sitharam TG (2013) Seismic site classification and correlation between standard penetration test N value and shear wave velocity for Lucknow City in Indo-Gangetic Basin. Pure Appl Geophys 170:299–318

Chapter 24
Intelligent Assessment of Axial Capacity of Pipe Piles Using High Strain Dynamic Pile Load Tests in Offshore Environment

Ramdev Gohil and C. R. Parthasarathy

Introduction

Historically used dynamic pile formulae are found to be highly unreliable due to its very little versatility and lack of incorporating essential parameters that affect the pile capacity [13]. The best method to test the pile is the static pile load test, giving the most accurate results in the field. But as realized, such static pile load tests are not possible to conduct in the offshore environment, which involves enormous setup space, cost, and time requirements. Hence, new methods like STATNAMIC pile load tests and dynamic pile load tests are found, which are quick and produce satisfactory results in the field. ASTM D4945-08 provides guidelines to perform such dynamic pile load tests [2]. One of the most practiced methods around the world for offshore-type environments is the high strain dynamic pile load test, based on Smith's 1D wave equation analysis approach [27]. The method is famous because of its little setup, cost, and enormous time saving in which pile test results can be achieved immediately after or during the pile driving itself. This uses fundamentals of stress wave propagation through the pile. When the pile head is struck with the hammer, it causes the compressional wave to generate and propagate forward, reflecting when it encounters resistance along the pile length and at the toe.

Force and velocity signals are collected during this impact event using the set of strain gauges and accelerometers attached near the tip of the pile. Then these measured data are analyzed in PDA, and pile resistance is calculated. More and more improvements have been made in this method such that the capacity obtained through this method is close to that obtained from actual static pile load tests by performing both the tests on the same piles [22]. But the capacity obtained only

R. Gohil (✉)
Indian Institute of Science, Bangalore 560012, India
e-mail: ramdevg@iisc.ac.in

C. R. Parthasarathy
Sarathy Geotech and Engineering Services, Bangalore, India

K. Muthukkumaran (eds.), *Soil Behavior and Characterization of Geomaterials*,
Lecture Notes in Civil Engineering 296, https://doi.org/10.1007/978-981-19-6513-5_24

from PDA is not reliable because it involves certain rigid assumptions. The damping parameter used in the analysis is not unique and very difficult to decide for different soils. Later on, CAPWAP was introduced, which proved beneficial and became a "must be done" analysis after performing PDA [20]. CAPWAP is the signal matching program that models the pile and soil as segments along the length and uses a linear spring-mass damping model to calculate the resistance of the pile along the shaft and at the toe. In this signal matching technique, both the force and velocity signals are initially recorded from the impact event. Then, by assuming few sets of parameters for soil and pile, the other quantity is calculated using one of the force or velocity curves. This estimated signal is then compared with the obtained one. The difference between the signals shows the amount of error in the assumption of the parameters. These parameters are then to be adjusted iteratively until both signals are matching satisfactorily. Then one can use this final set of assumed parameters to calculate the capacity of the pile. This is a comparatively easy and quick technique, and the accuracy of the calculated resistance is primarily based on the quality of the data collected.

Though this signal matching technique seems simple, it involves rigorous iterations by adjusting many parameters and requires a highly skilled user for its operation to judge these parameters used during the analysis. The damping parameter, in particular, is the quantity in a pile dynamic analysis that accounts for a variety of uncertainties. Other factors, for example, about offshore pile foundations, internal pipe friction may establish a more velocity-dependent resistance effect than outside friction. This problem would be amplified by the non-uniformities of the pipe pile, which act like minor end-bearing effects. Also, the actual damping behavior is not linear, and because of that, hammer type and energy level affect this calculated quantity. The time affects both blows per minute and duration of driving: hence, interruptions in pile work are known to make a significant contribution not only to the static but also the dynamic resistance components. Similarly, restrike tests show that soil setup behavior affects both the static and the dynamic components. Quake (elastic deformation of the pile) values are also affected by the above phenomena and pile size and partial plugging effects. There are no specific guidelines available that suggest the exact value of these parameters. All these problems cannot be considered while performing CAPWAP, and the test results vary from one person to another. And hence CAPWAP lacks a unique solution, and this result is not guaranteed to give the actual static pile capacity [12]. Many authors have tried to automate this process, but very little success has been achieved so far.

Many authors have used recently artificial intelligence (AI) approach in different fields of civil engineering like for predicting the strength of concrete, torsion capacity of beam, indicating settlement of footings and piles, classification of sites based on liquefaction assessment or site characterization, etc. [5, 7, 21, 24, 26, 29]. The problems in which output is dependent on many variables and no clear relation between inputs and outputs are known a priori; one can use machine learning tools effectively. Like a neural network, support vector machine, etc., these machine learning tools

require no prior relation to be defined between inputs and outputs. It learns this automatically from the examples given to it, working like what the human brain does. These tools best fit this problem of predicting pile capacity where it depends on many quantities, and the exact relation is unknown. With this inspiration, in this work, the neural network approach has been used to develop a model which can predict the pile capacity in the form of end bearing and shaft resistance separately when few related significant input parameters are given to the model.

Artificial Neural Network

In this work, an artificial neural network, one of the most developed tools in machine learning, is implemented to solve a critical problem of pile capacity evaluation. ANN is more potent than traditional statistical and mathematical methods when the problem requires complex qualitative or quantitative reasons, or if there are too many parameters to consider which are highly interdependent or the data is intrinsically noisy or error-prone [3].

The neural network is a mathematical model of the human brain that primarily consists of neurons or the nucleus, axons or the output connections, dendrites, or the input connections/wires. These neurons are arranged in layers and are connected with the other neurons in a different layer. Whenever there is an activity, like the brain sends electricity, a forward pass is made. Weights are attached with each connection to neurons according to their importance in calculating output. Then these weights are readjusted until the calculated result is satisfactory, matching with the actual one [9].

In this model, the dendrites are like the input features $x_1, x_2, \ldots, x_n$ and the output is the result of our hypothesis function. In addition, there will be a bias unit x_0 as the input unit to compensate for the error. Referring to Fig. 24.1 input nodes (layer 1), also known as the "input layer", go into other nodes (layer 2), which finally outputs the hypothesis function, known as the "output layer." There can be intermediate layers of nodes between the input and output layers called the "hidden layers." These intermediate or "hidden" layer nodes are labeled as $a_0, a_1, \ldots, a_n$ and called as "activation units." "Theta" parameters are called "weights", which are controlling function mapping from layer j to layer $j+1$. The sum of these weighted inputs and the bias form the net input signal as shown in Eq. (24.1)

$$z_k^{(2)} = \Theta_{k,0}^{(1)} x_0 + \Theta_{k,1}^{(1)} x_1 + \ldots + \Theta_{k,n}^{(1)} x_n \tag{24.1}$$

(e.g. here $z_k^{(2)}$ shows results for layer $j = 2$ and node k). Finally, this input is then sent to the transfer function, which serves as an activation function to calculate the output shown in Eq. (24.2)

$$h_\Theta(x) = g\left(z_k^{(2)}\right) \tag{24.2}$$

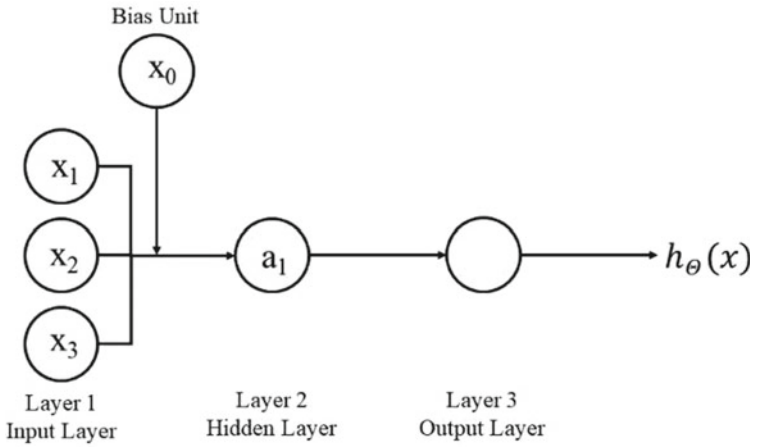

Fig. 24.1 Simple neuron model architecture

This transfer function can be sigmoid or linear [1]. The architecture determines how computations proceed. Architecture is a different combination of the number of hidden layers and the number of neurons in each hidden layer. Here in the feed-forward network, the connection is allowed in only one forward direction and repetitions are not allowed. The selection of input parameters should be carried out with different combinations of parameters, and then the one performing the best is to be selected. The data provided for generalization has to fall between the ranges of standardized data used while training for the best performance. For ANN, a separate set of data is needed for the validation purpose so that model can generalize well. Usually, two independent sets of data are used, one for training and others for testing the model. The data has to be pre-processed either by normalization or by transformation by scaling them within the limits of the transfer function to speed up the learning process. Once the first cycle of training is complete, the different model optimization processes can be used to improve the model weights after each cycle. Here the most common technique of back-propagation algorithm is used for the same. It involves adjusting the weights of neurons by calculating the gradient of the loss function or the error, which is then distributed from the output to input in the backward pass. Levenberg–Marquardt's (LM) algorithm is mainly used for all types of networks. Training and optimization are stopped after several iterations or when the training error reaches an effectively small value or when no or only minor improvement occurs in the accuracy. After the training part is completed, the model has to validate the results for the completely new set of unseen data. The results produced by this model for the new set of data have to be accurate to the actual results. The accuracy can be measured with some standard tools of statistics like root mean square error (RMSE) or mean absolute error (MAE) and coefficient of correlation (R), or the coefficient of determination (R^2).

Data Preparation

All the data are the results of the dynamic pile load tests conducted around the world by the authors. These also contain CPTs, and other site investigations are carried out near the pile locations. The pile test locations, as shown in Fig. 24.2, are: Persian Gulf (offshore Iran), Panna Field-Westcoast (offshore India), Arthit Field (offshore Thailand), Champion Field (offshore Brunei), Dong Do Field (offshore Vietnam), and Konowit Field (offshore Sarawak, Malaysia). The soil parameters used in this work are obtained from the results of CPTs. The main advantage of CPT is minimum disturbance to the soil while testing, unlike SPT or other tests or lab testing. Cone tip resistance q_c and sleeve friction f_s are the two critical parameters that are recorded while performing the test. The CPT results of these locations show that the general soil profile was consisted mainly of soft clays with intermediate layers of silts and sand in a few areas. No hard rock was observed at any depth from the analysis of the reports. Hence, this model has been developed for offshore marine environments with a dominating clay profile with or without silt/sand layers. Generally, piles are resting on hard silty clay or medium dense sand layers and are terminated as per the design and requirement criteria. Figure 24.3 shows that most piles are friction-dominating piles, whereas the end resistance obtained is very little. From the available CPT results using the appropriate methods for soft clay, undrained shear strength values can be found out [23]. Theoretical relation as shown in Eq. (24.3) is used to obtain the values of undrained shear strength of the soft clay where it was not already available.

$$S_u = \frac{q_t - \sigma_v}{N_{kt}} \tag{24.3}$$

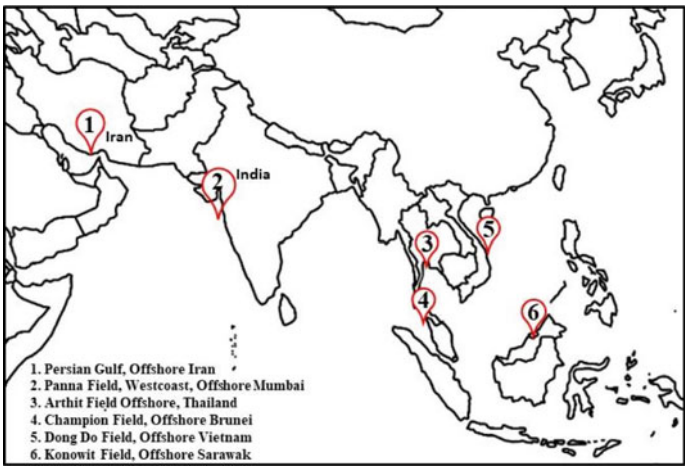

Fig. 24.2 Location of the tests conducted by the authors

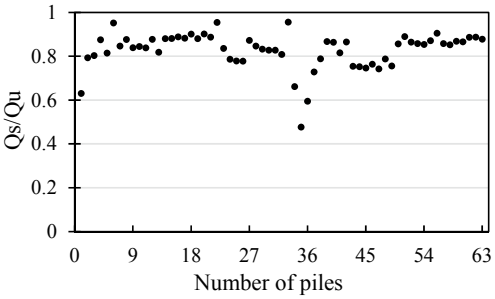

Fig. 24.3 Ratio of shaft resistance (Qs) to total pile capacity (Qu)

In above equation, cone resistance is related to the shear strength values. Here q_t represents the cone resistance values after applying the correction for pore pressure; σ_v represents the effective overburden stress; N_{kt} is the constant representing preliminary cone factor value that may lie between 14 and 16. The graph of this S_u along the pile length was already available from the soil reports for most cases. Similarly, the unit weight of the soil can also be determined from the CPT results. The results for the submerged unit weight of the soil are available from the soil investigation reports and CPT.

Around 100 pile test results from high strain dynamic pile load tests using CAPWAP were analyzed for the study. Out of that, only 63 final test results were chosen, which had all complete sets of data available; the rest were not selected. The number of piles per location is shown in Table 24.1. All these piles are steel pipe piles open at both ends. The diameter of these piles is in the range of 800–2200 mm. These data give information about pile geometry, soil properties, and pile driveability characteristics, including the pile diameter of the pile, its cross-sectional area at the tip, and the length of penetration of the pile in the soil. Soil properties information includes submerged unit weight of the soil along the pile length and near the pile tip. Also, it gives values of undrained shear strength in kPa units along the pile shaft and near the pile tip. Weighted average has been taken as a representative value along the pile length for shear strength and unit weight of soil. Whereas near the pile tip, the average value has been taken in between the region of three times the diameter of the pile above and below the pile tip. The information from CAPWAP analysis includes the observed number of blow counts, i.e. the number of blows required for the pile penetration of one meter and the force and velocity data procured while driving the pile. CAPWAP provides the ultimate axial pile capacity values at the end of driving and end bearing and shaft resistance separately. Table 24.2 provides some statistics about the data which is used in this analysis.

Model Inputs and Outputs

Selecting the most relevant input parameters is one of the most critical steps in developing a successful model using any technique. From the available literature and experience, pile bearing capacity is a function of soil properties and pile geometry. A review work by Fatehnia and Amirinia [6] provides a detailed report of the uses of

Table 24.1 Location of the tests carried out by authors

Field name	Location	Number of piles
Persian Gulf	Offshore Iran	5
Panna Field-Westcoast	Offshore India	34
Arthit field	Offshore Thailand	2
Champion field	Offshore Brunei	16
Dong Do field	Offshore Vietnam	3
Konowit field	Offshore Sarawak, Malaysia	3

Table 24.2 Statistics of the data used in the analysis

Parameter	Units	Max	Min	Mean	Std. Dev
Outer diameter	mm	2134	776	1551	457
Area	cm^2	3592.25	578.84	2061.27	1058.17
Length	m	114.5	35	84.1	20.4
$\gamma'_{(shaft)}$	kN/m^3	10.12	6.55	8.65	0.78
$\gamma'_{(tip)}$	kN/m^3	11.8	8	9.61	1.20
$Su_{(shaft)}$	kPa	304	27.9	168.97	70.39
$Su_{(tip)}$	kPa	600	150	354.77	147.20
BC	blows/m	1000	77	203	164.05
Q_u	MN	25.76	3.13	16.05	6.20

ANN in predicting pile capacity. From the publications available, many parameters are reviewed before selecting the final ones. Kordjazi et al. [10] and Baziar et al. [4] chose CPT results and pile geometry as main parameters along with the type of pile load tests and pile materials. Pal and Deswal [18] used dynamic test results and pile geometry similar to Maizir and Kassim [16]. Lee and Lee [11], Momeni et al. [17], and Samui [24] also used identical parameters for developing the regression models. Other authors have considered similar parameters for predicting pile capacity using neural networks [14, 19, 25]. So from these detailed reviews and a few trials and errors, eight input parameters are first selected for the analysis in the model: (i) OD-Outer Pile Dia., (ii) A-Cross section area of piles, (iii) L-Pile penetration length, (iv) $\gamma'_{(shaft)}$-the submerged unit weight of soil along the pile length, (v) $\gamma'_{(shaft)}$-the submerged unit weight of soil near tip, (vi) $S_{u(shaft)}$-shear strength along pile length, (vii) $S_{u(tip)}$-shear strength near pile tip, and (viii) BC-blow count per meter, i.e. number of blows required for the penetration of one meter. The skin friction resistance values f_s as obtained during CPT results are not used in this study as the literature suggest that this value does not represent the actual skin friction resistance as the cone has already penetrated the surface, and a very poor correlation is found between pile capacity and this value [23].

It is well known that the force and velocity signals obtained from the dynamic measurements during the test are most important in CAPWAP to predict the pile capacity. So, using this concept, Teh et al. [28] included these parameters as the inputs for predicting pile capacity. Similarly, along with the basic information of the pile and soil, these dynamic measurements obtained from strain gauges and accelerometers during the tests are also included in inputs. From the analysis of all the test reports, the force and velocity signal mainly dominated the first cycle of the wave from the time of impact to when the wave reached the pile head after reflecting from the toe (Fig. 24.4). This is very well according to wave propagation theory, where only fundamental mode is most important where most of the shaft resistance is mobilized. Using this fact and referring to work by [28], it was decided that the force and velocity–time histories are also to be included as the inputs along with the other parameters. Based on all the CAPWAP reports, it is decided to divide each force and velocity curve from time t_p and $(t_p + 2L/c)$ into 50 measurements each (t_p is the time of impact as shown in Fig. 24.4). This was achieved by digitizing the image and using the data extractor tool: Web Plot Digitizer. Hence, 50 force values and 50 velocity values are taken as the inputs for the ANN model. The velocity values are multiplied with the impedance of the pile to keep the unit the same as that of force data.

The ANN architecture for this model involves 106 neurons in the input layer. These consist of 50 force values and 50 velocity values. End-bearing capacity and shaft resistance of pile are predicted using two different models. For predicting end-bearing resistance, submerged unit weight and shear strength values near the pile tip are used. For predicting shaft resistance, submerged unit weight and shear strength values along the shaft are only considered. The ANN model makes sense only when input data are selected intelligently. The output for each model is only the end bearing

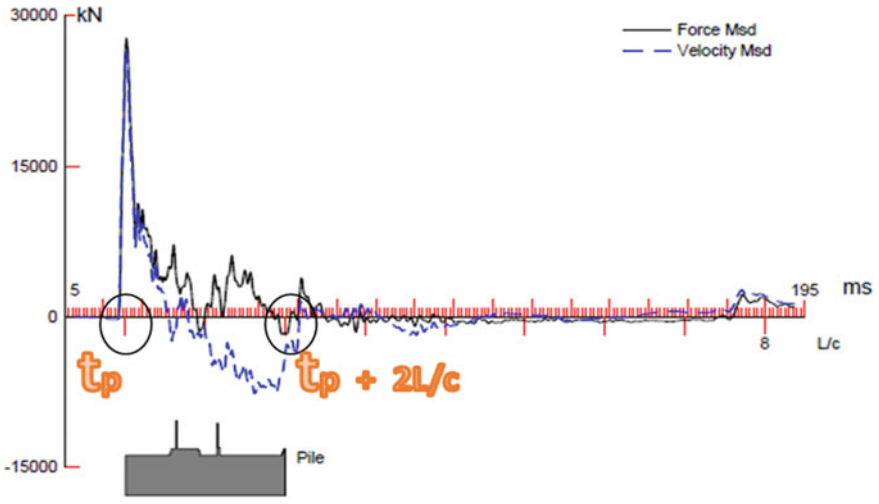

Fig. 24.4 Most significant period during the impact event

and shaft resistance values, respectively. These input and output data are then scaled between 0 and 1 using the max–min normalization technique as shown in Eq. (24.4) so that ANN treats all the data equally without any bias.

$$y_{i_{(n)}} = \frac{y_i - y_{min}}{y_{max} - y_{min}} \tag{24.4}$$

where y_{min}, y_{max} represents the minimum and maximum values of parameter y, respectively. y_i is the actual value, and $y_{i(n)}$ is the normalized value of that parameter. The input parameters having the same units are normalized in a group between 0 and 1. Out of the 63 test results, 50 results (around 80% total data) have been used for training, and the rest are used for testing the model, as found appropriate from literature studies. The most crucial part of ANN modeling is selecting the number of hidden layers, the number of neurons in each hidden layer, and the learning algorithm for the model. Here through trial and error, the best architecture is found out based on the performance in predicting target output values.

Combination of Different Architectures to Find the Best Model

Hornik et al. [8] stated that a single hidden layer with a sufficient number of neurons could approximate any continuous function. As such, the first model consists of a single hidden layer with ten hidden neurons in it. Using the Levenberg–Marquardt algorithm (LM) for optimization, the model is trained and then tested for a completely new set of data. Then other trials have been done by varying the number of hidden layers and the number of neurons in each layer. LM optimization algorithm is adopted for Model 1–5 and Bayesian Regularization algorithm is adopted for Model 6–10. For predicting shaft resistance, ten models have been trained, which are shown in following Table 24.3. Similarly, ten such models have been trained for predicting end-bearing values. As shown in Table 24.3, each model is run five times to ensure the repeatability of the results.

Results

Figure 24.5 shows the training results for Model 1 for shaft resistance. The result of training is satisfactory with R^2 value of 0.83, although it predicts one negative value. While testing this model for a new set of data, the model performs poorly with the R^2 of 0.76. The error bars in Fig. 24.6 show the deviation of the predicted values from their mean in five trials. It has been found that whenever the same model is run five times, the results obtained are not similar and have a maximum standard deviation of 28 MN for this very poor model. The model is said to have performed best only when the results of testing with an entirely new set of data are predicted with reasonable accuracy, and the repeatability of the result is ensured with more than one trial. Similarly, Models 2–10 are trained and tested for shaft resistance, and the results of testing are presented from Figs. 24.7, 24.8, 24.9 and 24.10.

Table 24.3 Different combination of ANN architecture adopted in this study

Levenberg–Marquardt algorithm		
Model number	Number of hidden layers	Number of neurons in each hidden layer
1	1	10
2	1	20
3	1	30
4	2	10
5	3	10
Bayesian regularization algorithm		
6	1	10
7	1	20
8	1	30
9	2	10
10	3	10

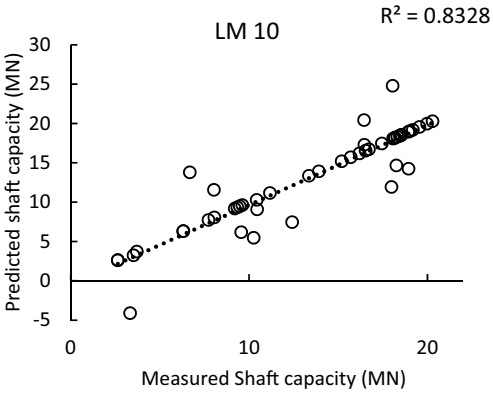

Fig. 24.5 Results of training of LM 10 model

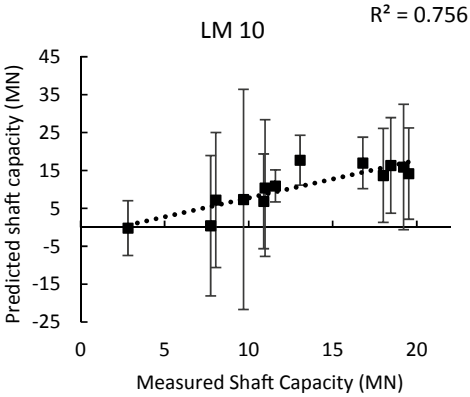

Fig. 24.6 Results of testing of LM 10 model

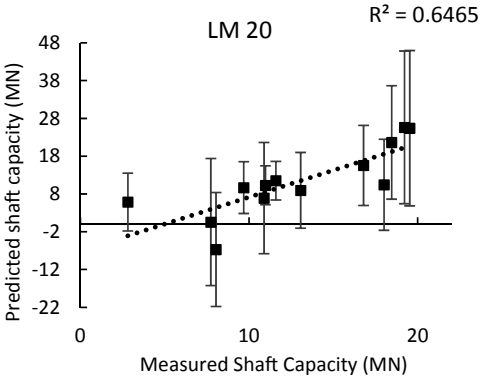

Fig. 24.7 Results of testing of LM 20 model

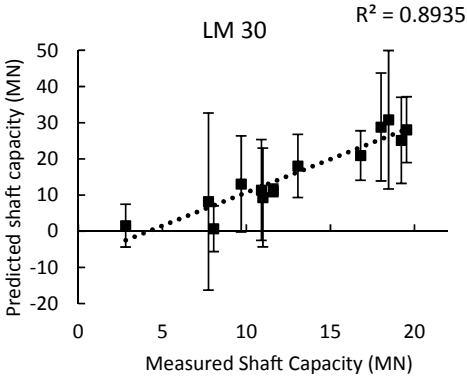

Fig. 24.8 Results of testing of LM 30 model

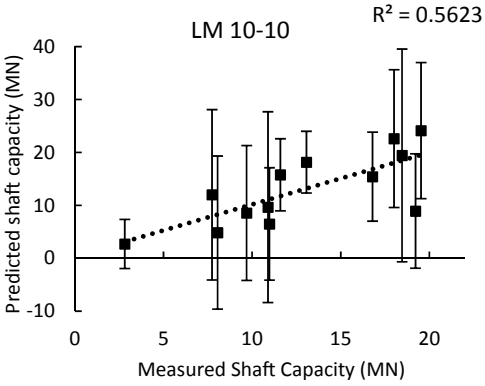

Fig. 24.9 Results of testing of LM 10-10 model

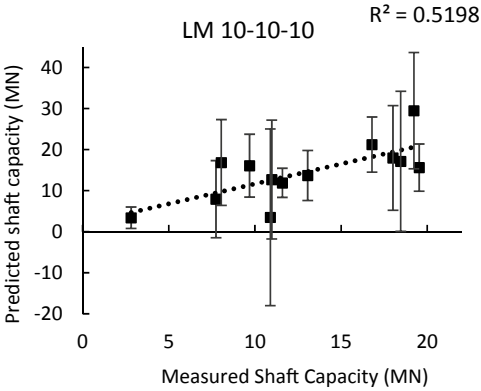

Fig. 24.10 Results of testing of LM 10-10-10 model

The best model using the LM algorithm is LM 30, which has R^2 value of 0.89; the error bars are huge, which states that repeatability is the issue. Increasing the number of hidden layers in the network has deteriorated the performance. Using the BR algorithm, Model 6–10 performed relatively better, as shown in Fig. 24.11 to. BR 30 was the best among all models, with R^2 value of 0.86. The maximum error obtained from all five trials for this model was 2.22 MN which shows good predicting power, and repeatability of the results is ensured. While using the BR algorithm with more hidden layers, the results didn't improve, but the cost of time increased a little. Also, for BR, the error bars on vertical axis reduced drastically compared to the LM algorithm. The average time taken for training the model varies from 4–8 min for BR models and 1–2 min for LM models. Hence, shaft capacity of the pile can be predicted with this BR model with good accuracy and repeatability.

Similarly, 1–10 models were trained for predicting end-bearing values with the end-bearing-related inputs. None of the models were able to predict the results with reasonable accuracy. Only the result of the best of these ten models is shown here in (BR 10-10-10). This leads to the critical realization that the force and velocity signals used in inputs from the time period of impact to the first cycle ($t_p + 2L/c$) contain information about the reflections from the shaft region only. The information about the toe reflection is present in the subsequent time cycles that are not taken into account in this study. Hence in this study, shaft capacity was predicted with

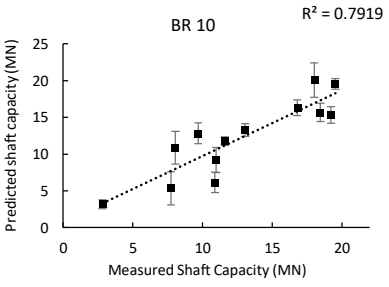

Fig. 24.11 Results of testing of BR 10 model

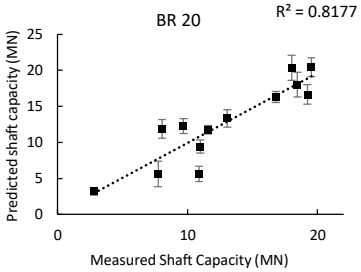

Fig. 24.12 Results of testing of BR 20 model

good accuracy, whereas poor correlations were obtained for end-bearing capacity (Figs. 24.12, 24.13, 24.14, 24.15 and 24.16).

Few more trials have been done where shaft capacity, end-bearing capacity, and the total capacity values were predicted in the single model after providing all the

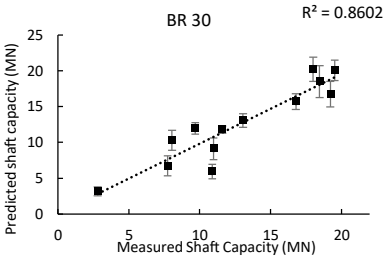

Fig. 24.13 Results of testing of BR 30 model

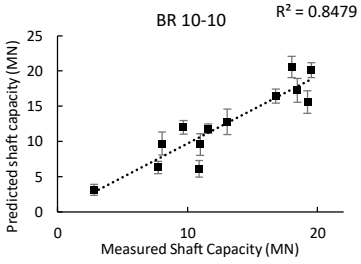

Fig. 24.14 Results of testing of BR 10-10 model

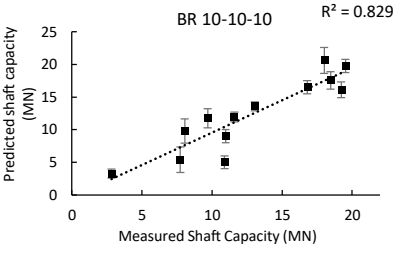

Fig. 24.15 Results of testing of BR 10-10-10 model

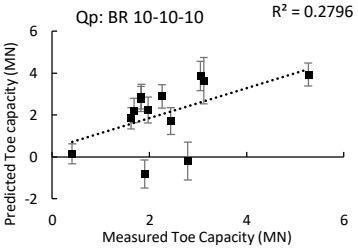

Fig. 24.16 Results of BR 10-10-10 model for predicting Qp

108 inputs. Again, the ten different models, as shown in Table 24.1, are trained five times each. Only the results of the testing phase are presented here. The best results obtained using the LM algorithm were very poor and hence not showed here. The model which performed best while using the BR algorithm is Model 3 (BR 30), as shown in Figs. 24.17, 24.18 and 24.19. This model outperforms all other models with R^2 value of 0.91 for shaft resistance and 0.86 for total capacity prediction. Although the end-bearing prediction is poor, it can predict the shaft resistance and the ultimate capacity quite well.

From literature, it is studied that in most of the problems, only LM algorithm is used. The LM algorithm used for training here was not up to the mark. The reason behind this behavior was analysed with more and more trials, as mentioned above. The results obtained were satisfactory during the training, but a poor correlation was obtained between measured and predicted values during testing a new set of data.

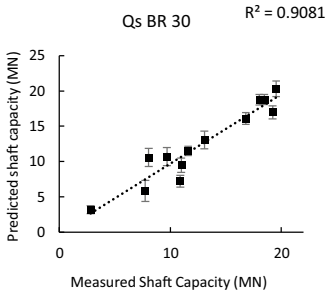

Fig. 24.17 Results of testing of BR 30 model (shaft capacity)

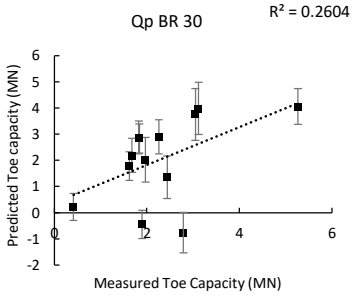

Fig. 24.18 Results of testing of BR 30 model (toe capacity)

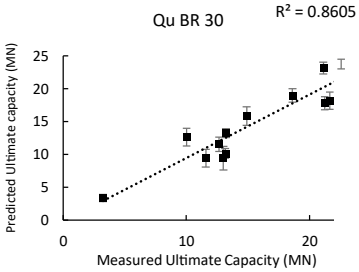

Fig. 24.19 Results of testing of BR 30 model (ultimate capacity)

This is called the overfitting of the problem, where the already seen data is memorized and predicted with high accuracy, but new data is predicted with poor accuracy. The reason behind this is that Levenberg–Marquardt training is more suitable for small and medium-sized networks if there is enough memory available in the system. However, as the number of weights in the network increases, the advantage decreases for the LM. This algorithm has the fastest convergence rate but was unable to capture any pattern in this problem. Hence though it gave results in a short time, the results were highly erroneous.

As seen from the results, the Bayesian regularization (BR) algorithm was able to predict the results quite well during the training and testing phase compared to the LM algorithm. When using BR, it is essential to let the algorithm run until the adequate number of parameters has converged and indicates that the algorithm has truly converged. Bayesian regularization provides better generalization performance than early stopping. This is because it does not require that a validation dataset be separate from the training data set like LM; it uses all the data. BR has an objective function that includes a residual sum of squares and the sum of squared weights to minimize estimation errors and to achieve an excellent generalized model. The details of the BR are beyond the scope of this work, and hence, only the advantages of BR over LM are explained here. Bayesian regularization minimizes a linear combination of squared errors and weights. It also modifies the linear combination so that the resulting network has good generalization qualities [15]. In contrast, LM only performs minimization on the squared errors and accordingly updates the weights.

Conclusion and Discussion

There have been many efforts made in the past to predict the pile capacity in the field, but none has been proved versatile enough when it comes to actual pile capacity assessment. This study covers the typical offshore environment where long steel pipe piles are used for the foundation. Several models have been developed using the artificial neural network, which uses dynamic stress wave data collected from the field while driving the pile. The data used here for training the model consists of 63 high strain dynamic pile load tests performed using PDA and CAPWAP, and the cone

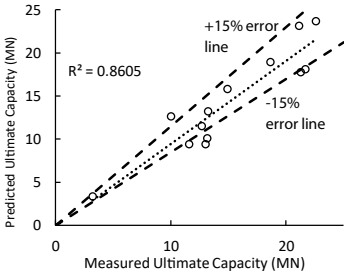

Fig. 24.20 Results of prediction for ultimate pile capacity

penetration tests are done to assess soil characteristics. The dynamic stress wave data and other properties of pile and soil have never been studied together before using artificial intelligent methods.

Hence, by incorporating both of these in this study, the results obtained are more rational and accurate. This work clearly takes advantage of the fact that there is a definite relationship between pile capacity and soil properties, pile properties, and the dynamic measurements obtained during the pile driving. Since this relationship is very complex to understand and define, the neural network is the best tool to evaluate the pile capacity. The BR 30 model predicted the shaft resistance and the total ultimate pile capacity with the highest accuracy based on selecting input parameters. Figure 24.20 shows that most of the predicted values were inside the range of 15% error.

This model can be used to predict pile capacity for such piles along with actual CAPWAP to get confidence on pile capacity obtained from CAPWAP. CAPWAP does not produce a unique result, and this analysis depends on many other factors and the personal experience of the user. It can be concluded that when an extensive network is to be trained, the BR algorithm works best in predicting results for new data as compared to the LM algorithm, which has been traditionally used for optimization in ANN.

References

1. Andrew NG (2018) Machine learning. Coursera, Stanford. https://www.coursera.org/learn/machine-learning/
2. ASTM (American Society for Testing and Materials)-D4945–17 (2017) Standard test method for high-strain dynamic testing of deep foundations. ASTM International, West Conshohocken, PA. https://doi.org/10.1520/D4945-17
3. Bailey DL, Thompson D (1990) Developing neural-network applications. J AI Expert 5(9):34–41
4. Baziar MH, Kashkooli A, Alireza (2012) Prediction of pile shaft resistance using cone penetration tests (CPTs). Comp Geotech 45:74–82
5. Das SK, Samui P, Sabat AK, Sitharam TG (2010) Prediction of swelling pressure of soil using artificial intelligence techniques. Environ Earth Sci 61:393–403
6. Fatehnia M, Amirinia G (2018) A review of genetic programming and artificial neural network applications in pile foundations. Int J Geo-Eng 9(1):2

7. Goh ATC, Goh SH (2007) Support vector machines: their use in geotechnical engineering as illustrated using seismic liquefaction data. Comp Geotech 34:410–421
8. Hornik K, Stinchcomebe M, White H (1989) Multilayer feed-forward networks are universal approximators. Neural Netw 2(3):356–366
9. Khuntia S (2014) Modelling of geotechnical problems using soft computing. M. Tech project in civil engineering, NIT Roorkee, India
10. Kordjazi A, Pooya N, Jaska MB (2013) Prediction of ultimate axial load-carrying capacity of piles using a support vector machine based on CPT data. Comp Geotech 55:91–102
11. Lee IM, Lee JH (1996) Prediction of pile bearing capacity using artificial neural networks. Comp Geotech 18:189–200
12. Liang R, Nawari NO (2000) Simplified neural network models for estimating soil resistance using dynamic pile test. In: Proceedings of the 6th international conference on the application of stress wave theory to piles. Sao Paulo, Brazil
13. Likins G, Rausche F, Goble GG (2000) High strain dynamic pile testing, equipment and practice. In: Proceedings of the 6th international conference on the application of stress wave theory to piles. Sao Paulo, Brazil
14. Lok MH, Che WF (2004) Axial capacity prediction for driven piles using ANN: model comparison. In: Geotechnical engineering for transportation projects. GSP 126
15. MacKay DJC (1992) Bayesian interpolation. Neural Comput 4(3):415–447
16. Maizir H, Kassim KA (2013) Neural network application in prediction of axial bearing capacity of driven piles. In: Proceedings of the international multi conference of engineers and computer scientists, IMECS, vol I. Hong Kong
17. Momeni E, Nazir R, Armaghani DJ, Maizir H (2015) Application of artificial neural network for predicting shaft and tip resistances of concrete piles. Earth Sci Res J 19(1):85–93. GEOTECHNICS
18. Pal M, Deswal S (2008) Modeling pile capacity using support vector machines and generalized regression neural network. J Geotech Geo-Environ Eng ASCE 134(7):1021–1024
19. Park HI, Cho CW (2010) Neural network model for predicting the resistance of driven piles. Mar Georesour Geotechnol 28(4)
20. PDA & CAPWAP Manual (2006) Pile Dynamics Inc. Cleveland Ohio, USA
21. Pooya NF, Jaksa MB, Kakhi M, McCabe BA (2009) Prediction of pile settlement using artificial neural networks based on standard penetration test data. Comp Geotech 36:1125–1133
22. Rausche F, Goble GG, Likins GE Jr (1985) Dynamic determination of pile capacity. J Geotech Eng 111(3):367–383
23. Robertson K, Cabal KL (2012) Guide to cone penetration testing for geotechnical engineering, 5th edn. Gregg Drilling & Testing, Inc.
24. Samui P (2008) Prediction of friction capacity of driven piles in clay using the support vector machine. Can Geotech J 45:288–295
25. Shahin MA (2010) Intelligent computing for modeling axial capacity of pile foundations. Can Geotech J 47(2):230–243
26. Shahin MA, Maier HR, Jaksa MB (2002) Predicting settlements of shallow foundations using artificial neural networks. J Geotech Geo-Environ Eng ASCE 128(9):785–93
27. Smith EAL (1960) Pile driving analysis with the wave equation. J Soil Mech Found Eng Div ASCE 86:35–61
28. Teh CI, Wong KS, Goh ATC, Jaritngam S (1997) Prediction of pile capacity using neural networks. J Comput Civ Eng 11(2):129–138. London 1–8
29. Yeh IC (1998) Modeling of strength of high-performance concrete using artificial neural networks. Cem Concr Res 28(12). USA

Chapter 25
Sinkholes: Trigger, Development, and Subsidence—A Review

Margi Dave and Ashish Juneja

List of Symbols

D_o	Diameter of defect in pipe
D	Diameter of cavity
H_c	Thickness of overburden soil
M_o	Mass flowrate of solids
N	Scale factor
Q_s	Volumetric flowrate of solids
Q_w	Volumetric flowrate of water
d_p	Average particle size
g	Acceleration due to gravity
ρ_b	Bulk density of granular packing
ρ_s	Density of a single grain
β	Angle of failure plane
ε	Porosity
φ	Internal friction angle
v_t	Terminal velocity of the individual grain in water
C, k	Dimensionless constants
c	Cohesion
γ	Unit weight of soil

M. Dave (✉) · A. Juneja
Department of Civil Engineering, Indian Institute of Technology, Bombay, India
e-mail: margidave007@gmail.com

K. Muthukkumaran (eds.), *Soil Behavior and Characterization of Geomaterials*,
Lecture Notes in Civil Engineering 296, https://doi.org/10.1007/978-981-19-6513-5_25

Introduction

Sinkholes are natural or anthropogenic localized ground collapse. The term "sinkhole" was originated to define the ground failure in karst terrains having underground cavities due to the presence of carbonate rocks such as limestone, dolomite, and gypsum which are soluble under certain conditions. In such terrains, a sinkhole is formed by two processes; dissolution followed by suffosion. Dissolution occurs as a result of the chemical reaction of carbonate rocks with weakly acidic water. This happens when ground or rainwater reacts with carbon dioxide to form carbonic acid which dissolves these rocks and creates cracks, fissures, and cavities. After this, the overburden soil collapses into the cavities to form a sinkhole.

Other than karst the reason behind underground void can be activities like mining, tunnelling, or even pipeline failure. Among these, buried pipelines are found as a potential source of frequent sinkholes in India. Rapid urbanization has increased the usage of underground conduits and so the subsequent risk. Pipelines become an active source of void when they get damaged. The failure of pipelines can be due to multiple reasons which may include poor workmanship, external or internal forces, ageing, sedimentation, or corrosion. Breakage in sewer pipes erodes the surrounding soil causing loss of soil-volume from embedment or backfill through the defect and in turn creates a sinkhole.

The paper discusses these two scenarios in detail. Both the cases are leading to the similar ultimate failure but they are characterized by different aspects. The study on the karstic ground defines the large-scale problem, where underground cavities are generally large enough to cause the bulk collapse of overburden soil. On the other hand, pipeline-induced sinkholes occur on account of internal erosion where the extent of damage and embedment soil properties play an important role. Figure 25.1 highlights the distinctive features of both the causes.

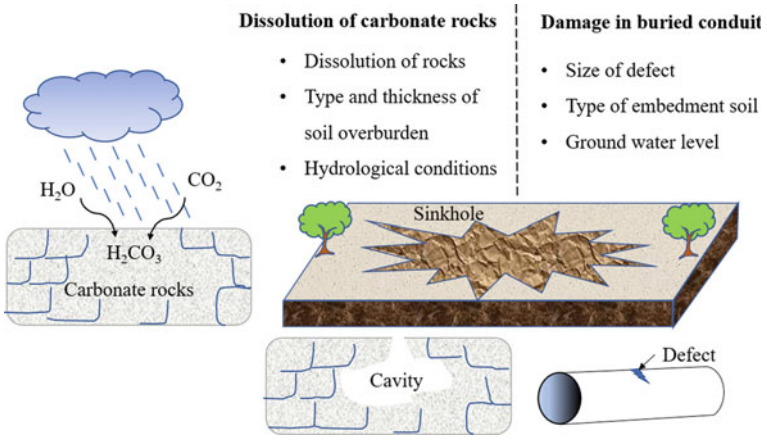

Fig. 25.1 Factors responsible for sinkhole in karstic as well as non-karstic grounds

Mechanism of Sinkhole Formation and Associated Factors

Sinkholes in Karstic Ground

The process triggers as soon as weathering of rock starts to form cavities. Weathering can be due to hydrological factors or human intervention. The reduction in groundwater level, either due to extraction or drought, is one main reason behind weathering. The groundwater remains less acidic in fully saturated condition. But when its level decreases, it allows air entry and accelerates the process of dissolution.

Based on the observation of past incidents, sinkholes are categorized into three; dissolution sinkhole, cover subsidence sinkhole, and cover collapse sinkholes [12] (see Fig. 25.2). Dissolution sinkholes occur where the carbonate bedrock is visible on the ground surface, weathering of which causes a pond-like depression. This kind of collapse has minimal threat due to its ground visibility. Cover subsidence sinkholes are similar to dissolution sinkholes, but in this case, the karst bed is covered with a thin layer of soil, suffosion of which creates a ground depression. When carbonate rocks are present at greater depth, cover collapse sinkhole occurs. In this case, soil migration into the void forms a secondary cavity in the overburden. As the process continues, the secondary cavity enlarges and ultimately collapses.

To study the effect of soil overburden above the cavity, Abdulla and Goodings [1] conducted centrifuge model tests to observe the failure patterns for different H_c/D conditions (see Fig. 25.3a–c). When $H_c/D < 0.25$, the failure plane is nonlinear with an average sloping angle of 61° with horizontal. When $H_c/D = 0.25$, the curved failure plane slightly overhangs at the top. For $H_c/D > 0.31$, the failure plane does not reach the top and forms a stable underground arch. This implies the increase in curvature of the failure surface with an increase in H_c/D. No clear evidence was found between the angle of the failure plane (β) and H_c/D. This observation can be generalized by defining a stability number as $N\Upsilon H_c/c$, which can predict the

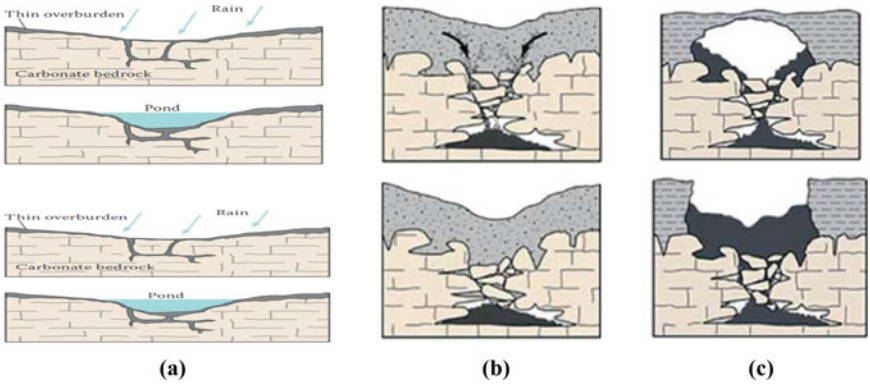

Fig. 25.2 Types of sinkhole **a** Dissolution sinkhole **b** Cover subsidence sinkhole **c** Cover collapse sinkhole (after Nel and Haarhoff [9])

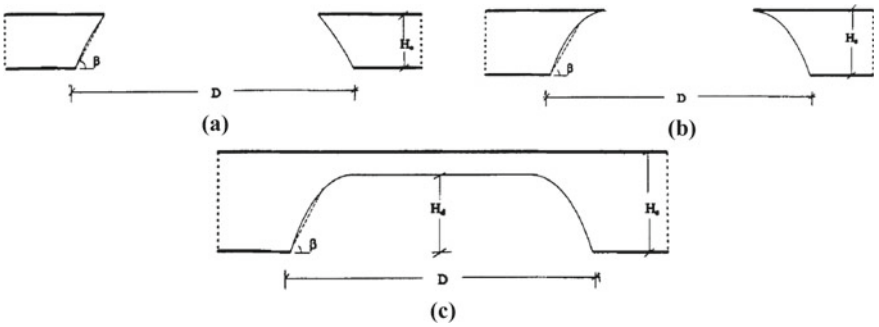

Fig. 25.3 Failure of sinkhole **a** $H_c/D < 0.25$ **b** $H_c/D = 0.25$ **c** $H_c/D > 0.31$ (after Abdulla and Goodings [1])

behaviour for different soils and at different scale of models. For $H_c/D <= 0.25$, the failure type is breakthrough plug and hence the stability is governed by H_c. Hence within this range of H_c/D, either increase in H_c (for fixed D) or a decrease in D (for fixed H_c) increases the value of the stability number. For $H_c/D > 0.31$, the failure geometry is no longer a function of H_c but is governed by D. The behaviour for the H_c/D ranging between 0.25 and 0.31 is unclear because of lack of model tests for this range [1].

The geometry of the sinkholes is characterized using volume ratio index (VRI), which is the ratio of the actual volume of the sinkhole to the volume of an elliptical cone having the same major radii, minor radii and depth as the sinkhole that has formed [7]. The value of VRI is 1 for cone shaped sinkhole, 2 for hemiellipsoid, and 3 for cylindrical sinkhole.

Sinkhole Due to Damaged Conduit

Damaged pipe creates sinkhole when the defect allows significant loss of soil mass through it. Not all damaged pipes lead to soil erosion since the ratio of the defect size, and the particle size is the governing factor. This phenomenon is analogous to the flow of grains through a hopper. Beverloo et al. [4] proposed an empirical equation for the flow of dry non-cohesive grains through a hopper with a circular orifice as

$$\mathrm{M_o} = C\rho_\mathrm{b} g^{0.5}\left(\mathrm{D_o} - \mathrm{kd_p}\right)^{2.5} \tag{25.1}$$

When high water table is present in the ground, the soil flow is seepage driven and is faster compared to dry flow. From the equation of Beverloo et al. [4], Wilson et al. [13] obtained an equation for wet granular flow as

$$\mathrm{M_o} = C\rho_\mathrm{s} v_\mathrm{t}\left(\mathrm{D_o} - \mathrm{kd_p}\right)^2 \tag{25.2}$$

If the ratio of defect size to particle size is small, then particles arch and jam around the defect. Equations 25.1 and 25.2 suggest that this critical ratio, k should be equal to D_o/d_p, below which no mass flow occurs. Thus, soil erosion initiates when k exceeds its critical value. It typically varies between 2 and 3.1 [5, 11, 13] and defines the periphery of "empty annulus". Guo et al. [5] and Tang et al. [11] analysed the mechanism of seepage driven sinkhole formation in granular soil through a small-scale physical model. Figure 25.4 shows the void development in uniformly graded granular soil. Upon the initiation of the defect in the pipe wall, its surrounding soil particles start to escape into the pipe along with water. Soon after the onset of erosion, the soil particles within the narrow slot above the defect, move towards the defect with the same velocity. This narrow slot behaves like a block and, is called as the mobilized zone. The velocity at which this mobilized zone moves depends upon particle size. Fine or coarse particles can reduce the velocity due to the reduction in the permeability and arching effect respectively. As the erosion progresses, the soil particles within the mobilized zone continue to wash out, and this volume is replaced by its eroded zone, which is shown as stage 2 of Fig. 25.4. It results in an increase in the width and, decrease in the height and the velocity of the mobilized zone. The zone of slip surfaces which is inclined at angle α separates the mobilized zone from the eroded zone. Within this zone, the particles slide and reach the mobilized zone. Angle α and the thickness of the slip surface decrease as the area occupied by the eroded zone increases. At the end of the erosion process, the angle of slip surfaces equals the ultimate friction angle of the soil [5, 8, 10, 11]. The final shear surface formed may not be smooth, as the downward drag of pore water imposes additional shear stress on soil particles to create a zigzag pattern [11].

The water head affects the dimension of the cavity, while particle size and defect size have little influence [5, 11]. The higher the initial water head, the larger is the cavity diameter (D). The equation to determine this diameter is [5]

$$D = \left[\left\{6(1+n).d^2.h_w\right\} \Big/ \left\{\tan\varphi + (1+n).(1-\varepsilon).\tan\varphi\right\}\right]^{1/3} \tag{25.3}$$

where n is equal to Q_s/Q_w and d is diameter of cylindrical test box because Eq. 25.3 was developed analytically using free fall arch theory [6]. Hence, this equation cannot directly be applied in determining field diameter of cavity.

The erosion mechanism is different for gap-graded soil, in which the downward seepage first mobilizes the finer particles available near the defect. When the fines are washed off, the coarse particles arch to form a stable structure around the defect, beyond which the movement of remaining fine particles occur within the matrix of the coarse particles. Erosion ceases in this self-healing mechanism. Therefore, the emphasis should be on making a wise choice for selecting the embedment fill.

Rate of erosion Guo et al. [5] experimentally deduced that the hydraulic gradient had little influence on the flowrate of the sand passing through the defect. This could be because of the small range of the applied water head in their tests. On the other hand, Zhang et al. [14] and Tang et al. [11] detected an increase in soil and water flowrate with the increase in the water head. Both the soil and water flowrate is

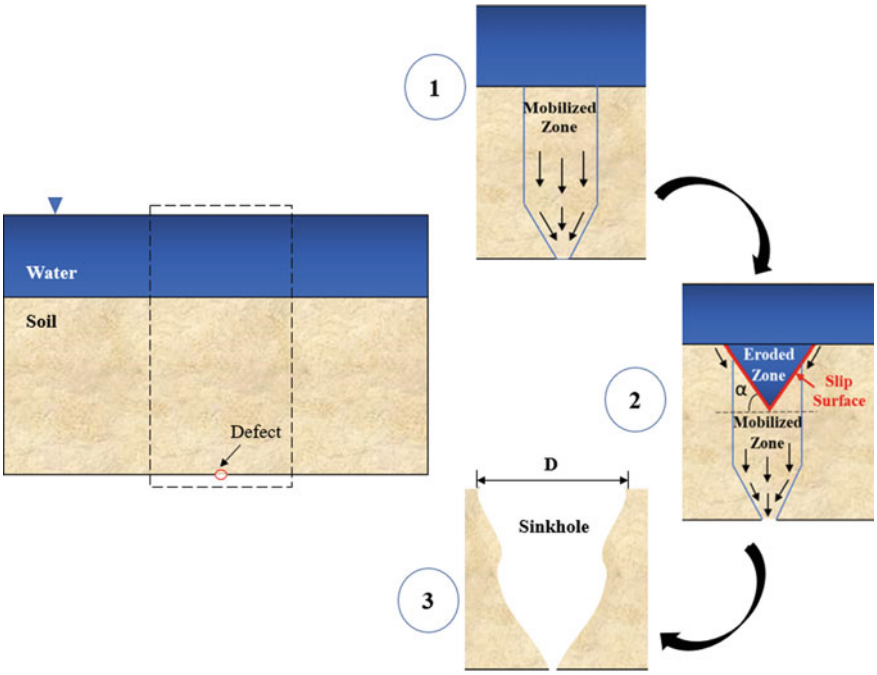

Fig. 25.4 Sinkhole formation in granular soil due to pipe defect (modified from Tang et al. [11])

linearly related and can be expressed as an empirical equation

$$Q_s / Q_w = 0.18 \ln\left(D_o / d_p\right) \tag{25.4}$$

Equation 25.4 is for soil with uniform gradation and is valid for D/d_p within 3.1–53.6. Zhang et al. [14] specially highlighted the significance of the hydraulic head in gap-graded soils because of the influence of water flow on the fine particles, which caused change in the soil skeleton.

Sinkhole Detection

The early detection of potential cavities can only prevent the sinkhole hazard. Ground penetrating radar (GPR) is a tool for non-destructive subsurface imagining, which can be used to detect underground cavities. However, it is difficult to obtain signals from deep cavities with GPR. The technique of photogrammetric analysis is another efficient method to detect sinkholes. Through remote sensing, Al-Halbouni et al. [2] were able to detect subsurface cracks and surface depression in sandy-gravel alluvium terrain before the collapse.

The sinkhole location can also be related to progressive groundwater level drops and its rate of formation can be related to the amplitude of these drops [3]. The cone of depression of groundwater occurs before any sign of surface sinkholes and this, in turn, can be used to predict the failure.

Conclusion

Sinkhole hazards significantly influence the economy and lives of a region. The research in this area is still at the developing stage because of numerous uncertainties associated with the phenomenon. In the case of karstic strata, groundwater chemistry decides the location of a sinkhole, while the size, thickness, and properties of overburden soil decide the geometry of failure. The increase in the ratio of overburden thickness to cavity diameter leads to dome type failure having a stable arch.

In the case of defective pipe, the occurrence of sinkhole depends on the extent of damage and the embedment soil material. The ratio of defect size and particle size are the primary factors responsible for erosion initiation. Along with them, the hydraulic gradient controls the rate of soil erosion. The seepage-induced wet granular flowrate is higher than dry granular flow. A high hydraulic gradient causes more soil loss. The position of the water level in the ground decides the location and geometry of the cavity. The radial extent of erosion increases with an increase in water head. The complete theorization of pipeline-induced sinkholes is not revealed yet, therefore the study of cavity in field is still a challenge. Additionally, the time-dependent growth of cavity is still to be explored.

References

1. Abdulla WA, Goodings DJ (1996) Modeling of sinkholes in weakly cemented sand. J Geotech Eng 122(12):998–1005
2. Al-Halbouni D, Holohan EP, Taheri A, Schöpfer MP, Emam S, Dahm T (2018) Geomechanical modelling of sinkhole development using distinct elements: model verification for a single void space and application to the Dead Sea area. Solid Earth 9(6):1341–1373
3. Alrowaimi M, Chopra M, Yun HB, Mokhtari S (2019) Experimental study of sinkhole failure related to groundwater level drops. J Test Eval 48(6):4402–4415
4. Beverloo WA, Leniger HA, Van de Velde J (1961) The flow of granular solids through orifices. Chem Eng Sci 15(3–4):260–269
5. Guo S, Shao Y, Zhang T, Zhu DZ, Zhang Y (2013) Physical modeling on sand erosion around defective sewer pipes under the influence of groundwater. J Hydraul Eng 139(12):1247–1257
6. Hilton JE, Cleary PW (2011) Granular flow during hopper discharge. Phys Rev E 84(1):011307. https://doi.org/110.1103/PhysRevE.84.011307
7. Hyatt JA, Jacobs PM (1996) Distribution and morphology of sinkholes triggered by flooding following tropical storm Alberto at Albany, Georgia, USA. Geomorphology 17:305–316
8. Lai JS, Shen HW (1996) Flushing sediment through reservoirs. J Hydraul Res 34(2):237–255

9. Nel DT, Haarhoff J (2011) The failure probability of welded steel pipelines in dolomitic areas. J S Afr Inst Civ Eng 53(1):9–21
10. Scheuerlein H, Tritthart M, Nunez-Gonzalez F (2004) Numerical and physical modeling concerning the removal of sediment deposits from reservoirs. In: Proceedings of the conference on hydraulic of dams and river structures. Taylor & Francis Group, London, pp 245–254
11. Tang Y, Zhu DZ, Chan DH (2017) Experimental study on submerged sand erosion through a slot on a defective pipe. J Hydraul Eng 143(9):04017026
12. Waltham T, Waltham AC, Bell FG, Culshaw MG (2005) Sinkholes and subsidence: karst and cavernous rocks in engineering and construction. Springer Science & Business Media
13. Wilson TJ, Pfeifer CR, Meysingier N, Durian DJ (2014) Granular discharge rate for submerged hoppers. Pap Phys 6:060009
14. Zhang DM, Du WW, Peng MZ, Feng SJ, Li ZL (2020) Experimental and numerical study of internal erosion around submerged defective pipe. Tunn Undergr Space Technol 97:103256

Chapter 26
Parametric Studies on Skirted Foundation Resting on Sandy Soil

Ongchuk Namgyal Lepcha, Plaban Deb, and Sujit Kumar Pal

Introduction

Foundations are the part of the structure which transfers the load of the structure to the earth. Based on the load quantity, structural requirement and soil quality foundation can be either shallow or deep foundations. The former type of foundation is usually provided to a structure imposed to a small load or when the bearing capacity of the soil is high enough to sustain the load coming from the structure, whereas deep foundations are provided when the soil below the foundation is soft and the water table is high. In some geotechnical problems, a shallow foundation may not be suitable and a deep foundation may become too conservative, in such cases semi-deep foundation such as an embedded block foundation, pier, and skirted foundation can be provided.

A skirted foundation is a surface or a shallow foundation in which a thin vertical steel plate is attached around the periphery of the foundation. This arrangement restricts the lateral movement of the soil below the foundation during shear deformation and transfers the load to a deeper level (skirt tip level). The bearing capacity of the skirted foundation can be assumed to have two components similar to monopile, that is (i) end bearing at skirt tip (V_b) and (ii) friction between soil and the skirt (V_s), as shown in Fig. 26.1.

Various numerical and physical model investigations have been performed for an axially loaded skirted foundation in the past to understand the behaviour of skirted foundation [1–12], and some of the previous studies are summarized in Table 26.1. In the comparison between the skirted foundation and the embedded block or pier foundation of the same depth, it is found that the skirted foundation provides bearing capacity and settlement value equivalent to that of the embedded foundation [6, 10].

O. N. Lepcha (✉) · S. K. Pal
Department of Civil Engineering, National Institute of Technology, Agartala 799046, India
e-mail: ongchukl@gmail.com

P. Deb
Department of Civil Engineering, Chandigarh University, Mohali 140413, India

K. Muthukkumaran (eds.), *Soil Behavior and Characterization of Geomaterials*,
Lecture Notes in Civil Engineering 296, https://doi.org/10.1007/978-981-19-6513-5_26

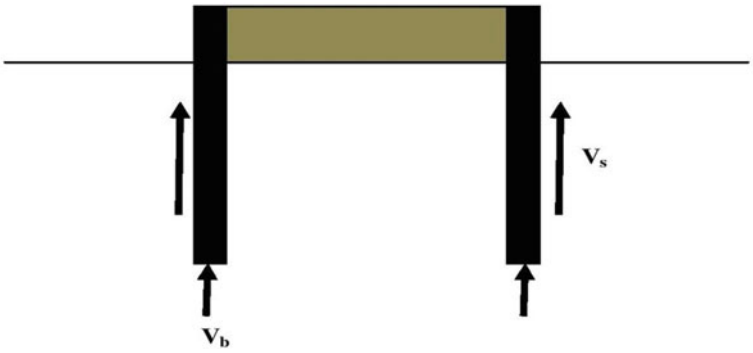

Fig. 26.1 Bearing capacity components of the skirted foundation

Table 26.1 Summary of literature review

References	Skirt parameter	Approaches
[1]	Dia (D) = 75, 100, and 150 mm L = 0, 100, and 150 mm	Experimental
[2]	δ_s = 28, 32, 35, and 38° L/D = 0.05, 0.25, 0.5, 0.7, 1.0, 1.25	Experimental
[3]	D = 50, 75, 100 mm L/D = 0, 0.5, 1, 1.5, and 2.0	Experimental
[4]	D = 20, 30, and 40 mm	Experimental
[5]	L/B = 0,1, 1.5, 2, and 2.5	Experimental
[6]	B = 1.5, 2.0, 2.5 m L/B = 0, 0.5, 1.0, 1.5, and 2.0 Pier foundation	Experimental Numerical
[7]	L/B = 0, 0.5, 1, and 1.5	Experimental
[8]	L/B = 0, 0.5, 1, and 1.5	Experimental
[9]	e/B = 0.05, 0.15, 0.25, and 0.35 θ_L = 10, 20, 30°, Skirt angle (θ_s) = 10, 20, 30, 45°	Experimental and numerical (PLAXIS)
[10]	Embedded foundation L/B = 0.2, 0.3, 0.5, 0.75, 1, and 1.2 Additional internal skirts	Numerical (ABAQUS)
[11]	(δ_s) = 15, 27, 35, 37° Thickness (t_s) = 0.25, 0.75, 1.5, 2.3, 3.125, 6 mm	Experimental
[12]	L/D = 0.1, 0.2, 0.3, 0.4, and 0.5	Numerical (AFENA)

This is because the soil inside the skirts behaves like an integrated part of the foundation thus behaving like a rigid foundation. This suggests that skirted foundation can be used to replace embedded block or pier foundation hence reducing the material cost. The presence of an internal skirt has the potential to further increase the bearing capacity and reduce the foundation settlement; however, insufficient skirts or spacing may result in a reduction in the total capacity of the foundation [13]. Numerical investigation performed on a skirted foundation in the presence of an additional internal skirt shows a slight decrease in bearing capacity as compared to externally skirted only [10]. When the skirts are provided in an inclination, the vertical bearing capacity of the strip foundation is found to increase and settlement reduces as the inclination or skirt angle increases. This is because, when the skirts are provided in angle, it virtually increases the area of the foundation as compared to the vertically skirted foundation [9, 14].

Finite Element Analysis

Extensive three-dimensional modelling using finite element software (ABAQUS) of vertically loaded square skirted foundation resting on the sand was performed to find the effect of the skirt length, internal skirt, and skirt angle on bearing capacity and settlement.

Material Properties

The soil property is taken from the experimental and numerical study conducted by Eid [6]. Purely frictional soil with an internal angle of friction equal to 35° was considered. Soil material is modelled as elastoplastic material using Mohr Coulomb plasticity theory and non-dilatants flow rule (i.e. angle of dilatancy = 0). Although the soil is non-dilatant and purely frictional, a small value of cohesion and dilatancy was provided as default in the software without much affecting the results.

The square foundation with a size equal to 2.5 m is taken for the analysis, the steel skirt of thickness 50 mm with different heights was rigidly attached around the circumference of the surface foundation, and additional internal skirts of length equal to external skirts were also taken for the analysis ($L/B = 0$, 0.5, 1.0, and 1.5). The skirt has a length equal to 2.5 m which was inclined at an angle of 0, 15, 20, and 25 with a vertical axis. The foundation and steel are modelled as a linearly elastic material. The material properties and foundation parameters are summarized in Table 26.2 and shown in Fig. 26.2.

Table 26.2 Properties of the material used

Parameters	Steel skirt	Surface foundation	Soil
Stress–strain hardening	Linear elastic	Linear elastic	Mohr Coulomb plasticity
Unit weight (kN/m^3)	78	22	16
Poison's ratio	0.2	0.2	0.3
Young's modulus (kN/m^2)	2×10^8	2×10^7	2×10^4
Dilation angle	–	–	0.1
Internal friction angle	–	–	35
Cohesion (kN/m^2)	–	–	1

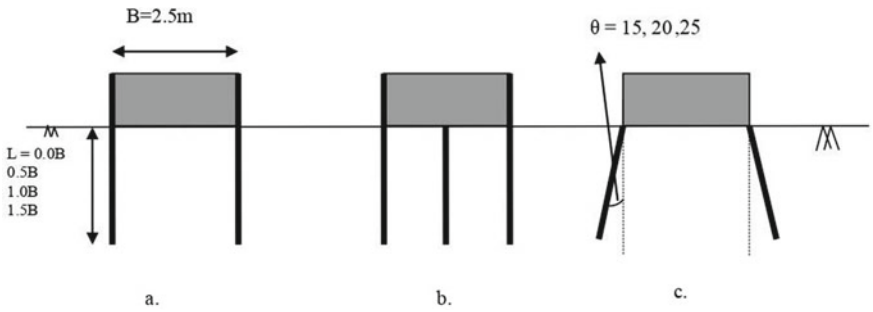

Fig. 26.2 Schematic diagram of **a** externally skirted, **b** internally skirted, and **c** skirt in angle

FEM Modelling and Meshing

The boundary of a soil geometry is located at a horizontal distance equal to 5*B* (*B* = width of foundation) from the footing edge and 5*B* vertically below the skirt tip level. This dimension is found sufficient to minimize the boundary effect [6]. The soil continuum is partitioned and locally seeded such that finer mesh is applied around the loaded area and coarser mesh away from the loaded region. This method can reduce the computational time without much affecting the accuracy of the results [15, 16]. The entire model is meshed and seeded using linear brick hex elements with reduced integration and hourglass control (C3D8R). Reduced integration when compared with full integration gives close results; thus, reduced integration is used for the analysis to save the analysis time. The skirted part of the foundation is embedded into the host region (soil) using embedded constraint, which generally ties the node of two parts. The meshing technique adopted for externally skirted foundation, internally skirted with $L/B = 1.0$, and skirt angle of 15° is shown in Fig. 26.3. The same meshing technique is applied for the entire remaining model.

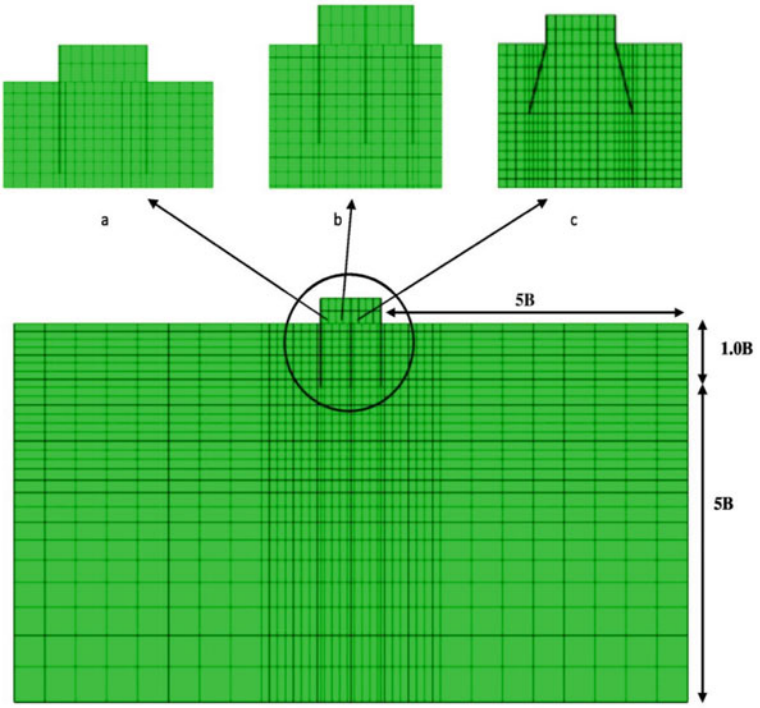

Fig. 26.3 Meshing for **a** externally skirted, **b** internally skirted, and **c** skirt in angle ($\theta = 15°$)

Boundary and Loading Conditions

The vertical sides of the soil are restraint for lateral movement (U1 = U2 = 0), and no rotational and translational movements are allowed at the bottom of the soil (ENCASTRE). Geostatic field stress was applied in the soil model as initial field stress. The analysis is divided into two static general steps. In the first step, soil gravity is applied and load is added in a later stage. The investigation consists of two kinds of study that is bearing capacity and settlement study. For the bearing capacity study, the displacement control loading method was implied in which the foundation is displaced in a vertically downward direction. The displacement control method was found to provide a better and more accurate result as compared to the load controlled method [10]. For settlement analysis, pressure load equal to 0.5 times the failure load corresponding to surface foundation obtained from bearing capacity analysis was used for all the models.

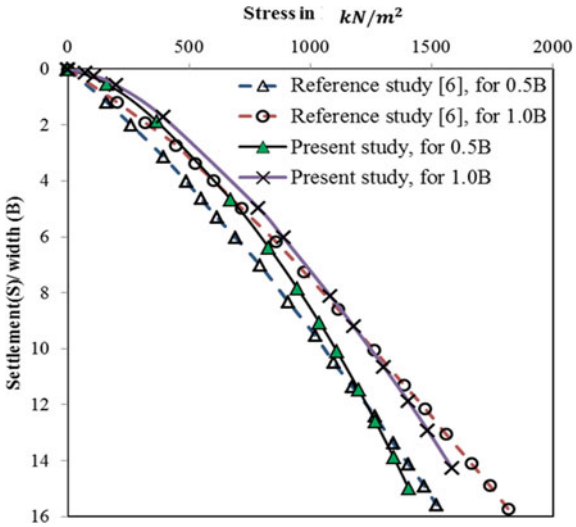

Fig. 26.4 Comparison between the present study with the reference study [6]

Result and Discussion

Validation

Since experimental data are not available, the result of this study is validated by comparing the result of the externally skirted foundation with the numerical result of the reference paper [6]. Figure 26.4 shows the result comparison between the present study with the reference study for an external skirted foundation. The bearing capacity has taken at 10% of the foundation settlement. The curve shows close agreement between the bearing capacities obtained from this study with the reference study. When the same amount of pressure load is applied, it is found that the settlement for the foundation with embedment ratio (*L*/*B*) equal to 1.0 was reduced by 45% and 50% as compared to the surface foundation, respectively, for the reference paper and the method adopted in the present study.

Effect of Skirt Length and Internal Skirts

The steel skirt of different heights is attached around the periphery of the surface foundation to investigate the effect of skirt length. Skirt length-to-foundation width ratio (*L*/*B*) of 0.0 (surface foundation), 0.5, 1.0, and 1.5 has taken in the analysis. An additional number of stiffeners or internal skirts are provided for all the foundations to study their effect on bearing capacity and settlement of the skirted foundation. The result of bearing capacity analysis for both externally skirted and internally skirted foundations is plotted in terms of stress versus settlement percentage curve

as shown in Fig. 26.5. Since there is no distinct breakpoint in the curve, the stress value corresponding to 10% of foundation settlement is considered as the failure load. From the curve, it can be seen that as the skirt length is increasing for both foundation arrangements, the failure load is also increasing. It is found that the bearing capacity of the skirted foundation is increasing by almost 2 times that of the surface foundation when the skirt embedment ratio (*L/B*) provided is equal to 1.0. This increase in bearing capacity is due to the fact that as the skirt length increases, the volume of soil to be mobilized during a failure is increasing and the load is being transferred to a deeper level. However, bearing capacity slightly reduces when an additional internal skirt is provided.

The result of settlement analysis for both the externally and internally skirted foundation is shown in Fig. 26.6. The settlement value observed for the surface foundation ($L/B = 0.0$) is 90 mm which decreases nonlinearly as the skirt length increases. The settlement value for an embedment ratio (*L/B*) equal to 1.5*B* is found to be 36 mm and 34.75 mm for only externally skirted and internally skirted, respectively, which corresponds to approximately 40% of the surface foundation settlement. Therefore, it is concluded that when the internal skirt is provided, the settlement of the skirted foundation and bearing capacity reduces slightly.

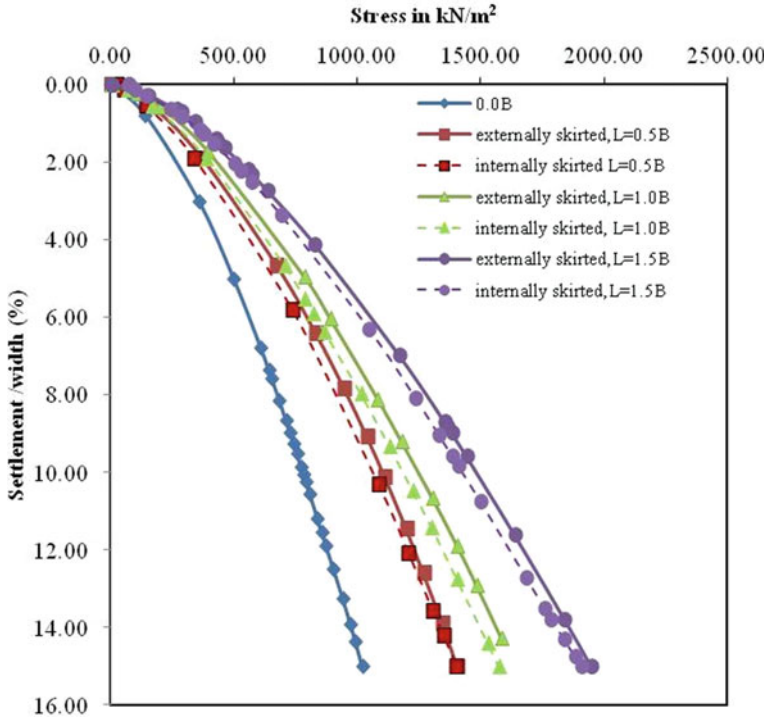

Fig. 26.5 Bearing capacity analysis result for both externally and internally skirted foundations

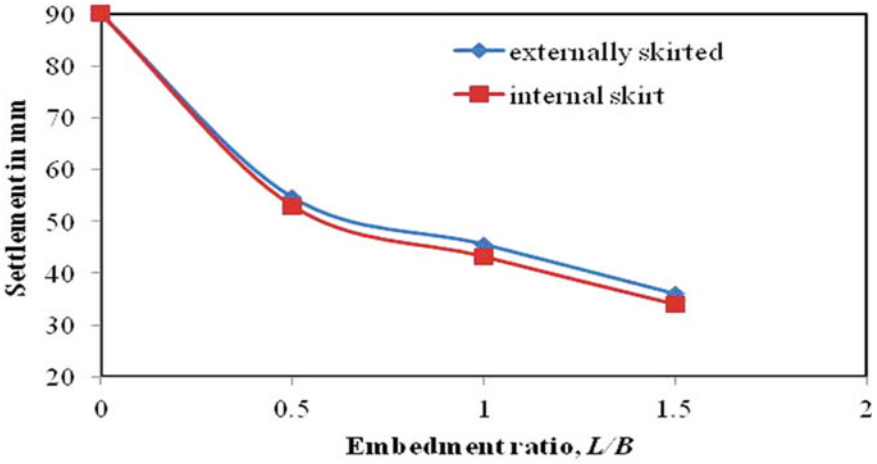

Fig. 26.6 Comparison of externally and internally skirted on settlement

Figures 26.7 and 26.8 show the vertical stress developed along the skirt length at an applied pressure load of 0.5 times the failure load for the surface foundation. From the figure, it can be seen that the maximum vertical compressive stress is developed at the foundation base level and it increases as the skirt length increases. It can be also seen from Fig. 26.7 that the stress in the skirt decreases along with the depth and gives an almost equal value of 3435 kN/m^2 at the skirt tip for all the embedment ratios.

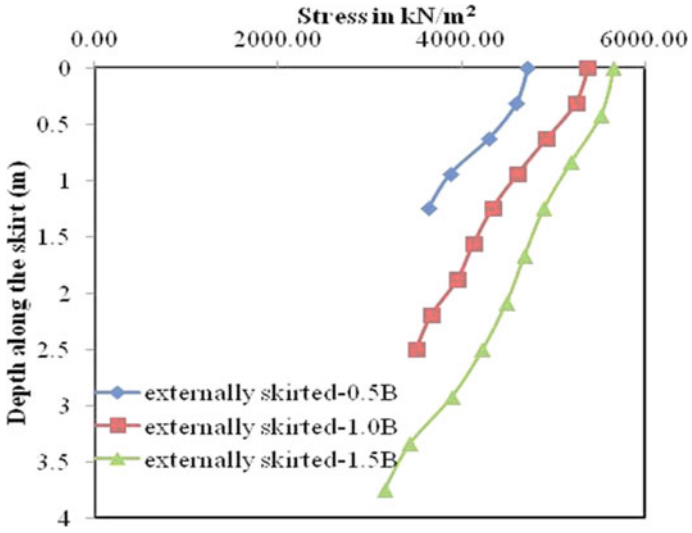

Fig. 26.7 Vertical stress along the skirt length for externally skirted

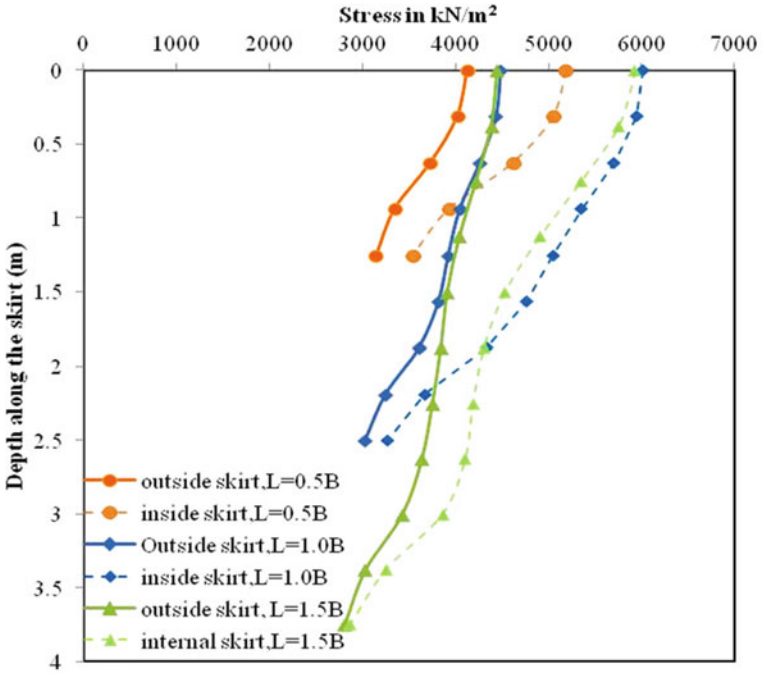

Fig. 26.8 Vertical stress developed in the internal skirt and the external skirt

Figure 26.8 compares the stress developed in the internal skirt and external skirt for the same applied pressure. It can be observed that for every embedment ratio, vertical stress developed in the internal skirt is greater than that of the stress in an external skirt. Similarly, this stress decreases along the skirt length and reaches the almost same value at the tip level for both internal and external skirt of all embedment ratios.

Effects of Skirts Angle

The skirt length equal to 2.5 m is provided at an inclination of 150, 200, and 250 to the surface foundation. Figure 26.9 shows the bearing capacity ratio versus skirt angle. Bearing capacity ratio (BCR) is the ratio of the bearing capacity of a skirt in angle to the bearing capacity of the surface foundation. The skirt angle, θ, equal to 0 corresponds to the vertically skirted foundation. It can be seen that when the skirt angle increases, the bearing capacity also increases. Bearing capacity when skirt angle (θ) is equal to 250 is found to be almost 1.8 times that of the surface foundation. The horizontal projection of the whole footing increases from B, in the case of vertically skirted, to $1.8B$ for the skirt angle, θ, equal to 250. Due to this,

the contact area in between the soil and the skirt increases, therefore increasing the bearing capacity.

The settlement characteristics for different skirt angles are shown in Fig. 26.10. It is observed that a foundation undergoes lesser settlement when skirts are provided in angle. The foundation undergoes lesser settlement as compared to the internally skirted foundation for the same external skirt length ($L = 1.0B$). It is found that settlement is reduced by 50–78% as compared to the surface foundation.

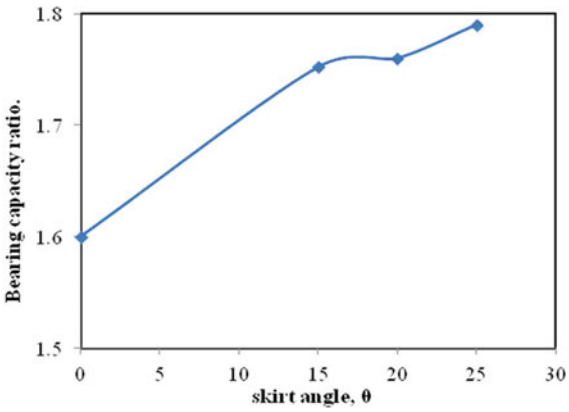

Fig. 26.9 Bearing capacity result for a skirt in angles

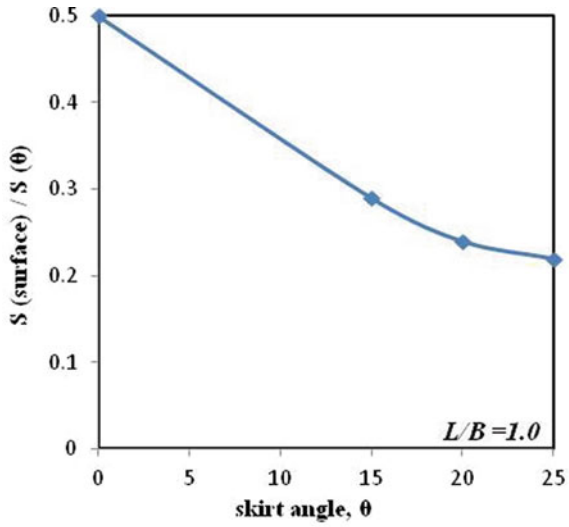

Fig. 26.10 Settlement analysis result of different skirt angle

Contour Diagram

The vertical stress and vertical displacement for externally skirted, internally skirted, and skirt in angle is shown in Fig. 26.11. It can be observed that the maximum stress is developed at the skirt tip level which shows that the skirt is transferring load to a deeper level, therefore increasing the bearing capacity. In the case of an internally skirted foundation, a major percentage of load is taken by the skirts, whereas for an externally skirted and inclined skirted, the load is shared between skirt tip, skirt side friction, and base of the foundation.

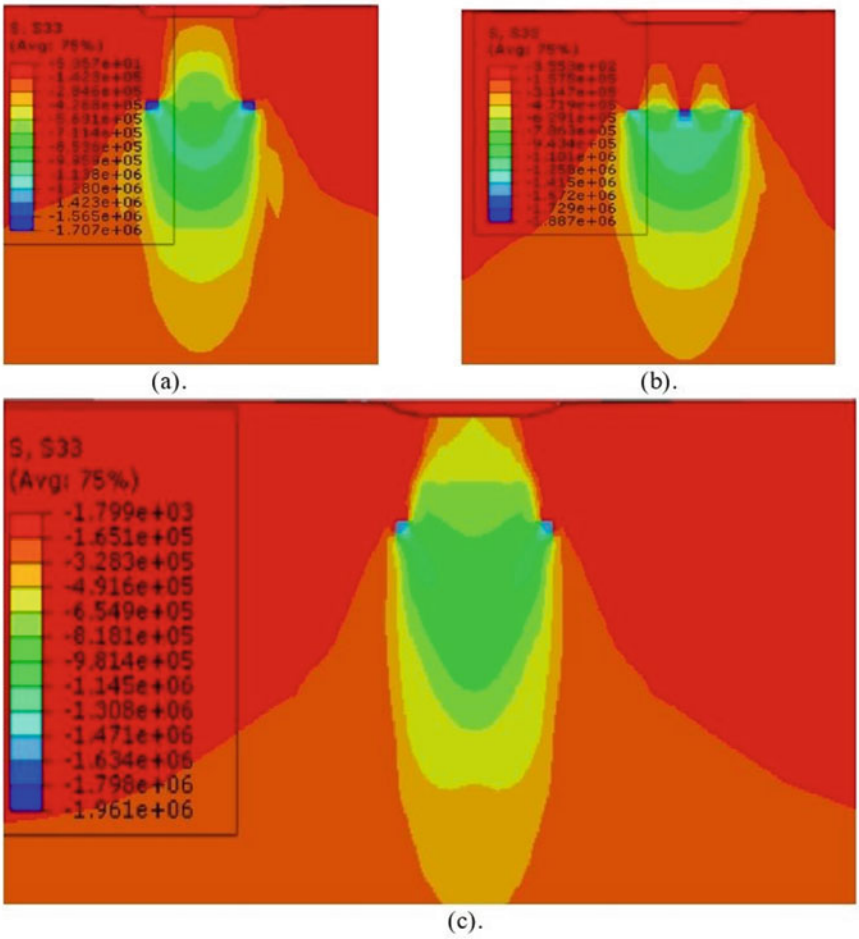

Fig. 26.11 Vertical stress contour for **a** externally skirted, **b** internally skirted, and **c** skirt in angle

Conclusion

Parametric studies are performed on the vertically loaded skirted foundation to study the effect of skirt length, internal skirt, and skirt inclination using finite element software. The following conclusions can be drawn from the numerical analysis.

- Bearing capacity increases and settlement decreases as the skirt length increases. Bearing capacity is increased up to 2 times that of surface foundation, and settlement is reduced by 60% as compared to surface foundation settlement when skirt length is equal to 1.5*B*.
- When an additional internal skirt is provided, both bearing capacity and settlement value of surface foundation reduce slightly.
- Bearing capacity is increased by 1.8 times that of surface foundation, and settlement is reduced by 78% as compared to surface foundation when skirt angle is 25°.

References

1. Listyawan AB, Kusumaningtyas N (2018) Bearing capacity of circular skirted footing on clay soil. MS&E 403(1):012019
2. Al-Aghbari MY, Mohamedzein YEA (2018) The use of skirts to improve the performance of a footing in sand. Int J Geotech Eng 14(2):134–141
3. Sajjad G, Masoud M (2018) Study of the behaviour of skirted shallow foundations resting on sand. Int J Phys Model Geotech 18(3):117–130
4. Barari A, Ibsen LB (2014) Vertical capacity of bucket foundations in undrained soil. J Civ Eng Manage 20(3):360–371
5. Azzam WR, Farouk A (2010) Experimental and numerical studies of sand slopes loaded with skirted strip footing. Electron J Geotech Eng 15(3):795–812
6. Eid HT (2013) Bearing capacity and settlement of skirted shallow foundations on sand. Int J Geomech 13(5):645–652
7. Ebrahimi SG, Rowshanzamir MA (2013) Experimental evaluation of bearing capacity of skirted footings. Civ Eng Architect 1(4):103–108
8. Wakil AZE (2013) Bearing capacity of skirt circular footing on sand. Alexandria Eng J 52(3):359–364
9. Saleh NM, Alsaied AE, Elleboudy AM (2008) Performance of skirted strip footing subjected to eccentrically inclined load. EDGE 13:1–33
10. Yun G, Bransby MF (2007) The undrained vertical bearing capacity of skirted foundations. Soils Found 47(3):493–505
11. Al-Aghbari MY, Mohamedzein YE (2004) Bearing capacity of strip foundations with structural skirts. Geotech Geol Eng 22(1):43
12. Hu Y, Randolph MF, Watson PG (1999) Bearing response of skirted foundation on nonhomogeneous soil. J Geotech Geoenviron Eng 125(11):924–935
13. Mana DS, Gourvenec S, Martin CM (2013) Critical skirt spacing for shallow foundations under general loading. J Geotech Geoenviron Eng 139(9):1554–1566

14. Pusadkar SS, Bhatkar T (2013) Behaviour of raft foundation with inclined skirt using PLAXIS 2D. In: Indian geotechnical conference, vol 3, no 6
15. Deb P, Pal SK (2020) Load-settlement and load sharing behaviour of piled raft foundation resting on layered soils. Acta Geotech Slov 1:71–86
16. Deb P, Pal SK (2021) Structural and geotechnical aspects of piled raft foundation through numerical analysis. Mar Georesour Geotechnol. Published on 28th June 2021. https://doi.org/10.1080/1064119X.2021.1943083

Chapter 27
Development of Foundation Suitability Maps for South Chennai Using GIS

Gowri S. Krishna and V. K. Stalin

Introduction

The recent growth of the construction activities has been accompanied by a need for better construction techniques, land use planning, and management, sustainable development, environmental planning which in turn will ensure efficient and economic outcomes. The successful planning and execution of any construction activity, as well as environmental hazards study and management, depends majorly on the subsoil investigation of the site and the subsequent determination of underlying soil and rock layers and their respective properties. The properties of the underlying soil, being a heterogeneous material, alter from one point to another in a site. In many cases, the subsurface data collection proves to be difficult and expensive due to issues such as inaccessibility, cost of equipment required, proximity to nearby structures. The different types of soil and rock test data already available are abundant and widely scattered. A spatial database management system can be used to map these surficial conditions as well as to determine the missing spatial data. Over the last four decades, geographical information system (GIS) has emerged as one of the major spatial database tools playing a key role in the studies of land suitability, ground response, hydrology studies, various hazard risks, and so on [1]. Geotechnical zonation maps can help in the preliminary planning stages of construction as well as in assessing the safety and economy of various engineering projects. Rajesh et al. [2] conducted a synoptic analysis of the safe bearing capacities of the soil in the

G. S. Krishna (✉) · V. K. Stalin
Division of Soil Mechanics and Foundation Engineering, Department of Civil Engineering, College of Engineering Guindy, Anna University, Chennai 600025, Tamil Nadu, India
e-mail: gowrismithakrishna@gmail.com

V. K. Stalin
e-mail: staliniisc@yahoo.co.in

K. Muthukkumaran (eds.), *Soil Behavior and Characterization of Geomaterials*,
Lecture Notes in Civil Engineering 296, https://doi.org/10.1007/978-981-19-6513-5_27

southern parts of Chennai, India, and subsequent digitization of varying depths using surfer-based Kriging interpolation methods. Sakunthala Devi and Stalin [3] explored various interpolation techniques to analyse the spatial continuity and variability of bearing capacity of pile of various diameters and embedded length as well as other important geotechnical parameters and developed ultimate bearing capacity maps for the study area of Chennai. Smith et al. [4] formed a digital borehole geotechnical database using Microsoft Access 2000 for the Mackenzie Valley/Delta region by compiling already available geological and geotechnical data of over 13,000 boreholes from the pipeline and field drilling programmes between 1970 and 1975. The complete database was also provided in GIS compatible format for both MapInfo and ArcView. Joshphar et al. [5] combined GIS with a relational database management system (RDBMS) to develop a web-based geotechnical information system that could perform online spatial queries, generation of professional bore logs, and various geotechnical analyses in Singapore. Divya and Dodagoudar [6] formed a digitally formatted and integrated spatial database using geotechnical data and GIS in the study area of Chennai, Tamil Nadu, India. The study also demonstrated the application of the developed subsurface model in evaluating the effectiveness of multichannel analysis of subsurface wave (MASW) tests to evaluate the depth to bedrock.

Objective of the Study

This study focuses on compiling already available geotechnical data obtained from boreholes using GIS to generate foundation suitability maps for South Chennai, Tamil Nadu, India. The objectives of the proposed study can be listed as follows:

1. To create a database management system using GIS and Microsoft Excel for collecting and utilizing geotechnical data from the wide range of borehole and laboratory data available in and around South Chennai.
2. To analyse spatial continuity and variation of geotechnical parameters using suitable interpolation techniques.
3. To calculate and generate safe bearing capacity and total settlement maps of soil for shallow foundations of lightly, moderately, and heavily loaded structures in the study area.

Methodology

The conceptual flowchart for the development of the geotechnical parameter maps is as shown in Fig. 27.1.

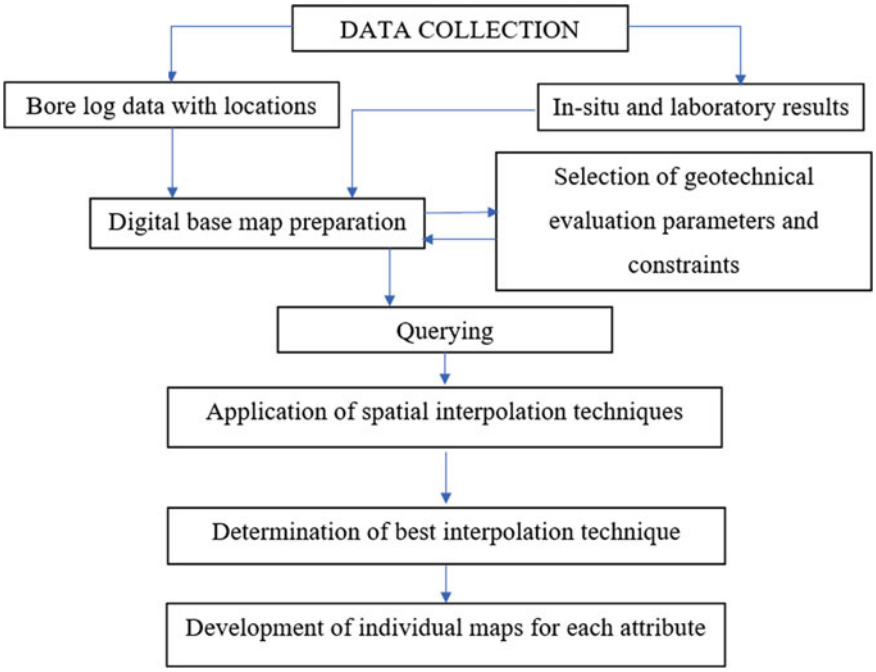

Fig. 27.1 Conceptual flowchart showing the proposed methodology

Details of the Study Area

The region along the Old Mahabalipuram Road (OMR) in Chennai has become the hub of various IT companies and industries accompanied by a huge rise in residential projects, educational institutions, national research laboratories, etc.

The study area of 88.932 km^2 considered in this project is along the OMR beginning from Perungudi to Kelambakkam and consists of mainly Pallikaranai, Oggiyamduraipakkam, Karapakkam, Shollinganallur, Navalur, Egattur, Siruseri, and Padur as shown in Fig. 27.2.

Data Collection

The data collected consist of spatial and non-spatial information. The spatial data consist of the latitudes and longitudes of the borehole locations used in the study which were mapped through a GPS survey. The geotechnical attributes and site details of all the borehole locations were collected. The non-spatial data contained city boundaries, arterial roads, rivers, marshlands, water bodies, etc. (Fig. 27.3).

Fig. 27.2 Base map of the study area in OMR (*Source* Imagery in ARCMAP 10.8)

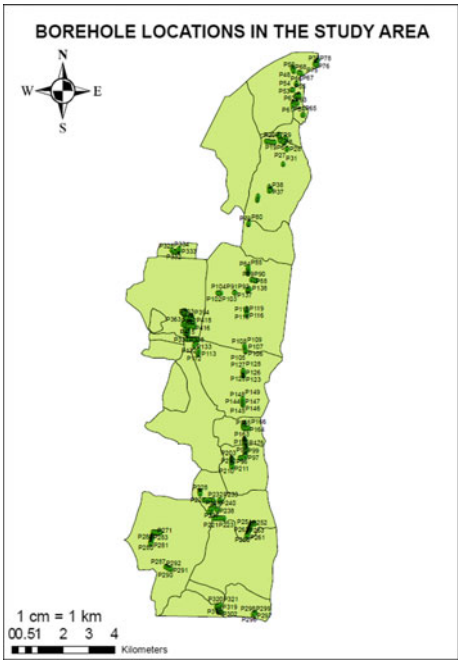

Fig. 27.3 Borehole locations in the study area in OMR

Fig. 27.4 Non-spatial data in the study area

Development of Base Map

A digitized base map with adequate control points and information is necessary for the development of a spatial database. The base map consisting of the study area boundaries starting from Perungudi to Kelambakkam was developed from Chennai city map and land use maps using ArcMap 10.8 software. The major non-spatial attributes in the study area such as city boundaries, main road, arterial roads, rivers, and waterbodies have been incorporated in the Chennai city map as shown in Fig. 27.4.

Formation of Geotechnical Database

The geotechnical data used in the study were collected from VRR Engineering Consultancy, Chennai. The geotechnical database was created using Microsoft Excel and consisted of borehole IDs, latitude, and longitude of each borehole, descriptions of the site, *N* values at various depths (0.75, 1.5, 2.25, 3, 3.75, 4.5, 5.5 m, etc.), soil classification, density details, cohesion, and angle of internal friction at varying depths.

The Excel sheet was then converted into a shapefile to integrate with the base map of the study area created. The borehole data were spatially plotted in the base map using the XY data, i.e. longitude and latitude of each borehole location. As a result,

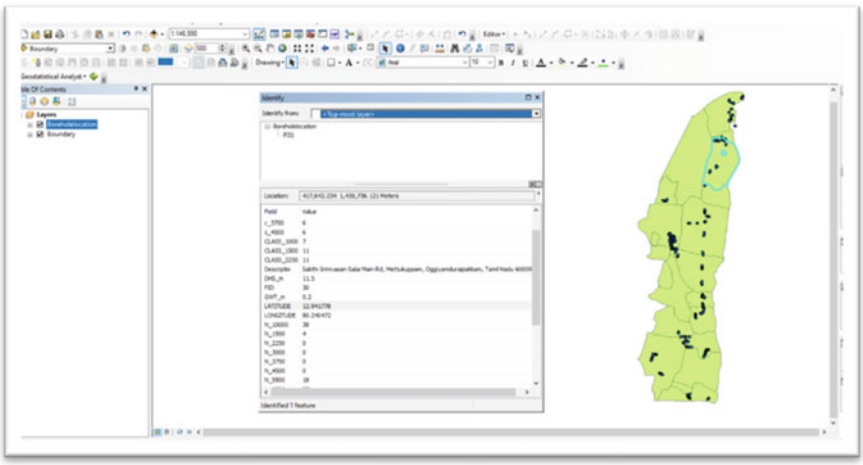

Fig. 27.5 Geotechnical data at the borehole location (Point ID: P31) in ArcMap

each point in the map could be accessed to get the borehole details of that particular location as shown in Fig. 27.5.

Mapping of Attribute Data Using Interpolation Technique

Interpolation methods in ArcMap 10.8 were used for predicting a continuous spatial surface from sampled point values in the study. The various spatial interpolation techniques used in this study are: Inverse Distance Weighted (IDW), Natural Neighbour, Spline, Kriging, and Topo to Raster interpolation. The determination of the best interpolation technique was done by using cross-validation. The spatial model has been developed using 374 borehole locations out of a total of 418 borehole locations in the study area. The geotechnical data of the remaining 44 borehole locations were compared with the observed values in the borelog and laboratory reports. The interpolation technique with the least RMSE error was adopted as the best method for generating the geotechnical parameter models.

Results and Discussions

Groundwater Table Map in the Study Area

The groundwater table distribution was developed from the borelog report of various borehole locations. The groundwater table depth map was developed using the Inverse

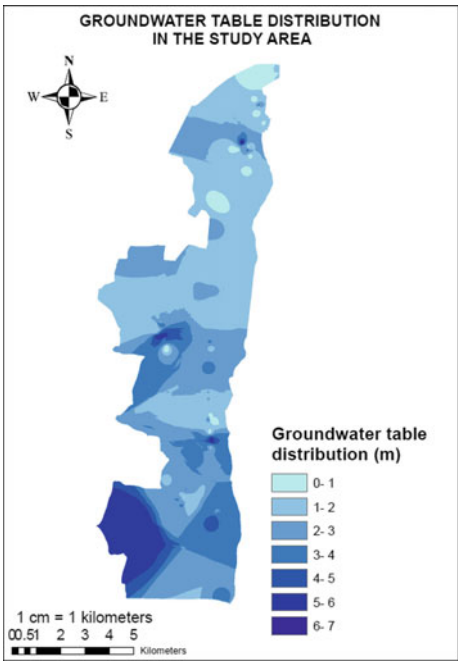

Fig. 27.6 Groundwater table distribution in the study area

Distance Weighting interpolation technique in the study area as shown in Fig. 27.6. Shallow groundwater table was found in some places towards the northern part of the study area due to the presence of nearby marshlands.

SPT N Value Map at Different Depths in the Study Area

The variation of SPT *N* value with respect to the depth in the study area was analysed and modelled using Topo to Raster interpolation. These *N* value maps can be used to find the *N* value at a particular location using the latitude, longitude, and the depth of the layer below ground level. The *N* value maps for depths 3, 4.5, and 6.5 m are shown in Figs. 27.7, 27.8 and 27.9. The SPT *N* values predominantly increased in value with increasing depth below ground level in the study area.

Soil Classification Map at Different Depths in the Study Area

The soil classification used in this study as per Unified Soil Classification System is poorly graded sand (SP), poorly graded sand with silt and gravel (SM-SP), clayey sand with gravel (SC), sand with low plasticity clay (SC-CL), sand with intermediate

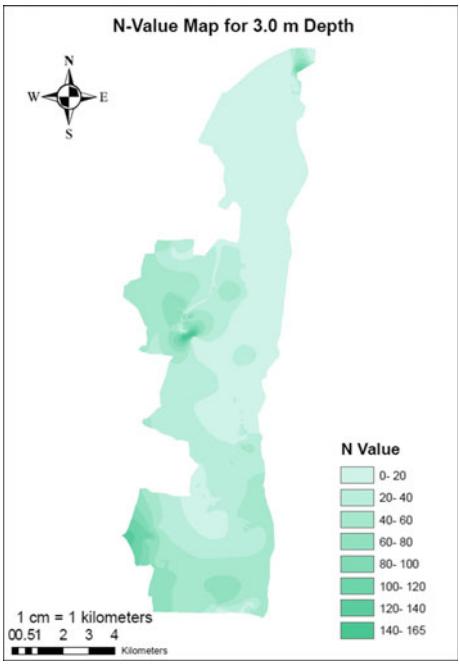

Fig. 27.7 SPT N value at 3.0 m depth

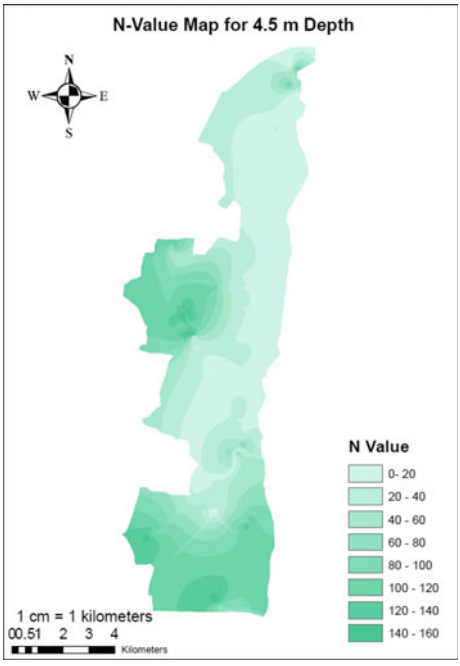

Fig. 27.8 SPT N value at 4.5 m depth

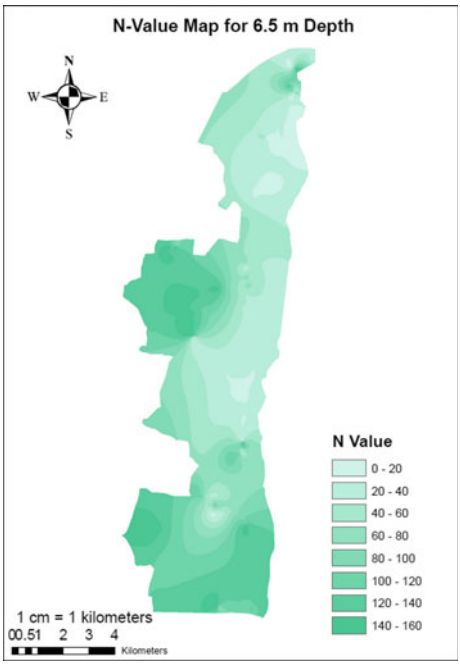

Fig. 27.9 SPT N value at 6.5 m depth

plasticity clay (SC-CI), and intermediate plasticity clay (CI). No problematic soils such as those containing peat, expansive clays, dispersive clays were found in the study area which can cause hindrances in construction activities. The variation of soil types with varying depth was analysed, and soil classification maps at depths varying between 0.75 and 10.0 m were generated using Inverse Distance Weighted interpolation. The soil classification maps at depths of 1.5, 2.25, and 3 m are as shown in Figs. 27.10, 27.11 and 27.12.

Safe Bearing Capacity Maps in the Study Area

The shallow foundation was assumed to be an isolated square footing. The safe bearing capacity (SBC) was calculated using IS equation as per IS 6403–1981 [7] at the sampled locations considering foundation width of 1.5 and 2 m. Bearing capacity calculations were done for depths of foundation 1.5, 2.25, and 3 m. The water table correction factor, shape factor, and depth factor were also taken into consideration. The cohesion, c, and angle of internal friction, φ, at the corresponding depths were adopted in the calculation. The maps were generated using Topo to Raster interpolation. The SBC maps with width of foundation of 1.5 m at various depths are as shown in Figs. 27.13, 27.14 and 27.15.

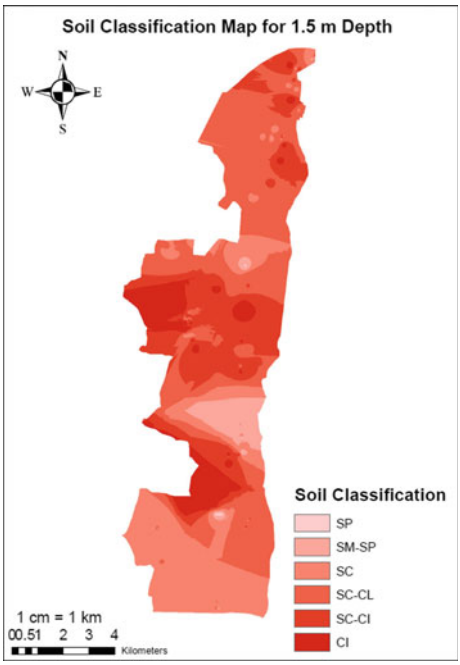

Fig. 27.10 Soil classification map at 1.5 m depth

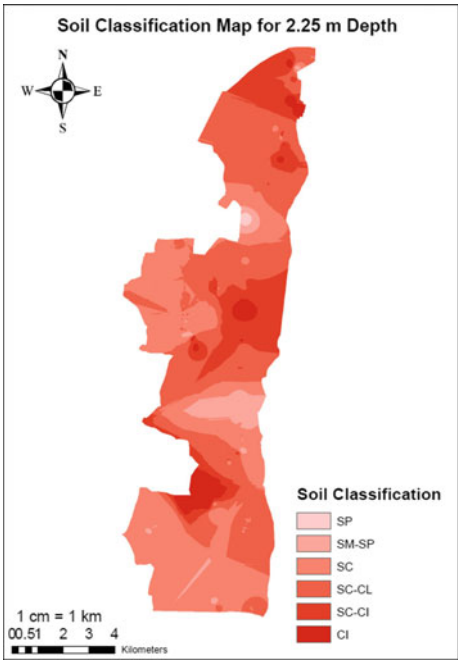

Fig. 27.11 Soil classification map at 2.25 m depth

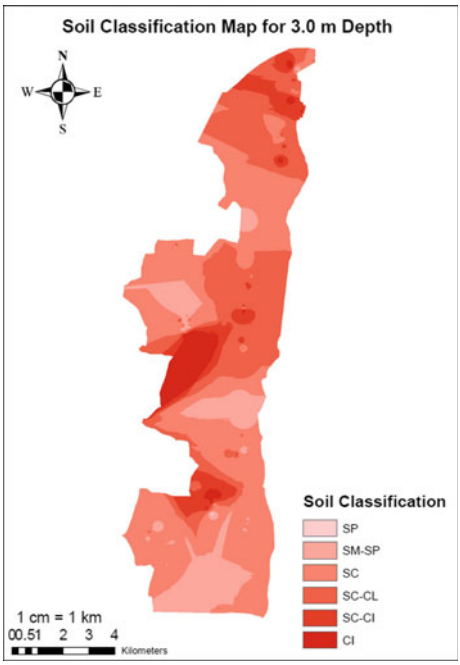

Fig. 27.12 Soil classification map at 3 m depth

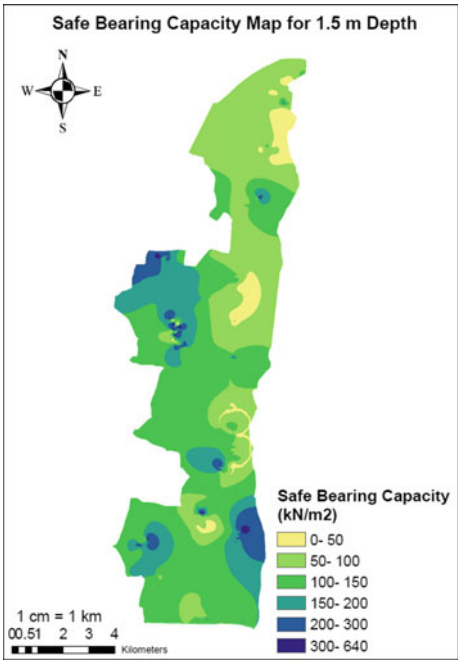

Fig. 27.13 SBC map at 1.5 m depth

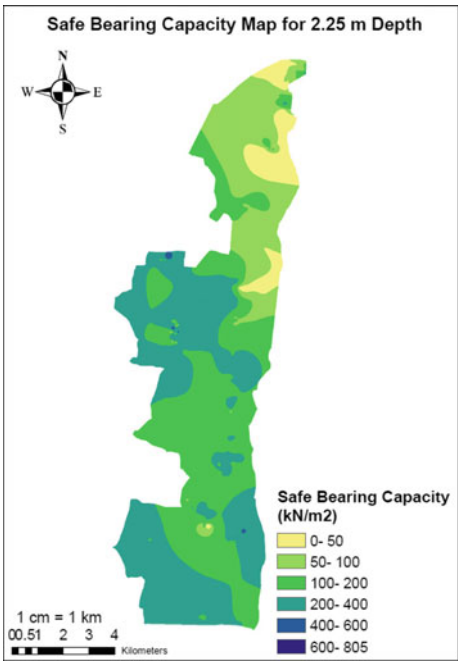

Fig. 27.14 SBC map at 2.25 m depth

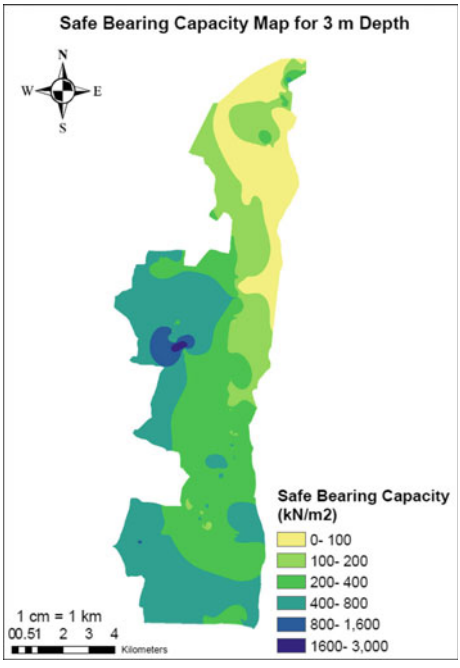

Fig. 27.15 SBC map at 3 m depth

SBC Map for 1.5 m Depth It is observed that 4.354% area has SBC between 0–50 kN/m^2, 32.839% between 50–100 kN/m^2, 44.555% between 100–150 kN/m^2, 14.089% between 150–200 kN/m^2, 3.957% between 200–300 kN/m^2, and 0.204% between 300–600 kN/m^2.

SBC Map for 2.25 m Depth It is observed that 5.966% has SBC between 0–50 kN/m^2, 17.862% between 50–100 kN/m^2, 38.385% between 100–200 kN/m^2, 37.673% between 200–400 kN/m^2, 0.114% between 400–600 kN/m^2, and 0.001% between 600–805 kN/m^2.

SBC Map for 3 m Depth It is observed that 14.637% has SBC between 0–100 kN/m^2, 17.201% between 100–200 kN/m^2, 32.344% between 200–400 kN/m^2, 33.932% between 400–800 kN/m^2, 1.698% between 800–1600 kN/m^2, and 0.189% between 1600–3000 kN/m^2.

Total Settlement Maps in the Study Area

The total settlement of the soil, S_T, in the study area due to foundation loading was calculated for 3 column loads: 250, 500, and 1000 kN considering lightly loaded, moderately loaded, and heavily loaded structures as per IS 875 (Part 1 and Part 2): 1987 [8, 9]. Total settlement of the soil layer was calculated as the summation of immediate (elastic) and consolidation settlement of soil layers up to an influence depth of 1.5B for width of foundation of 1.5 and 2 m and depth of foundation of 1.5, 2.25, and 3 m. Meyerhoff's correlation was used for calculating the elastic settlements of sandy soil based on standard penetration resistance, N, where average SPT N value between the bottom of the foundation to a depth of 2B and the bottom was considered. The elastic settlement of clayey soil was calculated using the equation based on theory of elasticity. The consolidation settlement of clayey soil was determined using the formula $S_c = \Delta\sigma m_v H$ where coefficient of volume compressibility (m_v) was calculated from the elasticity modulus (E_s) of the soil [10] which in turn depended on the SPT N value and the soil classification at various depths. The total settlement maps for the study area were developed using various interpolation techniques, and Inverse Distance Weighted interpolation was found to be the suitable method for developing the settlement maps using cross-validation process. These maps can be used to estimate the settlement of isolated foundations at different depths within the study area using the latitude, longitude, and depth of the foundation to be used.

Total Settlement Maps for a Moderately Loaded Structure in the Study Area. The column load in the case of a moderately loaded structure was approximated as 500 kN as per IS 875 (Part 1 and Part 2): 1987. The total settlement of the soil was calculated considering widths of foundations as 1.5 and 2 m with varying depth of foundation of 1.5, 2.25, and 3 m. The total settlements maps thereby developed are as shown in Figs. 27.16, 27.17, 27.18, 27.19, 27.20 and 27.21.

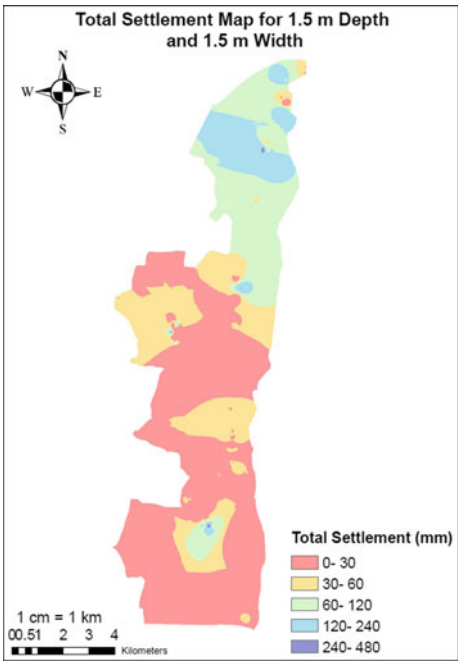

Fig. 27.16 Total settlement map for 1.5 m depth and 1.5 m width

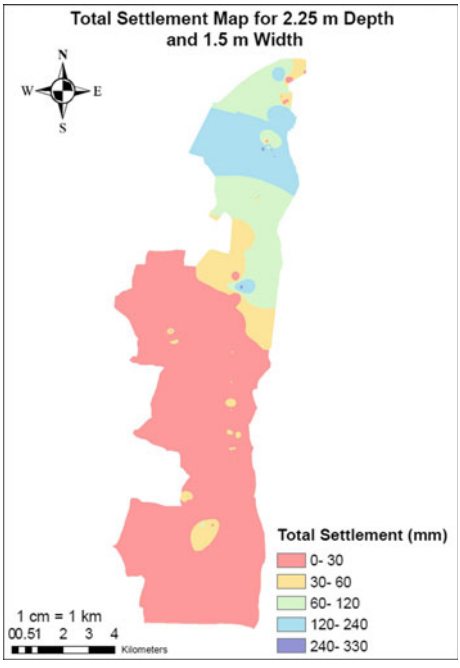

Fig. 27.17 Total settlement map for 2.25 m depth and 1.5 m width

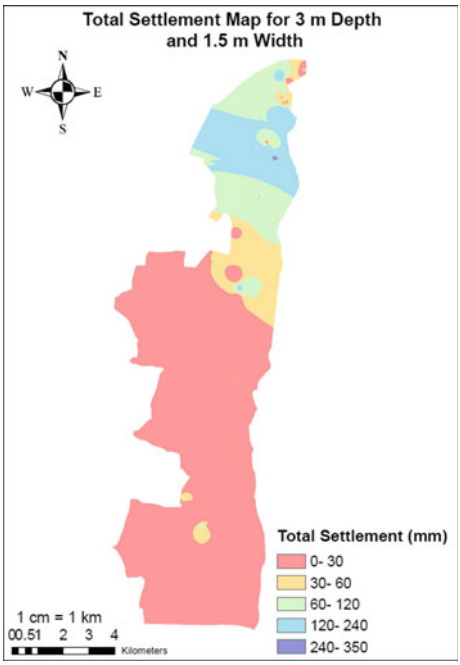

Fig. 27.18 Total settlement map for 3 m depth and 1.5 m width

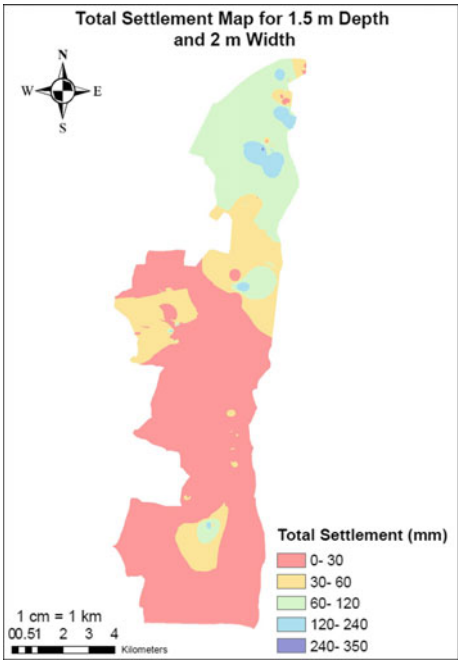

Fig. 27.19 Total settlement map for 1.5 m depth and 2 m width

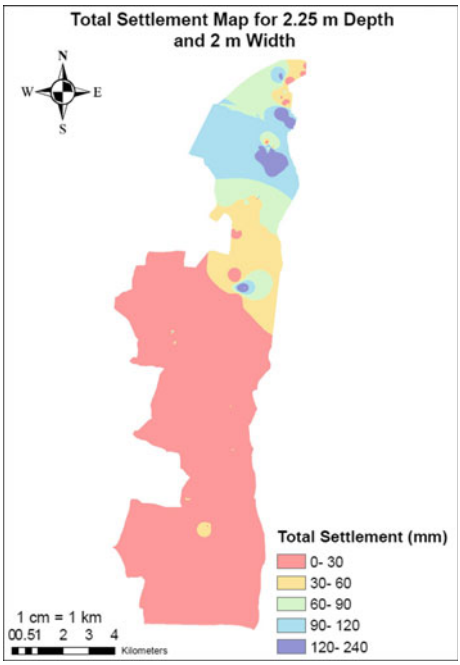

Fig. 27.20 Total settlement map for 2.25 m depth and 2 m width

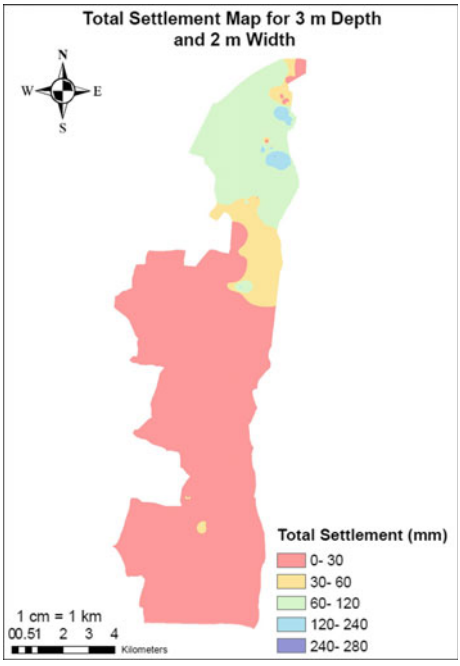

Fig. 27.21 Total settlement map for 3 m depth and 2 m width

Total Settlement Map for 1.5 m Depth and 1.5 m Width. It can be observed that the total settlement of 51.707% area is between 0–30 mm, 20.12% between 30–60 mm, 19.603% between 60–120 mm, 8.521% between 120–240 mm, and 0.049% between 240–480 mm.

Total Settlement Map for 2.25 m Depth and 1.5 m Width. It can be observed that the total settlement of 66.773% area is between 0–30 mm, 8.11% between 30–60 mm, 14.115% between 60–120 mm, 10.974% between 120–240 mm, and 0.028% between 240–330 mm.

Total Settlement Map for 3 m Depth and 1.5 m Width. It can be observed that the total settlement of 70.704% area is between 0–30 mm, 8.061% between 30–60 mm, 8.061% between 60–120 mm, 9.734% between 120–240 mm, and 0.032% between 240–350 mm.

Total Settlement Map for 1.5 m Depth and 2 m Width. It can be observed that the total settlement of 60.574% area is between 0–30 mm, 17.716% between 30–60 mm, 19.32% between 60–120 mm, 2.379% between 120–240 mm, and 0.011% between 240–360 mm.

Total Settlement Map for 2.25 m Depth and 2 m Width. It can be observed that the total settlement of 70.25% area is between 0–30 mm, 9.829% between 30–60 mm, 8.146% between 60–90 mm, 10.072% between 90–120 mm, and 1.703% between 120–240 mm.

Total Settlement Map for 3 m Depth and 2 m Width. It can be observed that the total settlement of 73.953% area is between 0–30 mm, 7.474% between 30–60 mm, 17.525% between 60–120 mm, 1.047% between 120–240 mm, and 0.002% between 240–280 mm.

Validation of Attribute Maps Developed

Cross-validation was done for groundwater table, depth of hard stratum, SPT *N* value, soil classification, safe bearing capacity, and total settlement maps. The values obtained from the field and laboratory tests and those observed in the developed maps were found to be in good agreement with each other. Mean error and root mean square error were also calculated to ensure minimum error in the interpolation techniques adopted. The comparison of actual safe bearing capacity with the corresponding values obtained from the maps is shown in Table 27.1.

Table 27.1 Comparison of actual safe bearing capacity and predicted safe bearing capacity for 1.5 m width and 1.5 m depth of foundation from the map

Borehole ID	Latitude	Longitude	Actual SBC (kN/m2)	Predicted SBC (kN/m2)
P5	12.9501389	80.2393889	56.783	50–100
P46	12.9703333	80.2451111	80.645	50–100
P56	12.9634444	80.2454444	16.168	0–50
P110	12.8743056	80.21	129.195	100–150
P117	12.8904444	80.2274722	48.791	0–50
P120	12.8668056	80.2263889	58.571	50–100
P152	12.8440833	80.2268611	161.159	150–200
P193	12.8227778	80.2153889	113.049	100–150
P215	12.8377778	80.2255833	64.608	50–100
P241	12.8143889	80.2306111	530.555	300–640
P273	12.8111667	80.1940278	116.463	100–150
P292	12.7981944	80.2006111	84.014	50–100
P343	12.8832222	80.2062778	225.746	200–300
P394	12.8870556	80.20775	214.052	200–300

Conclusions

A geotechnical database management system was developed using the data from already available borehole and laboratory tests for generating geotechnical attribute maps using various spatial interpolation techniques in South Chennai, Tamil Nadu, India, using Microsoft Excel and ArcMap 10.8. Geotechnical attribute maps can act as an aid in site investigation processes and provide an insight into the approximate value of safe bearing capacities and total settlement of soil in the study area which can be helpful in deciding the shallow foundation details. The following conclusions can be drawn from the proposed study:

1. The safe bearing capacity (SBC) of the soil (in kN/m2) was calculated using the IS equation as per IS 6403: 1981 considering widths of foundation 1.5 and 2 m at varying depths of foundation of 1.5, 2.25, and 3 m. Good bearing stratum with high bearing capacity was observed towards the southern parts of the study area, whereas the northern parts showed lower bearing capacity values due to the presence of waterlogged areas and shallow groundwater table.
2. The total settlement of soil was calculated considering loads from lightly, moderately, and heavily loaded structures for foundation widths of 1.5 and 2 m at different depths such as 1.5, 2.25, and 3 m. The soil present in the northern parts of the study area experienced more settlement when compared to that towards the southern areas.

3. Inverse Distance Weighted and Topo to Raster interpolation were identified as the best interpolation technique for developing the spatial attribute maps in the study.

References

1. David Rogers J, Luna R (2004) Impact of geographical information systems on geotechnical engineering. In: Proceedings: fifth international conference on case histories in geotechnical engineering. New York, NY
2. Rajesh S, Sankaragururaman D, Das A (2003) A GIS/LIS approach for study on suitability of shallow foundation at Southern Chennai, India. GISdevelopment.net. https://www.geospatialworld.net/article/a-gislis-approach-for-study-on-suitability-of-shallow-foundation-at-southern-chennai-india/
3. Sakunthala Devi S, Stalin VK (2011) Development of soil suitability map for geotechnical applications using GIS approach. In: Proceedings of Indian geotechnical conference December 15–17, paper no M-253. Kochi, pp 797–800
4. Smith SL, Burgess MM, Chartrand J, Lawrence DE (2005) Digital borehole geotechnical database for the Mackenzie Valley/Delta region. Geological survey of Canada, open file 4924. Ottawa, Ontario
5. Kunapo J, Dasari GR, Phoon K-K, Tan T-S (2005) Development of a web-GIS based geotechnical information system. J Comput Civ Eng 19(3):323–327
6. Divya Priya B, Dodagoudar GR (2018) An integrated geotechnical database and GIS for 3D subsurface modelling: application to Chennai City, India. Appl Geomatics 10:47–64
7. IS 6403 (1981) Code of Practice for determination of bearing capacity of shallow foundations. Bureau of Indian Standards, New Delhi
8. IS 875—Part 1 (1987) Code of practice for design loads (Other Than Earthquake) for buildings and structures—dead loads—unit weights of building material and stored materials. Bureau of Indian Standards, New Delhi
9. IS 875—Part 2 (1987) Code of practice for design loads (Other than Earthquake) for buildings and structures—imposed loads. Bureau of Indian Standards, New Delhi
10. Varghese PC (2012) Foundation engineering, 9th edn. PHI Learning Private Limited, New Delhi

Chapter 28
A Review on the Evaluation of Soil Liquefaction Potential Using Geospatial Technology

Hrik Chaudhury, Abhishek Kumar, and Rishikesh Bharti

Introduction

Earthquake is one of the most unpredictable devastating natural disasters. There has been a significant increase in the number of earthquakes since the last decade. Liquefaction stands to be one of the induced effects of such an event. Extensive studies are being conducted to understand this phenomenon in particular. Castro et al. [1, 2], Idriss [3, 4] had put forward theories on how to understand whether a soil will undergo liquefaction under a particular earthquake or not. Engineers till date follow these standard approaches to prepare liquefaction susceptibility maps. These maps in turn help in city planning, disaster control, and so on. The standard procedures available till date are based on geotechnical parameters, which need field investigation to be done. Field investigations are time-consuming and expensive. Also, every time it needs skilled person to supervise the procedure. In cases where a complicated terrain is encountered, it is nearly impossible to have access to conduct the in situ investigation. Such problems necessitate the need of remote sensing and the introduction of liquefaction to geospatial domain. Once we have a geospatial-based region specific or global model, it would be rather less complicated to understand the liquefaction extent of an area for a particular earthquake. Studies done so far have used models with geospatial parameters that are easily evaluated with the help of satellite data. In most of the works, proxy parameters are being used as research in this field at its nascent stage. Ramakrishnan et al. [5] used 13 boreholes in the Kutch region India for liquefaction assessment. Similar data for the Kutch region were also

H. Chaudhury (✉) · A. Kumar · R. Bharti
Department of Civil Engineering, Indian Institute of Technology, Guwahati 781039, India
e-mail: c.hrik@iitg.ac.in

A. Kumar
e-mail: abhiak@iitg.ac.in

R. Bharti
e-mail: rbharti@iitg.ac.in

K. Muthukkumaran (eds.), *Soil Behavior and Characterization of Geomaterials*,
Lecture Notes in Civil Engineering 296, https://doi.org/10.1007/978-981-19-6513-5_28

used by Zhu et al. [6], Baishe and Rashidan [7], and Oomen et al. [8]. Similar works are also available for other parts as well. This paper presents a summary of the work that have been done till date and attempts to enlighten the direction in which present research in this domain is progressing.

Existing Works

The endeavour to establish a geospatial model to evaluate liquefaction commenced in India from the beginning of the last decade. Ramakrishnan et al. [5] used the property of bare soil's inverse reflectance of visible and near infrared (VNIR) and shortwave infrared (SWIR) relation with soil moisture. Normalized DN value of postevent images, using the help of pre-event images are used for the purpose. Features whose reflectance do not change with temporal variation are chosen, and regression correlation was established to normalize DN values of the postevent images. In the work, two different satellite data and 6 different alternative day's acquired images were used. Geological data, SPT value, lithological features all were used to estimate field-based liquefaction assessment. Several band ratios were checked using 4 bands in the postevent image. The band ratio which was in accordance to field-based liquefaction assessment was chosen to be the liquefaction sensitivity index (LSeI) as;

$$\text{LSeI} = 1 + \frac{B3 - B2}{B3' - B2'} \tag{28.1}$$

On the basis of histograms, two classes were decided, i.e. LSeI > 2.6 is soil moisture with no change and LSeI < 2.6 is increased soil moisture. After getting the LSeI, it was required to check the reliability of this method. To do so, a small area was chosen and Liquefaction data from the Kutch region using 13 borehole investigations were incorporated. LSI was evaluated and correlated with the LSeI, and the following correlation was obtained:

$$\text{LSI} = 0.852\ \text{LSeI}^2 - 10.301\ \text{LSeI} + 24.076 \tag{28.2}$$

In another work, Knudsen and Bolt [9] had studied the factors influencing liquefaction which later became the inspiration to come up with the geospatial model. However, the model could not be used directly for the later analyses as it had the basic downside of oversampling of liquefaction area and under sampling of non-liquefaction area. Later, Zhu et al. [10] proposed a model to map liquefaction extent of an area where sampling was done in an unbiased way. Zhu et al. [10] used three parameters, viz. density, saturation, and dynamic load in the study. There were three study areas chosen because of their detailed liquefaction map. These were: Christchurch (New Zealand), Kobe (Japan), and Port-Au-Prince (Haiti). Proxy parameters were chosen as this was a geospatial model and had to have variables which can be easily determined. These are shear wave velocity for first 30 m of soil (V_{s30}) Wald and Allen

[11], normalized distance (ND), distance to river, elevation above closest water body, compound topographic index (CTI; Beven and Kirksy [12]). All the above variables are paradigmatic of soil density and saturation. Soil type was left out in the study. A linear relation is used with appropriate weightage assigned to every factor. The probability of liquefaction was calculated using the following regression model:

$$P(X) = \frac{1}{1 + e^{-x}} \tag{28.3}$$

where X is the summation of different proxies multiplied with appropriate weightage. Different models for different regions were used, and it was observed that a particular model performed better all other models. It was inferred that CTI is a better representation of saturation than distance to river in general. Also, it is made sure in this work that a global model is given which does not require ND which is valid for coastal region only. The global model includes PGA, CTI, and V_{s30}, and the regional model includes ND instead of $V_{s30.}$

In 2017, Zhu et al. [6] added 23 additional earthquakes from USA, Japan, China, Taiwan, and Bhuj region of India in the analysis to get a more precise model. Both liquefaction and non-liquefaction incidents were considered to minimize the sample biasness. All events in this study were classified in two broad categories, namely coastal event and non-coastal event. A few non-coastal events were encountered, which is quite natural as majority of tectonic regions are coastal. Zhu et al. [6] brought in additional proxy variables, viz. roughness, topographic position index, terrain roughness index, precipitation and aridity index in order to account for seasonal variation. In both the works from Zhu et al. [6, 11] sampling played an important role. In case where there were only points denoting the liquefaction or where they did not have data for the entire area, buffers were used around the points of liquefaction to minimize the drawback. To avoid biasness, 1000 random samples of liquefaction points were considered from one earthquake event. It was observed in the analysis that natural log of peak ground velocity (ln PGV) works better than natural log of peak ground acceleration (ln (PGA)). Moreover, PGV, V_{s30}, distance to coast, distance to river, and precipitation are the best parameters for coastal model and PGV, V_{S30}, water table depth and precipitation works for non-coastal data. It is to be noted that a threshold was fixed. PGV < 3 cm/s and $V_{s30} > 620$ would cause no liquefaction. For the Global model, the X variable to calculate probability of liquefaction was given as:

$$\begin{aligned} X = {} & 12.435 + .301 \ln \ln(PGV) - 2.615 \ln \ln(V_{s30}) \\ & + 5.556 \times 10^{-4}.\text{precipitation} - 0.0287(d_c).^{0.5} \\ & + 0.0666.d_r - 0.0369.d_r.(d_c).^{0.5} \end{aligned} \tag{28.4}$$

In another work, Baise and Rashidian [7] applied the geospatial model from Zhu et al. [6] on 27 different earthquakes including the one from Bhuj in addition to what Zhu et al. [6] to evaluate its efficacy. Baise et al. [13] published a paper in which they

reviewed the 2017 work. Baise et al. [13] concluded that Zhu et al. [6] overpredicted some of the liquefaction extent. Baise [13] based on Baise and Rashidian [7] proposed a modified model where the threshold for PGA is changed to 0.1 g. This model seemed to work better with some overprediction in 2015 Nepal earthquake and 2016 Kumamoto earthquake. Maurer [14] applied two global geospatial models Zhu et al. [6, 15] and one regional geospatial model Zhu et al. [6] on 9731 earthquake case histories from M_w 7.1, September 2010 Darfield earthquake, M_w 6.2, February 2011 Christchurch earthquake and M_w 5.7, February 2016 Valentine's Day earthquake. Maurier [14] also exhibits two geotechnical models from Idriss and Boulanger [16], and Boulanger and Idriss [17]. Maurier [14] concluded the geospatial model to be working very well for all the earthquakes.

In all of the studies, an extensive liquefaction map is used to develop the correlation. In practical situation, it is not practical to go at every corner in the vicinity of an earthquake. In such case, the convenient solution to these problems comes from remote sensing. Researchers have used pre- and postearthquake images to map earthquake induced damages Eguchi et al. [18]; Huyck et al. [19]; Kayen et al. [20]; Kohiyama and Yamazaki [21]; Mansouri et al. [22]; Rathje et al. [23, 24]. Once it is possible to know the first approximate areas undergoing liquefaction, a group of field investigators can go to the area for the detailed geotechnical investigation and prepare the required map of liquefaction extent of that area.

In addition to identification of liquefaction zones, there had been ongoing research to detect liquefaction damages from satellite image. Earlier there were only two computer-based techniques to identify liquefaction damage in the field using remote sensing. One of them was to use the difference between pre- and postearthquake images. This way it has its drawback in identifying whether the change is due to earthquake or non-earthquake phenomenon. The second approach is to use training data from the field and then perform supervised classification. This method definitely has the problem which is concerned with effort of the field investigator with which he/she should collect enough data for training.

Oomen et al. [8] tried to detect liquefied areas through Landsat ETM+ images. The work used thermal images and tasselled cap wetness images to do so. It was hypothesized that due to liquefaction, soil moisture content would be increasing and that can be detected in spectral bands which are sensitive to soil moisture content. The study area selected for the research work was of Kutch region, which is topographically uncomplicated. In case of moist soils, latent heat flux increases as phase change can eventuate with increase in heat energy but in dry soils the sensible heat increases because no substance for phase change is available then. Hence, in moist soils one can observe a decrease in sensible heat. Thermal infrared response is inversely proportional to soil moisture content. Thermal bands have coarse resolution, and thus to eliminate this, tasselled cap transformed wetness images have been used. The False Colour Composite of visible spectra gives us the terrain information. The area has two distinct features: a trench zone and a bet zone. The bet zone has scanty vegetation and is in the south-east part. Trench zone is in the northern part. The pre- and postearthquake images were corrected for seasonal variations. The difference in both the images with respect to thermal infrared showed that there was cooling in

the trench zone which was evident of the fact that liquefaction has occurred there. After analyzing the same study with tasselled cap transformed wetness images, it was found that more of the area is wet. This is because of the resolution capacity. So, it is concluded that tasselled cap transform wetness image would give liquefaction for a larger area, but thermal images would give more concentrated liquefaction areas. At last, when the remote sensing images were compared to field mapping, it seemed that the images were not able to capture the wetness or coolness in the bet zone which is mainly because of the moisture retention capacity of the soil.

Baik et al. [25] performed investigation for liquefied soils using remote sensing. The study area was Pohang which suffered earthquake of magnitude 5.4 in 2017. In the work, synthetic aperture radar was used. Microwave region of the EM spectrum is not affected by atmosphere and Baik et al. [25] used this fact. Coherence value of the image pairs was studied. Coherence value decreases due to earthquake owing to the signal mismatch and is called decorrelation. The disadvantage related to this method is the spatial resolution. In this work, visible spectra and SWIR were also used to study the liquefaction-affected area. For optical analysis, three Normalized Difference Water Index DWI from McFeeters [26], Geo [27], and Xu [28] were used as:

$$\mathrm{NDWI_{Gao}} = \frac{\mathrm{NIR_{860\,nm}} - \mathrm{SWIR_{1600\,nm}}}{\mathrm{NIR_{860\,nm}} + \mathrm{SWIR_{1600\,nm}}} \tag{28.5}$$

$$\mathrm{NDWI_{Mcfeeters}} = \frac{\mathrm{Green_{560\,nm}} - \mathrm{NIR_{860}}}{\mathrm{Green_{560\,nm}} + \mathrm{NIR_{860}}} \tag{28.6}$$

$$\mathrm{mNDWI_{Xu}} = \frac{\mathrm{Green_{560\,nm}} - \mathrm{SWIR_{1600}}}{\mathrm{Green_{560\,nm}} + \mathrm{NIR_{860}}} \tag{28.7}$$

The NDWI given by Gao [27] uses NIR and SWIR bands of 860 nm wavelength and 1600 nm, respectively. The NDWI given by Mcfeeters [26] uses green band of 560 nm wavelength and NIR band of 860 nm wavelength, whereas Xu [28] used green band of 560 nm wavelength, NIR band of 860 nm wavelength, and SWIR band of 1600 nm.

Also, one index known as TDLI (temporal difference liquefaction index) is used. In this index, only one band is used, i.e. SWIR band 2 (2200 nm), which is sensitive to soil moisture content. In NDWI, SWIR band-1 is used as that is more sensitive to vegetation's moisture content. However, as liquefaction seems to be more relevant to bare soils, SWIR band 2 is used in case of TDLI.

$$\mathrm{TDLI} = \frac{\mathrm{Pre\_earthquake\_SWIR_{2200}}_{nm} - \mathrm{Post\_earthquake\_SWIR_{2200\,nm}}}{\mathrm{Pre\_}e\mathrm{arthquake\_SWIR_{2200}}_{nm} + \mathrm{Post\_earthquak}e\mathrm{\_SWIR_{2200\,nm}}} \tag{28.8}$$

Detailed analysis shows that SAR data was not helpful in finding any decorrelation in the areas undergone by sand blows. Whereas there was decorrelation in urban areas where building have been tilted or ground have been deformed but it is hard to say if really this was due to liquefaction. Through analysis of $\mathrm{NDWI_{gao}}$ [27], it was found

that around the epicenter, increase in water content was highest where as in the farmland water content decreased due to the temporal resolution. Pre-event image was just after the farming days which led to a decreased water content in the postevent images. NDWI McFeeters [26] and $NDWI_{xu}$ [28] did not do any better. In addition, Sentinel data were a slightly better because of their temporal and spatial resolution. TDLI analysis was the best among all the methods. There was noise because of high rise building, steep slope, and sun's azimuth angle. Otherwise TDLI for sentinel gave more or better results than the other indices.

Linigam et al. [29] proposed a GIS approach to identify risk of liquefaction for an area. This approach used LANDSAT ETM^+ and ASTER data. Four different indices like simple ratio (SR), Normalized Difference Vegetation Index (NDVI), Transformed Normalized Difference Vegetation Index (TNDVI), Soil Adjusted Vegetation Index (SAVI), and Modified Normalized Difference Water Index (MNDWI) were used as defined below where ρ_{NIR} is reflectance in red band, ρ_{RED} is the reflectance in red band, L is the correction factor, and the bands mentioned are the bands from LANDSAT ETM^+:

$$\mathrm{SR} = \frac{\rho_{\mathrm{NIR}}}{\rho_{\mathrm{RED}}} \tag{28.9}$$

$$\mathrm{NDVI} = \frac{\rho_{\mathrm{NIR}} - \rho_{\mathrm{RED}}}{\rho_{\mathrm{NIR}} + \rho_{\mathrm{RED}}} \tag{28.10}$$

$$\mathrm{TNDVI} = \left(\frac{\mathrm{Band4} - \mathrm{Band3}}{\mathrm{Band4} + \mathrm{band3}} + .5\right)^{0.5} \tag{28.11}$$

$$\mathrm{SAVI} = \left(\frac{\mathrm{NIR} - \mathrm{RED}}{\mathrm{NIR} + \mathrm{RED} + L}\right) \times (1 + L) \tag{28.12}$$

All of these indices together take care of the soil and water-related aspect in geospatial domain. Using multicriteria decision making in ARCGIS, liquefaction area map and risk assessment map could be created.

Conclusion

The effort to totally come up with an efficient, accurate geospatial model for liquefaction assessment is still ongoing. Such models are of absolute necessity in countries like India for its diverse, inaccessible challenging terrain. All the dominant parameters affecting the liquefaction phenomenon could not be considered because of the complexity of evaluation of those parameters through remote sensing. Model given by Zhu et al. [6] and Baise et al. [7] considers only Kutch region coastal liquefaction data. Thus, for the heterogenous soil condition in India, more liquefaction scenarios from different parts of India, especially North-East India, should be incorporated in such models. In future, there is scope to achieve more accurate proxy variables. However,

geotechnical investigation should be given priority in these studies to develop the models or even to validate those. Region-specific method to detect liquefied area should be used and validated through geotechnical investigations.

References

1. Castro G, Poulos SJ (1977) Factors affecting liquefaction and cyclic mobility. J Geotech Eng Div 103(6):501–516
2. Poulos SJ, Castro G, France JW (1985) Liquefaction evaluation procedure. J Geotech Eng 111(6):772–792
3. Seed HB, Idriss IM (1971) Simplified procedure for evaluating soil liquefaction potential. J Soil Mech Found Div 97(9):1249–1273
4. Seed HB, Idriss IM, Arango I (1983) Evaluation of liquefaction potential using field performance data. J Geotech Eng 10993):458–482
5. Ramakrishnan D et al (2006) Mapping the liquefaction induced soil moisture changes using remote sensing technique: an attempt to map the earthquake induced liquefaction around Bhuj, Gujarat, India. Geotech Geol Eng 24(6):1581–1602
6. Zhu J, Baise LG, Thompson EM (2017) An updated geospatial liquefaction model for global application. Bull Seismol Soc Am 107(3):1365–1385
7. Baise LG, Rashidian, V. (2017). Validation of a geospatial liquefaction model for Noncoastal Regions including Nepal. USGS Award G16AP00014. Final Technical Report
8. Oommen T et al (2013) Documenting earthquake-induced liquefaction using satellite remote sensing image transformations. Environ Eng Geosci 19(4):303–318
9. Knudsen K, Bott J (2011) Geologic and geomorphic evaluation of liquefaction case histories for rapid hazard mapping, 2011. Seismol Res Lett 82:334
10. Zhu J et al (2015) A geospatial liquefaction model for rapid response and loss estimation. Earthq Spectra 31(3):1813–1837
11. Wald DJ, Allen TI (2007) Topographic slope as a proxy for seismic site conditions and amplification. Bull Seismol Soc Am 97(5):1379–1395
12. Beven KJ, Kirkby MJ (1979) A physically based, variable contributing area model of basin hydrology. Hydrol Sci Bull 24:43–69
13. Baise LG, Rashidian V (2018) A geospatial approach to liquefaction assessment for rapid response and loss estimation. In: Geotechnical earthquake engineering and soil dynamics v: seismic hazard analysis, earthquake ground motions, and regional-scale assessment. Reston, VA: American Society of Civil Engineers, pp 1–10
14. Maurer BW, Bradley BA, van Ballegooy S (2018) Liquefaction hazard assessment: satellites vs. in situ tests. In: Geotechnical earthquake engineering and soil dynamics v: liquefaction triggering, consequences, and mitigation. Reston, VA: American Society of Civil Engineers, pp 348–356
15. Zhu J, Daley D, Baise LG, Thompson EM, Wald DJ, Knudsen KL (2014) A geospatial liquefaction model for rapid response and loss estimation. Earthq Spectra 31(3):1813–1837
16. Idriss IM, Boulanger RW (2008) Soil liquefaction during earthquakes. Monograph MNO12, EERI, Oakland, CA, 261
17. Boulanger RW, Idriss IM (2014) CPT and SPT based liquefaction triggering procedures. Report No. UCD/CGM. -14/01, Center for Geotech. Modelling, Civil & Environmental Eng., UC Davis, CA
18. Corbane C et al (2011) A comprehensive analysis of building damage in the 12 January 2010 MW7 Haiti earthquake using high-resolution satellite and aerial imagery. Photogram Eng Remote Sens 77(10):997–1009
19. Huyck CK et al (2006) Reconnaissance technologies used after the 2004 Niigata Ken Chuetsu, Japan, earthquake. Earthq Spectra 22(1_suppl):133–145

20. Kayen, R et al (2006) Terrestrial-LIDAR visualization of surface and structural deformations of the 2004 Niigata Ken Chuetsu, Japan, earthquake. Earthq Spectra 22(1_suppl):147–162
21. Kohiyama M, Yamazaki F (2005) Damage detection for 2003 Bam, Iran, earthquake using Terra-ASTER satellite imagery. Earthq Spectra 21(1_suppl):267–274
22. Mansouri B et al (2005) Earthquake-induced change detection in the 2003 Bam, Iran, earthquake by complex analysis using Envisat ASAR data. Earthq Spectra 21(1_suppl):275–284
23. Rathje, Ellen M., et al. "Damage patterns from satellite images of the 2003 Bam, Iran, earthquake." Earthquake Spectra 21.1_suppl (2005): 295–307.
24. Rathje EM, Adams BJ (2008) The role of remote sensing in earthquake science and engineering: opportunities and challenges. Earthq Spectra 24(2):471–492
25. Baik H, Son Y-S, Kim K-E (2019) Detection of liquefaction phenomena from the 2017 Pohang (Korea) earthquake using remote sensing data. Remote Sens 11(18):2184
26. McFeeters SK (1996) The use of the normalized difference water index (NDWI) in the delineation of open water features. Int J Remote Sens 17:1425–1432
27. Gao B-C (1996) NDWI—a normalized difference water index for remote sensing of vegetation liquid water from space. Remote Sens Environ 58:257–266
28. Xu H (2006) Modification of normalised difference water index (NDWI) to enhance open water features in remotely sensed imagery. Int J Remote Sens 27:3025–3033
29. Shankar Lingam S, Thomas V, Padmanaban R (2013) Inventory of liquefaction area and risk assessment region using remote sensing

Chapter 29
Reuse of Demolished Old Brick Powder in Brick Making

G. V. Ramana, Sarojini Paul, V. Ramana Murthy, and Kola Vikas

Introduction

Bricks are universally accepted walling material due to their suitability for handling along with strength and durability [1, 2]. Clay bricks have been the most sought-after materials traditionally for wide range of engineering and monumental works [3] However, this preference to clay bricks resulted in enormous depletion of top fertile soil [4]. In this connection, several researchers all over the world promoted the use of alternative materials such as waste materials like fly ash, rice husk ash [4, 5], and other industrial by-products either individually or along with clay. The following wastes are examples of exciting and suitable additives for bricks production: granite and marble wastes [6], wastewater sludge, coal fly ash, degraded municipal solid waste, waste glass sludge, quarrying wastes, bricks kiln dust, shale, sewage sludge [2], coal gangue powder, iron ore tailings, and electrolytic manganese residue which are exciting and suitable additives for bricks production [7]. Reutilization of different residues in fired bricks production [8, 9] can be a successful strategy, due to the waste production reduction as well as decreased clay utilization. It is also a practical solution to reduce environmental problems and costs in the building sector [10].

In the present work, an attempt is made to reuse the old demolished brick powder in the making of clay bricks so that the precious top soil can be saved

G. V. Ramana · S. Paul (✉) · V. R. Murthy · K. Vikas
Department of Civil Engineering, National Institute of Technology, Warangal 504006, India
e-mail: sarojinip648@gamil.com

G. V. Ramana
e-mail: gvramana@nitw.ac.in.com

V. R. Murthy
e-mail: gvramana@nitw.ac.in.com

K. Vikas
e-mail: kvikas1@student.nitw.ac.in

K. Muthukkumaran (eds.), *Soil Behavior and Characterization of Geomaterials*,
Lecture Notes in Civil Engineering 296, https://doi.org/10.1007/978-981-19-6513-5_29

Table 29.1 Chemical composition of brick powder

Oxides	SiO_2	Al_2O_3	Cao	MgO	K_2O	Na_2O	SO_3	LOI
Brick powder	54.92	14.68	6.90	2.13	2.34	1.03	0.89	7.67

from inevitable utilization for brick making. These alternative approaches could be useful for sustained development of the construction industry.

Methodology

For the present work, the following materials are used.

Brick Powder

The buildings which are built in the early 90's are in the verge of failure, their life span has come to an end. Hence, there are many such demolished buildings found near NITW campus and also inside the campus. The brick powder is collected from those demolished structures. The bricks were in deteriorated form, as they were very old. The chemical composition of brick powder is presented in Table 29.1.

Clay (Raw Material)

Clay is taken from the place called Madepally near National Institute of Technology campus, and the properties of soil are presented in Table 29.2. All the below tests were carried out as per SP 36 (Part 1): 2006.

Table 29.2 Basic properties of soil

Type of Soil	MDD, g/cc	OMC (%)	Gradation			Atterberg Limits		IS Classification and type
			Gravel, %	Sand, %	Fines, %	Liquid limit, %	Plastic limit, %	
Clay	1.82	15.45	0	11	89	59	20	CH

Mould

The mould which is used in the preparation of bricks is cube-shaped mould having dimensions 7.06 cm × 7.06 cm × 7.06 cm.

Preparation of Bricks and Test Procedure

The brick earth from a local brick manufacturing unit is collected and tested for its grain size distribution and plastic properties. The brick powder is obtained by crushing the bricks followed by sieving. Now the bricks are made from the clay brick powder mix in the proportion of 60:40, 50:50, 40:60, respectively, as shown in Table 29.3 using brick mould at suitable water content (Fig. 29.1). The wet bricks are sun-dried for 2 days before keeping them in furnace for 16 h (Fig. 29.2). The burning temperature was varied as 800 °C, 900 °C, and 1000 °C in order to understand the influence of burning temperature for the modified composition of brick earth (Fig. 29.3). Later, the burnt bricks (Fig. 29.4) were subjected compressive strength and water absorption as per IS: 1077–1992.

Table 29.3 Brick proportions and respective temperatures

Temperature (°C)	Pure earth bricks	800	900	1000
Clay: brick powder (% by dry weight)	100:0	60:40	50:50	40:60
Mix designation	CB	BS1	BS2	BS3

Fig. 29.1 Bricks prepared of different proportion

Fig. 29.2 Brick before firing

Fig. 29.3 Firing under process

Fig. 29.4 Brick after firing

Results and Observations

Influence of Brick Powder on Compressive Strength

Table 29.4 presents the compressive strength test results on bricks prepared with different brick earth (clay) and brick powder proportions namely CB, BS1, BS2, and BS3. The variation of strength values w.r.t increased brick powder is plotted in Fig. 29.5. The compressive strength of brick shows a decreasing trend, as the amount of brick powder added goes on increasing. It can also be observed from this table that the compressive strength of brick specimens is increased for 40% brick powder, and beyond this content, the strength reduction is noted for the range of temperatures used for burning the bricks. Even with 60% brick powder added with the brick earth, the strength of brick is more than 7MPa which corresponds to the second-class brick.

Table 29.4 Influence of brick power on compressive strength values

Proportions (% by weight) break earth-brick powder	Mix designation	Brick strengths (N/mm^2)/temperatures (°C)		
		800	900	1000
100–0	CB	6.4	10.25	11.55
60–40	BS1	16.25	14.3	12.6
50–50	BS2	13.1	10.65	9.55
40–60	BS3	10.45	9.6	9.15

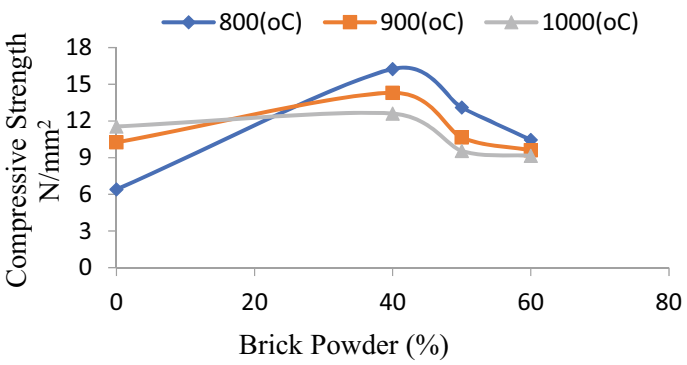

Fig. 29.5 Variation of strength values w.r.t increased brick powder

Table 29.5 Water absorption values

	Water absorption values (%)		
	800 (°C)	900 (°C)	1000 (°C)
CB	6.4	10.25	11.55
BS1	16.25	14.3	12.6
BS2	13.1	10.65	9.55
BS3	10.45	9.6	9.15

Influence of Burning Temperature on Compressive Strength

It can be seen from Table 29.5 that conventional bricks, the compressive strength is increasing with temperature. However, for the bricks with brick powder mix, the burning temperature beyond 800 °C is regulating in lower strength. This trend could be attributed to the presence of pre-burnt brick powder in the mix.

Water Absorption

The percentage of water absorption of brick specimens is plotted in Fig. 29.6 and also presented same in Table 29.4. It can be observed that the percentage of water absorption across the specimen is in the range of 7.44–14.97%. For the strength greater than 10.5 MPa (for I class brick), the water absorption is less than 15%, and for II class brick strength (7–10.5 MPa), the water absorption is in the range 9.15–14.3%. These water absorption values are within the allowable limits as per IS: 1077-1989.

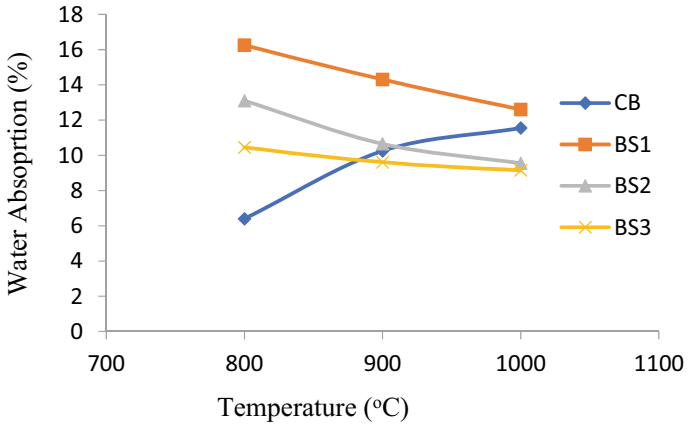

Fig. 29.6 Water absorption values with variation in temperature

Conclusions

The following conclusions are drawn based on the laboratory study carried out on bricks made by admixing old brick powder with brick earth.

1. The addition of old brick powder has shown significant increase in the compressive strength of prepared bricks. Addition of 40% brick powder by the weight of dry soil is found to be optimum for strength gain within the range of temperatures tried in this study.
2. The strength of conventional brick is increasing with increasing burning temperature. However, upon the addition of brick powder, burning temperature beyond 800 °C is causing reduction in strength.
3. The water absorption of brick specimens is in the range of 7–13% which is within the allowable range of 12.5–20% as per IS specifications.

This study indicates that use of old brick powder in the brick making could be environmentally sustainable method by saving considerable top fertile soil from its utilization in brick making. Further, the disposal problem of old demolished brick could be simultaneously addressed.

References

1. Konta J (1995) Clay and man, clay raw materials in the service of man. Appl Clay Sci 10:275–335
2. Dondi M, Marsigli M, Fabbri B (1997) Recycling of industrial and urban wastes in brick production—a review. Tile Brick Int 13(3):218–225
3. Orhan M, Demir I (1998) An experimental research on reduction of shrinkage limit values of the brick clay. Gazi University Fen Bilimleri Dergisi 11(2):383–390
4. Youssef N, Rabenantoandro AZ, Dakhli Z et al (2019) Reuse of waste bricks: a new generation of geopolymer bricks. SN Appl. Sci. 1:1252. https://doi.org/10.1007/s42452-019-1209-6
5. Subashi De Silva GHMJ et al (2018) Effect of waste rice husk ash (RHA) on structural, thermal and acoustic properties of fired clay bricks. J Build Eng 18:252–259
6. Dondi M, Marsigli M, Fabbri B (1997) Recycling of industrial and urban wastes in brick production—a review (Part 2). Tile Brick Int 13(4):302–315
7. Ducman V, Kopar T (2007) The influence of different waste additions to clay product mixtures. Mater Technol 41(6):289–293
8. Dos Reis GS et al (2020) Fabrication, microstructure, and properties of fired clay bricks using construction and demolition waste sludge as the main additive. J Cleaner Prod 258:120733
9. Karaman S, Ersahin S, Gunal H (2006) Firing temperature and firing time influence on mechanical and physical properties of clay bricks. J Sci Ind Res 65:153–159
10. Alleman J, Berman N (1984) Constructive sludge management: biobrick. J Environ Eng 110(2):301–311

Chapter 30
Cycle Time Analysis and Optimization of Resources, Cost, and Time Involved in Marine Piling Construction

K. Muthukkumaran, V. V. G. Sai Aditya, and P. Devahi

Introduction

For the past few decades, pile foundation has been used for various marine structures such as wharves and jetties. Marine piling is the mechanism of supporting the offshore structures by deep foundations into ground sea level. In general, optimization of construction projects for minimum resources, time, and maximum profit has been of greater importance [1]. Planning and scheduling aim at the proper execution of work according to the project plan schedule and can apply remedial measures in the event of any several deviations occur [2]. Monitoring the progress of the project with respect to the time, performance, scheduling, and resources throughout the actual implementation of the project can identify the delay area which requires timely proceedings to be taken [3]. The task of finishing off a construction site within an estimated time is the most crucial task among project managers [4]. Unavoidable delays and costs in projects may happen due to improper coordination and communication between the line managers [5]. Optimizing the performance of the different techniques adopted at one stage of the construction process may not be beneficial if the methods used are not up to the efficient level [6]. The time–cost analysis is a crucial parameter in quick and high-budget building projects, which actually demonstrates the alternative paths and optimum one for faster completion of any project [7]. The conventional methods of time–cost analysis have not provided the limelight on typical project characteristics, mainly precedence relations among the activities, constraints involving external time, and activity planning, which are more significant factors in illustrating the actual building [8].

K. Muthukkumaran · V. V. G. Sai Aditya · P. Devahi (✉)
National Institute of Technology, Tiruchirappalli, India
e-mail: devahi.civil@gmail.com

K. Muthukkumaran (eds.), *Soil Behavior and Characterization of Geomaterials*,
Lecture Notes in Civil Engineering 296, https://doi.org/10.1007/978-981-19-6513-5_30

In the present study, the complete cycle time of marine piling of two live projects has been evaluated, and optimization has been done with respect to identifying the optimum resources, minimum time, and cost consumed.

Study Region

The live projects considered for the present study are Mumbai Coastal Road Project (MCRP) Package-1 and Mumbai Trans Harbour Link Project (MTHL), estimated at around ₹14,262 crores. The MCRP (Package-1) comprises a 3.82-km-long highway (between CH 5+900 m and CH 9+720 m) proposed from Priyadarshini Park to Baroda Palace, along with the interchanges at Amerson Garden and Haji Ali. The Haji Ali interchange furnishes the connections between the existing Khan Abdul Gaffer Khan Road. This particular bridge connects the Sewri South Mumbai and Chirle village, whereas the road bridges Mumbai Pune Expressway and Western Freeway. The sea link comprises a 27-m six-lane highway, including the crash barrier, an edge strip, and two emergency exit lanes. This project was awarded by the MMRDA in November 2017. It got initiated in April 2018, and the expected completion period is 54 months (Fig. 30.1).

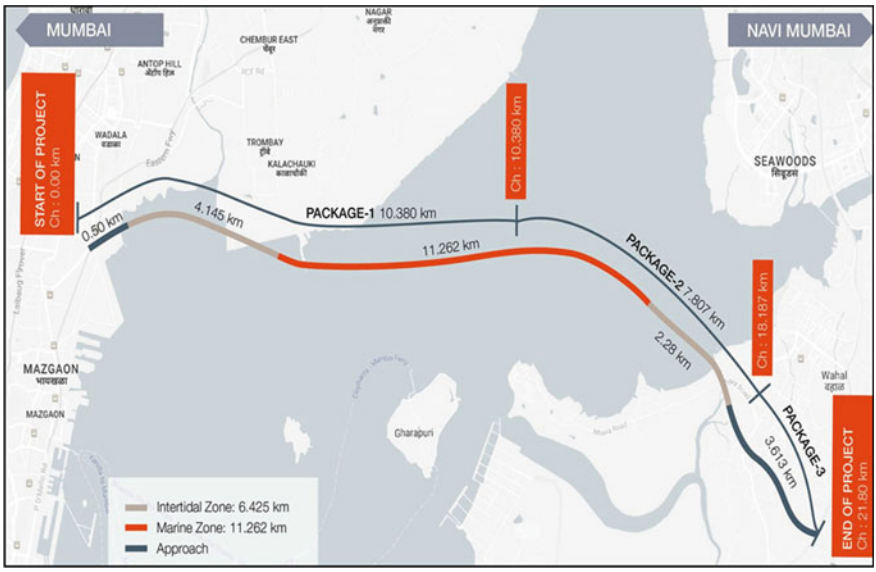

Fig. 30.1 Layout of the MTHL project

Methodology

The project is divided into two phases. Phase 1 deals primarily with time and its optimization. Phase 2 deals with the optimization of cost and resources. Each phase consists of three parts. Cycle time data of both the projects shall be prepared in the first part. Optimization of the same shall be carried out with different variables in the second part. Results shall be analyzed and compared in the third part.

Drilling is done using Bauer BG 25. The thickness of the liner is 6mm. The total drilling duration, including the idle and breakdown time, is 1.5 days, which is almost double the time excluding the idle and breakdown time. The total time taken for drilling, reinforcement, and concreting is 36.83, 32.57, and 2.64. The last time in which a pile of 1m diameter and 10.1m deep can be completed is 35.2 h. Total drilling time, including idle time, is 36.83 h, whereas actual drilling time is 18.33 hours. Idle time is almost 18.5 h.

Results and Discussions

Labor, material, & plant cost (direct cost) are calculated for two projects. The total direct cost incurred for executing a marine pile in MCRP is ₹633,159. Indirect is considered 13% of the direct cost, accounting for ₹82,311. The total direct cost incurred for executing a marine pile in MCRP is ₹3639,315. Indirect is considered 13% of the direct cost, around ₹473,111. Crashing is an element introduced at a lesser cost, mainly for enhancing the resources. Cost and schedule trade-offs are utilized for fetching the high possible compression, contributing the least incremental cost. The average productivities observed for the rig from the drilling cycle time of the MCRP project are 1.38 and 1.08, whereas the MTHL project is reflected in the range of 1.88 and 1.00. Thus, it is evident that the strata are soil, then RCD is better than rig and vice-versa in the case of the weathered rock.

The average time required for drilling is 18.33 h, whereas if the equipment works at 100% efficiency, the time required is 10.64 h, and 42% of the time can be saved per pile in MCRP (Refer Table 30.1). The maximum % of the time that can be saved by improving the productivity in MCRP is 5%. The maximum % of the time that can be saved by improving the productivity in MTHL is 6%. The amount of cost saved through time optimization has been summarized in Table 30.2.

Time optimization of 19 % reflected the increased cost of 1.29%. Similarly, by optimizing the time by 17% and 14%, the % increase in cost is 1.25% and 1%, respectively. In the MTHL project, optimizing the time by 9% and 5%, the % increase in cost is 0.48% and 0.21%, respectively (Figs. 30.2 and 30.3).

Table 30.1 Summary of time optimization results in both projects

Description	MCRP (RIG)	MTHL (RCD)
Drilling productivity in soil	1.38 m/h	1.88 m/h
Drilling productivity in weathered rock	1.08 m/h	1.00 m/h
Maximum saving of time in days	72 days	108 days
Maximum % savings of time	5%	6%
Maximum no of days optimized	87 days	169 days
Maximum % of time optimized	6%	10%
Method of placement of concrete	Tremie	Boom Placer

Table 30.2 Summary of cost optimization results in both projects

Description	MCRP (RIG)	MTHL (RCD)
Cost of executing a marine pile (direct cost)	₹633,159	₹3,639,315
Cost of executing a marine pile (indirect cost)	₹82,311	₹473,111
Cost of executing a marine pile (total cost)	₹715,470	₹4,112,426
Minimum cost of executing a pile	₹638,565	₹3,676,291
Maximum % of cost optimized	0.83%	1.02%
Normal duration of executing a pile	20.97 h	86.4 h
Least duration of executing a pile	12.64 h	76.1 h

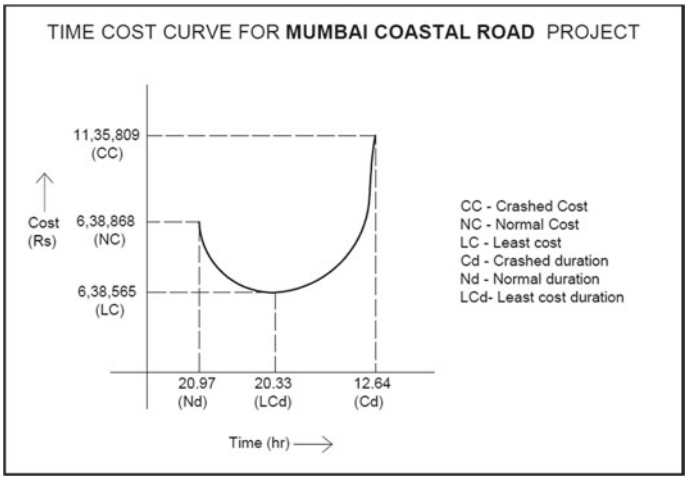

Fig. 30.2 Time cost curve of MCR project

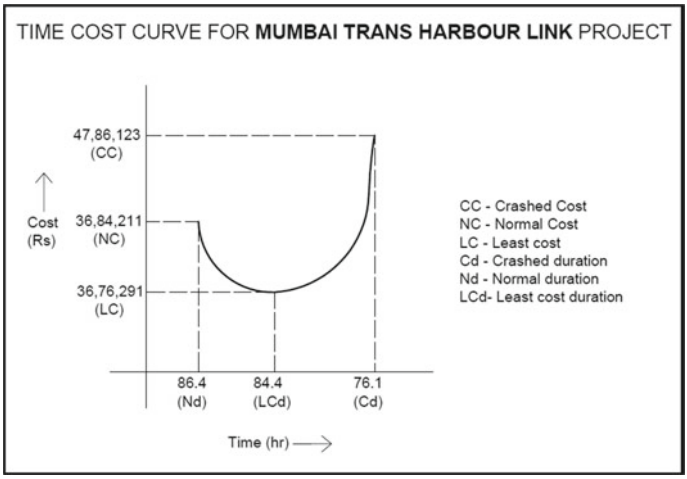

Fig. 30.3 Time cost curve of MCR project

The productivity of RCD is higher than the rig in soil strata. The productivity of the rig is higher than RCD in weathered rock strata. 42% of the time can be saved per one pile in MCRP and 9% of the time in MTHL when the equipment works at its 100% efficiency. A maximum of 6% of the total project duration can be saved in MTHL, and 5% of the total project duration can be saved in MCRP at peak productivity. The maximum % of the cost that can be optimized in MCRP and MTHL is 0.83% and 1.02%, respectively.

Conclusions

- Reverse circulation drilling (RCD) rig can drill 0.5m more depth when compared with rotary drilling rig in the soil strata in a span of one hour.
- Rotary drilling rig can drill 0.08 m more depth when compared with RCD rig in the weathered rock strata in a span of an hour.
- For a pile of 1m diameter and 10 m deep, tremie concreting takes less time than boom placer concreting. A savings of 2% in time is observed by tremie concreting.
- For a pile of 2.2 m diameter and 24 m deep, tremie concreting takes more time than boom placer concreting. A saving of 19% of the time is observed by boom placer concreting.

References

1. Mali P, Lokhande A, Kadam S, Shirole S, More P, Velhal A (2017) Time and cost optimization by MSP software. Int J Eng Sci Res Technol 6:400–407
2. Shu W, Cai K, Xiong NN (2021) Research on strong agile response task scheduling optimization enhancement with optimal resource usage in green cloud computing. Futur Gener Comput Syst 124:12–20. https://doi.org/10.1016/j.future.2021.05.012
3. Chassiakos AP, Sakellaropoulos SP (2005) Time-Cost optimization of construction projects with generalized activity constraints. J Constr Eng Manag 131:1115–1124. https://doi.org/10.1061/(asce)0733-9364(2005)131:10(1115)
4. Cui R, Han W, Su X, Zhang Y, Guo F (2020) A multi-objective hyper heuristic framework for integrated optimization of carrier-based aircraft flight deck operations scheduling and resource configuration. Aerosp Sci Technol 107:106346. https://doi.org/10.1016/j.ast.2020.106346
5. Jaswanth SMB, Kumar P (2018) Optimization of planning, scheduling, and control of high rise construction projects. Int J Civ Eng Technol 9:914–922
6. Rajguru A (2015) Effective techniques in cost optimization of construction project: an review. Int J Res Eng Technol 04:464–469. https://doi.org/10.15623/ijret.2015.0403078
7. Li S, Zhao Y, Xiao W, Yue W, Wu T (2021) Optimizing ecological security pattern in the coal resource-based city: a case study in Shuozhou City China. Ecol Indic 130:108026. https://doi.org/10.1016/j.ecolind.2021.108026
8. Zayed TM, Halpin DW (2005) Pile construction productivity assessment. J Constr Eng Manag 131:705–714. https://doi.org/10.1061/(asce)0733-9364(2005)131:6(705)

Chapter 31
Modelling Soil Water Retention Curve for Cohesive Soil Using Artificial Neural Network

A. G. Sharanya, M. Heeralal, and T. Thyagaraj

Introduction

A considerable component of a pavement's construction is compacted subgrade soil. The increased structural capability of the subgrade soil can improve pavement strength, culminating in thinner and more expensive pavement systems. Unsaturated subgrade soil is prevalent in the compacted subgrade. In pavement design, the resilient modulus (Mr) of the pavement materials is found to be the essential input property. There are many prediction models for determining the resilient modulus of compacted subgrade soils which can be considered in two main categories: Stress-dependent models and moisture-sensitive models. The importance of considering the effect of moisture variation for resilient modulus determination has been highlighted by many researchers [1, 2]. The moisture-dependent models are developed with the suction potential as the main parameter. The consideration of matric suction has been widely accepted for the prediction of resilient modulus of natural soils evaluated, whereas little research has affirmed the use of total suction potential which is a sum of matric and osmotic suction [3].

The evaluation of pavement subgrade performance by taking modulus variation with suction into account must be done systematic way. Soil suction is a fundamental concept that describes a soil's modulus behaviour [4]. The determination of suction for soil can be carried out by either direct or indirect measurement procedures such as pressure plate method, tensiometers, and filter paper method. These experimental procedures are time-consuming and highly sensitive to testing conditions. Thus the

A. G. Sharanya (✉) · M. Heeralal
National Institute of Technology, Warangal, India
e-mail: sharanyaag@student.nitw.ac.in

T. Thyagaraj
Indian Institute of Technology, Madras, India

K. Muthukkumaran (eds.), *Soil Behavior and Characterization of Geomaterials*,
Lecture Notes in Civil Engineering 296, https://doi.org/10.1007/978-981-19-6513-5_31

determination of SWCC for a particular soil is a tedious process. The works of literature [5, 6] affirm the use of several empirical procedures to determine the SWCC by determining the fitting parameters of water content and suction data fitting equations.

There exist very few research works [7–9] that have utilized an artificial intelligence platform to observe the efficiency of basic soil properties to determine the suction potential of various types of geomaterials. The works have been focused on determining the correlation between basic soil properties and the fitting parameters of the Fredlund and Xing equation, 1994 specific to unbound materials using an artificial neural network (ANN). Some works have identified genetic programming (GP) as an efficient platform to generate SWCC by predicting the gravimetric water content corresponding to chosen suction values.

The available literature sources confirm the necessity to develop a simplified procedure for generating SWCC using basic soil properties and the current study focuses on the applicability of ANN to develop the SWCC for fine-grained subgrade soils of varying plasticity nature. The study addresses the network model suitable to predict the fitting parameters of the widely accepted Fredlund and Xing Equation, 1994 [10] from five basic soil properties.

Numerical Analysis

Artificial Neural Network

Artificial neural networks (ANNs) are algorithms that are inspired by the architecture and characteristics of the human brain. These platforms encourage ANNs to perform tasks like learning, reasoning, recognizing, decision making, quantitative forecasting, namely regression, and so on, with the help of the intellectual, which can provide a variety of responses. In the largest context, these systems have an input and output layer; additionally, they become multilayer ANNs due to the presence of one or more hidden layers in the network structure.

A learning algorithm known as backpropagation will be used for the current study. This is one of the most efficient learning algorithms used to train multilayer ANNs, and it allows the weight values of connections to be predicted in an iterative process by this network. This operation is performed by upgrading weights to the previous layer of the network, i.e. backward, and thus gradually reducing the deviation from the real value, following the deviation/error value transfer that results in outputs from artificial nodes within each layer. The transfer function can be a sigmoidal, hyperbolic tangent, binary step, or radial basis. The transfer function used in this study is finalized by performing numerous trials of training sessions.

Database Collection

The study requires a huge dataset for the efficient generation of the neural network model to predict the correlation of basic soil properties with the fitting parameters of Fredlund–Xing Eqs. (31.1) and (31.2) (Fredlund and Xing 1994).

$$S = C(h) \times \left[\frac{1}{\left\{ \ln\left[e + \left(\frac{h}{a_f} \right)^{b_f} \right] \right\}^{c_f}} \right] \tag{31.1}$$

where,

Correction factor defined as

$$C(h) = 1 - \frac{\ln\left(1 + \frac{h}{h_r}\right)}{\ln\left[1 + \left(\frac{1.45 \times 10^5}{h_r}\right)\right]} \tag{31.2}$$

S degree of saturation (%)

H soil matric suction (psi)

a_f, b_f, c_f, h_r fitting parameters.

The fitting parameter a_f is attributed to the air entry value of the soil in psi, b_f is correlated with the rate of water removal from the soil as suction augments, c_f is associated with the water content corresponding to the soil residual content, and the last parameter h_r is related to the soil residual suction (psi).

NCHRP 9-23A [11] was preferred as the database containing the tested results of basic soil properties such as grain size distribution, liquid limit, plasticity index, gravimetric water content, saturated volumetric water content, saturated hydraulic conductivity, and California bearing ratio, as well as fitting parameters for the FX Eq. (31.1).

The dataset contained 3500 samples with plasticity index values greater than 10%. The database was selected because it contained all of the necessary soil properties to achieve the study's goal.

Development of Neural Network

The neural network (NN) was framed with five input parameters provided as an input layer, one hidden layer with 'N' neurons, and one output layer. The output parameter includes a_f, b_f, and c_f. The study utilized MATLAB R2018a aided with the "neural net fitting" application to generate the feasible ANN model.

Several trials of varying the number of neurons in the hidden layer and varying the quantum of samples used for testing, validating, and training the model have been used to develop the neural network that worked best to correlate the selected input parameters with the fitting parameters. The Levenberg–Marquardt backpropagation method was chosen to develop the model, ensuring that the measured and predicted values were as close as possible.

Results and Discussion

The neural network model finalized for the proposed input and output parameters is shown in Fig. 31.1. The three-layered NN model adopted for this study was obtained from training 75% of the dataset and 15% of data to validate and test the proposed model. The best network was selected based on the minimum RMSE and maximum R-value of the output [7].

Figures 31.2, 31.3 and 31.4 show the neural network output comparing the measured fit parameters (a_f, b_f, and c_f) with the predicted values. The proposed ANN model has an R^2 value of 0.82 for predicting the b_f parameter, where the data are distributed in a certain range; however, the distribution along the line of equity is more uniform in the prediction of a_f and c_f, and the R^2 value is lower as compared for b_f. This confirms the significant contribution of the ANN model to the reliable prediction of matric suction of plastic subgrade soils.

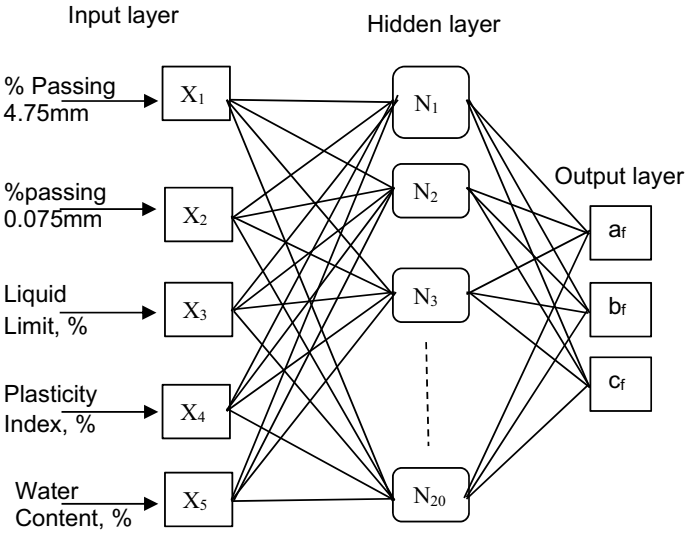

Fig. 31.1 Proposed optimal artificial neural network model for predicting the fit parameters

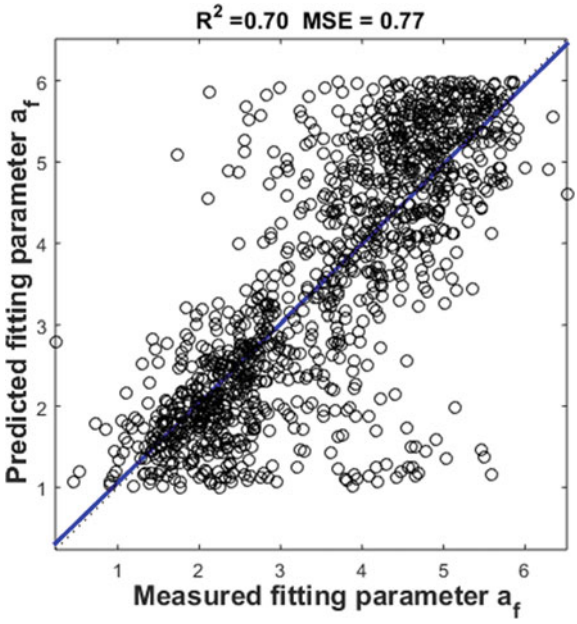

Fig. 31.2 Measured versus the predicted value of parameter a_f

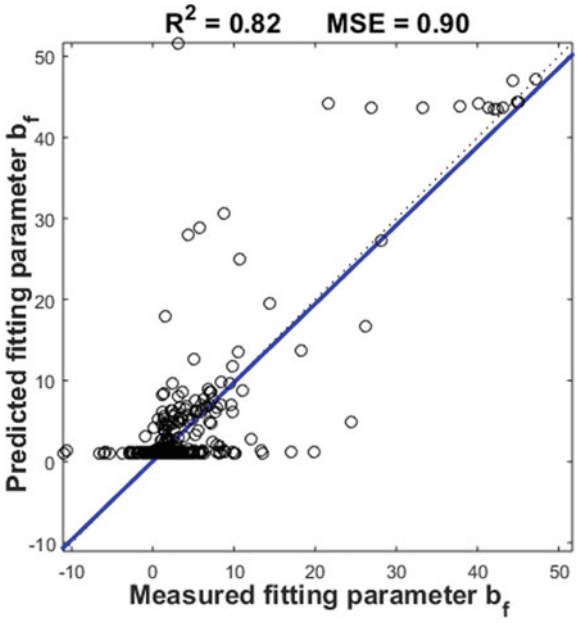

Fig. 31.3 Measured versus the predicted value of parameter b_f

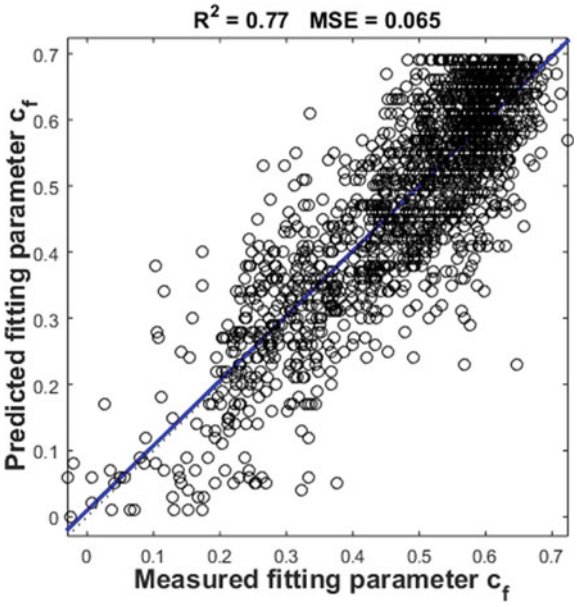

Fig. 31.4 Measured versus the predicted value of parameter c_f

Table 31.1 Range of parameters used for optimal ANN model

SWCC fit parameter	Range	No. of samples	R^2 value
a_f (kPa)	10–45	1738	0.70
b_f	0.5–0.99	1152	0.82
c_f	0.01–0.69	2293	0.77

The prediction accuracy of the proposed optimal NN model is limited to the selective range of fit parameter values as listed in Table 31.1. There were numerous trials in developing the model which was framed by setting limits in the range of fit parameter values selected for developing the ANN model.

Although the proposed ANN model can effectively predict the SWCC fitting parameters, the SWCC prediction accuracy must be investigated with the existing data sources and experimental results. The sensitivity analysis of the independent soil properties needs to be carried out to understand the influence and ambiguity associated with the chosen soil properties.

References

1. Khoury NN, Zaman MM (2004) Correlation between resilient modulus, moisture variation, and soil suction for subgrade soils. Transp Res Record 99–107
2. Sawangsuriya A, Edil TB (2005) Evaluating stiffness and strength of pavement materials. In: Proceedings of the institution of civil engineers: geotechnical engineering, vol 158, pp 217–230

3. Rahman M, Tarefder R (2015) Assessment of molding moisture and suction on resilient modulus of lime stabilized clayey subgrade soils. Geotech Test J 38(6):840–850
4. Sawangsuriya A, Edil TB, Bosscher PJ (2009) Modulus-suction-moisture relationship for compacted soils in Postcompaction State. J Geotech Geoenvironmental Eng 135(10):1390–1403
5. Zapata CE, Houston WN, Walsh KD (2003) Soil-water characteristic curve variability. Adv Unsaturated Geotech 99:84–124
6. Zapata CE, Perera YY, Houston WN (2009) Matric suction prediction model in new AASHTO mechanistic-empirical pavement design guide. Transp Res Rec 2101:53–62
7. Saha S, Gu F, Luo X, Lytton RL (2018) Prediction of soil-water characteristic curve using artificial neural network approach. Am Soc Civil Eng (ASCE) 124–134
8. Johari A, Ghassem H, Arsalan G (2006) Prediction of soil–water characteristic curve using genetic programming. J Geotech Geoenvironmental Eng 132
9. Aubertin M, Mbonimpa M, Bussière B, Chapuis RP (2003) A model to predict the water retention curve from basic geotechnical properties. Can Geotech J 40(6):1104–1122
10. Fredlund DG, Anqing X (1994) Equations for the soil-water characteristic curve. Can Geotech J 31(4):521–532
11. Zapata CE (2010) A national database of subgrade soil-water characteristic curves and selected soil properties for use with the MEPDG. NCHRP Report 9–23A, Washington, D.C

Chapter 32
A Comparative Study of Undrained Shear Strength of Offshore Cohesive Soils by Different Methods

T. Chikkanna, C. R. Parthasarathy, and Prashanth Talkad

Introduction

There are numerous test methods available to estimate the undrained shear strength of cohesive deposits, and there are limitations on their applications based on the condition of the samples. The most common laboratory and field tests methods to determine the shear strength of soil are triaxial compression test, unconfined compression test, falling cone test, lab vane shear test, pocket penetrometer, cone penetration test, in situ vane test, etc. [1]. Among all the test methods adopted in the offshore geotechnical investigation, the undrained shear strength (Su) by torvane (TV), miniature vane (MV), pocket penetrometer (PP), and unconsolidated undrained triaxial test (UU) on the undisturbed samples recovered is very widely used in arriving the ground model. This paper attempts to present from a large database of authors' works, the difference of the undrained shear strength from these methods, and a recommendation to develop the ground model.

T. Chikkanna (✉) · C. R. Parthasarathy · P. Talkad
R&D, Sarathy Geotech and Engineering Services Pvt. Ltd, Bangalore, India
e-mail: chikkanna@sarathygeotech.com

C. R. Parthasarathy
e-mail: partha@sarathygeotech.com

P. Talkad
e-mail: prashanth@sarathygeotech.com

K. Muthukkumaran (eds.), *Soil Behavior and Characterization of Geomaterials*,
Lecture Notes in Civil Engineering 296, https://doi.org/10.1007/978-981-19-6513-5_32

Sampling and Testing Methods

Sampling

Undisturbed samples (UDS) are obtained with a wire line operated system using appropriate wall thickness sampling tubes based on nature of the sediment. Typically, the UDS samples are collected in 1000-mm-long and 74/76-mm-diameter tubes. The database of the undrained shear strength presented in this paper comprises tests on samples from offshore India (East Coast & West Coast), Middle East (Iran & Saudi Arabia), and Southeast Asia (Indonesia, Malaysia, and Vietnam). The variation in basic properties of the samples is summarized in Table 32.1 The consistency of cohesive soils as outlined by Karl et al. [2] is presented in Table 32.2 for quick reference.

Table 32.1 Soil index properties

S. No.	Name of the experiments	Range of values
1	Moisture content (%)	10 to 70
2	Bulk density (kN/m^3)	15 to 22
3	Submerged density ((kN/m^3)	5–13
4	Liquid limit (%)	27–113
5	Plastic limit (%)	15–42
6	Percentage finer (passing 75 μm, %)	66–99
7	Percentage of SILT (%)	42–69
8	Percentage of CLAY (%)	3–90
9	Specific gravity	2.64–2.77

Table 32.2 Soil classification based on shear strength

S. No.	Soil consistency	Undrained shear strength (kPa)
1	Very soft	< 12
2	Soft	12 to 25
3	Firm	25 to 50
4	Stiff	50 to 100
5	Very stiff	100 to 200
6	Hard	> 200

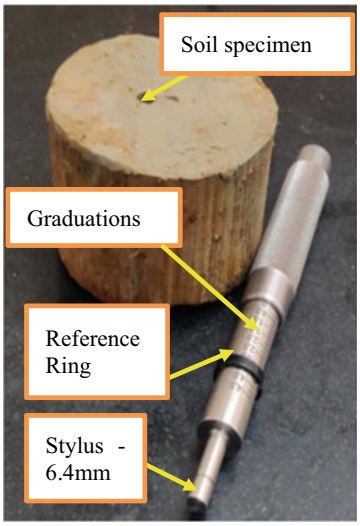

PP-Adapter for testing very low shear strength

Fig. 32.1 Pocket penetrometer apparatus

Pocket Penetrometer

The pocket soil penetrometer (PP) is a simple tool to directly evaluate the unconfined compressive strength of cohesive soils [3]. The test procedure is being developed by ASTM Standards Committee bearing No WK 27,337.

The pocket penetrometer (PP) shown in Fig. 32.1 is a small apparatus to obtain a very quick approximate shear strength of cohesive soil on-board geotechnical vessel. Normally, the pocket penetrometer test is carried out by pushing the stylus into the flat soil surface up to the calibrated groove machined into the stylus at 0.25 (about 6.4 mm—one diameter of stylus) from the end. The resistance of a calibrated internal spring registers the penetration force on an engraved scale. It has a direct-reading scale in kg/cm^2, which corresponds to equivalent unconfined compressive strength (q_u), and hence, the half value of q_u is equal to the value of undrained shear strength (Su). When testing extremely low shear strength cohesive soils, an adapter can be used which scales the area by 16 times, thus reading obtained using the adapter is divided by 16 times for the determining UCC values with adaptor. However, in the present database no pocket penetrometer values were reported for shear strength of less than 25 kPa.

Torvane

Torvane, shown in Fig. 32.2, is a small hand-operated vane device to estimate the undrained shear strength of cohesive samples [4]. It consists of a disc with thin radial

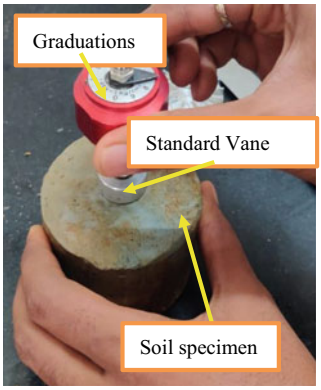

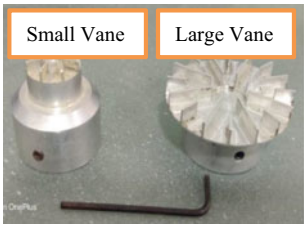

TV- Adapters

Fig. 32.2 Torvane (TV)

Table 32.3 Torvane usage

Vanes	Maximum undrained shear strength (kPa)	Multiplication constant	Usage and remarks
Standard	0–20	0.2	Very soft CLAY
Large	0–100	1	Firm to stiff CLAY
Small	0–250	2.5	Stiff to very stiff CLAY

vanes protruding from one face. The disc is pressed against a flat surface of the soil until the vanes are fully embedded. Torque is then applied to the disc by torsional spring (with a uniform vertical pressure) until the soil enclosed within the vanes is sheared from the sample. The rotation of the torsion spring is calibrated to indicate the soil shear strength (S_u) directly. This device has three vanes, namely small (for high shear strength with a multiplication factor of 2.5), standard (with a multiplication factor of unity), and large shear vane (with a multiplication factor of 0.2). The usage and stress ranges from the torvane are summarized in Table 32.3**.**

Miniature Vane

ASTM D 4648 M [5] outlines miniature vane (Fig. 32.3) as a standard test method to measure the undrained shear strength of cohesive soils typically used in offshore geotechnical laboratories. The test is conducted by inserting a 4-bladed vane into the undisturbed soil and activating the torque by manual or electrical motor. As the spring rotates slowly, the torque transmitted from the vane to the soil increases until soil shear failure occurs. The undrained shear strength of the sample is computed from the observed angular displacement of the calibrated spring by using Eq. (32.1).

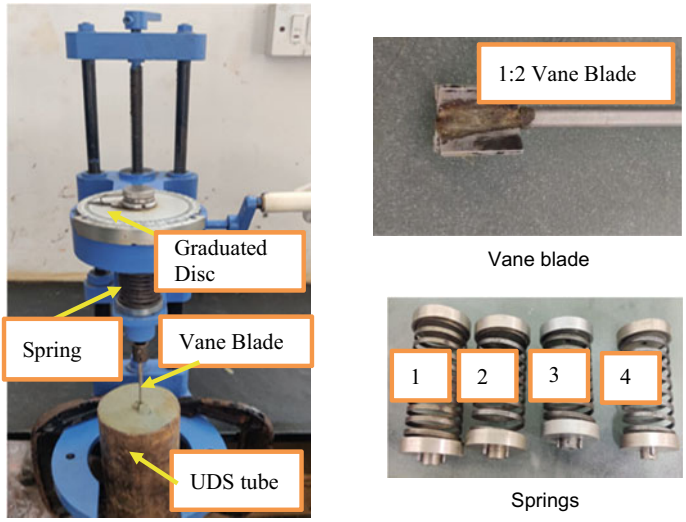

Fig. 32.3 Miniature vane (MV)

$$T = \tau * K \tag{32.1}$$

Where

T torque, lbf·ft [N·m]

τ undrained shear strength, lbf/ft^2 [Pa], and

K vane blade constant, ft^3 [m^3]

For various combinations of vane size and spring stiffness, a calibration constant (kPa/degree) can be tabulated for ready reference to determine the undrained shear strength.

Although Bureau of Indian Standards reference IS 2720 (Part XXX) 1980-reaffirmed 2007 presents the lab vane test procedures, the capacity is limited to only 50 kPa vis-à-vis about 160-180 kPa by ASTM 4648. Therefore, IS 2720 (Part xxx) procedures are not referenced.

Unconsolidated Undrained Triaxial Test (UU)

In this test, a soil specimen is enclosed in a thin rubber membrane and subjected to a confining pressure equal to the computed total overburden pressure at sample depth or a maximum of 3000 kPa. The specimen is then loaded axially (at a constant rate of strain) to failure or 15% of the initial height of the specimen, whichever is earlier [3, 6]. No drainage is allowed either under the influence of the confining pressure or during the axial loading. The undrained shear strength is computed as one-half

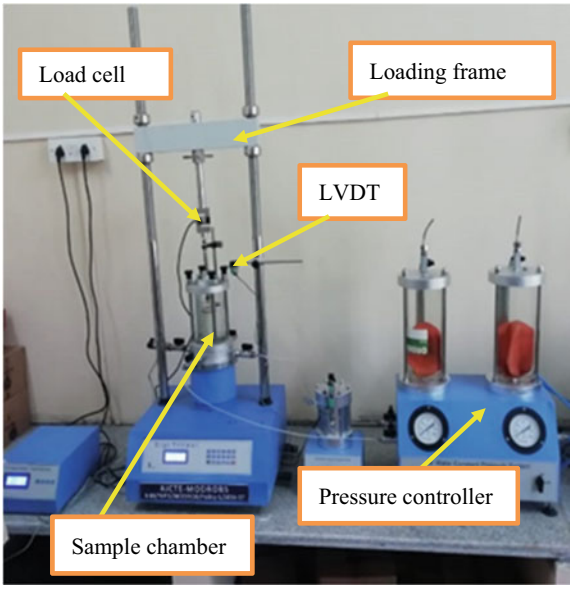

Fig. 32.4 UU triaxial setup

the difference between the total axial stress at failure and confining pressure (1/2 of deviator stress) see Fig. 32.4.

The above four methods are routinely used in every offshore geotechnical investigation campaigns to measure the undrained shear strength.

Results and Discussion

A total of 346 data points are presented in this paper collated from the author's database. The depth vs undrained shear strength from all four methods are illustrated in Figs. 32.5, 32.6, 32.7 and 32.8. For Soft to Very Soft CLAYS, MV and TV are performed and comparison presented in Fig. 32.9, which suggests both TV and MV are in very good comparison for Very Soft CLAY range (up to 12.5 kPa), while TV measures slightly higher shear strength in the Soft CLAY (12.5–25 kPa) range. Since UU triaxial test cannot be performed for Su less than 20 kPa due to difficulty in handling the specimens, the same is not presented, and pocket penetrometer with a large adaptor has also not been presented due to limited data points.

Figure 32.10 presents the comparison of Su values between torvane (TV) and UU triaxial. In the Su range of 25–150 kPa, both TV and MV have reasonably good agreements. Beyond 150 kPa, TV underpredicts the shear strength; perhaps this same can be attributed to the operator error in not applying uniform vertical pressure during shear; thus the TV could slip instead of shear. Therefore, with undrained shear strength above 150 kPa, more reliance to UU triaxial shall be made.

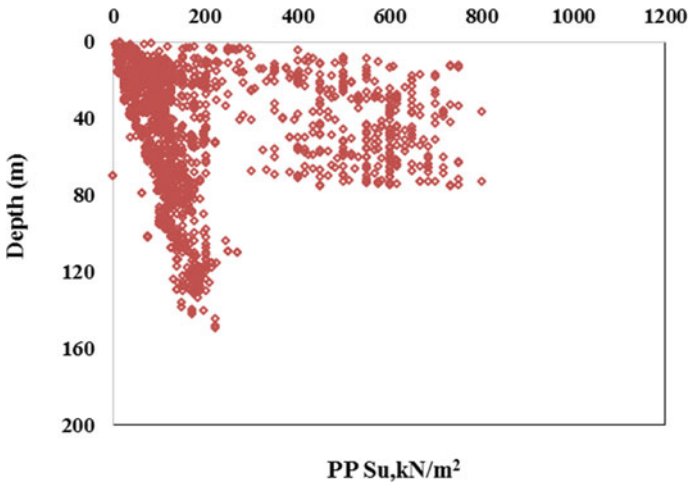

Fig. 32.5 Undrained shear strength (kN/m^2) by pocket penetrometer versus depth

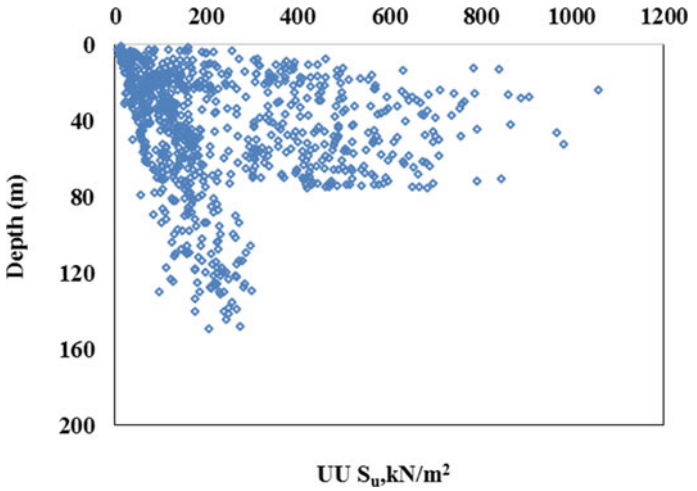

Fig. 32.6 Undrained shear strength (kN/m^2) by UU triaxial test versus depth

Figure 32.11 presents the comparison of Su values between miniature (MV) and UU triaxial. In the Su range of 25–150 kPa, both TV and MV have very good agreements. Beyond 150 kPa, MV limits the capacity of the test, and therefore, undrained shear strength UU triaxial is the preferred method.

Figure 32.12 presents the comparison of Su values between pocket penetrometer (PP) and UU triaxial. In the Su range of 25–250 kPa, both PP and UU have reasonably good agreements. Beyond 250 kPa, PP has large scatter compared to the undrained shear strength. Since UU triaxial considers the stress history by applying confining

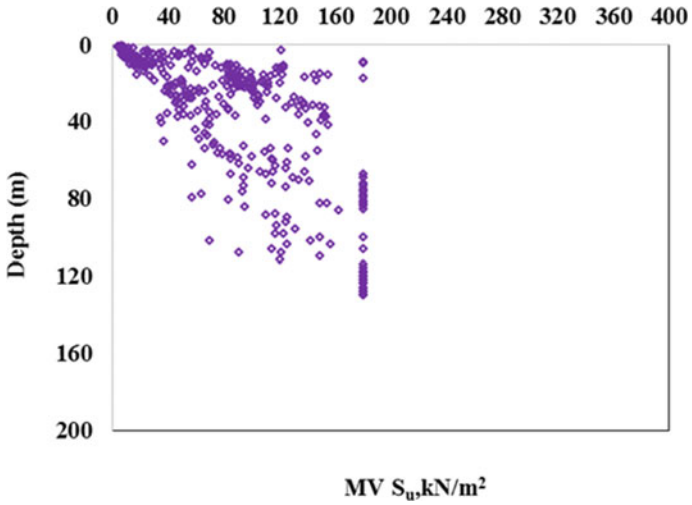

Fig. 32.7 Undrained shear strength (kN/m^2) by miniature vane test versus depth

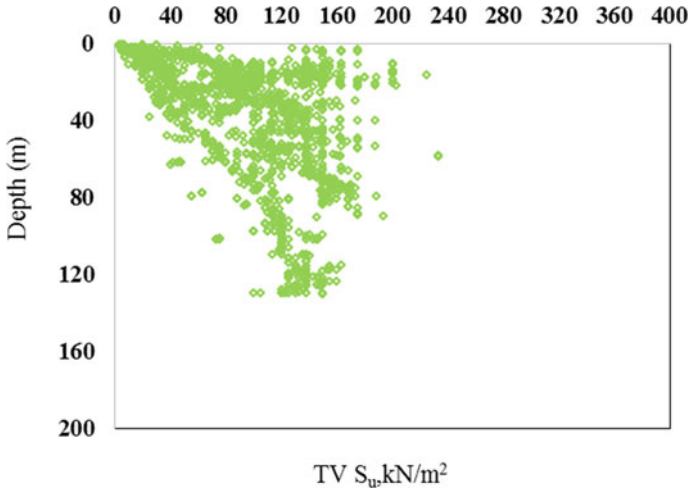

Fig. 32.8 Undrained shear strength (kN/m^2) by Torvane test versus depth

pressure, UU is a preferred method for Hard CLAYS to Very Hard CLAYS. Essentially, these Hard CLAYS are heavily over consolidated from offshore Middle East locations.

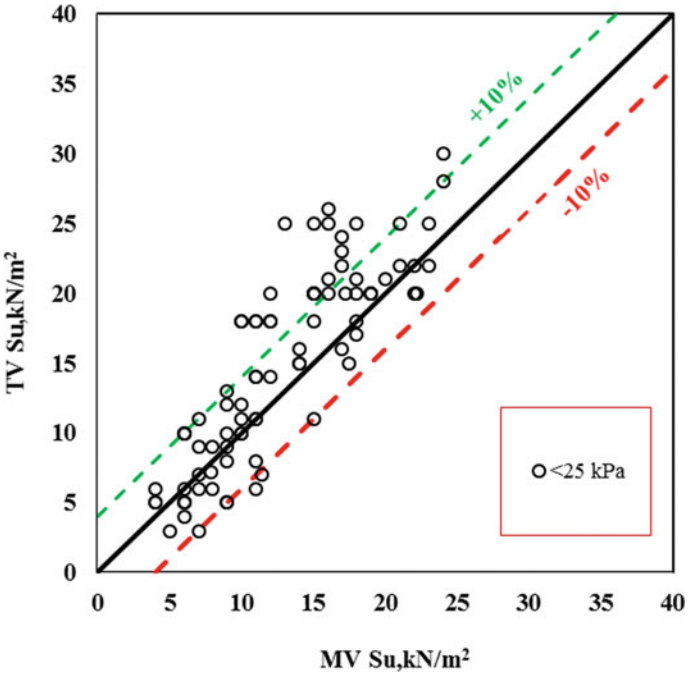

Fig. 32.9 Comparison of Su (kN/m^2) by torvane (TV) and miniature vane (Mv)—very soft to soft CLAYS)

Summary and Conclusion

Undrained shear strength is one of the primary parameters used for designing/assessing the foundation of offshore structures. Routinely, in the Offshore Geotechnical Investigation, the undrained shear strength by torvane (TV), miniature vane (MV), unconsolidated undrained triaxial test (UU), and pocket penetrometer (PP) is adopted at least for every meter of samples recovered. From the author's large database, the undrained shear strength by various methods is compared and summarized as below:

a. The undrained shear strength by TV and MV has a very good agreement in the Very Soft CLAY consistency (up to 12.5 kPa), while TV slightly measures higher shears strength in the Soft CLAY consistency (12.5–25 kPa). But both the methods can be used to develop the ground model.
b. Torvane (TV) and miniature vane (MV) have a good agreement with UU in the strength range of 25–150 kPa, beyond which the measurements are limited by the capacity of the apparatus. UU triaxial can be relied up for the ground model. In the Very Stiff consistency, the operator's error slipping the vane blade rather than shearing has serious consequence of under predicting the undrained shear

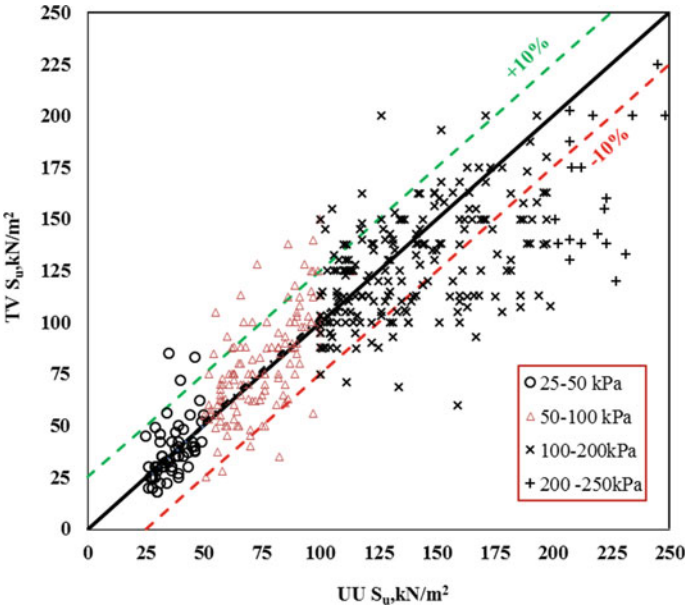

Fig. 32.10 Comparison of Su (kN/m^2) by Torvane (TV) and UU Triaxial

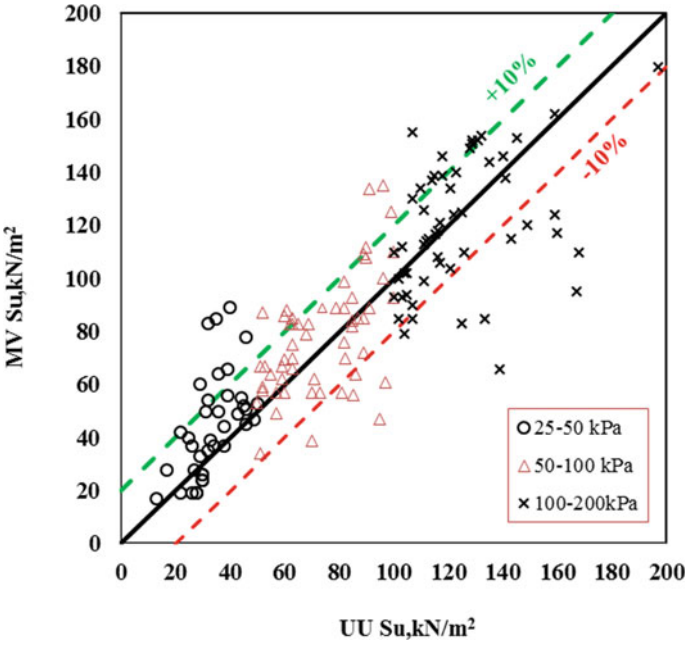

Fig. 32.11 Comparison of Su (kN/m^2) by miniature vane (Mv) and UU triaxial

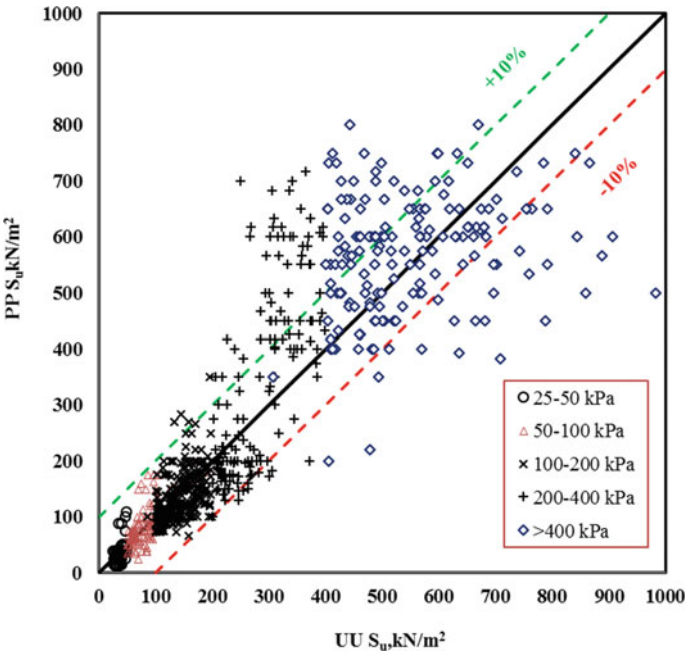

Fig. 32.12 Comparison of Su (kN/m^2) by pocket penetrometer (PP) and UU triaxial

strength. Therefore, skill and experience of the technicians direct the reliability of measurement.

c. Pocket penetrometer also has a good agreement up to about 250 kPa with UU, but has a larger scatter on the heavily over consolidated offshore Middle East soils in Hard to Very Hard CLAYs. UU triaxial again is the preferred method developing the ground model in Hard and Very Hard cohesive soils.

References

1. Domas G, Gintaras Z, Saulius G, Sonata G (2019) Research of undrained shear strength of till fine soils (moraine). In: 13th International conference on modern building materials, structures and techniques, Lithuania
2. Karl T, Ralph BP, Gholamreza M (1996) Soil mechanics in engineering practice. Wiley Inter Science Publication 3rd edn
3. Azhar SY (2017) Capability of pocket penetrometer to evaluate unconfined compressive strength of baghdad clayey soil. Al-Nahrain J Eng Sci 21(1):66–73
4. Grabowski RC (2014) Measuring the shear strength of cohesive sediment in the field Geomorphol Tech Part 1(Sec. 3.1)
5. ASTM D4648 M (2013) Standard test method for laboratory miniature vane shear test for saturated fine-grained clayey soil1
6. Head KH (1994) Manual of soil laboratory testing. Halsted, New York